Consistent Phase Field Modeling of Anisotropic Fracture

With Applications to Composites

Gowri Menon

TU Delft

Consistent Phase Field Modeling of Anisotropic Fracture

With Applications to Composite Materials

by

Gowri Menon (5447372)

in partial fulfilment of the requirements for the degree of
Master in Science in Aerospace Engineering

Project duration:
November 2025 - June 2026

Graduation Committee:

Chair:	Dr. John-Alan Pascoe
Examiner:	Dr. Steven Hulshoff
Responsible supervisors:	Dr. Sergio Turteltaub & Dr. Bianca Giovanardi

Delft University of Technology
Faculty of Aerospace Engineering

TU Delft

Preface

This thesis was completed as part of the Master's program at the Aerospace Structures and Materials department of the Aerospace Engineering faculty. It also marks the end of my five-year journey at TU Delft. These years have been truly remarkable, and I owe much of that to the people I have had the privilege of meeting along the way. My sincere gratitude goes to everyone involved, from professors to teaching assistants and administrative staff; thank you for your time, effort, and dedication to creating such a supportive learning environment.

First and foremost, I would like to thank my supervisors, Dr. Sergio Turteltaub and Dr. Bianca Giovanardi. I deeply appreciate the time and effort both of you dedicated to guiding me. Both of you patiently discussed and reviewed my weekly progress during our Tuesday afternoon meetings, which at times extended well into the evening. This thesis is the result of many insightful discussions and creative explorations, and the passion you both share for research has been a central source of inspiration. I am also incredibly grateful for the support and compassion you have shown me, extending beyond the scope of this thesis to me as a person. Thank you.

To my friends, thank you for making my years in Delft so memorable. It has been lovely getting to know each of you! I will always look back fondly on the dinners we shared and the laughs we had. Wei Wei and Simi, thank you for being like older sisters to me from the first day we met. To my bestie, from thinking of publishing together to talking about Jet Lag, I've enjoyed all our conversations (and a special thank you for introducing me to Sophisticated Sodas). To my favorite neighbor, thank you for all the lifts and the long walks. Your company is unparalleled, and I have always had so much fun with you! Rashmiii, thank you for making these last two years in ASM so much more enjoyable! And, to the not-so-obvious feminist, thank you for being you :)

I would also like to thank my friends and teachers from Rivers. I would not be who I am today if it weren't for all of you. And, to Mr. Van Kollenburg, thank you for always believing in me.

To my grandparents and to my parents, എത്ര പറഞ്ഞാലും തീരാത്ത സ്നേഹവും നന്ദിയും.

ഓം ശ്രീ ഗുരുഭ്യോ നമഃ
ശ്രീ ഗുരുവായൂരപ്പാ ശരണം

Gowri Menon
The Netherlands, June 2026.

Abstract

As engineering materials increase in complexity, their tailored microstructures give rise to advanced fracture processes. Despite independent attempts to address this challenge, a generalized framework capable of accounting for fracture anisotropy and mode-mixity in a consistent manner within phase field modeling remains to be further explored. In light of this, the main research question that guided this thesis was:

How can advanced fracture processes be modeled in a unified thermodynamically consistent framework?

The proposed methodology introduced a direction- and mode-dependent fracture energy to model crack resistance in a physically consistent manner. Contrary to methods commonly seen in the literature that implicitly prescribe anisotropy using a structural tensor, the anisotropic fracture energy is explicitly defined by a function that takes the crack orientation and mode-mixity as arguments. The crack orientation is inferred from the damage gradient. Mode-mixity is characterized by identifying the crack plane and thereby obtaining the normal and tangential tractions. Unlike available methods in the literature for computing mode-mixity, this approach has the benefit that it is robust enough to be used in anisotropic contexts. Furthermore, the coupling between anisotropy and mode-mixity was introduced such that the framework naturally recovers several well-established formulations as limiting cases.

The proposed framework was applied to several numerical examples. By suppressing the dependency of fracture energy on both direction and mode-mixity, the isotropic mode-independent case was retrieved. Under these conditions, the single-edge notched tension test and single-edge notched shear test were investigated. The obtained results were found to be in good agreement with reference solutions available in the literature.

By suppressing the dependency of mode-mixity on fracture energy, the anisotropic mode-independent formulation was obtained. Under these conditions, a comparison was performed to investigate the differences between the standard approach in the literature for introducing fracture anisotropy and the proposed consistent approach. To facilitate a direct comparison, the energetics of the proposed formulation were derived to match the structural tensor-based approach. Yet even under these conditions, it was observed that introducing anisotropy through a consistent framework leads to different behavior compared to the structural tensor-based approach.

By suppressing the dependency of fracture energy on crack orientation, isotropic mixed-mode conditions were recovered. The model performance under these conditions was investigated using two benchmark problems, namely uniaxial compression tests of specimens containing one internal flaw and two internal flaws. The obtained crack patterns showed good agreement with reference numerical results available in the literature as well as with experimental observations, demonstrating that the proposed method for quantifying mode-mixity is feasible. Furthermore, simulations including mixed-mode effects yielded significantly different crack paths compared to mode-independent assumptions, highlighting the necessity of accounting for mode-mixity.

Lastly, to demonstrate the full capabilities of the proposed framework, more advanced fracture processes observed in composites were investigated, namely, crack migration and transverse matrix cracking. These are examples in which both anisotropy and mode-mixity influence the observed crack-path response. Two cross-ply laminate examples were investigated, and the predicted behavior was compared against experimental evidence. It was shown that the framework captured the experimentally observed trends correctly. In the crack migration problem, increasing the ratio of the load application point distance to the delamination front was found to increase the crack migration offset. In the transverse matrix cracking case, the fracture pattern showed several symmetric parallel cracks, similar to experimental findings. Overall, it was shown that the proposed framework offers a unified and consistent way of treating anisotropic and mixed-mode fracture. Due to the flexibility of the framework, it can be naturally extended to model fracture processes in a wide range of materials.

Contents

List of Symbols

$+\eta_0, -\eta_0$	Ends of localization zone	$[-]$
α	Anisotropic fracture energy parameter	$[-]$
α_m	Material property to describe the fracture energy profile	$[-]$
$\bar{\theta}$	Crack propagation angle based on the maximum tangential stress criterion	[deg]
β	Alternative anisotropic fracture energy parameter	$[-]$
β_m	Material property to describe the fracture energy profile	$[\mathrm{J/m^2}]$
$\boldsymbol{\sigma}$	Stress tensor	[Pa]
$\boldsymbol{\varepsilon}$	Linearized strain tensor	$[-]$
χ	Mode-mixity parameter	$[-]$
ϵ	Alternative length scale	[m]
Γ	Admissible crack set	$[-]$
γ	Crack surface density functional	$[1/\mathrm{m}]$
λ	Lame's first parameter	[Pa]
λ_l	Lagrange multipliers	$[-]$
μ	Shear modulus	[Pa]
Ψ_0	Initial elastic energy density	$[\mathrm{J/m^3}]$
ψ_0^+	Undamaged tensile elastic energy density	$[\mathrm{J/m^3}]$
ψ_0^-	Undamaged compressive elastic energy density	$[\mathrm{J/m^3}]$
ψ_d	Fracture energy density	$[\mathrm{J/m^3}]$
ψ_e	Elastic energy density	$[\mathrm{J/m^3}]$
ψ_e^+	Tensile elastic energy density	$[\mathrm{J/m^3}]$
ψ_e^-	Compressive elastic energy density	$[\mathrm{J/m^3}]$
Ψ_{bulk}	Bulk potential energy	[J]
Ψ_{ext}	External potential energy	[J]
Ψ_{frac}	Fracture potential energy	[J]
Ψ_{total}	Total potential energy	[J]
$\Psi_{\text{tot. fracture}}$	Total dissipated energy from multiple damage mechanisms	[J]
ρ	Penalty parameter	$[-]$
σ	Normal traction	[Pa]
σ_{cr}	Critical stress	[Pa]
τ	Tangential traction	[Pa]
τ_t	An instance of simulation time	$[-]$
θ	Crack orientation	[deg]
θ^*	Expected propagation angle based on maximum energy release rate criterion	[deg]
θ'_m	Material property to describe the fracture energy profile	[deg]
$\theta_s, \theta_0, \theta_1$	Constants to characterize the fiber path	[deg]
$\tilde{\theta}$	Preferential anisotropy orientation	[deg]
φ	Damage gradient orientation	[deg]
ϑ	Geometric crack function	$[-]$
$\xi_1, \xi_2, \ldots$	Coefficients of the geometric crack function	$[-]$
ζ	Position from crack	[m]
η	Entropy density per unit volume	$[\mathrm{J/(Km^3)}]$
$\boldsymbol{b}$	Body force	[N]
$\boldsymbol{b}_g$	Boundary vector for the consistent formulation	$[1/\mathrm{m}]$
$\boldsymbol{b}_s$	Boundary vector for the classical formulation	$[1/\mathrm{m}]$
$\boldsymbol{b}_{g,bc}$	Boundary condition for the consistent formulation	$[1/\mathrm{m}]$
$\boldsymbol{b}_{s,bc}$	Boundary condition for the classical formulation	$[1/\mathrm{m}]$
$\boldsymbol{q}$	Heat flux	$[\mathrm{W/m^2}]$
$\boldsymbol{u}$	Displacement field	[m]

$\boldsymbol{u}^e$	Nodal displacement vector	[m]
$\mathbb{C}$	Stiffness tensor	[Pa]
$\mathbb{C}_+$	Tensile part of the stiffness tensor	[Pa]
$\mathbb{C}_-$	Compressive part of the Stiffness tensor	[Pa]
$\mathbb{D}$	Degradation tensor	$[-]$
$\mathbb{M}$	Fourth order transformation tensor	$[-]$
$\mathbf{A}$	Second-order structural tensor	$[-]$
$\mathbf{a}$	Unit vector in the direction of the preferential plane	$[-]$
$\mathbf{a}^\perp$	Unit vector perpendicular to the preferential plane	$[-]$
$\mathbf{B}^d$	Derivative of phase field shape matrix	$[1/\mathrm{m}]$
$\mathbf{B}^u$	Derivative of displacement shape matrix	$[1/\mathrm{m}]$
$\mathbf{D}$	Murakami damage tensor	$[-]$
$\mathbf{d}^e$	Nodal phase field vector	$[-]$
$\mathbf{e}_i$	Principal material directions	$[-]$
$\mathbf{f}_0$	Fixed traction	[N]
$\mathbf{g}$	A vector function	$[-]$
$\mathbf{g}_d$	Regularized additional gradient term	$[\mathrm{J/m^3}]$
$\mathbf{G}_{c,\theta}$	Direction crack resistance tensor	$[\mathrm{J/m^2}]$
$\mathbf{G}_{c0}$	Crack resistance normal to the principal directions	$[\mathrm{J/m^2}]$
$\mathbf{K}_{dd}$	Phase field tangent matrix	[J]
$\mathbf{K}_{du}$	Phase field displacement coupling matrix	$[\mathrm{J/m}]$
$\mathbf{K}_{ud}$	Phase field displacement coupling matrix	[N]
$\mathbf{K}_{uu}$	Mechanical stiffness	$[\mathrm{N/m}]$
$\mathbf{m}$	Unit crack normal vector	$[-]$
$\mathbf{n}$	Outward unit normal vector	$[-]$
$\mathbf{N}^d$	Shape function matrix for phase field	$[-]$
$\mathbf{N}^u$	Shape function matrix for displacement field	$[-]$
$\mathbf{n}_a$	Principal strain directions	$[-]$
$\mathbf{n}_c$	Modified unit crack normal vector	$[-]$
$\mathbf{Q}_a$	Rotation tensor describing orientation	$[-]$
$\mathbf{R}_u$	Displacement residual vector	[N]
$\mathbf{R}_u$	Phase field residual vector	[J]
$\mathbf{t}$	Unit vector in the crack propagation direction	$[-]$
$\mathcal{H}$	Helmholtz energy	[J]
$\mathcal{H}_L$	History variable for longitudinal fiber energy	$[\mathrm{J/m^3}]$
$\mathcal{H}_v$	History variable for the undamaged tensile elastic energy	$[\mathrm{J/m^3}]$
$\mathcal{H}_{TII}$	History variable for transverse shear energy	$[\mathrm{J/m^3}]$
$\mathcal{H}_{TI}$	History variable for transverse matrix energy	$[\mathrm{J/m^3}]$
$\mathcal{H}_{TL}$	History variable for in-plane shear energy	$[\mathrm{J/m^3}]$
$\tilde{\mathbf{g}}_d$	True additional gradient term	$[\mathrm{J/m^3}]$
$a_1, a_2, ...$	Calibration coefficients for mixed-mode degradation functions	$[-]$
c	Nonzero constant	$[-]$
c_0	Scaling parameter	$[-]$
d	Damage variable	$[-]$
d_f	Fiber damage phase field	$[-]$
d_m	Matrix damage phase field	$[-]$
$D_{\text{classical}}$	Accumulated dissipation in the classical model	$[\mathrm{J/m^2}]$
$D_{\text{consistent}}$	Accumulated dissipation in the consistent model	$[\mathrm{J/m^2}]$
E	Energy functional	[J]
E_0	Young's modulus	[Pa]
E_m	Energy function for fracture energy	$[\mathrm{J/m^2}]$
e_{ea}	Principal strains	$[-]$
f	A scalar function	$[-]$

f_c	A formulation of the crack energy density	[J/m^3]
f_t	Failure strength	[Pa]
g	Degradation function	$[-]$
G_c	Fracture energy	[J/m^2]
g_f	Fiber degradation function	$[-]$
G_L	Fracture energy for longitudinal fiber failure	[J/m^2]
g_m	Matrix degradation function	$[-]$
g_s	Shear matrix degradation function	$[-]$
G^{β}_{max}	Energy release rate for crack growth into material β	[J/m^2]
$G_{c,II}$	Mode II fracture energy	[J/m^2]
$G_{c,I}$	Mode I fracture energy	[J/m^2]
G^{β}_c	Energy release rate for crack growth of material β	[J/m^2]
$G_c^{\text{interface}}$	Energy release rate for crack growth of the interface	[J/m^2]
g_L	Longitudinal fiber degradation function	$[-]$
G_{TII}	Fracture energy for transverse shear failure	[J/m^2]
g_{TII}	Transverse shear degradation function	$[-]$
G_{TI}	Fracture energy for transverse matrix failure	[J/m^2]
g_{TI}	Transverse matrix degradation function	$[-]$
G_{TL}	Fracture energy for in-plane shear failure	[J/m^2]
g_{TL}	In-plane shear degradation function	$[-]$
G_T	Energy release rate for crack growth along interface	[J/m^2]
H	Heaviside function	$[-]$
H_0	Threshold history variable	[J/m^3]
i	Displacement increment number	$[-]$
k	Iteration number	$[-]$
k_0	Initial slope of softening curve	[Pa/m]
K_I	Mode I stress intensity factor	[Pa$\sqrt{\text{m}}$]
K_{II}	Mode II stress intensity factor	[Pa$\sqrt{\text{m}}$]
l	Length scale	[m]
l^*	Anisotropic length scale	[m]
m	Material property to describe the fracture energy profile	$[-]$
s	Alternative phase field variable	$[-]$
T	Absolute temperature	[K]
t	Terminal simulation time	$[-]$
U_c	Critical displacement	[m]
w_{frac}	Fracture contribution to energy density in localization zone	[J/m^3]
w_c	Ultimate crack opening	[m]

List of Abbreviations

LEFM	Linear Elastic Fracture Mechanics
SENT	Single-Edge Notched Tension
SENS	Single-Edge Notched Shear
OHT	Open Hole Tension
VSCL	Variable Stiffness Composite Laminates

List of Figures

List of Tables

1: Introduction

It has been a little over a century since Griffith published his work "The phenomena of rupture and flow in solids" [8], changing the field of fracture mechanics. He demonstrated that crack growth is governed by an energetic balance: when sufficient elastic energy is available to create new crack surfaces, propagation becomes energetically favorable. This regards fracture as a process that occurs due to the competition between the energy stored in the bulk material and the energy required for crack propagation. Since then, the field has undergone substantial development, with the rise of several numerical modeling techniques, such as cohesive zone modeling [9], continuum damage mechanics [10], peridynamics [11], and phase field modeling [12], all sharing a common goal: to predict the nucleation and propagation of cracks.

Due to its mathematical versatility, phase field modeling has shown significant potential for modeling a multitude of isotropic fracture processes, including but not limited to ductile fracture [13], dynamic fracture [14], hydrogen-embrittlement fracture [15], etc. Within this framework, fracture is formulated as an energy minimization problem over all admissible displacement and crack fields, closely following the energetic principles originally proposed by Griffith. Rather than representing cracks as geometric discontinuities, phase field modeling approximates fracture through a spatially distributed damage field governed by a continuous scalar variable. This damage variable transitions between intact and fully broken. The advantage of this approach is that because the model is based on the minimization of energy, it requires no prior information on the crack location or propagation direction. In addition, it offers the possibility of incorporating more complex constitutive theory [16].

Modern aviation stands at the intersection of several demanding challenges. The pursuit of cleaner aviation and reduced emissions continues to drive the development of lightweight structural solutions [17], while the increasing demand for versatile and optionally autonomous aircraft leads towards multi-objective designs [18]. Addressing many of these challenges requires innovation in structural design and material selection, and the use of composites has emerged as a promising solution. Yet at the center of all efforts, the pursuit of safety remains paramount. The flexibility offered by composites also brings forth additional challenges for modeling their failure. Due to their non-homogeneous internal structure, they exhibit anisotropic elastic response and fracture behavior. As a result, they can incur various types of damage mechanisms such as matrix cracking, fiber-matrix debonding, delamination, and fiber breakage. These mechanisms are strongly coupled and may evolve simultaneously, making the prediction of failure significantly more complex [19].

To understand the failure of composites, it is important to characterize the *intralaminar* and *interlaminar* fracture behavior. Here, intralaminar refers to crack propagation within individual plies and interlaminar to growth between plies. Owing to the directional arrangement of reinforcing fibers, the intralaminar fracture resistance depends strongly on the orientation of crack propagation relative to the underlying microstructure. In contrast, the interlaminar fracture response is governed primarily by the loading condition, commonly referred to as the fracture opening mode. The resistance can vary significantly depending on whether the crack is driven by opening deformation (Mode I), in-plane sliding or shear (Mode II), or out-of-plane tearing (Mode III) [20]. For structural design and predictive analysis, a reliable numerical representation of these fracture mechanisms is required. In practice, composite structures rarely experience pure-mode loading conditions; instead, fracture processes typically occur under mixed-mode loading [21]. Consequently, accurate modeling of both intralaminar and interlaminar fracture in composites requires accounting for the combined effects of fracture anisotropy and mode-mixity.

Phase field modeling has been used to model fracture processes in composite materials. Yet the modeling of composites brings forth two challenges, the first being to augment the framework to allow anisotropic fracture energy distributions and have a method to distinguish between different failure mechanisms. Since its introduction by Teichtmeister et al. [22], the popular method to deal with anisotropic fracture energy distributions in the literature is to make use of a *structural tensor*. In such cases, a tensor is introduced to act on the damage gradient to implicitly describe a direction-dependent fracture energy. Yet despite its popularity and ease of implementation, there is a limited understanding of what this structural tensor entails. Some authors even argue that it modifies the surface energy of the crack in a physically inconsistent manner [23]. This concern becomes more prevalent in the case of phase field models for composites, where multiple failure mechanisms are introduced through separate energy decompositions, all sharing the same structural tensor.

An alternative approach is to bypass the use of structural tensors by *consistently* defining a direction-dependent fracture energy function that takes the crack orientation as an argument. Even though this approach offers more flexibility (as any thermodynamically permissible fracture energy function can be used), it has only rarely been explored in the literature [23, 24]. In addition, there is little understanding of how the two approaches compare. In their work, Li et al. [25] showed that the structural tensor formulation can be interpreted as arising from a truncated Taylor series expansion of the fracture energy. In such a case, the consistent approach could be seen as a generalization of the structural tensor-based approach. However, to the best of the author's knowledge, a formal investigation of this has not been done.

Furthermore, existing works employing explicitly defined direction-dependent fracture energies have largely neglected the influence of fracture mode-mixity. Yet, for modeling composites, this is a necessity. Motivated by the work of Zhao et al. [3], who introduced a mode-dependent fracture energy to model fracture processes in isotropic rocks, this thesis investigates the potential of incorporating a direction- and mode-dependent fracture energy to consistently model fracture processes. Motivated by the discussion above, a natural application of this methodology is to predict fracture processes in composite materials. In parallel, the thesis also aims to investigate how fracture anisotropy represented through a structural tensor compares with an explicitly defined direction-dependent fracture energy function.

To address this research objective, this thesis is structured into four parts, which are described below.

Literature Review

- Chapter 2 presents an overview of the numerical methods used to model fracture.
- Chapter 3 presents an in-depth review of how phase field modeling has been used to model isotropic fracture.
- Chapter 4 presents the extensions proposed to phase field modeling to model anisotropic fracture and evaluates the state-of-the-art methods.

Methodology

- Chapter 5 derives and discusses the mathematical framework of the proposed formulations.
- Chapter 6 presents the numerical implementation of the model.

Discussion of Results

- Chapter 7 presents the verification plan and discusses the preliminary results related to isotropic mode-independent fracture.
- Chapter 8 evaluates the model results obtained under anisotropic mode-independent conditions.
- Chapter 9 discusses the predictive capability of the framework under isotropic mixed-mode conditions.
- Chapter 10 examines some more complex fracture processes involving fracture anisotropy and mode-mixity.

Closure

- Chapter 11 concludes the research project by reflecting on the original research question and goals.
- Chapter 12 provides recommendations for future work.

Figure 1.1: Cascade overview of the thesis structure.

Literature Review

2: Overview of Modeling Fracture

This chapter acts as a preface to the literature review. It provides an overview of the necessity of, and approaches to, modeling fracture. The challenge of understanding and predicting fracture has evolved significantly over time. To understand the methods proposed and discussed in this thesis, it is useful to understand the landscape of the discipline. This is done in the following sections. Firstly, Section 2.1 presents the scope of this review. This is followed by Section 2.2 wherein a brief history of fracture mechanics is given. Thereafter, from Section 2.3 to Section 2.7, different numerical methods are discussed.

2.1. Scope of Review

To position the methods discussed in this thesis, first, the fundamental principles are introduced, along with the historical development of the field. Thereafter some of the modeling strategies are discussed. To this end, a literature review is done with the following objectives:

- Present a historical account on how predicting and modeling fracture has been developed.
- Establish the different classes of methods that have been and are used to model fracture.

2.2. A Historical Perspective

In engineering materials, a commonly encountered failure mode is fracture. As a result, significant attention has been devoted to predicting crack initiation and propagation with the aim of preventing crack-induced failure. As made-made structures increased in size and significance, ensuring their resilience became increasingly important to prevent fracture and collapse. This was to ensure that they would not fracture and collapse. Yet before the study of fracture was formalized as known today, the first concepts were related to the scaling of structural strength [26]. The initial works of bridging scale and fracture were done by da Vinci [26, 27], where he performed strength tests on iron wires, hypothesizing that the strength of these wires is inversely related to their length.

A century later, Galileo [26, 28] expanded on this idea by identifying the correct scaling laws for bars under tension. He found parallels with the natural world namely how small animals have slender anatomies, whereas larger animals have bulky bones, and he termed this generalization the “weakness of the giants”. This prompted him to further explore the idea that the size has an effect on the failure stress. Towards the late 19th century, as the use of structural steel grew, so did the associated fracture events. These events started to draw the attention of many to understand this phenomenon. People of the time shared the idea that [29]

“*[Effects of percussion and frost upon iron...] is one of the most important subjects that engineers of the present day are called upon to investigate. The lives of many persons, and the property of many more, will be saved if the truth of the matter be discovered— lost if it be not.*”

Ultimately, it is still this aim that drives the study of fracture mechanics today.

Since then, the development of fracture mechanics has been shaped by the work of many researchers. The following paragraphs provide a historical overview; however, it is still selective and does not aim to capture the complete history of the field. Instead, it highlights contributions that are most pertinent to the objectives of this thesis.

Perhaps what can be claimed as the foundation of modern fracture theories lies in the works explored by Griffith [8]. Interestingly enough, the pioneering works of fracture stemmed from a desire to understand the effect of scratches on fatigue. Using Inglis’ [30] conclusion that the stress at the vertex of an elliptical hole in a perfectly elastic body approaches infinity as the ellipse is shrunken into a line crack, Griffith showed that scratches in a component can increase the stress and strain level by a factor. Yet it appeared that, provided the scratches on the component were geometrically similar, the maximum strain or stress obtained was identical. This, however, contradicted the fatigue results and the criterion of rupture, one that was well-established at the time, urging him to transition from stress criteria to energy-based methods [26]. Griffith hypothesized that producing a fracture required a minimum amount of work.

It is interesting to note that Wieghardt [31] had rejected the strength criteria before Griffith, but because of different reasons. Wieghardt noticed that the stresses at the front of a sharp crack remain infinite regardless of how small the applied stress is. The established stress criteria at the time proposed that rupture occurs at a point when a critical threshold is exceeded, yet if there are infinite stresses at arbitrarily small loads, this leads to a contradiction. In fact, Cotterell [26] notes that the concept of stress intensity factors "just slipped through Wieghardt's fingers".

Regardless, it was later Irwin [32] that brought Griffith's theory into an engineering context, thereby establishing Linear Elastic Fracture Mechanics (LEFM). The stress at the crack tip, as predicted by LEFM, is infinite. This motivated Irwin to develop the notion of a stress intensity factor through which he related the elastic energy released for a unit increase in crack area to the stress field at the crack tip. In engineering, this concept has proved to be extremely useful as it can be used as a design parameter to explain the fracture process, while also describing the elastic behavior of cracked objects [33]. Despite the usefulness of LEFM, because it is a one-parameter model, it is only dependent on the current state and does not take the history into account. To address this, Wells [34] introduced the notion of the crack opening displacement to understand fracture under conditions of large plastic deformation.

Yet both the linear and plastic elastic fracture mechanics models carry the inherent limitation that both require there to be an initial crack. In addition, the fracture propagation zone must be small in comparison to the size of the specimen. The desire to address both of these aspects is what prompted the concept of the fracture propagation zone.

The first formulations of fracture mechanics in terms of the fracture propagation zone were envisioned by Barenblatt [9]. Using the observations of Zheltov and Khristianovich [35] that the opposite faces of the crack should be smoothly closed at the tip, Barenblatt hypothesized that there must be an inner zone wherein at equilibrium, forces produce equal and opposite stress intensity factors. Thus, within this zone, the atomic cohesive forces are important and dependent on the crack opening. Dugdale [36] used the concept of fracture propagation zones to model the stress at the tip of the crack. He demonstrated that non-uniformly decreasing cohesive stresses influence crack closure in a similar manner to the uniformly distributed stresses associated with plastic yielding. Thus, while Barenblatt considered the interactomic forces at the crack tip, Dugdale studied the modeling of plastic deformations. Both these works laid the foundation for cohesive zone models.

Alongside this, in the 20th century, several other types of modeling approaches were also developed. In fact today, computational modeling serves as an indispensable tool for doing so and has thus been extensively studied. Yet still, the predictive modeling of cracks remains a significant challenge in solid mechanics [16]. Indeed, as emphasized by Prof. Z. P. Bažant in his acceptance speech for the 2009 Timoshenko Medal,

"The mechanics of damage and quasi-brittle fracture, with its scaling and interdisciplinary coupling, is a problem of the same dimension (as turbulence), which will not be closed even a century from now".

The field of computational fracture mechanics is ever-evolving. The following paragraphs detail the different modeling strategies further.

2.3. Cohesize Zone Modeling

Extending upon LEFM, Barenblatt [9] and Dugdale [36] introduced methods where the fracture process zone is modeled, that is, models wherein the sharp crack is replaced by a cohesive zone. Since their introduction in the mid-20th century, cohesive zone models have been used to model various phenomena related to damage, including the growth of cracks, adhesive contact of non-conforming surfaces, fracture of adhesive joints [37], and stability of interfaces [38].

Classically, the modeling approach is phenomenological in nature [39]. The strength of the material determines the onset of damage, and the evolution is governed through a fracture energy approach specified through the damage evolution model. Within this damage evolution model, the relation between the traction and separation is prescribed. There are also classes of cohesive zone models wherein the tractions are derived as the gradients of a potential [40, 41]. In such cases, the parameters of the potential are not directly related to the physically occurring failure process, but often this has little influence on the results obtained [40]. Although Hui et al. [39] note that whenever there is a deviation from the ideal scenario, then these particularities become important.

Despite the advantages of the modeling approach, it does suffer from some limitations. One of such limitations is the lack of mesh objectivity in numerical results. As evident from the description of the technique, to model cracks, it is required that the mesh conforms to the crack geometry or at least that the mesh is fine enough to provide enough candidate crack paths. In addition, despite the attention that has been given to developing robust cohesive zone models, in some cases, the proposed formulations are not thermodynamically consistent, particularly when attempting to model mixed-mode fracture. This is because cohesive laws are not inherently thermodynamically consistent and rather require special attention to ensure that principles of thermodynamics are not violated [42].

2.4. Extended Finite Element Method (XFEM)

The extended finite element method technique is a direct extension of classical finite element methods designed for dealing with discontinuities. Melenk and Babuška [43] originated the method from the partition-of-unity finite element method. In this modeling technique, the notion of enriched elements are introduced; elements that have additional degrees of freedom that may be activated. The benefit of this is that the finite element mesh can be constructed independently of the geometry of the discontinuities. However, despite the advantages, these methods do suffer from some limitations. When using enriched finite element methods, the discontinuity surface has to be explicitly tracked. As a result, such approaches often require a method capable of representing the crack's topology as well as an associated crack tracking algorithm. However, this becomes particularly challenging for problems with arbitrary and complex crack paths [44].

2.5. Continuum Damage Mechanics

While fracture mechanics deals with macroscopic cracks of finite length, the discipline of continuum damage mechanics is focused on micro-defects and their evolution. In this framework, the evolution of these micro-defects are governed phenomenologically by so-called "damage variables". Unfortunately, the implementation of this approach within the context of finite element methods suffer from excessive mesh dependence due to the lack of an internal length scale parameter [10]. Hence, to the classical formulation, several regularization theories have been proposed. For instance, Simo and Ju introduced a viscous regularization to mimic the experimentally observed phenomenon of microcrack retardation at higher strain rates [45]. Bazant et al. [46] noted that the mesh sensitivity was caused by issues related to strain softening, size effects, and spurious localization, and thus developed a nonlocal continuum concept in which these limitations were addressed. Other regularization efforts include gradient damage models, and gradient-enhanced damage models [16]. These methods try to incorporate information from the surrounding neighborhood into the damage distribution [47].

2.6. Peridynamics

Classical continuum mechanics is capable of determining the deformation response of structures and materials when subject to external loading by neglecting the atomistic structure. However, the limitation is that this approach falls short in the presence of discontinuities. Peridynamics is a non-local theory first proposed by Silling [11] designed to tackle these limitations. In this theory, the governing partial differential equations of classical continuum mechanics are replaced with integral ones. As a result, there is no difficulty in dealing with discontinuous displacements, as the difficulty of resolving discontinuities using (spatial) partial derivatives is avoided.

The original formulation, also termed "bond-based peridynamics", assumed that the interaction forces between material points are equal in magnitude and opposite to each other [11]. However, it was later noted that this assumption imposes constraints on the type of materials and deformations that can be modeled. As a result, an extended formulation was proposed, termed "state-based peridynamics", in which this assumption was relaxed [11]. Attributed to the flexibility of the approach, the method has shown significant potential in modeling crack propagation and failure under impact damage [48]. Furthermore, from a modeling perspective, it is advantageous that the method does not require knowledge of a pre-existing crack or algorithms to track the evolution of the crack [49].

2.7. Phase Field Modeling

Phase field modeling of fracture, like peridynamics, is also a non-local theory [16]. It is closely related to the variational approach to brittle fracture and was first conceptualized in the 1990s. It is grounded in Griffith's theory, as it tries to find the displacement field and the "crack set" that minimizes the total potential energy of solids undergoing fracture [44]. Despite its popularity for simulating fracture, the methodology of phase

field modeling extends the domain of fracture and is extensively used for modeling various other interfacial problems, such as, solidification dynamics [50], hydrogen embrittlement [15], viscous fingering [51], etc. In all these cases, under this approach, systems with sharp interfaces are modeled by using a continuous field variable that describes the different phases within the system using a smooth transition. For the case of fracture this parameter denotes the extent of damage, ranging from a pristine specimen to a fully broken one. Thus, under this approach the crack is represented by a scalar field, and its propagation is modeled using an evolution equation [52].

The merits of phase field modeling are two-fold: firstly, its capability for simulating complicated fracture processes, and secondly, its flexibility. As the model is based on an energy minimization principle, no prior information of a pre-defined crack is required, and rather, the process of crack initiation, growth, and coalescence can be robustly predicted in a thermodynamically consistent manner. In addition, the evolution of damage can be computed on a fixed mesh, through which the task of tracking crack surfaces is bypassed [52]. Due to the variational structure, the approach can be extended to three-dimensional domains straightforwardly. Despite these advantages, the modeling approach is computationally expensive as, sufficiently refined meshes are required in damaged regions, and the convergence rate of the solver is slow [16, 52].

3: Phase Field Modeling of Isotropic Fracture

This chapter presents the first phase of the literature review on phase field modeling for fracture. It provides the theoretical basis of phase field modeling in the context of isotropic fracture, extensions that have been proposed to the classical methodology, and the state-of-the-art models that have been developed. It is to be noted that, given the breadth of the topic, the theory pertaining to, the mathematical details governing, and the implementation of *anisotropic* fracture are not discussed in this chapter. These notions are formalized in Chapter 4.

Firstly, Section 3.1 presents the scope of the literature review and the guiding questions that will be addressed. This is followed by Section 3.2, which establishes the framework of phase field modeling for isotropic fracture, including the mathematical and theoretical background. The numerical implementation strategies are discussed in Section 3.3. Lastly, the application domains to which phase field modeling has been applied to are presented in Section 3.4

3.1. Scope of Review

Given the growing relevance of modeling fracture in engineering and materials science, considerable attention has been devoted to robust numerical methods capable of capturing crack initiation and propagation. Owing to the mathematical flexibility of phase field modeling, it has emerged as a powerful and widely adopted framework. To advance further into this topic, it is essential to understand the governing principles, the methodology, and the approaches that have been taken thus far. To facilitate this, the following objectives are conceptualized:

- Establish the theoretical foundations and capabilities of phase field modeling for fracture.
- Review the methods that have been taken to model isotropic fracture within the phase field modeling community.
- Identify and explore how phase field models have been used to model isotropic fracture in different contexts.

Guided by these objectives, the literature study aims to address the following questions.

1. What is the mathematical setting in which phase field modeling exists?
2. What are the necessary conditions to take into account for obtaining physically meaningful results?
3. What strategies have been utilized to implement phase field modeling?
4. To what domains has the classical phase field modeling formulation been extended to, and how have those reformulations been proposed?

3.2. Phase Field Modeling

Phase field modeling, as formulated within the mechanics community, is rooted in the theory of variational calculus. The implementation of this theory finds itself within a regularization problem. This section is dedicated to building the framework of the theoretical basis and presenting the mathematical model. To this end, seven aspects are dealt with:

1. *The variational approach to brittle fracture*: a discussion of the minimization problem, the regularized formulation of the problem, and the notion of the crack surface density function.
2. *The geometric crack function*: details pertaining to the phase field representation of a sharp crack topology by a diffuse “smeared” crack.
3. *The classical formulation*: the mathematical details describing the classical formulation of phase field modeling.
4. *The energetic degradation function*: an explanation on how the stored energy responds to changes in the crack phase field.
5. *Global response of commonly adopted models*: a comparison of the critical stress for models commonly adopted in the literature.
6. *Thermodynamic considerations*: the conditions that arise to ensure that the modeling framework is thermodynamically permissible.
7. *Implementation aspects*: additional remarks on the considerations required to obtain physically meaningful results.

3.2.1. Variational Approach to Brittle Fracture

Phase field modeling of fracture has largely been developed by two separate communities, namely the "physics" and the "mechanics" communities. Both approaches have been developed rather independently and derive the constitutive and phase field evolution equations differently. While the former extends from the Landau and Ginzburg phase transition theory, the latter is an extension of Griffith's theory of fracture. Two critical distinctions between the models are that the physics community neither introduces a length scale parameter to represent the diffuse crack nor includes the fracture energy in the free energy. Moreover, the types of problems solved by both methods are also different. The models developed by the physics community are primarily concerned with modeling dynamic fracture. Whereas, traditionally, the focus of the mechanics community has been on quasi-static brittle fracture [44].

The phase field models developed by the mechanics community are based on the variational approach of brittle fracture as proposed by Francfort and Marigo [12]. Under this formulation, an energy functional is constructed for representing the complete fracture process, starting from crack initiation to propagation and branching. As a result, the fracture process is seen as the consequence of minimizing the energy functional over all admissible displacement fields and crack sets. This energy functional, E, is given as follows:

$$E(\mathbf{u},\Gamma) = \int_{\Omega} \Psi_0(\boldsymbol{\varepsilon}(\mathbf{u}))\,\mathrm{d}V + \int_{\Gamma} G_c\,\mathrm{d}S, \tag{3.1}$$

where $\Gamma \subset \Omega$ is the admissible crack set, $\mathbf{u}$ is the displacement field discontinuous across Γ, $\boldsymbol{\varepsilon}$ is the standard linearized strain tensor given by $\frac{1}{2}(\nabla\mathbf{u} + (\mathbf{u})^{\mathrm{T}})$, Ψ_0 is the elastic energy density, and G_c is the fracture energy, that is, the critical energy release rate.

To facilitate the numerical implementation, Bourdin et al. [53] proposed the so-called *regularized variational fracture model* based on the Ambrosio and Tortorelli [54] regularization. In this regularized framework, a sharp crack is replaced by a diffuse crack, and thereby the sharp crack surface is regularized by the following functional:

$$\int_{\Gamma} \mathrm{d}S \approx \int_{\Omega} \gamma(d,\nabla d)\,\mathrm{d}V, \tag{3.2}$$

where γ is known as the crack surface density functional, and d is a variable introduced to denote damage, such that $d = 0$ is fully intact material and $d = 1$ is fully damaged.

As a result, the surface energy is approximated as

$$\int_{\Gamma} G_c\,\mathrm{d}S \approx \int_{\Omega} G_c\gamma(d,\nabla d)\,\mathrm{d}V\ . \tag{3.3}$$

From these equations, it is noticed that the regularized formulation introduces an auxiliary variable, d, to represent the crack topology. This variable is independent of the mesh and geometry to avoid dealing with the free discontinuity sets of the displacement field. Furthermore, it denotes the nature of damage and ranges from intact to fully broken. Although the proof of this is omitted, it is noted that the original variational approach to fracture gets recovered from the regularized formulation as the transition zone length, that is, the length scale, l, approaches zero in the sense of $\Gamma-$ convergence (which is a form of variational convergence that ensures the convergence of a minimizer [16], this is further elaborated below). Based on this, the energy functional is given by

$$E(\mathbf{u},d) = \int_{\Omega} (1-d)^2\Psi_0(\boldsymbol{\varepsilon}(\mathbf{u}))\,\mathrm{d}V + \int_{\Omega} G_c\frac{1}{2}\left[\frac{1}{l}d^2 + l|\nabla d|^2\right]\mathrm{d}V\ . \tag{3.4}$$

> ***Remark 3.1***
>
> Wu et al. [16] describe $\Gamma-$ convergence, as a form of variational convergence that ensures the convergence of a minimizer. More specifically, it requires that the convergence of minimizers be local and stable under continuous perturbations [55].

Combining these two equations, it is apparent that the crack surface density functional is given by the quadratic form

$$\gamma(d,\nabla d) = \frac{1}{2}\left(\frac{1}{l}d^2 + l|\nabla d|^2\right)\ . \tag{3.5}$$

Section 3.2.2 elaborates on this surface density in more length.

Remark 3.2

Historically, the energy functional as formulated by Bourdin et al. [53] was of the form

$$E(\mathbf{u}, s) = \int_\Omega s^2 \Psi_0(\boldsymbol{\varepsilon}(\mathbf{u}))\, \mathrm{d}V + \int_\Omega G_c \left[\frac{1}{4\epsilon}(1-s)^2 + \epsilon |\nabla s|^2 \right] \mathrm{d}V, \tag{3.6}$$

where s is introduced to denote the lack of damage and ϵ is the length scale parameter that controls the transition zone between fully damaged and pristine material.

While Equation 3.4 and Equation 3.6 may appear different, due to the relations $\epsilon = l/2$, and $s = 1 - d$, both forms are equivalent. Regardless, it is important to note that while $s = 0$ denotes a fully damaged material, $d = 0$ denotes a fully pristine material. Nowadays, Equation 3.4 is more commonly seen in the literature.

3.2.2. Geometric Crack Function

A characteristic of phase field modeling is the diffuse representation of a crack. To understand what this entails, firstly, the topology of a sharp crack is introduced. To this end, consider an infinitely expanded bar with a sharp crack at the axial position of $\zeta = 0$. In such a case, the crack topology is expressed as follows:

$$d(\zeta) = \begin{cases} 1 & \text{when } \zeta = 0, \\ 0 & \text{otherwise}, \end{cases} \tag{3.7}$$

where $d(\zeta)$ denotes the so-called *crack phase field*.

This crack phase field can also be used to represent diffuse cracks smeared within a localization band. The width of this band is governed by the length scale parameter. For the quadratic crack surface density functional introduced in Equation 3.5, a solution to the spatial representation of the crack is given by

$$d(\zeta) = \exp\left(-\frac{|\zeta|}{l} \right). \tag{3.8}$$

This crack phase field satisfies the conditions that

$$d(0) = 1, \qquad \text{and} \qquad \lim_{\zeta \to \pm\infty} d(\zeta) = 0\,. \tag{3.9}$$

As a side remark, note that this type of model is also referred to as the AT2 model, where the A and T stand for Ambrosio and Tortorelli, and the 2 refers to the order of the crack function.

The diffuse representation of this crack is visualized in Figure 3.1 for some reference length scale values.

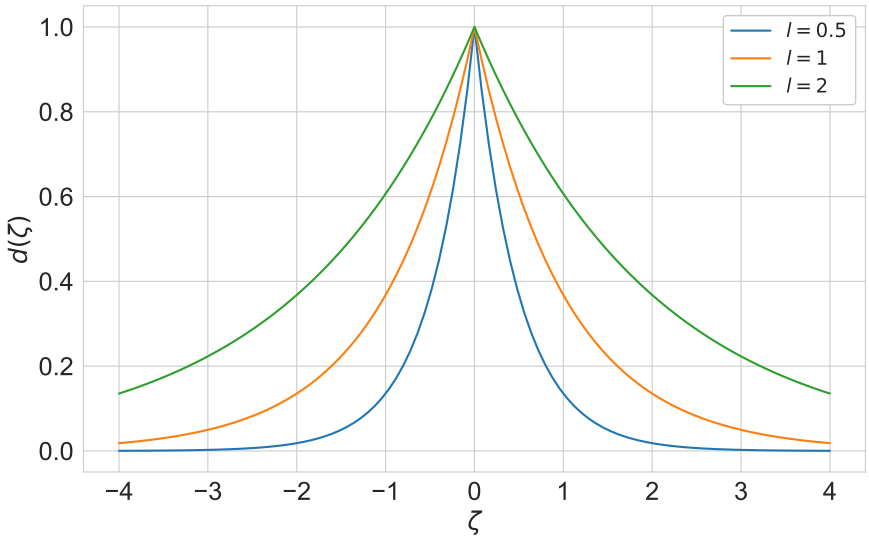

Figure 3.1: Diffuse representation of a crack at $\zeta = 0$ for length scale values of 0.5, 1, and 2.

From this figure, two points are of relevance. Firstly, it is apparent that the length scale parameter directly influences the bandwidth of the crack, with a higher value leading to a more diffuse nature. Furthermore, it is evident that when using the quadratic function, the sharp crack is regularized into a diffuse crack with *infinite support*. Support, here, refers to the domain where a function is not zero; to exemplify, a sharp crack naturally has a point support. A consequence of having an infinite support is that to determine the phase field at a given point, the phase field evolution equation must be solved in the entire computational domain.

Remark 3.3

While this does not directly follow from the figure, it is also noted that when a quadratic crack surface density function is used, it is not possible to recover a purely linear elastic response prior to the onset of damage. This is because the phase field begins to evolve for arbitrarily small loading levels. In other words, it has no *damage threshold*. For geometric crack functions with a damage threshold, there is a critical level for the driving force that must be exceeded before damage initiation occurs [16, 56].

The quadratic function is not unique, and there have been attempts to consider different crack surface density functionals. In fact, any functional that satisfies the following form is permissible [16]:

$$\gamma(d, \nabla d) = \frac{1}{c_0}\left[\frac{1}{l}\vartheta(d) + l|\nabla d|^2\right], \tag{3.10}$$

where $\vartheta(d)$ is the geometric crack function, and $c_0 = 4\int_0^1 \sqrt{\vartheta(\hat{d})}\,\mathrm{d}\hat{d}$ is a scaling parameter introduced so that the sharp crack surface is recovered for a fully softened crack.

While several functions can satisfy Equation 3.10, for modeling localized failure in solids from both a theoretical and numerical perspective, it is desired to have crack surface density functions with finite support [57]. Since then, other functions have been proposed, of which the most common ones are summarized in Table 3.1. Pham et al. [47] proposed a non-standard phase field model using a linear crack surface density function which has a support of $4l$. As a side remark, it is noted that this is also referred to as the AT1 model. A characteristic of these alternative formulations is that the damage variable is no longer guaranteed to remain between 0 and 1, and hence the phase field boundedness has to be explicitly enforced [16].

Table 3.1: The geometric crack functions that have been used in different models, and the corresponding crack phase fields and supports.

Model	$\vartheta(d)$	$d(\zeta)$	Support
AT2	d^2	$\exp\left(-\frac{\lvert\zeta\rvert}{l}\right)$	∞
AT1	d	$\left(1-\frac{\lvert\zeta\rvert}{2l}\right)^2$	$4l$
Wu	$2d-d^2$	$1-\sin\left(\frac{\lvert\zeta\rvert}{l}\right)$	πl

3.2.3. Classical Formulation

Consider a domain $\mathcal{B}$ in the reference configuration that has an external boundary denoted by $\partial\mathcal{B}$ and an internal crack discontinuity that evolves, denoted by Γ.

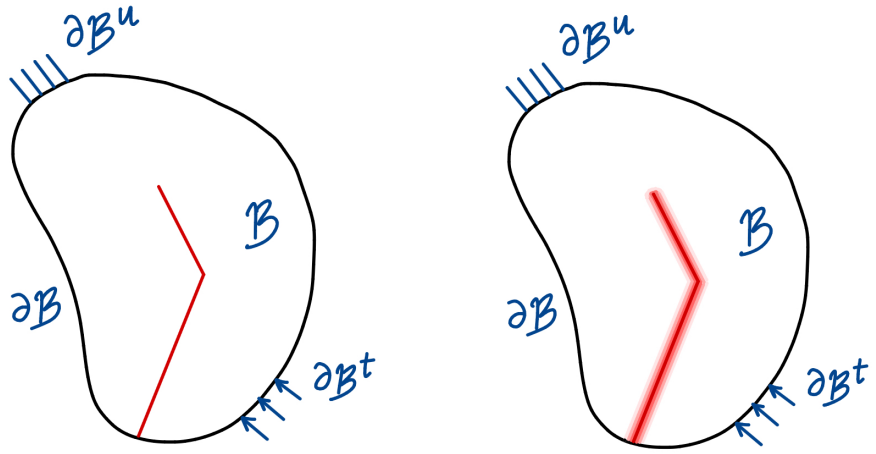

Figure 3.2: Schematic of the solid domain with a sharp crack (left) and a diffuse crack (right).

The total potential energy in a system based on the variational principle for quasi-static fracture is given by

$$\Psi_{\text{total}} = \Psi_{\text{bulk}} + \Psi_{\text{frac}} - \Psi_{\text{ext}}, \tag{3.11}$$

where Ψ_{bulk}, Ψ_{frac}, and Ψ_{ext} are the bulk, fracture, and external potential energy, respectively. These three terms are elaborated below.

Firstly, the potential of external forces can be further expressed as

$$\Psi_{\text{ext}} = \int_{\mathcal{B}} \mathbf{b} \cdot \mathbf{u} \, \mathrm{d}V + \int_{\partial \mathcal{B}_s} \mathbf{f}_0 \cdot \mathbf{u} \, \mathrm{d}S, \tag{3.12}$$

where $\mathbf{b}$ refers to the body force, $\mathbf{u}$ represents the displacement field imposed on the Dirichlet boundary, and $\mathbf{f}_0$ is the fixed traction on the Neumann-type boundary $\partial\mathcal{B}$.

Based on the Griffith energy principle and the regularized phase field approximation (see discussion Section 3.2.1), the fracture energy can be approximated as

$$\Psi_{\text{frac}} = \int_{\Gamma} G_c \, \mathrm{d}S \approx \int_{\mathcal{B}} G_c \gamma(d, \nabla d) \, \mathrm{d}V = \int_{\mathcal{B}} \frac{G_c}{c_0} \left[\frac{\vartheta(d)}{l} + l |\nabla d|^2 \right] \mathrm{d}V, \tag{3.13}$$

where d is the phase field variable that ranges from 0 (a pristine material) to 1 (a fully damaged material), G_c represents the critical energy release rate, γ refers to the crack surface density functional, ϑ is the geometric crack function, l is the regularized length scale parameter that determines the width of the diffuse crack, and c_0 is a normalization parameter defined by

$$c_0 = 4 \int_0^1 \sqrt{\vartheta(\hat{d})} \, \mathrm{d}\hat{d}, \tag{3.14}$$

such that the sharp crack surface is recovered for a fully softened crack. For the quadratic crack density function, c_0 is equal to 2.

At this point, a brief remark is made on the length scale parameter. When this parameter approaches zero, the regularized crack surface becomes equivalent to the sharp crack in the sense of $\Gamma-$convergence. In addition, in such a case, LEFM is recovered. However, this has the issue that stresses become unbounded [53]. As a result, this length scale cannot be regarded as merely a numerical parameter. This is further discussed in Section 3.2.5.

Lastly, the bulk energy is equal to the elastic energy, as is typical for elastic solids

$$\Psi_{\text{bulk}} = \int_{\mathcal{B}} \psi_e(\boldsymbol{\varepsilon}, d) \, \mathrm{d}V, \tag{3.15}$$

where $\psi_e(\boldsymbol{\varepsilon}, d)$ is the elastic energy density of the damaged medium.

Based on Equation 3.12 through Equation 3.15, Equation 3.11 can be expressed as

$$\Psi_{\text{total}} = \int_{\mathcal{B}} \psi_e(\boldsymbol{\varepsilon}, d)\,\mathrm{d}V + \int_{\mathcal{B}} \frac{G_c}{c_0}\left[\frac{\vartheta(d)}{l} + l|\nabla d|^2\right]\,\mathrm{d}V - \int_{\mathcal{B}} \mathbf{b}\cdot\mathbf{u}\,\mathrm{d}V - \int_{\partial\mathcal{B}_s} \mathbf{f}_0\cdot\mathbf{u}\,\mathrm{d}S\,. \tag{3.16}$$

Crack initiation occurs when this total potential energy reaches a critical value, and hence the phase and displacement field are determined by solving the following minimization problem:

$$(\mathbf{u}, d) = \text{Arg}\{\text{inf}[\Psi_{\text{total}}(\mathbf{u}, d)]\}, \tag{3.17}$$

for all permissible displacement and phase fields.

To derive the governing equations, the first variation of the energy function is considered. To simplify notation and to keep it generic, the crack surface density is written in condensed form by γ. Thus, the energy functional is given by

$$\Psi_{\text{total}} = \int_{\mathcal{B}} \psi_e(\boldsymbol{\varepsilon}, d)\,\mathrm{d}V + \int_{\mathcal{B}} G_c\gamma(d, \nabla d)\,\mathrm{d}V - \int_{\mathcal{B}} \mathbf{b}\cdot\mathbf{u}\,\mathrm{d}V - \int_{\partial\mathcal{B}_s} \mathbf{f}_0\cdot\mathbf{u}\,\mathrm{d}S\,. \tag{3.18}$$

The first variation of the energy function is then given by the following equation, where the arguments are suppressed for conciseness:

$$\delta\Psi_{\text{total}} = \int_{\mathcal{B}} \frac{\partial\psi_e}{\partial\boldsymbol{\varepsilon}}\delta\boldsymbol{\varepsilon}\,\mathrm{d}V + \int_{\mathcal{B}} \frac{\partial\psi_e}{\partial d}\delta d\,\mathrm{d}V + \int_{\mathcal{B}} G_c\left(\frac{\partial\gamma}{\partial d}\delta d + \frac{\partial\gamma}{\partial\nabla d}\cdot\delta\nabla d\right)\,\mathrm{d}V - \int_{\mathcal{B}} \mathbf{b}\cdot\delta\mathbf{u}\,\mathrm{d}V - \int_{\partial\mathcal{B}_s} \mathbf{f}_0\cdot\delta\mathbf{u}\,\mathrm{d}S\,. \tag{3.19}$$

To further analyze this equation, the first variation of displacement is decoupled from the first variation due to the phase field. In such a case, the first variation of displacement is given by

$$\delta_u\Psi_{\text{total}} = \int_{\mathcal{B}} \frac{\partial\psi_e}{\partial\boldsymbol{\varepsilon}}\delta\boldsymbol{\varepsilon}\,\mathrm{d}V - \int_{\mathcal{B}} \mathbf{b}\cdot\delta\mathbf{u}\,\mathrm{d}V - \int_{\partial\mathcal{B}_s} \mathbf{f}_0\cdot\delta\mathbf{u}\,\mathrm{d}S\,. \tag{3.20}$$

Noting that by virtue of thermodynamic reasoning, stress, $\boldsymbol{\sigma}$, is the partial derivative of the energy density with respect to strain, the following is obtained:

$$\delta_u\Psi_{\text{total}} = \int_{\mathcal{B}} \boldsymbol{\sigma}\delta\boldsymbol{\varepsilon}\,\mathrm{d}V - \int_{\mathcal{B}} \mathbf{b}\cdot\delta\mathbf{u}\,\mathrm{d}V - \int_{\partial\mathcal{B}_s} \mathbf{f}_0\cdot\delta\mathbf{u}\,\mathrm{d}S\,. \tag{3.21}$$

By using the divergence theory, the standard equation of equilibrium is obtained, namely

$$\delta_u\Psi_{\text{total}} = \int_{\mathcal{B}} (\nabla\cdot\boldsymbol{\sigma} + \mathbf{b})\cdot\delta\mathbf{u}\,\mathrm{d}V - \int_{\partial\mathcal{B}_s} (\boldsymbol{\sigma}\cdot\mathbf{n} - \mathbf{f}_0)\cdot\delta\mathbf{u}\,\mathrm{d}S\,. \tag{3.22}$$

To obtain the phase field evolution equation, the first variation due to the phase field is considered, namely

$$\delta_d\Psi_{\text{total}} = \int_{\mathcal{B}} \frac{\partial\psi_e}{\partial d}\delta d\,\mathrm{d}V + \int_{\mathcal{B}} G_c\frac{\partial\gamma}{\partial d}\delta d\mathrm{d}V + \int_{\mathcal{B}} G_c\frac{\partial\gamma}{\partial\nabla d}\cdot\delta\nabla d\,\mathrm{d}V\,. \tag{3.23}$$

To rewrite the third term, it is useful to consider integration by parts, given by

$$\int_\Omega \nabla f\cdot\mathbf{g}\,\mathrm{d}V = \int_\Omega (\nabla\cdot(f\mathbf{g}) - f\nabla\cdot\mathbf{g})\,\mathrm{d}V = \int_{\partial\Omega} f\mathbf{g}\cdot\mathbf{n}\,\mathrm{d}S - \int_\Omega f\nabla\cdot\mathbf{g}\,\mathrm{d}V, \tag{3.24}$$

where f, and $\mathbf{g}$ are two functions and $\mathbf{n}$ is the unit vector normal to $\partial\Omega$.

Applying this to the third term in Equation 3.23, one obtains

$$\int_{\mathcal{B}} \frac{\partial\gamma}{\partial\nabla d}\cdot\delta\nabla d\,\mathrm{d}V = \int_{\mathcal{B}} \frac{\partial\gamma}{\partial\nabla d}\cdot\nabla\delta d\,\mathrm{d}V = \int_{\partial\mathcal{B}} \left(\frac{\partial\gamma}{\partial\nabla d}\cdot\mathbf{n}\right)\delta d\,\mathrm{d}S - \int_{\mathcal{B}} \nabla\cdot\left(\frac{\partial\gamma}{\partial\nabla d}\right)\delta d\,\mathrm{d}V\,. \tag{3.25}$$

Substituting Equation 3.25 into Equation 3.23, the first variation is given by

$$\delta_d\Psi_{\text{total}} = \int_{\mathcal{B}} \frac{\partial\psi_e}{\partial d}\delta d\,\mathrm{d}V + \left[\int_{\mathcal{B}} G_c\left(\frac{\partial\gamma}{\partial d}\right)\delta d\,\mathrm{d}V - \int_{\mathcal{B}} G_c\nabla\cdot\left(\frac{\partial\gamma}{\partial\nabla d}\right)\delta d\,\mathrm{d}V + \int_{\partial\mathcal{B}} G_c\left(\frac{\partial\gamma}{\partial\nabla d}\cdot\mathbf{n}\right)\delta d\,\mathrm{d}S\right]\,. \tag{3.26}$$

This can be simplified to the following form:

$$\delta_d \Psi_{\text{total}} = \int_{\mathcal{B}} \left[\frac{\partial \psi_e}{\partial d} + G_c \partial_d \gamma \right] \delta d \, \mathrm{d}V + \int_{\partial \mathcal{B}} G_c \left(\frac{\partial \gamma}{\partial \nabla d} \cdot \mathbf{n} \right) \delta d \, \mathrm{d}S, \tag{3.27}$$

where

$$\partial_d \gamma = \frac{\partial \gamma}{\partial d} - \nabla \cdot \left(\frac{\partial \gamma}{\partial \nabla d} \right) . \tag{3.28}$$

For the crack density function as given in Equation 3.10, the following is obtained:

$$\partial_d \gamma = \frac{1}{c_0} \left[\frac{\vartheta'(d)}{l} - 2l\Delta d \right] . \tag{3.29}$$

Equation 3.22 and Equation 3.27 should hold for any arbitrary $\delta \mathbf{u}$ and δd, and hence the integrands must be equal to zero. Thus, based on the variational principle, the minimization problem results in the following two governing differential equations:

$$\begin{aligned} &\nabla \cdot \boldsymbol{\sigma} + \mathbf{b} = 0 \quad \text{in } \mathcal{B}, \\ &\frac{\partial \psi_e}{\partial d} + \frac{G_c}{c_0} \left(\frac{\vartheta'(d)}{l} - 2l\Delta d \right) = 0 \quad \text{in } \mathcal{B} . \end{aligned} \tag{3.30}$$

In addition, the coupled displacement and phase fields should also satisfy the following mechanical boundary condition:

$$\begin{cases} \mathbf{u} = \mathbf{u}_0 & \text{on } \partial \mathcal{B}_u, \\ \boldsymbol{\sigma} \cdot \mathbf{n} = \mathbf{f}_0 & \text{on } \partial \mathcal{B}_s, \end{cases} \tag{3.31}$$

where $\partial \mathcal{B}_u$ and $\partial \mathcal{B}_s$ are two disjoined parts of the boundary where a fixed displacement $\mathbf{u}_0$, and a fixed traction $\mathbf{f}_0$ are applied, respectively; and the following phase field boundary condition:

$$\nabla d \cdot \mathbf{n} = 0 \quad \text{on } \partial \mathcal{B} . \tag{3.32}$$

3.2.4. Energetic Degradation Function

An important aspect that has not been discussed so far is how the stored energy density responds to the presence of damage. This dependency is governed by the degradation function. In the AT2/AT1 models, a quadratic degradation function of the form $(1-d)^2$ is often used. However, similar to the geometric crack function, this choice of degradation function is not unique; rather, any function is permitted provided the following conditions are satisfied:

- When there is no damage, there is no degradation, and when the specimen is fully damaged, the degradation function returns a completely broken state. Hence, the following should hold: $g(0) = 1, \quad \text{and} \quad g(1) = 0$.
- The degradation function must be monotonically decreasing, i.e., $g'(d) < 0$.
- To ensure that the localization band does not grow orthogonally, the following must hold: $g'(1) = 0$.

Possible Degradation Functions

Satisfying these constraints, common choices for the degradation function are given in Table 3.2.

Table 3.2: Various degradation functions that have been proposed and the corresponding authors.

Degradation function, $g(d)$	Author
$(1-d)^2$	Bourdin et al. [53]
$\frac{(1-d)^2}{(1-d)^2+Q(d)}, \quad Q(d) = d + pd^2$	Lorentz et al. [58, 59]
$\frac{(1-d)^p}{(1-d)^p+Q(d)}, \quad Q(d) = a_1 d + a_1 a_2 d^2 + a_1 a_2 a_3 d^3$	Wu [57]

A subtlety here is that the choice of degradation function and length scale are directly related to the global response of the solid. While perhaps it is intuitively expected that the degradation function and the crack surface density functional have an effect on the global response, the length scale (so far) has only been introduced as a regularization parameter. However, it can be shown mathematically and numerically that classical phase field modeling for brittle fracture fails in predicting a length scale independent global response [57]. In fact, the length scale has a direct effect on the critical stress value [16]. In other words, although it is a regularization parameter, it is also effectively a material parameter. This aspect is further illustrated and discussed in Section 3.2.5.

The coupling between the length scale and global response can be unfavorable, and thus, to overcome this, Wu [57] proposed a set of optimal characteristic functions that are calibrated based on common softening laws used in cohesive zone modeling. Fittingly, they have since been known as cohesive zone regularized degradation functions. Under this framework, both the failure strength and the traction-separation law are independent of the incorporated length scale parameter. However, the length scale should still be smaller than a *characteristic length scale* to ensure convexity of the energy degradation function. This upper bound imposed on the length scale parameter can introduce stringent mesh requirements when analyzing very large structures or in high-strength materials. To further overcome these issues, there have been alternative phase field modeling formulations that removes the upper bound constraint on the length scale altogether [60, 61].

3.2.5. Comparison of Global Responses

So far the different components comprising a phase field model have been discussed (the crack surface density and the degradation function). It has been shown that there are several options for both. In the literature, three models are often adopted. In this subsection, the global responses of these three models are considered. These models are:

- **AT2**: a quadratic geometric crack surface is combined with the quadratic degradation function.
- **AT1**: a linear geometric crack surface is combined with the quadratic degradation function.
- **Cohesive zone modeling inspired**: a polynomial geometric crack surface is combined with a rational degradation function.

AT2

Perhaps the most commonly adopted model is the AT2 model. Yet, despite its popularity, the global response is length scale dependent. It can be shown that for the AT2 model, the critical stress, σ_{cr} is given as follows [56]:

$$\sigma_{cr} = \frac{3}{16}\sqrt{\frac{3E_0G_c}{l}} \quad \Rightarrow l = \frac{27E_0G_c}{256\sigma_{cr}^2} \,. \tag{3.33}$$

The second relation follows naturally; as E_0 (the Young's modulus), G_c, and σ_{cr} are material properties, to satisfy Equation 3.33 for critical stress of the material, the length scale must be chosen appropriately. For completeness, a derivation of this expression is presented in Appendix A.

AT1

A popular alternative model is the AT1 model. This model has the benefit that there is a lower limit for damage initiation. In other words, an infinitesimal strain does not introduce an infinitesimal increase in phase field. However, a consequence of this is that the lower bound of the phase field variable is not directly enforced, and hence must be accounted for. In such a case, the expressions for the critical stress, and thereby for the length scale parameter, are given as follows [56]:

$$\sigma_{cr} = \sqrt{\frac{3E_0G_c}{8l}} \quad \Rightarrow l = \frac{3E_0G_c}{8\sigma_{cr}^2} \,. \tag{3.34}$$

The stress-strain curves for both the AT1 and AT2 model are visualized in Figure 3.3.

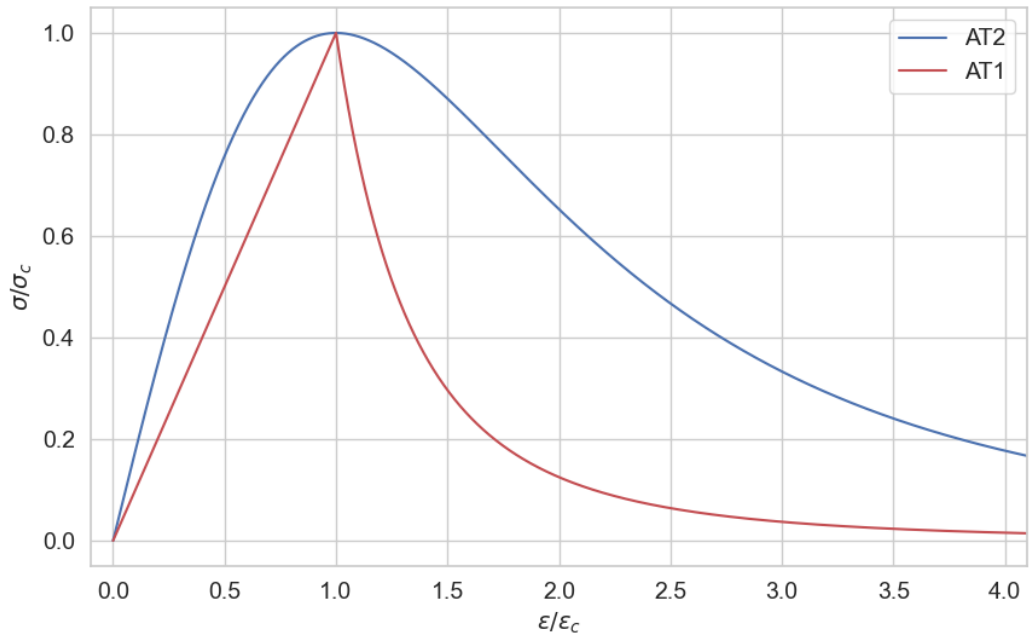

Figure 3.3: Stress plotted as a function of strain for the AT1 and AT2 models.

Equation 3.34 and Equation 3.33 show that the critical stress of the phase field models is governed by the choice of the length scale parameter. Previously, the length scale was assumed to be a purely numerical parameter that influences the nature of the crack, such that as it approaches zero, the sharp crack limit is retrieved. Yet, this analysis shows that it also affects the critical stress values, and hence must be chosen appropriately for each material. It is not difficult to imagine that for large-scale structures composed of brittle materials, choosing appropriate values for the length scale can result in excessively fine meshes, leading to unreasonable computational runtime. Needless to say, this can bring forth unfavorable computational challenges. This motivated the development of length-scale-independent frameworks, as discussed below.

Cohesive Zone Modeling Inspired Degradation Functions

Inspired by cohesive zone modeling, different forms of degradation functions and geometric crack surface functions have been proposed, termed cohesive zone modeling-inspired degradation functions. Wu laid the foundation for proposing a family of degradation functions that converge to a cohesive zone model in the sharp crack limit. Moreover, his framework is presented in a manner to facilitate length-scale-invariant global responses. In other words, the length scale remains purely a numerical parameter that governs the diffuse nature of the crack. To satisfy these objectives, Wu [57] considers the following general form for the degradation function:

$$g(d) = \frac{1}{1+\phi(d)}, \qquad \text{where } \phi(d) = \frac{Q(d)}{(1-d)^p}, \tag{3.35}$$

$p > 0$ for the exponent and $Q(d)$ is a continuous function greater than zero given by

$$Q(d) = a_1 d + a_1 a_2 d^2 + a_1 a_2 a_3 d^3 + ... \tag{3.36}$$

where the coefficients $a_1, a_2, ...$ can be calibrated based on the material properties.

Furthermore, unlike the AT2/AT1 models, Wu proposes a polynomial form for the geometric crack function, namely

$$\vartheta(d) = \xi_1 d + \xi_2 d^2 + ... + \xi_m d^m, \tag{3.37}$$

such that the coefficients $\xi_1, ...\xi_m$ satisfy the partition of unity, i.e.,

$$\vartheta(1) = 1 \qquad \Rightarrow \qquad \sum_{i=1}^{m} \xi_i = 1\ . \tag{3.38}$$

Despite the possibility of higher-order polynomials, Wu performed his analysis for the quadratic form

$$\vartheta(d) = \xi d + (-\xi + 1)d^2, \tag{3.39}$$

where ξ can take on any value between 0 and 2 (inclusive). This is because for other values of ξ it cannot be ensured that $\vartheta(d) < 0$ and $\vartheta(d) > 1$ for all $d \in [0, 1]$.

Under these conditions, Wu derived the expressions for the constants $a_1, a_2, ..$ such that the global response for a softening bar under tension is equivalent to a desired cohesive zone model. In general, these are given by

$$a_1 = \frac{2E_0 G_c}{f_t^2}\frac{\xi}{c_0 l}, \tag{3.40}$$

$$a_2 = \frac{1}{\xi}\left[\left(-\frac{4\pi\xi^2}{c_0}\frac{G_c}{f_t^2}k_0\right)^{\frac{2}{3}} + 1\right] - (p+1), \tag{3.41}$$

$$a_3 = \begin{cases} 0, & p > 2, \\ \dfrac{1}{a_2}\left[\dfrac{1}{\xi}\left(\dfrac{c_0 w_c f_t}{2\pi G_c}\right)^2 - (1+a_2)\right] & p = 2, \end{cases} \tag{3.42}$$

where w_c is the ultimate crack opening, f_t is the failure strength, and k_0 is the initial slope of the softening curve.

As evident from these equations, a_1 is a material property and does not depend on the target softening law. Whereas, a_2 and a_3 *are* determined from the target softening law. The derivations required to obtain these expressions are not detailed here; the interested reader is referred to [57]. In this work, Wu also derived the values of a_2 and a_3 for common softening laws. For instance, it can be shown that for linear softening $a_2 = -0.5$ and $a_3 = 0$.

3.2.6. Thermodynamic Considerations

As with any constitutive modeling method, some attention is devoted to ensuring that the framework is thermodynamically consistent. The remainder of this section is dedicated to presenting the framework for the classical formulation. However, it should be noted that whenever modifications are proposed to the constitutive modeling, ensuring that the proposed model remains thermodynamically admissible is essential. The following analysis provides insight into the methodology and identifies the necessary and sufficient conditions.

The fracture of materials involves a dissipation of energy, and hence this discussion should be accompanied by a consideration of the second law of thermodynamics, which is also known as the dissipation inequality [62]. The second law of thermodynamics can be combined with specific constitutive models (including fracture models) to determine the conditions that the models should satisfy such that their predictions are thermodynamically consistent and, thus, admissible (i.e., the predictions automatically satisfy the dissipation inequality). In the context of continuum mechanics, this method is known as the Coleman-Noll procedure and it is commonly applied with the second law expressed in the local form of the dissipation inequality [62], i.e.,

$$-\dot{\mathcal{H}} - \eta\dot{T} + \boldsymbol{\sigma} : \dot{\boldsymbol{\varepsilon}} - \frac{\boldsymbol{q}}{T}\cdot\nabla T \geq 0, \tag{3.43}$$

where $\mathcal{H}$ is the Helmholtz energy, η is the entropy density per unit volume, T is the absolute temperature, $\boldsymbol{q}$ is the heat flux vector and a superimposed dot indicates a time derivative.

If the fracture process is assumed to occur isothermally (hence $\dot{T} = 0$ and $\nabla T = \mathbf{0}$), then

$$\boldsymbol{\sigma} : \dot{\boldsymbol{\varepsilon}} - \dot{\mathcal{H}} \geq 0, \tag{3.44}$$

at every point $\mathbf{x}$ in a solid domain Ω.

In the case of a coupled displacement-damage system, the Helmholtz energy is given as the sum of the elastic and fracture energy density, i.e.,

$$\mathcal{H} = \psi_e(\boldsymbol{\varepsilon}, d) + \psi_d(d, \nabla d), \tag{3.45}$$

where ψ_d denotes the fracture energy density.

Based on the previous assumption, the time rate of change of the Helmholtz energy is given by

$$\dot{\mathcal{H}} = \frac{\partial \mathcal{H}}{\partial \boldsymbol{\varepsilon}} : \dot{\boldsymbol{\varepsilon}} + \frac{\partial \mathcal{H}}{\partial d}\dot{d} + \frac{\partial \mathcal{H}}{\partial \nabla d}\cdot\nabla\dot{d}, \tag{3.46}$$

where the relevant partial derivatives are given by

$$\frac{\partial \mathcal{H}}{\partial \boldsymbol{\varepsilon}} = \frac{\partial \psi_e}{\partial \boldsymbol{\varepsilon}}, \qquad \frac{\partial \mathcal{H}}{\partial d} = \frac{\partial \psi_e}{\partial d} + \frac{\partial \psi_d}{\partial d}, \qquad \frac{\partial \mathcal{H}}{\partial \nabla d} = \frac{\partial \psi_d}{\partial \nabla d}. \tag{3.47}$$

Hence, the Clausius-Duhem inequality becomes

$$\left(\boldsymbol{\sigma} - \frac{\partial \psi_e}{\partial \boldsymbol{\varepsilon}}\right) : \dot{\boldsymbol{\varepsilon}} - \left(\frac{\partial \psi_e}{\partial d} + \frac{\partial \psi_d}{\partial d}\right) \dot{d} - \frac{\partial \psi_d}{\partial \nabla d} \cdot \dot{\nabla} d \geq 0, \tag{3.48}$$

which must be valid at any point and for any admissible deformation.

It is possible to impose deformations rates such that the sign of the first term (3.48) inequality changes from positive to negative. Since thermodynamic admissibility requires that this inner product must be non-negative for all possible deformation rates, then necessarily the term in parentheses must be zero, i.e.,

$$\sigma - \frac{\partial \psi_e}{\partial \boldsymbol{\varepsilon}} = \mathbf{0} \, .$$

To analyze the second and third terms in (3.48) , these are integrated by parts in the domain (or an arbitrary sub-domain of it), i.e.,

$$\begin{aligned} -\int_\Omega \left(\left(\frac{\partial \psi_e}{\partial d} + \frac{\partial \psi_d}{\partial d}\right) \dot{d} + \frac{\partial \psi_d}{\partial \nabla d} \cdot \dot{\nabla} d\right) \mathrm{d}V = &-\int_\Omega \frac{\partial \psi_e}{\partial d} \dot{d} + G_c \left[\left(\frac{\partial \gamma}{\partial d}\right) \dot{d} - \nabla \cdot \left(\frac{\partial \gamma}{\partial \nabla d}\right) \dot{d}\right] \mathrm{d}V \\ &- \int_{\partial\Omega} G_c \left(\frac{\partial \gamma}{\partial \nabla d} \cdot \mathbf{n}\right) \dot{d} \, \mathrm{d}S, \end{aligned} \tag{3.49}$$

where it is assumed, as before, that $\psi_d(d, \nabla d) = G_c \gamma(d, \nabla d)$ and the vector $\mathbf{n}$ refers to the outward unit normal vector to the boundary.

The term over the volume can be expressed locally at any point $\mathbf{x} \in \Omega$

$$\left[-\frac{\partial \psi_e}{\partial d} - G_c \left(\frac{\partial \gamma}{\partial d} - \nabla \cdot \frac{\partial \gamma}{\partial \nabla d}\right)\right] \cdot \dot{d} \geq 0, \tag{3.50}$$

and it is assumed that it should independently satisfy the dissipation inequality (i.e., independent of the boundary term). Similarly, at any point $\mathbf{x} \in \partial\Omega$ on the boundary, the dissipation inequality indicates that

$$-\frac{\partial \gamma}{\partial \nabla d} \cdot \mathbf{n} \geq 0 \, . \tag{3.51}$$

Equation 3.50 leads to the first-order stability conditions, namely the Karush-Kuhn-Tucker conditions:

$$\dot{d} \geq 0, \qquad f_d(d, \nabla d) \geq 0, \qquad f_d(d, \nabla d) \cdot \dot{d} = 0, \tag{3.52}$$

where

$$f_d(d, \nabla d) = \left[-\frac{\partial \psi_e}{\partial d} - G_c \left(\frac{\partial \gamma}{\partial d} - \nabla \cdot \frac{\partial \gamma}{\partial \nabla d}\right)\right] \, .$$

3.2.7. Implementation Aspects

When implementing phase field modeling to get physically meaningful results, two aspects are of particular interest, namely the implementation of tension–compression splitting and irreversibility. Tension-compression splitting refers to the fact that cracks do not grow under compression. Irreversibility, on the other hand, follows from the previous discussion of thermodynamic considerations. It refers to the notion that cracks cannot heal; that is, damage is irreversible.

Tension-Compression Splitting

The first implementation aspect of interest is dealing with tension-compression splitting. Within the classical formulation of the problem, there is no distinction between tension and compression, and thus, the total elastic energy is degraded. In other words, crack propagation is affected by the tensile and compressive elastic energy equivalently, and hence, the total elastic energy is given by

$$\psi_e(\boldsymbol{\varepsilon}, d) = g(d) \psi_0(\boldsymbol{\varepsilon}), \tag{3.53}$$

where ψ_0 represents the elastic energy density of the medium in the undamaged state and $g(d)$ refers to the energetic degradation function that satisfies the following conditions:

$$g(0) = 1, \quad g(1) = 0, \quad g'(d) < 0, \text{ and } \; g'(1) = 0 \, . \tag{3.54}$$

Yet, this means that cracks can also grow in pure compression, leading to physically inconsistent results. As only the tensile stress should contribute to damage, reformulations have been proposed. Under such formulations, only the tensile component of the elastic energy is degraded, namely,

$$\psi_e(\boldsymbol{\varepsilon}, d) = g(d)\psi_0^+(\boldsymbol{\varepsilon}) + \psi_0^-(\boldsymbol{\varepsilon}), \tag{3.55}$$

where $\psi_0^+(\boldsymbol{\varepsilon})$, and $\psi_0^-(\boldsymbol{\varepsilon})$ denote the undamaged tensile and compressive elastic energy respectively.

However, determining the tensile component of the elastic energy is not unique, and no decomposition can be considered optimal. There are several options, but in this context, two popular methods are discussed: the model proposed by Amor et al. and Miehe et al. The first contributions towards isolating the tensile and compressive components of the elastic energy were proposed by Amor et al. [63]. They decomposed the elastic energy into volumetric and deviatoric parts, from where the tensile part of the volumetric strain and the entirety of the deviatoric part are degraded. Around the same time, Miehe et al. [64, 65] proposed a different split of energy based on the spectral decomposition of the strain tensor. In this model, the strain tensor is decomposed into tensile and compressive contributions as follows:

$$\boldsymbol{\varepsilon} = \sum_{a=1}^{3} e_{ea}\mathbf{n}_a \otimes \mathbf{n}_a = \boldsymbol{\varepsilon}_+ + \boldsymbol{\varepsilon}_-, \tag{3.56}$$

where e_{ea}, $\mathbf{n}_a$ $(a = 1, 2, 3)$ refer to the principal strains and principal strain directions respectively.

This yields

$$\boldsymbol{\varepsilon}_\pm = \sum_{a=1}^{3} \langle \varepsilon_{ea} \rangle_\pm \mathbf{n}_a \otimes \mathbf{n}_a \ . \tag{3.57}$$

where

$$\langle \boldsymbol{\varepsilon} \rangle_\pm = \frac{1}{2}(\boldsymbol{\varepsilon} \pm |\boldsymbol{\varepsilon}|) \ . \tag{3.58}$$

Based on this, the tensile and compressive parts of the initial elastic energy is given for isotropic materials by

$$\psi_e^\pm = \frac{\lambda}{2}\langle \mathrm{tr}\boldsymbol{\varepsilon} \rangle_\pm^2 + \mu \mathrm{tr}(\boldsymbol{\varepsilon}_\pm^2), \tag{3.59}$$

where μ and λ are the Lamé coefficients.

For a more general class of materials, the expression above can be written into the following form:

$$\psi_e^\pm = \frac{1}{2}\boldsymbol{\varepsilon}_\pm \cdot \mathbb{C}\boldsymbol{\varepsilon}_\pm, \tag{3.60}$$

where $\mathbb{C}$ is the stiffness tensor.

From here it follows that (for isotropic materials), the stress is given by

$$\boldsymbol{\sigma} = g(d)[\lambda \langle \mathrm{tr}\boldsymbol{\varepsilon} \rangle_+ \mathbf{I} + 2\mu\boldsymbol{\varepsilon}_+] - \lambda \langle \mathrm{tr}\boldsymbol{\varepsilon} \rangle_- \mathbf{I} + 2\mu\boldsymbol{\varepsilon}_- \ . \tag{3.61}$$

As the stiffness tensor corresponds to the derivative of the stress with respect to strain, in a variationally consistent setting, the tensile, $\mathbb{C}_+$, and compressive, $\mathbb{C}_-$, parts of the stiffness tensor are given by

$$\begin{aligned}
\mathbb{C}_\pm = {} & \lambda H(\pm \mathrm{tr}\boldsymbol{\varepsilon})\mathbf{I} \otimes \mathbf{I} + 2\mu \sum_{a=1}^{3} H(\pm\varepsilon_{ea})\mathbf{n}_a \otimes \mathbf{n}_a \otimes \mathbf{n}_a \otimes \mathbf{n}_a \\
& + \mu \sum_{\varepsilon_{ea} \neq \boldsymbol{\varepsilon}_{eb}} \left[\frac{\langle \boldsymbol{\varepsilon}_{ea} \rangle_\pm - \langle \boldsymbol{\varepsilon}_{eb} \rangle_\pm}{\boldsymbol{\varepsilon}_{ea} - \boldsymbol{\varepsilon}_{eb}} (\mathbf{n}_a \otimes \mathbf{n}_b \otimes \mathbf{n}_a \otimes \mathbf{n}_b + \mathbf{n}_a \otimes \mathbf{n}_b \otimes \mathbf{n}_b \otimes \mathbf{n}_a) \right] \\
& + \mu \sum_{a \neq b, \boldsymbol{\varepsilon}_{ea} = \boldsymbol{\varepsilon}_{eb}} \left[H(\pm\boldsymbol{\varepsilon}_{ea})(\mathbf{n}_a \otimes \mathbf{n}_b \otimes \mathbf{n}_a \otimes \mathbf{n}_b + \mathbf{n}_a \otimes \mathbf{n}_b \otimes \mathbf{n}_b \otimes \mathbf{n}_a) \right],
\end{aligned} \tag{3.62}$$

where H is the heaviside function, i.e.,

$$H(x) = \begin{cases} 0 & \text{for } x \leq 0, \\ 1 & \text{for } x > 0 \ . \end{cases} \tag{3.63}$$

In this case, the degraded stiffness tensor is given by

$$\mathbb{C}(d) = g(d)\mathbb{C}_+ + \mathbb{C}_- \,. \tag{3.64}$$

Remark 3.4

In the context of anisotropic materials, several related formulations have also been proposed in the literature. Although these are not developed for isotropic materials, they are still relevant to the present discussion because they directly address the distinction between tensile and compressive behavior. For instance, Zhang et al. [66] proposed a model in which tension-compression splitting is based on the spectral decomposition of the stress tensor. This method has been further used in modeling the anisotropic fracture of additively manufactured parts [67].

Remark 3.5

In the literature, the models in which there is no distinction between tension and compression are referred to as "isotropic", and models that do distinguish between tension and compression are referred to as "anisotropic". This terminology of isotropic and anisotropic is not related to the conventional usage of the terms from continuum mechanics, and rather only refers to the nature in which the elastic energy is degraded. To avoid confusion, this terminology of isotropy is not used and is rather explicitly referred to as tension-compression splitting.

In models where tension-compression splitting is accounted for in a variationally consistent manner, the stress-strain relation is highly nonlinear and hence computationally more expensive to solve. To address this limitation, Ambati et al. [1] introduced a hybrid formulation under which the tension-compression split is kept for the elastic energy, and a linear momentum balance relation is used. These relations are summarized mathematically in Equation 3.65.

$$\boldsymbol{\sigma} = \frac{\partial \psi}{\partial \boldsymbol{\varepsilon}} = g(d)\mathbb{C}\boldsymbol{\varepsilon}, \quad \text{and} \quad \mathbb{C}(d) = g(d)\mathbb{C}_0 \,. \tag{3.65}$$

The computational effort of this method is similar to the computational effort of the formulation without tension-compression splitting. As a result, it has been favored for many future works [16]. This formulation, however, is variationally inconsistent since the stress field and the crack phase field evolution are associated with different energy functions. Yet, this is permitted as it does not violate the second law of thermodynamics [68]. Furthermore, this "hybrid" notion can be generalized to any case where the constitutive material behavior is degraded distinctly from the driving energy [69].

Irreversibility

Following the discussion of thermodynamic considerations, the phase field modeling problem classically results in a constrained variational inequality. The traditional and original approach to imposing the constraint that damage cannot heal is through enforcement of the variational inequality that stems from the Karush–Kuhn–Tucker conditions. In other words, the damage evolution problem is formulated as a constrained minimization problem, which results in the following variational inequality:

$$\dot{d} \geq 0, \tag{3.66}$$

$$\frac{\partial \psi_e}{\partial d} + \frac{G_c}{c_0}\left(\frac{\vartheta'(d)}{l} - 2l\nabla^2 d\right) \geq 0, \tag{3.67}$$

$$\dot{d}\left[\frac{\partial \psi_e}{\partial d} + \frac{G_c}{c_0}\left(\frac{\vartheta'(d)}{l} - 2l\nabla^2 d\right)\right] = 0, \tag{3.68}$$

$$\nabla d \cdot \mathbf{n} \geq 0, \tag{3.69}$$

$$\dot{d}\nabla d \cdot \mathbf{n} = 0 \,. \tag{3.70}$$

From an implementation perspective, this problem results in minimizing the total energy under box constraints to ensure damage irreversibility, implying that the minimum damage bound is updated at each increment.

As an alternative, Miehe et al. [64, 65] reformulated the irreversibility constraint through introducing the history variable. They showed that by locally tracking the maximum undamaged tensile elastic energy and using that instead of the local tensile elastic energy, the constrained variational inequality can be resolved into a constrained equality, thereby simplifying numerical implementation significantly. This history variable, $\mathcal{H}_v$, is defined as follows

$$\mathcal{H}_v = \max_{0 \leq \tau_t \leq t} (\psi_0^+), \tag{3.71}$$

where τ_t is an instance before or equal to the current instance t.

Under this formulation, the problem is simplified to

$$g'(d)\mathcal{H}_v + \frac{G_c}{c_0}\left(\frac{\vartheta'(d)}{l} - 2l\nabla^2 d\right) = 0\ . \tag{3.72}$$

While Equation 3.71 presents the standard definition for the history variable, this only holds for the case where there is a split between tension and compression, and the AT2 model, that is, when the quadratic geometric crack function is used along with the quadratic degradation function. For other choices of geometric crack density function and degradation function, the history variable has a threshold. This threshold can be derived by considering the following [56]:

$$g'(d)\mathcal{H}_v + \frac{G_c}{c_0}\frac{\vartheta'(d)}{l} = 0\ . \tag{3.73}$$

The minimum value of $\mathcal{H}_v$ occurs at the onset of damage initiation, and hence Equation 3.73 can be rearranged to state

$$H_0 = \frac{-G_c}{c_0 l}\frac{\vartheta'(0)}{g'(0)}\ . \tag{3.74}$$

Hence, the history variable is given by

$$\mathcal{H}_v = \max_{0 \leq \tau_t \leq t} (\psi_0^+, H_0)\ . \tag{3.75}$$

For the models of interest Table 3.3 summarizes the relevant length scale parameters, the lower bound for the history variable, the critical displacement, and the critical stress.

Table 3.3: The fracture-strength consistent length scale, the lower bound for the history variable, the critical displacement, and the critical stress for the AT2, AT1, and Wu models.

Model	l	H_0	U_c	σ_{cr}
AT2	$\frac{27E_0G_c}{256\sigma_{cr}^2}$	0	$\sqrt{\frac{G_c}{3lE_0}}$	$\frac{3}{16}\sqrt{\frac{3E_0G_c}{l}}$
AT1	$\frac{3E_0G_c}{8\sigma_{cr}^2}$	$\frac{3G_c}{16l}$	$\sqrt{\frac{3G_c}{8lE_0}}$	$\sqrt{\frac{3G_cE_0}{8l}}$
Wu	-	$\frac{\sigma_{cr}^2}{2E_0}$	$\frac{\sigma_{cr}}{E_0}$	σ_{cr}

Although the approach using the history variable has gained significant traction and has almost become the norm in current formulations of phase field modeling, this approach does suffer from variational inconsistency [70]. As a result, researchers have sought to quantify the differences between the two formulations (the treatment of irreversibility using the history variable and without using the history variable). To this end, Barki et al. [56] recently revisited the formulation of irreversibility of both methods and noted that for phase field models without damage thresholds, introducing the history variable has a marginal effect on the results obtained. However, for phase field models with a damage threshold, there are discrepancies between the two methods in both the global response and the force-displacement behavior. In the case of micro-structures with several cavities, both formulations also result in different crack paths. Yet, still, the history variable method is more widely adopted and provides results that are consistent with experimental findings.

In a separate study, Bharali et al. [71] identified that the nature of the error introduced when using the history variable is often non-quantifiable. As a result, they propose a micromorphic approach in which the phase field becomes a local variable and an additional micromorphic variable is introduced to regularize the fracture problem. It is claimed that the proposed methodology facilitates easier implementation; however, to the best of the author's knowledge, it has not been used outside their scope of work thus far.

An alternative, variationally consistent method for ensuring damage irreversibility is using the augmented Lagrangian approach. This approach was first introduced by Wheeler et al. [70], and has since been used in other contexts, for example, for modeling dynamic cohesive fracture [72]. In this approach, the aim is to find a solution for the following minimization problem:

$$\begin{aligned} &\min\ \psi(\mathbf{u}, d, \nabla d) \\ &\quad \text{such that } d \in \{d | 0 \leq d^{n-1} \leq d \leq 1\}, \end{aligned} \tag{3.76}$$

where the previous solution $(\mathbf{u}^{n-1}, d^{n-1})$ is known.

Under this methodology, the idea is that this problem can be approximated by,

$$\min\ \psi(\mathbf{u}, d, \nabla d) + \frac{1}{2\rho}||\langle \lambda_l + \rho(d^{n-1} - d)\rangle_+||^2 + \frac{1}{2\rho}||\langle \lambda_l + \rho(1-d)\rangle_-||^2, \tag{3.77}$$

where λ_l is the Lagrange multiplier and ρ is a penalty kernel.

Thus Equation 3.77 introduces two penalty terms. The first is introduced to enforce damage irreversibility by ensuring that the damage variable can only monotonically increase. The second term is considered to ensure that the damage variable does not exceed unity. The authors note that in most contexts, namely if the boundedness of the phase field variable is ensured, it is not necessary to add this term [72].

3.3. Implementation Strategies

As with any computational framework, its numerical implementation is of critical importance for practical applicability. To this extent, three aspects are discussed. Firstly, the numerical methods in which phase field modeling can be implemented are detailed. This is followed by a discussion on the solution schemes that can be considered to solve the coupled field equations. Lastly, the bottlenecks of the strategies are investigated along with methods that have been proposed to improve the numerical implementation.

3.3.1. Numerical Methods

Classically, the partial differential equations involved are solved within the framework of finite element methods. This has been done utilizing several open-source packages or through commercial software, such as FEniCS, DEAL.II, MOOSE, Abaqus, and COMSOL. Although commercial software, such as Abaqus, do not have a built-in phase field model, several reformulations have been implemented. For instance, Molnar et al. [73] presented a 2D and 3D Abaqus implementation of a robust staggered phase field solution for modeling brittle fracture. Through their work, Bhomwick and Liu [74] implemented a phase field model to robustly handle distorted meshes in Abaqus. Zhou et al. [75] studied quasi-brittle and dynamic fracture using a COMSOL implementation. Yet, it is also common to implement such models using open-source packages [76, 77].

When high-order phase field equations are used, that is, phase field models with higher order derivatives of the phase field, more smoothness of the exact solution is desired. These are difficult to capture within finite element methods, and hence other numerical methods have been considered. Examples of such methods include iso-geometric analysis and so-called meshless methods. Borden et al. [78] presented one of the first formulations of phase field modeling using an iso-geometric analysis-based approach to investigate fourth-order phase field modeling of brittle fracture. By exploiting the increased regularity, the convergence rate of the numerical simulation is improved, and it has been able to capture complex 3D crack patterns. Amiri et al. [79] proposed a meshless method applying a fourth-order phase field model for fracture based on the local maximum entropy approximates.

There have also been attempts to extend this further. To be able to robustly model irregular problem geometries, and specifically with the aim of generating meshes with irregular shapes, Aldakheel et al. [80] formulated a framework using virtual element methods. In this formulation, the number of nodes in an element is a flexible number that can change over the course of the simulation. There have also been attempts to solve this using

vastly different approaches. For instance, Chen et al. [81] introduced a Fast Fourier Transform algorithm to solve the phase field model of brittle fracture in a staggered manner. This method retains the advantages of parallel implementation while maintaining simplicity for mesh generation. This framework was extended by Ma and Sun [82], where they applied a Fast Fourier Transform-based solver in the context of high-order and multi-phase field fracture.

3.3.2. Solution Schemes

Once discretized, the governing equations can either be solved through monolithic or staggered schemes. Monolithic schemes solve both the displacement and phase field variables simultaneously. However, due to the non-convex nature of the energy functional, such methods are prone to low numerical stability. To overcome this challenge, staggered schemes have shown remarkable potential. Under such an approach, the partial differential equations are decoupled. Thus, at a given time step, the displacement field is first solved for using a fixed phase field, and then, based on the updated displacement field, the phase field equation is solved for [44]. When using a staggered approach, it is important to track the convergence of the solution.

A consequence of using staggered approaches is that often very small loading increments and many staggered iteration can be required for convergence [1]. When the constitutive stiffness tensor is degraded distinctly from the elastic energy, within a staggered approach, the stiffness matrix is constant and thus convergence is attained within one iteration. However, if a variationally consistent model is used to account for tension-compression splitting, then the resulting equations are highly non-linear, and several staggered iterations may be required to reach convergence, resulting in low computational efficiency. To combat this issue, Kristensen and Martines-Paneda [83] evaluated the potential of using monolithic quasi-Newton solution schemes. They note that under such an approach, the computational time is reduced by several orders of magnitude.

3.3.3. Advancements

Over the years, several advancements to the numerical implementation of phase field models have been proposed, targeted at improving the rate of convergence and the computational effort involved. This includes introducing high-order phase field models and adaptive mesh strategies. Due to their increased regularity, high-order methods offer higher convergence rates, making it more numerically favorable [78].

As mentioned previously, one of the limitations of phase field modeling is the computational effort involved. Often, very fine meshes are required under very small displacement increments for convergence. In light of this, and to reduce the computational cost involved, adaptive mesh strategies have been proposed [44]. These approaches dynamically concentrate computational effort in regions of interest, such as near crack tips and evolving fracture zones, while maintaining coarser discretizations elsewhere.

One example of an adaptive mesh approach was proposed by Heister et al. [84]. In their method, they introduce a predictor-corrector mesh adaptivity technology to reduce computational cost. Their proposed method has the following characteristics:

- the strain remains fixed and small during the computation,
- the error is controlled by the strain and not the element size,
- it is ensured that the strain is smaller than the element size within the crack region.

An alternative method was proposed by Wick [85] in which a posterior error estimate was coupled with an adaptive mesh refinement technology. The methodology is based on the partition of unity and has the benefit that it does not require there to be strong residual or jumps over element edges. Other approaches include h-adaptive phase field methods [86, 87]. Unlike adaptive mesh refinement schemes that require knowledge of a pre-fixed crack path, here a predictor-corrector scheme is used to guide the adaptivity process. This is loosely done in the following manner:

1. the coupled system with a coarse mesh is solved, and an initial crack path is predicted,
2. based on a defined refinement threshold, it is judged whether a mesh refinement is required,
3. if a refinement is required, all fields are solved for again using the refined mesh.

As the refinement is done adaptively based on the identification of the crack tip, the CPU time required and the memory usage are significantly reduced. Adaptive remeshing has also been done for more complex problems; for instance, Yu and Hou [88] considered such a framework in the context of composite structures. There have also been attempts to extend this approach beyond finite element methods, for instance, Nguyen-Thanh et

al. [89] have shown how to apply this method in the context of anisotropic fracture within an isogeometric meshfree collocation method.

This topic remains an active area of research. Recently, Tian et al. [77] considered an adaptive finite element method based on the recovery-type posterior error estimates by transforming the gradient of the numerical solution into a smoother function space. The difference between the recovered gradient and the original numerical gradient is considered an estimate for the error to guide the adaptive mesh refinement process.

3.4. Application Extensions

Attributed to the flexibility exhibited by phase field modeling in the context of fracture, there have been numerous attempts to extend the framework to capture more complex loading patterns and material behavior. Such extensions can be broadly categorized into two domains, namely as either an *extension to the observed physical phenomenon*, or to *the class of materials the modeling approach is applied to*. To resolve the ambiguity in these terms, it is to be noted that *extension of the observed physical phenomenon* refers to accounting for fracture in conjunction with other processes such as ductile, dynamic, fatigue, or mixed-mode fracture. Whereas, *extending the class of materials the modeling framework is applied to* refers to augmenting the framework to capture the failure patterns exhibited by certain material classes. To this end, failure of rocks, composites, and other spatially non-homogeneous materials are of particular interest.

In accordance with the theory and discussion presented thus far, the extensions considered in this subsection lie within the context of isotropic fracture, and hence, composites (in particular) are not elaborated on as they exhibit anisotropic fracture. Furthermore, it is to be noted that the extensions presented here are all in their own capacity significant areas of research, and thus, there is an abundance of literature surrounding each of these topics. In favor of conciseness and because the current scope is not related to dynamic, ductile, and fatigue fracture, a complete treatment of these topics is not provided. Despite this, the discussion serves to show the versatility of, and gain inspiration from, the domains in which phase field modeling has been utilized.

3.4.1. Ductile Fracture

Over the years, the brittle phase field model has been extended to model ductile fracture and fracture with finite deformations. In these formulations, the stored energy functional is decomposed into an elastic and plastic component, yet the fracture component remains largely unchanged. The plastic energy density is often expressed in terms of a plastic internal variable, but the plastic deformation does not affect, and is not affected, by the phase field evolution [16]. However, by introducing this internal variable, the phase field problem is no longer linear, and hence the computational cost associated with solving the relevant fields increases significantly. In attempts to tackle the high computational effort associated with solving these coupled fields, through separate works, Miehe et al. [13], Borden et al. [90], and Kuhn et al. [91] proposed formulations in which they introduce a plastic degradation function for the plastic energy density. In their frameworks, the same degradation function is used for both the plastic and elastic energy density. Although this is not a strictly necessary choice, this has been shown to be favorable for reducing computational time.

3.4.2. Dynamic Fracture

Another branch of fracture that is of interest is dynamic fracture. Bourdin et al. [14], and Hofacker and Miehe [92] proposed the first frameworks to model diffuse dynamic fracture, and simulate the complex crack patterns that arise. This extension is founded on two assumptions:

- the phase field does not affect the kinetic energy,
- the fracture energy is independent of the crack velocity.

Through this methodology, it has been possible to numerically replicate experimentally observed crack branching and dynamic crack instability (that is, the phenomenon where many small crack branches are present). Extending on this formulation, other frameworks with incremental novelty have been proposed, but in most cases, the models aim to predict crack paths rather than the crack speeds. Thus, despite the success seen for capturing complex crack patterns, it still remains an area of research to predict crack velocities accurately, and deal with velocity-dependent fracture energy [16].

3.4.3. Fatigue

Similar to fracture, another phenomenon under which cracks propagate is fatigue. As a result, recently, there have been numerous attempts at modeling fatigue through phase field methods. For completeness, some of the methodologies taken are given. In such models, unlike the case of brittle fracture, the fracture energy

is also degraded. Alessi et al. [93] presented a variational phase field model in which this degradation was implemented using a dissipation potential depending on the accumulated strain. To this end, Carrara et al. [94] proposed a model in which the degradation of the fracture energy was modified such that it acts on both the local and gradient terms of the fracture dissipative energy. The advantages of this formulation lie in its ability to also model the decrease in resistance towards crack propagation.

While these models were able to reproduce S-N curves and crack growth rate curves, the relationship between crack evolution and the number of fatigue load cycles was still not accounted for. To overcome this limitation, Schreiber et al. [95] formulated a framework to characterize this relationship by introducing an additional energy term into the phase field model. Later, they extended their approach to introduce another energy term to account for irreversible fatigue damage [96, 97]. Regardless, as most attempts are phenomenological and do not directly consider damage mechanisms, moving towards multiscale phase field fatigue fracture models with more explicit physics is still a developing area of research [52].

3.4.4. Mixed-Mode Fracture

Another extension to which phase field modeling has been applied is mixed-mode fracture. This has been mostly studied in the case of rock fracture. This is because the fracture behavior in rocks is strongly dependent on the loading mode. To be able to characterize this, the classical phase field modeling approach is modified to include a methodology to account for mixed-mode fracture. Inherently, phase field modeling does not distinguish between different opening modes, as the fracture process follows from the minimization of the energy functional. When doing so, the implicit assumption made is that the fracture energy is the same for all opening modes [44]. This, however, is inconsistent with reality, and hence modifications have been proposed to account for the different critical energy values associated with the different opening modes. One of the first works that investigated this was done by Zhang et al. [98], in which a reformulation of the phase field evolution equation was presented. In their model, they decomposed the history variable of the tensile elastic energy into different modes, thereby allowing for each mode to be governed by its respective critical energy release rate. This is a crucial distinction, as the critical energy release rate for the different modes can differ by orders of magnitude.

Remark 3.6

Alongside accounting for the different critical energy release rates, the notion of splitting the history variable into modes has also allowed for more “physics-informed” methods of degradation. In other words, this approach allows for anisotropic degradation, that is, situations where different energy components are degraded distinctly. In most cases, introducing anisotropic degradation is accompanied by the introduction of multiple damage variables leading to multi-phase field models [99], or multiple degradation functions [3, 100].

Recently, Zhang et al. [62] proposed a new phase field model with a loading-based degradation function to simulate mixed-mode failure in the context of isotropic materials and fracture. They use a thermodynamically consistent framework in which the fracture energy and the Benzeggagh and Kenane mixed-mode criterion are embedded into the phase field evolution equation. Based on the crack orientation with respect to the principal material axes at damage initiation, the extent of mode-mixity is determined and used as an input to the degradation function. As phase field models do not require or determine the orientation of the crack explicitly, in this model, the orientation is computed as the angle that maximizes the loading function at damage initiation. However, the fact that the mode-mixity at a material point will change during damage evolution is not accounted for.

3.4.5. Spatially Non-Homogeneous Materials

The discussions so far have considered the material properties in a specimen to be uniform, that is, they have been for spatially homogeneous materials. However, in aerospace and energy applications, as well as for morphing technologies, introducing materials with spatially varying material properties has been of interest. As a result, there has been significant interest in investigating fracture in spatially non-homogeneous materials. This constitutes a broad class of materials, including functionally graded materials and composites. However, as previously mentioned, the latter exhibits anisotropic fracture, and it is not considered here. Yet, functionally graded materials in the context of isotropic fracture are an active field of research. Particularly in the context of functionally graded materials, to establish the phase field framework, it is necessary to have a micromechanical model for determining the effective elastic and fracture properties at a spatial point.

In the pioneering works of extending phase field modeling to functionally graded materials, Hirshikesh et al. [101] presented a modeling strategy in which the material properties varied spatially. Under their formulation, they used a Mori-Tanaka homogenization scheme to determine the effective elastic properties and the rule of mixtures to approximate the critical energy release rate. In their formulation, they only consider the critical energy release rate as a material composition-dependent fracture property. However, this assumption is not unequivocally true. Depending on the choice of the degradation function used, the length scale parameter is related to the critical stress [57]. In functionally graded materials, as both base materials have different critical stresses, their length scale parameters will also be different, implying that the length scale parameter should be dependent on material composition. There are degradation functions in which the global response is independent of the length scale; however, in the paper, the quadratic degradation function is used, which is not length scale invariant.

Motivated by this inconsistency, Kumar et al. [102] performed a study in which they investigated crack propagation using consistent length scale values. They note that the difference in length scale values can span across one order of magnitude, and hence, its influence on fracture cannot be neglected. As a result, in their work, they consider it to be a numerical parameter implicitly dependent on spatial position through the material composition at a point. Furthermore, they employ the rule of mixtures to estimate the elastic material properties.

4: Phase Field Modeling of Anisotropic Fracture

This chapter presents the second phase of the literature review. It serves to provide an overview of how phase field modeling has been extended to simulate anisotropic fracture. The modeling strategies to account for anisotropic fracture propagation and degradation are formalized, followed by an extensive review of the state-of-the-art models that have been proposed, particularly within the context of composites and spatially inhomogeneous materials. This review closes with identifying the research gap and the research question guiding the thesis.

Firstly, Section 4.1 presents the scope of this literature review and the guiding questions that will be addressed. This is followed by Section 4.2 in which the methods that have been utilized to model anisotropic fracture propagation are presented. Section 4.3 establishes the frameworks used for modeling anisotropic degradation. The necessity of these notions for modeling fracture in composites is dealt with in Section 4.4, where also the state-of-the-art models are discussed. A similar analysis is performed in the context of spatially inhomogeneous materials in Section 4.5. Based on all preceding discussions, Section 4.6 identifies the research gap, the research question, and the research goals of this thesis.

4.1. Scope of Review

The previous chapter established the theoretical foundations of phase field modeling for isotropic fracture. While many of these concepts remain valid, modeling anisotropic fracture introduces additional complexities. This chapter, therefore, reviews phase field approaches for modeling anisotropic fracture. To ensure a thorough discussion, the following research objectives are identified:

- Understand how phase field modeling has been extended to account for anisotropic fracture propagation.
- Review the methods that have been taken to model anisotropic fracture within the phase field modeling community.
- Identify and assess state-of-the-art phase field models for simulating fracture in both spatially constant and inhomogeneous anisotropic materials.

Guided by these objectives, the literature study aims to address the following questions.

1. What does the scope of anisotropic fracture entail?
2. What are the additional aspects to consider when extending phase field modeling to account for anisotropic fracture?
3. What are the current state-of-the-art models for simulating anisotropic fracture in composites?
4. What are the current state-of-the-art methods for modeling anisotropic fracture in spatially non-homogeneous materials?

With the increasing relevance of complex materials with engineered properties optimized for various applications, such as fiber-reinforced composites and ceramic-matrix composites [103], extending the framework of phase field modeling to simulate anisotropic fracture has gained significant attention. Within this context, two types of anisotropy can be identified, namely:

- *Anisotropic fracture propagation*: due to the anisotropy in fracture energy (also referred to as the directional dependence of fracture energy), certain orientations are favored for crack propagation.
- *Anisotropic degradation*: as a consequence of the damage and loading state, material properties are degraded differently.

Remark 4.1

In the literature, the terms are sometimes used interchangeably; however, it should be noted that neither forms of anisotropy imply that the other form must be present.

In the following subsections, the literature that explores either type of anisotropy is discussed. Firstly, the background theory related to *what* these terms entail, and *how* they are accounted for, is presented. This is followed by a review of the state-of-the-art approaches employing phase field modeling in the context of composites and spatially non-homogeneous anisotropic materials.

4.2. Anisotropic Fracture Propagation

To account for fracture anisotropy, two classes of methods are identified: one using *structural tensors* and the other by defining a *direction-dependent fracture energy*. The former is far more popular and has been extensively used in the literature, whereas the latter has been reported less commonly. However, the latter has the potential to resolve some of the issues seen with the former. The following paragraphs explore both in more detail.

4.2.1. Structural Tensor-Based Approach

One of the first attempts to address anisotropic fracture propagation was done by Teichtmeister et al. [22]. In their method, they proposed the introduction of a structural tensor (of either second or fourth order) to describe the nature of fracture anisotropy. The number of parameters used to characterize the tensor depends on the symmetry of the material, namely, whether it exhibits transversely isotropic, orthotropic, or cubic anisotropy. This structural tensor is then used to modify the energetic and stress-like failure criteria to characterize the intrinsic anisotropy. Under this formulation, the crack surface density function is modified to read

$$\gamma(d, \nabla d; \mathbf{A}) = \frac{1}{2}\left[\frac{1}{l}d^2 + l(\nabla d \cdot \mathbf{A}\nabla d)\right], \tag{4.1}$$

where $\mathbf{A}$ denotes the structural tensor.

In the transversely isotropic (and 2D orthotropic) case, Teichtmeister et al. [22] define it as

$$\mathbf{A} = \mathbf{I} + \alpha(\mathbf{a} \otimes \mathbf{a}), \tag{4.2}$$

where α has been referred to in [22] as the *penalty parameter* and $\mathbf{a}$ is a unit vector in the direction of the preferential orientation.

By introducing the structural tensor, it can be shown that the fracture energy is effectively modified to be direction-dependent. Li et al. [25] justify the introduction of structural tensors by showing that they emerge when the fracture energy density is represented through a truncated Taylor series expansion. Regardless, the nature of the structural tensor *implicitly* defines the dependence of the fracture energy on the crack orientation [22]. As a result, for the form presented in Equation 4.2, the extent of anisotropy is characterized by α, where a higher value makes it more energetically favorable for crack propagation to prefer a certain orientation. Naturally, if this parameter is set to zero, then the isotropic case is retrieved.

In some literature, α has been treated as a numerical parameter; however, there have been attempts to motivate its physical interpretation. Notably, through their research, Zhang et al. [104] have shown the relation between α and the fracture energies dissipated by cracking along the weak and strong failure directions. While this provides a physical explanation for the choice of α, they note that for composite materials, the difference between the critical energy release rate of the fibers and matrix can be vastly different. In such cases, it is numerically unfeasible to consider the physically motivated α value. This is because, by introducing α, the effective length scale in a perpendicular direction has a magnitude $\sqrt{\alpha}$ times greater, and thus the crack in that direction is more diffuse. As this huge variation in the effective internal length scale is undesired, the parameter is numerically set to an acceptable number.

> ***Remark 4.2***
>
> While in the literature it is common to refer to α as the penalty parameter, as motivated by Zhang et al. [104], α is not *really* a penalty parameter. In numerical models, a penalty parameter is used to enforce constraints, ill-conditioning control, regularization, etc. Yet, in this case, there are no such constraints. Rather, α is a numerical parameter that quantifies the difference in the critical energy release rate in distinct directions. As a result, for the remainder of this thesis, the terminology of "penalty" parameter is not used, and rather α is described as the *anisotropic fracture energy* parameter.

It is to be noted that the formulation presented above for defining the structural tensor is not unique. Inspired by the work of Clayton and Knap [105], Nguyen et al. [106] proposed an alternative formulation, namely

$$\mathbf{A} = \mathbf{I} + \beta(1 - \mathbf{a}^{\perp} \otimes \mathbf{a}^{\perp}), \tag{4.3}$$

where $\mathbf{a}^{\perp}$ denotes the unit vector that is perpendicular to the preferential plane and β is used to penalize the damage on planes not normal to $\mathbf{a}^{\perp}$.

Both these formulations result in what is called “weak anisotropy”, where the term weak is used to indicate that there are certain *preferential* directions. However, some materials, such as crystals or those with cubic symmetry, are known to have *forbidden* directions. In such cases, this is referred to as strong anisotropy [107]. This can be modeled using the same framework, but the structural tensor should be of fourth order. This is so that it acts on the higher-order gradient terms of the phase field variable [107].

As this method modifies the surface crack energy functional, it is important to revisit the variational problem. As the only modification is to the crack surface density functional, the majority of the derivation presented in Section 3.2.3 remains the same. In fact, the mechanical problem is identical to the isotropic case, namely, the standard equation of equilibrium is obtained

$$\delta_u \Psi_{\text{total}} = \int_{\mathcal{B}} (\nabla \cdot \boldsymbol{\sigma} + \mathbf{b}) \cdot \delta \mathbf{u} \, \mathrm{d}V - \int_{\partial \mathcal{B}_s} (\boldsymbol{\sigma} \cdot \mathbf{n} - \mathbf{f}_0) \cdot \delta \mathbf{u} \, \mathrm{d}S \, . \tag{4.4}$$

For the phase field, the variation with respect to the damage variable retains the following form:

$$\delta_d \Psi_{\text{total}} = \int_{\mathcal{B}} \left[\frac{\partial \psi_e}{\partial d} + G_c \partial_d \gamma \right] \delta d \, \mathrm{d}V + \int_{\partial \mathcal{B}} G_c \left(\frac{\partial \gamma}{\partial \nabla d} \cdot \mathbf{n} \right) \delta d \, \mathrm{d}S, \tag{4.5}$$

where

$$\partial_d \gamma = \frac{\partial \gamma}{\partial d} - \nabla \cdot \left(\frac{\partial \gamma}{\partial \nabla d} \right) \, . \tag{4.6}$$

However, as the crack surface density has changed, $\partial_d \gamma$ becomes

$$\partial_d \gamma = \frac{1}{c_0} \left[\frac{\vartheta'(d)}{l} - 2l \nabla \cdot (\mathbf{A} \nabla d) \right] \, . \tag{4.7}$$

From this equation, it is straightforward to note that in the isotropic case, that is when the structural tensor is the identity tensor, $\mathbf{A} = \mathbf{I}$, then $\nabla \cdot (\mathbf{A} \nabla d) = \Delta d$, as derived previously for the isotropic case.

Furthermore, revisiting the boundary conditions, it follows naturally that the introduction of the structural tensor does not change the mechanical boundary conditions. Thus, the following mechanical boundary conditions hold

$$\begin{cases} \mathbf{u} = \mathbf{u}_0 & \text{on } \partial \mathcal{B}_u, \\ \boldsymbol{\sigma} \cdot \mathbf{n} = \mathbf{f}_0 & \text{on } \partial \mathcal{B}_s \, . \end{cases} \tag{4.8}$$

where $\partial \mathcal{B}_u$ and $\partial \mathcal{B}_s$ are two disjoined parts of the boundary where a fixed displacement $\mathbf{u}_0$, and a fixed traction $\mathbf{f}_0$ are applied, respectively.

However, the phase field boundary condition is

$$[\mathbf{A} \nabla d] \cdot \mathbf{n} = 0 \qquad \text{on } \partial \mathcal{B} \, . \tag{4.9}$$

where again, in the isotropic case ($\mathbf{A} = \mathbf{I}$), this resolves into the previously seen

$$\nabla d \cdot \mathbf{n} = 0 \qquad \text{on } \partial \mathcal{B} \, . \tag{4.10}$$

Motivated by this framework, Bryant et al. [100] proposed the first work for modeling mixed-mode fracture in anisotropic rocks by combining the notions used for isotropic mixed-mode fracture with anisotropic fracture propagation. Through introducing distinctive critical energy release rates, they formulated a kinematically consistent model capable of replicating secondary cracks. This model is an example of how accounting for anisotropic fracture propagation does not imply that (stiffness) degradation must be anisotropic. As in their formulation, the stiffness tensor is degraded isotropically by the quadratic degradation function. A particular novelty in their framework is that it uses knowledge of the crack orientation. As phase field modeling does not intrinsically determine or output this orientation, the crack angle is determined as the angle that maximizes the normalized and non-dimensionalized mixed-mode strain energy, that is, the so-called $\mathcal{F}$-criterion [100].

4.2.2. Direction-Dependent Fracture Energy-Based Approach

Despite the flexibility of introducing fracture anisotropy using a structural tensor, as hinted by Zhang et al. [104], there are two main modeling consequences, namely:

- an orientation-dependent crack interface width,
- alteration of the crack surface energy in a physically inconsistent manner.

These issues are well known in the literature [108, 109]; yet, little systematic effort has been devoted to addressing these shortcomings. Rather, it is often bypassed by taking a value that offers a compromise between sufficiently "favoring" the preferred orientation without leading to very diffuse behavior in orthotropic directions.

The first work that addressed these problems was done by Rezaei et al. [24]. In their model, they proposed a formulation in the context of crystalline structures that uses a direction-dependent fracture energy. While the structural tensor implicitly defines a direction-dependent fracture energy, in this framework, the dependence on crack orientation is explicitly defined. The orientation of the crack is inferred from the damage gradient. A consequence of this is that anisotropy is introduced in both the gradient and potential terms of the crack surface density function. As this formulation allows for explicitly defining the dependency of fracture energy on orientation, they propose a function that is the sum of several frequency energy functions. Mathematically, it has the following form:

$$G_c(\theta) = \sum_m E_m(\theta) = \sum_m \beta_m \left[1 + \alpha_m \sin^2(m(\theta + \theta'_m))\right], \tag{4.11}$$

where β_m, α_m, θ'_m, and m are material parameters to describe the fracture energy profile, and θ is the orientation of the crack, which is inferred from the damage gradient.

Very recently, Prajapati et al. [23] proposed another framework in which they also introduce a direction-dependent fracture energy. They note that this treatment of anisotropy leads to a uniform diffuse interface thickness irrespective of the difference in magnitude of directional G_c values. In their model, they define the crack energy density, f_c to be

$$f_c = \frac{1}{2} G_c(\nabla d) \left(\frac{1}{l} \vartheta(d) + l |\nabla d|^2 \right) . \tag{4.12}$$

In this equation $G_c(\nabla d)$ is the root-squared-orthotropy function defined by (where their notation is adopted)

$$G_c(\nabla d) = \sqrt{\mathbf{G}_{c,\theta}^2 : \mathbf{n}_c \otimes \mathbf{n}_c}, \tag{4.13}$$

where

$$\mathbf{G}_{c,\theta} = \mathbf{Q}_a \mathbf{G}_{c0} \mathbf{Q}_a^T, \tag{4.14}$$

with $\mathbf{Q}_a$ being a rotation tensor describing orientation and $\mathbf{G}_{c0}$ defined by

$$\mathbf{G}_{c0} = \text{diag}(G_{c0,1}, G_{c0,2}) . \tag{4.15}$$

In other words, it represents the crack resistance normal to the principal directions $\mathbf{e}_i$.

Revisiting the variational problem under this formulation is slightly more involved; however, as this method will be discussed in more detail throughout the thesis, this discussion is omitted here. Rather this is detailed in Chapter 5.

4.3. Anisotropic Degradation

The topic of anisotropic degradation is a growing field of research, and at large, two approaches can be identified: those that use multiple damage variables and those that use a single damage variable. The models using multiple damage variables lead to multi-phase field frameworks. In such cases, the damage variables can be degraded distinctly. For the single-damage models, anisotropic degradation is introduced through the use of multiple distinct degradation functions.

In the context of composites, multi-phase field models have been shown to be rather promising as it is possible to account for independent damage evolution and distinct energetic and stiffness degradation [110]. On the contrary, single-phase field models with anisotropic degradation have been explored within the context of rock-like materials [3]. Although such a formulation does not characterize independent damage evolution, it leverages the computational benefit of only requiring one damage variable while still capturing the direction-dependent effects of damage.

In the following discussion, several classes of models are presented to explain the scope of work that has been done. Most of these models are tailored to specific applications, but the notions explored are versatile.

4.3.1. Multi-damage Variable Models

One of the pivotal developments in multi–phase field fracture modeling is the formulation introduced by Bleyer and Alessi [111]. Their framework extended the notions of modeling anisotropic fracture in composites to account for different damage mechanisms and damage evolution rates. Their modeling approach introduces two separate damage variables (and hence evolution equations), for the fiber and matrix phase, respectively. In such a case, the total dissipated energy, $\Psi_{\text{tot. fracture}}$, is given as the sum of the energy densities associated with all fracture mechanisms, namely

$$\Psi_{\text{tot. fracture}}(d, \nabla d) = \sum_{i=1}^{n} \int_{\Omega} G_c^i \gamma_i(d_i, \nabla d_i)\, \mathrm{d}V, \tag{4.16}$$

where

$$\gamma_i(d_i, \nabla d_i) = \frac{1}{2l_i}(d_i^2 + l_i^2 \nabla d_i \cdot \nabla d_i)\ . \tag{4.17}$$

The coupling between the damage variables is introduced through the (degraded) stiffness tensor. The stiffness tensor is degraded using a diagonal degradation tensor where the entries are based on different damage variables. This makes it possible to characterize the damage evolution in the longitudinal direction distinctly from damage in the transverse direction. This approach is introduced within the context of composites, and to understand the method more, some mathematical details are presented. Firstly, recall that the stiffness tensor for orthotropic materials in a 2D setting is given by

$$\mathbb{C}_0 = \begin{bmatrix} C_{11} & C_{12} & 0 \\ C_{12} & C_{22} & 0 \\ 0 & 0 & C_{66} \end{bmatrix}. \tag{4.18}$$

Unlike the previous cases, where the degradation function returns a scalar, in this framework, a degradation tensor of the following form is defined:

$$\mathbb{D}(d) = \begin{bmatrix} 1-d_1 & 0 & 0 \\ 0 & 1-d_2 & 0 \\ 0 & 0 & \sqrt{(1-d_1)(1-d_2)} \end{bmatrix}, \tag{4.19}$$

where, d_1 and d_2 represent the two damage variables.

In such a case, the degraded stiffness tensor is given by

$$\begin{aligned} \mathbb{C}(d) &= \mathbb{D}(d) : \mathbb{C}_0 : \mathbb{D}(d) \\ &= \begin{bmatrix} (1-d_1)^2 C_{11} & (1-d_1)(1-d_2)C_{12} & 0 \\ (1-d_1)(1-d_2)C_{12} & (1-d_2)^2 C_{22} & 0 \\ 0 & 0 & (1-d_1)(1-d_2)C_{66} \end{bmatrix}. \end{aligned} \tag{4.20}$$

Although this is a specific application, the authors note that the robustness and flexibility of the approach provide a general framework that can allow for more complex constitutive behaviors to be considered.

In a separate work, Fei et al. [99] formulated a double phase field model for mixed-mode fracture in rock materials, within the context of isotropic fracture propagation. By introducing two damage variables, each corresponding to an opening mode in 2D, the framework is able to simulate both tensile fracture and frictional shear fracture. To this end, they degrade the failure modes distinctly using cohesive zone regularized degradation functions as proposed by Wu [57]. Furthermore, it is noted that to correctly account for cohesive tensile and friction shear fracture, knowledge of the crack orientation is required. As a result, they introduce a crack

direction-based decomposition of the strain energy into tensile, shear, and compressive components. In their framework, the crack orientation is determined as the local direction for a material point that maximizes the $\mathcal{F}$-criterion. It is important to note that, unlike the previous models that used global knowledge of the crack orientation, in this model, the crack orientation is taken to be a local variable to prevent the overlapping of different opening modes at the same material point.

Multi-phase field approaches inherently demand higher computational efforts but also require careful consideration of what constitutes "fully damaged". For instance, in the works of Nguyen [106], the degradation function is a product, and hence if one damage variable goes to one, then the specimen is fully damaged, that is, there is complete degradation of elastic stiffness. However, Bijaya et al. [112] acknowledge this as a limitation stemming from using degradation functions dependent on all damage variables. In some contexts, it is more intuitive that damage should cease to grow when all damage variables reach one, yet accounting for this requires a reformulation. Despite the robustness and flexibility guaranteed by this approach, introducing multiple damage variables is computationally expensive, and hence, single-damage variable models have been considered.

4.3.2. Single-damage Variable Models

In favor of computational efficiency, it is desired to leverage the capabilities of anisotropic degradation using a single damage variable. In such a case, the anisotropy in degradation stems from using distinct degradation functions. In the literature, most such models originate from applications where fracture propagation is isotropic, yet the residual material behavior is anisotropically degraded.

In their work, Zhao et al. [3] investigated the failure mechanisms of rock-like materials under compression by performing a direction decomposition to determine the tensile and shear failure energetic terms. Within the context of isotropic fracture propagation, their framework allows for degrading each opening mode distinctly. As noted previously, employing such a split also allows for a consistent treatment of the critical energy release rates between opening modes. Yet in this case, rather than accounting for the different critical energy release rates by splitting the driving force into components, they propose an alternative method where an "equivalent" critical energy release rate is determined based on the relative angle between the direction of motion and the direction of crack opening. In this framework, the crack orientation is determined based on the assumption that mode I is most dominant, and as a result, the angle is computed directly from the first eigenvector of the stress tensor. To limit the numerical burden required for determining the crack orientation and direction of motion, these are taken to be history state variables.

A vastly different and novel method for accounting for anisotropic stiffness degradation was proposed by Esteves et al. [113] (based on their previous work [114]). Within the context of isotropic materials and isotropic fracture propagation, they introduce a fourth-order degradation tensor capable of modeling anisotropic degradation. Through introducing this tensor, the need for a single or a set of damage variable(s) is bypassed. This tensor is an internal variable that evolves based on the thermodynamics of the system and thereby degrades the elasticity of the material.

4.4. Within the Context of Composites

Having seen what the notions of anisotropic fracture propagation and degradation entail, the state-of-the-art modeling approaches that have been applied to composites are examined. To do so, first some definitions are formalized, and thereafter the proposed formulations are presented. Specifically, a distinction is made between single-damage and multi-damage models.

4.4.1. Formalizing Definitions

Prior to discussing the models, three aspects related to the modeling approaches taken are defined. Thereafter, some terminology is introduced to facilitate comparing the state-of-the-art models. These are considered below.

Aspect 1. Scale

The first aspect is related to the "scale" of modeling. Progressive damage in composite laminates can be modeled from different length scales. Here, scale refers to the finest (spatial) resolution that can be resolved within the proposed modeling approach. In the context of composites, three scales can be identified [115]:

- *Macroscopic length scale*: the laminate is homogenized based on the classical laminate theory.
- *Mesoscopic length scale*: individual plies are modeled explicitly, but the microstructure of the ply is neglected using homogenization schemes.

- *Microscopic length scale*: the material's local mechanical behaviors are simulated such that these can be further used as input for homogenized models at larger length scales.

While most studies are focused on modeling within a particular scale, there have been attempts to consider trans-scale fracture. Often, cracks in fiber-reinforced composites initiate and propagate at the microscale level during loading, but can progressively result in the macroscopic failure of the material. Some recent attempts are discussed. Song et al. [116] proposed a model to simulate this process. They formulated a collaborative multiscale phase field model wherein a region-based phase field model was used for characterizing matrix cracking, fiber breaking, and interface debonding. Furthermore, a two-mode phase field model was implemented to simulate axial and transverse fracture modes at a macroscale. To facilitate the exchange of information between scales, a bridging model was developed.

Another modeling framework that investigated trans-scale fracture behavior was developed by Mitrou et al. [117]. However, unlike the previous case, where the different scales are explicitly modeled, they present an equivalent single-layer approach wherein the multidirectional thin-ply laminates' fracture properties are taken into account. In fact, the anisotropic fracture propagation in multidirectional laminates is modeled by modifying the scaling constants of the structural tensor. Rather than prescribing a value for the anisotropic fracture energy parameter, these scaling constants are determined based on the lay-up, the elastic properties of the lamina, and the fracture energy of the 0° ply.

Recently, Yue and Yuan [118] proposed a different methodology to address the different scales in composites. To simulate material degradation of fibrous composite materials, they derived a model based on inter- and intralaminar decomposition. The delamination behavior through the thickness direction is characterized using the interlaminar model. The intralaminar model accounts for the directional dependence of fracture energy. In this model, a reduced-order homogeneization method is used, where the fiber phase is described using a classical continuum damage model and the degradation of the matrix is simulated using a phase field model.

Aspec 2. Ease of Damage Initiation
Another aspect to consider is the ease of damage initiation. In composite materials, the critical energy release rate differs significantly for each failure mode, with the value for matrix cracking typically being much smaller. It is also recognized that the required fracture energy for damage initiation is strongly dependent on the fracture opening mode [20]. As a result, accounting for anisotropic fracture propagation alone does not guarantee sufficient accuracy [115].

Aspect 3. Modeling the Interface
The third aspect of relevance is how the interface is modeled. A failure mechanism that is often encountered is debonding. Debonding is defined differently based on the scale under consideration. For instance, in a macroscopic model, it refers to the failure mechanism that occurs between adjacent plies, whereas in a microscopic model, it occurs between the fibers and matrix [115]. Traditionally, cohesive zone models have been able to simulate debonding problems in a consistent manner, producing results that align well with experimental observations. As a result, to account for debonding, introducing cohesive zone methods in phase field models has received significant attention. Such hybrid frameworks can be introduced in a multitude of ways.

The first types of cohesive phase field models introduced a fracture energy function that was dependent on a set of history variables. The idea was that the derivative of these history variables with respect to the displacement jump would yield the cohesive traction separation law [119, 120]. Although in cohesive zone modeling it is not difficult to determine the crack opening, in phase field modeling, this is far from trivial, and as a result, an auxiliary variable was introduced to facilitate this. This variable was defined based on the traction continuity condition. A limitation of this approach was that crack propagation could only be modeled along pre-defined crack paths [119].

To overcome these limitations, an alternative approach was formalized by Freddi and Iurlano [121], wherein the energetic degradation function that depends on the length scale was introduced. The length scale parameter was incorporated in the degradation function such that the surface energy was not released abruptly. While this notion was rather promising, the results obtained were dependent on the length scale used. Motivated by this, Wu [57] proposed a unified phase field regularized cohesive zone model that can both characterize desired traction separation laws and remain length scale invariant. The degradation function parameters are related to the material properties and the cohesive law. Feng and Li [122, 123] extended these notions to

allow for mixed-mode cohesive laws. In both of these frameworks, through modifying the geometric crack function, the necessity for the auxiliary variable becomes obsolete.

Introducing Terminology
In the literature, several reformulations have been proposed to account for various physical phenomena observed in composites, and there is some overlap in the approaches taken. For ease of understanding, some terms are introduced to categorize the models and to help identify gaps in research. These terms are not directly from literature but rather serve to guide the reader. Stemming from the previous discussion, it is evident that to fully characterize progressive damage, three aspects are of importance:

1. *Fracture propagation*: how does anisotropy in fracture properties influence the damage path.
2. *Damage mechanisms*: how does the nature of loading influence the ease of damage initiation.
3. *Damage evolution*: how does a given damage state influence the extent of degradation on material properties.

To establish these terms within the context of phase field modeling, the following relations are noted where the bullet numbers below directly corresponding to the bullet numbers above.

1. To model the anisotropy in fracture propagation requires dealing with the direction-dependent nature of the fracture energy.
2. To have a *complete treatment* of the different damage mechanisms, the different fracture energies and failure strengths should be accounted for.
3. Lastly, to address damage evolution, an attempt must be made to characterize the independent nature of damage evolution for the different constituents.

Having established the scope of modeling aspects, the following paragraphs discuss the state-of-the-art models. For ease of comparison, the models have been grouped into either multi-damage models, and single-damage models.

4.4.2. Multi-damage Variable Models

One class of methods to account for the anisotropic propagation of fracture, the different damage mechanisms involved, and the different rates of damage evolution, is multi-phase field modeling approaches. Multi-damage variable models have the benefit that they can deal with different damage rates. In the literature, this is done in two ways: either a constituent-based split or a failure mechanism-based split. The former refers to the split between fiber and matrix. Whereas the latter is based on the energy split proposed by Quintanas-Corominas et al. [124]. Under this approach, the possible damage mechanisms (longitudinal fiber, in-plane shear, transverse shear, and transverse matrix) are obtained by splitting the elastic energy into different components based on the effective stresses. Such a split implicitly requires a distinction between the fiber and matrix phases. As a result, it is noted that models that employ a mechanism-based split also account for the different constituents. Thus the damage mechanism-based split is an extension of, rather than a replacement for, the constituent-based split.

While multi-phase field formulations can account for all three aspects, they do not always do so. For instance, to be able to characterize multiple cracking behaviors involving various fracture mechanisms, including brittle and ductile fracture for composites composed of multiple phases, Yuan et al. [125] consider a multi-phase field fracture model. In their formulation, they introduce two damage variables and define a driving force for each idealized phase. However, for a phase, the critical energy release rate is assumed constant, and both phases are degraded isotropically.

Recently, Kumar et al. [126] used a multi-phase field formulation combined with the Puck failure criterion to model the initiation of fracture in fiber and matrix separately. Similar to most existing literature, they use the structural tensor to account for anisotropic fracture propagation, and consider two damage variables to account for fiber and matrix damage independently. They opt for a constituent-based split of the driving energy from where the fiber and matrix components are normalized with their respective critical energy release rates. While this split accounts for the different critical energy release rates, the difference in failure strengths of the two phases is only *weakly* considered. Here, weakly is used as both terms are degraded using a quadratic degradation function, both with distinct length scale parameters. However, within their work, the length scale is taken to be a numerical parameter and is not chosen through a formal treatment of the critical material stress.

Both of these limitations are tackled in the model proposed by Su et al. [110], where a multi-phase field regularized cohesive zone model is founded based on the distinct failure mechanisms in composites. Similar to the previous models, they introduce two damage variables. However, unlike the previous works, they consider a damage mechanism-based splitting wherein the critical energy release rates of each failure mechanism are considered. Each of these energy terms is degraded using cohesive zone regularized degradation functions that take the different failure strengths into account. In addition, in their framework, they model the initiation of typical failure modes experimentally observed in composites using the Hashin failure criteria.

It is interesting to note that in their model, the stiffness is degraded anisotropically, inspired by continuum damage mechanics approaches. Specifically, they characterize damage using the *Murakami-Ohno damage model*. Under this formulation, there is a damage value associated with each orthogonal direction, based on which the Murakami damage tensor, $\mathbf{D}$, is defined as

$$\mathbf{D} = \sum D_i(\mathbf{n}_i \otimes \mathbf{n}_i), \tag{4.21}$$

where, D_i is a principal damage value and $\mathbf{n}_i$ are the principal unit vectors.

The damaged stiffness tensor, adopting their notation, is then determined from the undamaged stiffness tensor through

$$\mathbb{C}^{-1}(\mathbf{D}) = \mathbb{M}^T(\mathbf{D}) : \mathbb{C}_0^{-1} : \mathbb{M}(\mathbf{D}), \tag{4.22}$$

where, $\mathbb{M}(\mathbf{D})$ if a fourth order transformation tensor.

For completeness, this means that in Voigt notation, the damaged stiffness tensor can be represented as follows:

$$\mathbb{C}(\mathbf{D}) = \begin{bmatrix} (1-D_f)^2 C_{11} & (1-D_f)(1-D_m)C_{12} & 0 \\ (1-D_f)(1-D_m)C_{12} & (1-D_m)^2 C_{22} & 0 \\ 0 & 0 & (1-D_s)^2 C_{66} \end{bmatrix}. \tag{4.23}$$

Lastly, the damage variables D_f, D_m, and D_s are related to the fiber and matrix phase fields using the following relation:

$$D_f = 1 - \sqrt{g_f(d_f)}, \qquad D_m = 1 - \sqrt{g_m(d_m)} \qquad D_s = 1 - \sqrt{g_s(d_f) g_s(d_m)}, \tag{4.24}$$

where g_f, g_m, and g_s denote the degradation functions of the fiber, transverse matrix, and shear matrix, respectively, and d_f and d_m represent the fiber and matrix phase fields.

At around the same time, Wang et al. [69] identified that the challenge of modeling mixed-mode fracture within a phase field modeling framework lies in the difficulty of incorporating a reasonable mixed-mode cohesive law. As a result, they proposed a formulation to characterize mixed-mode fracture in fiber-reinforced composites within a thermodynamically consistent framework. They show that their cohesive zone model effectively and rigorously characterizes the Hashin failure criteria for crack initiation and the power law criterion for crack propagation. The details of the method are rather similar to the previous model, as a damage mechanism-based splitting of the elastic energy is considered, allowing for a consistent treatment of the critical energy release rates. Each energetic component is degraded using a cohesive zone regularized degradation function, and the Murakami-Ohno model is used for degrading the stiffness tensor. Recently, Wang and Chen [127] also used a similar methodology, however, by considering the maximum stress criterion to predict the onset of fiber damage, and the Hashin, Puck, and LarC03 criteria for predicting the initiation of matrix damage.

Multi-phase field models have also been extended to three-dimensional domains and multi-physics settings. For instance, Kumar and Sain [128] formulated a multi-phase field model to simulate bulk and interfacial fracture in 3D composites, by using uncoupled 3D traction-separation laws to represent the interface constitutive behavior. In another work, Zhang et al. [129] presented a multi-phase field model to simulate thermal-deformation fracture in fiber-reinforced composite polymers with holes. In both cases, the quadratic degradation function is considered, and only tension-compression splitting is accounted for.

While the previous multi-phase field models introduced different damage variables to account for both constituents, there have been formulations where the distinct damage variables correspond to other parameters. To investigate delamination under buckling loads, Wang et al. [130] proposed a 3D multi-phase field model to simulate the interlaminar failure of the laminated plates based on the phase field values of $n-1$ adhesive layers and Reddy's higher-order shear deformation theory. In their model, each damage variable corresponds to an adhesive layer. However, within a layer, the different failure mechanisms are not accounted for as an AT2 model is used with only a tension-compression split.

4.4.3. Single-damage Variable Models

Most methods of modeling fracture in composites use a multi-phase field model, and as a result, fewer attempts characterize progressive damage using a single damage variable. From a numerical perspective, there is motivation for adopting single-damage models. One of the limitations of phase field modeling lies in its computational expense, and by introducing multi-phase field models, this is heightened. However, within the current formulations, it is difficult to account for both different damage mechanisms and rates. For instance, Sagar et al. [131] present a thermodynamically consistent phase field fracture model for elastoplastic solids undergoing ductile fracture. Although they define the phase field driving energy based on both a local damage propagation indicator and an energy barrier dependent on the local damage onset criterion, the degradation after the onset of damage is done isotropically using the quadratic degradation function.

While it may be difficult to account for the different damage rates, the presence of different fracture energies can be addressed. By splitting the driving force into separate components, the different critical energy release rates can be accounted for. In their work, Jain et al. [132] present an adaptive phase field method to model fracture propagation in orthotropic composites where the strain energy is decomposed into fiber, matrix mode-I, and matrix mode-II components. Although similar to the paper above, once split, all energetic components are degraded isotropically, as is the stiffness tensor. A similar methodology was used by Mrunmayee et al. [133] to also model mixed-mode fracture in composites.

Noting that matrix compression failure and fiber buckling under structural compression are not correctly modeled, Zhang et al. [134] present a phase field model that incorporates the fracture driving force based on the LaRC03 failure criterion. Here, the driving force for the composite is reformulated using existing failure criteria for matrix, fiber kinking, and fiber tensile failure, and thus is split into these components. Once split, the components are degraded isotopically using the quadratic degradation function.

Other single-damage models have also attempted to model other types of composite behavior. For instance, in their work, Guo et al. [135] considered an anisotropic micropolar single-damage phase field model to capture size effects that are introduced by the microstructural features on crack initiation and propagation. The anisotropic micropolar elasticity and the Tsai-Hill criterion are coupled into a phase field framework within the context of modeling composite failure behavior. Konica and Sain [136] noted that phase field modeling neglects the dependence of constituent-level factors on the failure mechanisms in composites. In particular, the effect of the viscoelasticity or plasticity of the matrix is not taken into account. As a result, they developed a homogenized coupled thermo-mechanical constitutive model for considering the viscoelasticity of the polymer matrix in fiber-reinforced composites.

Recently, for the first time, there has been an attempt to also account for the different failure strengths. Yu et al. [137] proposed a unified anisotropic phase field model with a new crack surface density function, where the effects of fiber and matrix fracture properties and their length scale parameters are taken into account. They derive a single-phase field model whose driving force is defined based on the critical energy release rates and length scale parameters of the fiber and matrix phases. To account for the different damage mechanisms, a failure mechanism-based energy split is considered where the terms are degraded using consistent Wu-based degradation functions, and the Murakami-Ohno model is used to degrade the stiffness tensor. However, as it is a single-damage model, the different damage evolution rates of the different phases are not accounted for. Rather, it is assumed that the damage incurred by the fibers is equal to the damage incurred by the matrix.

4.5. Within the Context of Spatially Non-Homogeneous Materials

The prior discussion of phase field modeling in composites was restricted to cases where the materials were idealized to have spatially homogeneous properties. However, as engineering materials increase in complexity, the discussion of anisotropic fracture in the context of spatially non-homogeneous materials is of growing interest. In the case of composites, this can refer to two cases:

- *Models accounting for the heterogeneous nature of composites*: as the term entails, composites are materials composed of two or more distinct constituents with differing mechanical and fracture properties, such as fibers and matrix. In the majority of the models seen so far, at the structural scale, they are modeled using homogenized or effective material properties. However, the influence of microscale heterogeneity on crack initiation, propagation, and interaction with material interfaces is significant, and this class of models addresses this.
- *Models for simulating fracture in Variable Stiffness Composite Laminates (VSCL)*: even within a homogeneous modeling framework, VSCL have spatially varying fiber orientations, thereby resulting in spatially varying elastic and fracture properties.

The last case may seem rather specific, but the topic is of increasing relevance. Over recent years, VSCL have gained significant traction, particularly due to advancements in automated fiber placement [138] and their potential in aerospace applications [18]. Furthermore, this class of materials can also include anisotropic functionally graded materials. Within the context of anisotropic fracture, this class of materials remains under-researched, and many of the notions explored above can be revised and extended.

In the context of composites, several works have aimed at modeling fracture propagation, taking the heterogeneous nature of the material into account. Bourdin, Bhattacharya, and colleagues [139, 140] have, over the past several years, investigated how the effective fracture energy of a specimen is influenced by elastic heterogeneities and spatial variations in fracture energy. Their work aims to model crack tortuosity arising from the geometry and distribution of heterogeneities, investigating how microscale material contrast and structural features can significantly alter macroscopic crack paths and apparent energy. Recently, these notions have been extended to develop mathematically rigorous asymptotic homogenization theories [141, 142].

Li et al. [143] presented some of the first works in predicting microcrack evolution in highly heterogeneous solids while accounting for the complex microstructures and strong interactions between constituents. They proposed a coupled cohesive phase field model capable of predicting microfracture evolution and interfacial debonding in quasi-brittle composites. Crack nucleation and propagation are described using a gradient damage formulation, while interface properties are regularized through the interaction between matrix and inclusion properties, as well as the finite width of the interface. The authors show that interfacial dissipation is influenced by both matrix and reinforcement toughness, and they explicitly incorporate this effect into the crack phase field formulation. A quasi-quadratic degradation function is adopted to govern the phase field evolution.

Around the same time, through a vastly different approach, Jeulin [144] tackled a similar problem. By noting that the crack paths are strongly affected by local fluctuations in fracture energy, Jeulin modeled the fracture properties as realizations of random fields. In such materials, differences between transgranular and intergranular fracture energies can induce strong anisotropy due to the presence of weak crystallographic planes. The proposed approach is extended to account for heterogeneous and anisotropic fracture energy distributions. Rather than relying on finite element discretizations, all material properties are treated as realizations of random fields, and Fast Fourier Transform techniques are used to efficiently solve the equilibrium equations. Although no numerical simulations are presented, the framework offers a promising direction for large-scale stochastic fracture modeling.

Liu and Yuan [145] present a multiscale model for fibrous composites in which the matrix phase is described using a phase field formulation, while the fiber phase is represented by a classical constitutive model. The overall composite response is obtained through averaging and homogenization techniques. Within a reduced-order homogenization framework, a representative unit cell at the mesoscale is introduced under the assumption of local periodicity. This unit cell is partitioned into several locally homogeneous subdomains, and macroscopic material responses are computed by volumetric averaging of the state variables over all partitions. For fibrous composites, the fiber and matrix phases are naturally treated as separate partitions within this framework.

You et al. [146] demonstrate that the macroscopic fracture behavior of heterogeneous materials can differ markedly from that of homogeneous solids, notably through anisotropic fracture energy and strain-gradient effects. To capture these features, they propose a novel multiscale phase field modeling framework. Using a two-scale asymptotic expansion, they derive an equivalent coupled multi-field boundary value problem that incorporates a strain-gradient elasticity submodel alongside a homogenized phase field submodel. The effective elastic constitutive relations and fracture properties are obtained through homogenization procedures. Furthermore, by employing a spectral decomposition of the stress tensor, the tensile and compressive contributions are clearly separated, allowing for a physically consistent description of crack initiation and propagation.

Within the context of spatially non-homogeneous materials, anisotropy can refer to either elastic material properties and/or fracture properties. This is because in the case of functionally graded materials, the elastic properties are spatially dependent, but the preferred fracture plane does not necessarily have to be spatially varying, and in fact, in the literature, this is often not the case [147]. However, recently, Sidharth and Rao [148, 149] extended their exponential shape function-based phase field modeling framework [150] to consider the case of anisotropic fracture propagation by including the anisotropic structural tensor. In both works, anisotropic degradation is not considered. In the case of VSCL, both the fracture plane and elastic properties vary spatially. Models related to this class of materials are further discussed below.

A special class of spatially non-homogeneous materials is VSCL. However, unlike the case above, these also inherently have spatially non-homogeneous preferred fracture planes. This problem was first investigated by Hirshikesh et al. [76]. They introduced a framework wherein the local fiber orientation varies with spatial location. In their approach, they idealized a laminated composite as a homogeneous linear-elastic orthotropic material in which the effective elastic properties are computed using the rule of mixtures. Furthermore, the effective fracture properties are determined through two approaches: one based on the minimum between the critical energy release rate of the fibers and matrix, and the other through the rule of mixtures. However, within their study, they do not consider anisotropic degradation or differentiate between the different failure modes present.

Yu and Hou [88] presented a method to model variable stiffness composites using an adaptive phase field model based on the remeshing technique. Consistent with supporting literature, they present a framework in which the local angle is used to construct the structural anisotropy tensor. However, to account for the different critical energy release rates, they split the driving force into distinct contributions. Despite this, the degradation of the driving force is done isotropically, using a quadratic degradation function. To account for the different failure strengths, they use the matrix fracture properties to determine the associated length scale parameter.

Unlike the previous single-damage models, Pan et al [151] proposed a multi-phase field model to simulate fracture propagation in VSCL. They restricted their focus to modeling tensile and shear-dominant failure and hence only introduced two damage variables. Although a multi-phase field formulation allows for anisotropic degradation, in their methodology, they use the same degradation function and set the length scale parameter to be equal and based on the mesh size. A limitation of this strategy is that the treatment of the failure strengths is not done in a physically consistent manner. However, as they split the driving force, the different critical energy release of the fiber and matrix phases are accounted for.

4.6. Research Gap, Question & Goals

The works above have shown phase field modeling as a particularly promising approach of modeling fracture in composite materials. While several independent formulations have successfully addressed specific aspects such as fracture propagation, constituent-level degradation, or mode-dependent behavior, these efforts remain largely fragmented. Moreover, the physical implications of some of these modeling strategies are still unclear. It is clear that from a physical perspective, any numerical model constructed to simulate anisotropic fracture propagation in composites will have to address the dependency of fracture properties on direction and opening mode. The following paragraphs evaluate how the existing frameworks meet this goal.

As evidently seen from the literature review, most anisotropic phase field models use the structural tensor to effectively define a direction-dependent fracture energy. However, there is a lack of clarity on understanding what such a modification to the gradient energy represents [111][23]. Li et al. [25] interpret the structural tensor formulation as a truncated Taylor series approximation of an anisotropic fracture energy density. Within this interpretation, the structural tensor-based approach can be understood as a reduced-order representation of a more general orientation-dependent fracture energy. In such a case, it is reasonable to question whether the approach of defining the direction-dependence of fracture energy explicitly is actually a "more accurate" generalization of the structural tensor-based approach. As a result, it remains to be investigated how this method of explicitly prescribing the dependence of fracture energy on orientation compares to using a structural tensor.

In addition, the structural tensor-based approach also introduces an orientation-dependent regularization length scale that is directly related to the degree of prescribed anisotropy [22]. As a result, physically consistent values cannot be used for the fracture anisotropy parameter [104]. It could be argued that this is merely a visual artifact, but that is not the case, as phase field modeling infers crack propagation from the ease of damage accumulation. As anisotropic length scales can lead to artificially diffuse crack zones in certain orientations, these can act as spurious nucleation sites for damage. This limitation is also resolved by introducing the directional dependency directly in the fracture energy. However, this approach has been applied only to crystalline structures [24] and very recently to multiphase solids with isotropic elastic properties [23]. Furthermore, both these works only consider opening in mode I; thus, extending it to mixed-mode cases remains unexplored.

In phase field modeling for composites, to account for the different fracture energies associated with different mechanisms, anisotropic phase field models split the driving force into different failure mechanisms and use the respective fracture energy [124][126][110][69][134][88]. In such cases, the driving force resembles the following form:

$$\left[g_L'(d)\frac{\mathcal{H}_L}{G_L} + g_{TI}'(d)\frac{\mathcal{H}_{TI}}{G_{TI}} + g_{TII}'(d)\frac{\mathcal{H}_{TII}}{G_{TII}} + g_{TL}'(d)\frac{\mathcal{H}_{TL}}{G_{TL}}\right] - \frac{1}{c_0}\left[\frac{\vartheta'(d)}{l} - 2l\,\nabla\cdot(\mathbf{A}\nabla d)\right], \tag{4.25}$$

where, $\mathcal{H}_L$, $\mathcal{H}_{TI}$, $\mathcal{H}_{TII}$, $\mathcal{H}_{TL}$ are the history terms for the energy associated with the failure modes of longitudinal fiber, transverse matrix, transverse shear, and in-plane shear, G_L, G_{TI}, G_{TII}, and G_{TL} are the fracture energies of those failure modes, and g_L, g_{TI}, g_{TII}, and g_{TL} are the degradation functions of those failure modes.

A merit of this formulation is that it allows for a complete consideration of the various fracture energies and strengths. However, when this approach is combined with the structural tensor, it implicitly assumes that all decomposed driving force components inherit the same directional dependence. Yet, different failure mechanisms often exhibit distinct anisotropic behavior. In such cases, the physical implications of the structural tensor remain unclear.

It is also well known that the fracture opening mode has a direct influence on fracture energy in composites. As a result, it is worth investigating current mixed-mode phase field formulations in both anisotropic and isotropic contexts, as successful strategies from the latter can be introduced into this new context. As seen from the literature review, often, mixed-mode phase field models employ a similar decomposition strategy to account for mode-mixity effects in crack propagation. The different fracture energies are accounted for by splitting the driving force into opening mode contributions [98][132][100][133] from where the distinct fracture energies are used to normalize the driving terms. However, in the context of composites, this has the previously identified limitation. An alternative strategy was proposed by Zhao et al. [3] by introducing a mode-dependent fracture energy. Extending this idea to anisotropic contexts and specifically for composites has not been investigated.

Furthermore, all these works are primarily developed in the context of constant stiffness composite laminates, where material directions remain fixed in space. However, recent studies have extended phase field modeling to VSCL, in which the fiber orientation varies spatially [76] [88] [151]. However, tackling the aforementioned limitations within the context of both constant and VSCL remains to be researched.

Based on all preceding discussions, the following research question is identified:

How can advanced fracture processes be modeled in a unified thermodynamically consistent framework?

To solve this question, the following four goals are identified:

- Develop a thermodynamically consistent, generalized framework that can account for both anisotropic fracture and varying mode-mixity.
- Present a critical comparison of a structural tensor-based formulation with a direction-dependent fracture energy-based formulation for anisotropic fracture.
- Determine a method to account for varying mode-mixity in a thermodynamically permissible manner that is compatible with anisotropic fracture.
- Specialize the proposed framework to the case of VSCL.

Methodology

5: Mathematical Framework

Based on the research question and goals identified in Chapter 4, this chapter presents the proposed methodology. The primary objective is to develop a generalized phase field framework that provides sufficient flexibility to accommodate a wide range of fracture processes. The chapter is split into two parts, where the first introduces the general framework and its theoretical foundations, while the second investigates a chosen formulation. The first part of the chapter begins by detailing the scope of the model in Section 5.1. This is followed by Section 5.2, where a comparison of existing methods to the proposed model is presented. The variational problem for the proposed formulations is revisited in Section 5.3.

The second part of the chapter deals with applying the proposed framework. To this end, a possible direction-dependent fracture energy function is defined in Section 5.4. This proposed function is investigated and analyzed in Section 5.5 and Section 5.6. This is followed by presenting a formulation for the mode-dependent fracture energy in Section 5.7. Thereafter, a formulation for the combined direction- and mode-dependent fracture energy is discussed in Section 5.8. Lastly, the thermodynamic permissibility of the model is examined in Section 5.9.

5.1. Scope of Model

The modeling framework is developed to address the research goals outlined previously. For clarity, these objectives are reiterated below:

1. Develop a thermodynamically consistent, generalized framework that can account for both anisotropic fracture and varying mode-mixity.
2. Present a critical comparison of a structural tensor-based formulation with a direction-dependent fracture energy-based formulation for anisotropic fracture.
3. Determine a method to account for varying mode-mixity in a thermodynamically permissible manner that is compatible with anisotropic fracture.
4. Specialize the proposed framework to the case of VSCL.

Remark 5.1

Regarding the fourth research goal, as identified during the literature review, a truly unified damage model for composites would require capturing the behavior and interactions of the different failure mechanisms. While it is possible to address these failure mechanisms individually in 2D spaces (as commonly done in the literature), because they exist in orthogonal spaces, this would require a 3D model. To exemplify, delamination is an interply phenomenon, whereas matrix cracking is an intraply phenomenon. Thus, the framework should allow for identifying when a mechanism acts and how it interacts with other mechanisms for both initiation and propagation. Within the scope of this thesis, a fully 3D model is not developed, but rather the analysis is restricted to 2D. The natural extension of the present work lies in the generalization to a 3D setting, wherein additional constitutive structure would be required to explicitly couple the different failure mechanisms and their respective evolution laws.

This chapter presents the mathematical formulation proposed to address these objectives, with particular emphasis on fully addressing the second objective. The aspects related to the numerical implementation are treated in Chapter 6, while the results obtained using the proposed framework are discussed in Chapter 7, Chapter 8, Chapter 9, and Chapter 10. As a result, in this chapter, the following aspects are discussed:

1. Establish the nature of the proposed fracture energy density, and compare this formulation to existing methods.
2. Revisit the variational problem for the proposed formulations.
3. Establish the nature of a direction-dependent fracture energy under mode-independent conditions.
4. Compare the proposed direction-dependent fracture energy under mode-independent conditions to existing methods.
5. Establish a dependency of the fracture energy on mode-mixity.
6. Propose a method to determine the extent of mode-mixity.
7. Present and formalize a dependency of fracture energy on both direction and mode-mixity.

8. Formalize the thermodynamic permissibility of the proposed model.

Each of these requirements is discussed in more detail in the following subsections.

5.2. Fracture Energy Formulation

Throughout the literature review, different formulations have been identified, each aiming to extend classical phase field modeling to account for some particular material behavior. The formulations differ in the constitutive modeling of the crack surface energy. The relevant ones are named and summarized below:

$$\begin{aligned}
&\psi_d^{\text{iso, fixed}}(d, \nabla d) = G_c \gamma(d, \nabla d) && \text{Isotropic mode-independent formulation [64],} \\
&\psi_d^{\text{iso, mixed}}(\chi, d, \nabla d) = G_c(\chi) \gamma(d, \nabla d) && \text{Isotropic mixed-mode formulation [3],} \\
&\psi_d^{\text{cl. aniso}}(d, \nabla d; \mathbf{A}) = G_c \gamma(d, \nabla d; \mathbf{A}) && \text{Classical anisotropic formulation [22],} \\
&\psi_d^{\text{cs. aniso}}(d, \nabla d) = G_c(\nabla d) \gamma(d, \nabla d) && \text{Consistent anisotropic formulation [24],}
\end{aligned} \tag{5.1}$$

where χ denotes the mode-mixity.

Comment on terminology

As evident from Equation 5.1, the formulation using the structural tensor to introduce anisotropy in fracture is termed the classical anisotropic formulation, and the formulation that uses an explicitly defined direction-dependent fracture energy is referred to as the consistent anisotropic formulation.

However, these methods do not allow for a coupled treatment of mode-mixity and anisotropy. As a result, two formulations are proposed, namely

$$\begin{aligned}
&\psi_d^A(\chi, d, \nabla d, \mathbf{m}) = G_c(\chi, \mathbf{m}) \gamma(d, \nabla d) && \text{Proposed formulation A ,} \\
&\psi_d^B(\chi, d, \nabla d; \mathbf{A}) = G_c(\chi) \gamma(d, \nabla d; \mathbf{A}) && \text{Proposed formulation B,}
\end{aligned} \tag{5.2}$$

where $\mathbf{m}$ denotes the unit vector in the direction of the crack normal (inferred from the damage gradient).

Thus, the proposed formulations can be interpreted as generalizations of the classical and consistent approaches to the mixed-mode case. The comparison of the two approaches directly contributes to addressing the second research goal, namely, to investigate how the introduction of fracture anisotropy via a structural tensor compares to its introduction through a direction-dependent fracture energy.

Remark 5.2

Unlike the models in the literature that model fracture anisotropy consistently by taking the damage gradient as the governing argument, the proposed formulation A instead employs the crack normal. This distinction is critical, as it renders the fracture energy independent of the magnitude of the damage gradient and dependent solely on its orientation.

Comment on terminology

Whenever the effect of fracture energy on mode-mxiity is suppressed (as in Section 5.4), the *proposed formulation A* and *proposed formulation B* are referred to as simply *consistent* and *classical* formulations.

Prior to discussing the formulations in more detail, the relation between the damage gradient and crack orientation, along with some relevant notation, is introduced. The required definitions and geometric interpretation are illustrated in Figure 5.1. This figure considers a 2D case; however, the notions could be extended to a 3D setting if required.

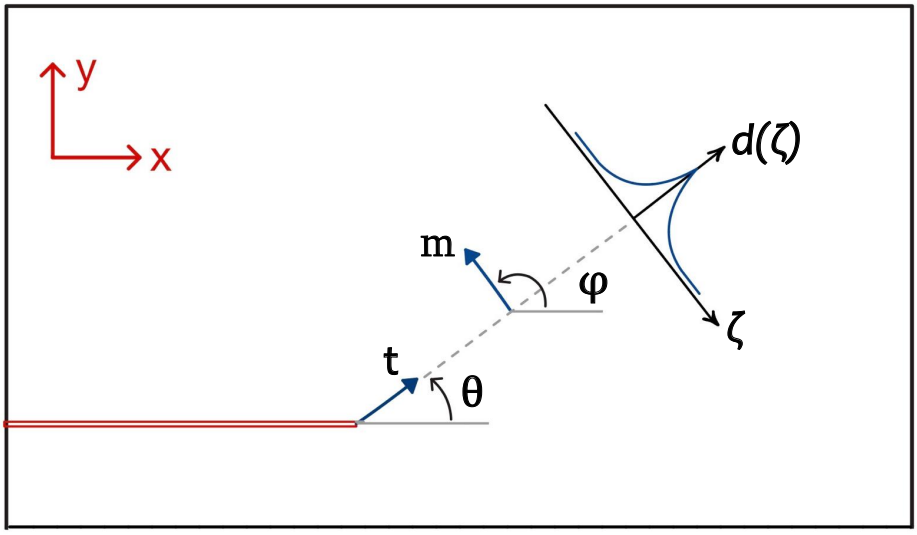

Figure 5.1: Geometrical interpretation of damage variable, damage gradient, and crack orientation.

To establish the relation between the damage gradient and crack orientation, consider a crack that is propagating in a direction denoted by **t**. Phase field modeling employs a diffuse representation of cracks, in which the damage variable attains its maximum value along the crack path and gradually decreases in magnitude with increasing distance from it. In other words, $d(\zeta)$ will have its highest value in the orientation of the crack and will decrease in a perpendicular direction (see the $d(\zeta)$ graph in Figure 5.1). The damage gradient is oriented towards this perpendicular direction. As a result, the following holds:

$$\mathbf{t} \perp \mathbf{m} \qquad \Rightarrow \theta = \varphi - \frac{\pi}{2}, \tag{5.3}$$

where φ denotes the orientation of the damage gradient and θ denotes the crack orientation.

Given a coordinate system, the angle of the crack normal can be computed from its components. For a Cartesian coordinate system, this is as follows:

$$\varphi = \arctan\left(\frac{[\mathbf{m}]_y}{[\mathbf{m}]_x}\right), \tag{5.4}$$

from where it is trivial to compute θ.

5.3. Revisiting the Variational Problem

To compare and understand proposed formulations A and B, the variational problem is revisited for both cases. The governing equations are described below.

5.3.1. Proposed Formulation A

Unlike the previous cases, the proposed formulation makes the fracture energy dependent on the crack orientation (related to the damage gradient, as detailed previously) and mode-mixity. Thus, the energy functional is given by

$$\Psi_{\text{total}} = \int_{\mathcal{B}} \psi_e(\boldsymbol{\varepsilon}, d)\,\mathrm{d}V + \int_{\mathcal{B}} G_c(\chi, \mathbf{m})\gamma(d, \nabla d)\mathrm{d}V - \int_{\mathcal{B}} \mathbf{b}\cdot\mathbf{u}\,\mathrm{d}V - \int_{\partial\mathcal{B}_s} \mathbf{f}_0\cdot\mathbf{u}\mathrm{d}S\,. \tag{5.5}$$

Similar to what was presented in the literature review, the first variation of displacement is decoupled from the first variation due to the phase field. As a result, the following is obtained:

$$\delta_{\mathbf{u}}\Psi_{\text{total}} = \int_{\mathcal{B}} \frac{\partial\psi_e}{\partial\boldsymbol{\varepsilon}}\delta\boldsymbol{\varepsilon}\,\mathrm{d}V - \int_{\mathcal{B}} \mathbf{b}\cdot\delta\mathbf{u}\,\mathrm{d}V - \int_{\partial\mathcal{B}_s} \mathbf{f}_0\cdot\delta\mathbf{u}\,\mathrm{d}S\,. \tag{5.6}$$

Noting that the stress is the partial derivative of the energy density with respect to strain, Equation 5.6 can be written as

$$\delta_{\mathbf{u}}\Psi_{\text{total}} = \int_{\mathcal{B}} \boldsymbol{\sigma}\delta\boldsymbol{\varepsilon}\,\mathrm{d}V - \int_{\mathcal{B}} \mathbf{b}\cdot\delta\mathbf{u}\,\mathrm{d}V - \int_{\partial\mathcal{B}_s} \mathbf{f}_0\cdot\delta\mathbf{u}\,\mathrm{d}S\,. \tag{5.7}$$

By using the divergence theorem, the standard equation of equilibrium is obtained

$$\delta_{\mathbf{u}}\Psi_{\text{total}} = \int_{\mathcal{B}} (\nabla \cdot \boldsymbol{\sigma} + \mathbf{b}) \cdot \delta\mathbf{u}\, \mathrm{d}V - \int_{\partial\mathcal{B}_s} (\boldsymbol{\sigma} \cdot \mathbf{n} - \mathbf{f}_0) \cdot \delta\mathbf{u}\, \mathrm{d}S\,. \tag{5.8}$$

Thus, the governing equations for the mechanical problem are

$$\begin{aligned} \nabla \cdot \boldsymbol{\sigma} + \mathbf{b} &= 0 \quad && \text{in } \mathcal{B}, \\ \boldsymbol{\sigma} \cdot \mathbf{n} &= \mathbf{f}_0 && \text{on } \partial\mathcal{B}_s\,. \end{aligned} \tag{5.9}$$

It is to be noted that this is identical to the equations obtained for the isotropic case. This is expected as this reformulation has introduced no change to the mechanical problem.

However, the variation with respect to the damage variable is different. Unlike the previous cases, the fracture energy is dependent on the gradient of the damage, and hence the product rule must be applied to the crack energy functional. As a result, an additional term is obtained as expressed in the equation below

$$\delta_d\Psi_{\text{total}} = \int_{\mathcal{B}} \frac{\partial\psi_e}{\partial d}\delta d\, \mathrm{d}V + \int_{\mathcal{B}} G_c(\chi, \mathbf{m}) \left(\frac{\partial\gamma}{\partial d}\delta d + \frac{\partial\gamma}{\partial\nabla d} \cdot \delta\nabla d \right) \mathrm{d}V + \int_{\mathcal{B}} \frac{\partial G_c}{\partial\nabla d}\gamma(d, \nabla d) \cdot \delta\nabla d\, \mathrm{d}V\,. \tag{5.10}$$

To rewrite the terms involving $\delta\nabla d$, integration by parts is used. For completeness, the general formula is written below

$$\int_\Omega \nabla f \cdot \mathbf{g}\, \mathrm{d}V = \int_\Omega (\nabla \cdot (f\mathbf{g}) - f\nabla \cdot \mathbf{g})\, \mathrm{d}V = \int_{\partial\Omega} f\mathbf{g} \cdot \mathbf{n}\, \mathrm{d}S - \int_\Omega f\nabla \cdot \mathbf{g}\, \mathrm{d}V, \tag{5.11}$$

where f, and $\mathbf{g}$ are two functions and $\mathbf{n}$ is the unit vector normal to $\partial\Omega$.

Applying this to the last term in Equation 5.10 results in

$$\int_{\mathcal{B}} \frac{\partial G_c}{\partial\nabla d}\gamma(d, \nabla d) \cdot \delta\nabla d\, \mathrm{d}V = \int_{\partial\mathcal{B}} \left(\frac{\partial G_c}{\partial\nabla d}\gamma(d, \nabla d) \cdot \mathbf{n} \right) \delta d\, \mathrm{d}S - \int_{\mathcal{B}} \nabla \cdot \left(\frac{\partial G_c}{\partial\nabla d}\gamma(d, \nabla d) \right) \delta d\, \mathrm{d}V\,. \tag{5.12}$$

In view of Equation 5.12, Equation 5.10 reads

$$\begin{aligned} \delta_d\Psi_{\text{total}} = \int_{\mathcal{B}} \frac{\partial\psi_e}{\partial d}\delta d\, \mathrm{d}V &+ \int_{\mathcal{B}} G_c(\chi, \mathbf{m}) \left(\frac{\partial\gamma}{\partial d} \right) \delta d\, \mathrm{d}V - \int_{\mathcal{B}} \nabla \cdot \left(G_c(\chi, \mathbf{m}) \frac{\partial\gamma}{\partial\nabla d} \right) \delta d\, \mathrm{d}V \\ &+ \int_{\partial\mathcal{B}} \left(G_c(\chi, \mathbf{m}) \frac{\partial\gamma}{\partial\nabla d} \right) \cdot \mathbf{n}\, \delta d\, \mathrm{d}S - \int_{\mathcal{B}} \nabla \cdot \left(\gamma(d, \nabla d) \frac{\partial G_c}{\partial\nabla d} \right) \delta d\, \mathrm{d}V \\ &+ \int_{\partial\mathcal{B}} \left(\gamma(d, \nabla d) \frac{\partial G_c}{\partial\nabla d} \right) \cdot \mathbf{n}\, \delta d\, \mathrm{d}S\,. \end{aligned} \tag{5.13}$$

Equation 5.13 can be rearranged to the following form:

$$\begin{aligned} \delta_d\Psi_{\text{total}} = &\int_{\mathcal{B}} \left[\frac{\partial\psi_e}{\partial d} + G_c\frac{\partial\gamma}{\partial d} - \nabla \cdot \left(G_c\frac{\partial\gamma}{\partial\nabla d} + \gamma\frac{\partial G_c}{\partial\nabla d} \right) \right] \delta d\, \mathrm{d}V \\ &+ \int_{\partial\mathcal{B}} \left[\left(G_c\frac{\partial\gamma}{\partial\nabla d} + \gamma\frac{\partial G_c}{\partial\nabla d} \right) \cdot \mathbf{n} \right] \delta d\, \mathrm{d}S\,. \end{aligned} \tag{5.14}$$

Thus, based on the variational principle, the governing equation for the phase field becomes

$$\frac{\partial\psi_e}{\partial d} + G_c\frac{\partial\gamma}{\partial d} - \nabla \cdot \left(G_c\frac{\partial\gamma}{\partial\nabla d} + \gamma\frac{\partial G_c}{\partial\nabla d} \right) = 0 \qquad \text{in } \mathcal{B}, \tag{5.15}$$

with the following boundary condition:

$$\left(G_c\frac{\partial\gamma}{\partial\nabla d} + \gamma\frac{\partial G_c}{\partial\nabla d} \right) \cdot \mathbf{n} = 0 \qquad \text{on } \partial\mathcal{B}\,. \tag{5.16}$$

5.3.2. Proposed Formulation B

Next, the variational structure of proposed formulation B is considered. Under this formulation, the fracture energy only has a dependency on mode-mixity; the directional dependence is retained in the geometric crack surface density function. Thus, the energy functional is given by

$$\Psi_{\text{total}} = \int_{\mathcal{B}} \psi_e(\boldsymbol{\varepsilon}, d)\,\mathrm{d}V + \int_{\mathcal{B}} G_c(\chi)\gamma(d, \nabla d; \mathbf{A})\,\mathrm{d}V - \int_{\mathcal{B}} \mathbf{b}\cdot\mathbf{u}\,\mathrm{d}V - \int_{\partial\mathcal{B}_s} \mathbf{f}_0\cdot\mathbf{u}\mathrm{d}S\ . \tag{5.17}$$

The energy potential written in this form is similar to the classical anisotropic case, with the exception that the fracture energy is dependent on mode-mixity. However, because mode-mixity is not a field variable, it does not change the resulting governing equations. As a result, they are given as follows:

$$\begin{aligned} \nabla\cdot\boldsymbol{\sigma} + \mathbf{b} &= 0 \quad && \text{in}\,\mathcal{B}, \\ \boldsymbol{\sigma}\cdot\mathbf{n} &= \mathbf{f}_0 && \text{on}\,\partial\mathcal{B}_s\ . \end{aligned} \tag{5.18}$$

For the phase field, the variation with respect to the damage variable retains the following form:

$$\delta_d\Psi_{\text{total}} = \int_{\mathcal{B}} \left[\frac{\partial\psi_e}{\partial d} + G_c(\chi)\left(\frac{\partial\gamma}{\partial d} + \nabla\cdot\frac{\partial\gamma}{\partial\nabla d}\right)\right]\delta d\,\mathrm{d}V + \int_{\partial\mathcal{B}} G_c(\chi)\left(\frac{\partial\gamma}{\partial\nabla d}\cdot\mathbf{n}\right)\delta d\,\mathrm{d}S, \tag{5.19}$$

However, from Equation 5.19, the phase field boundary condition now becomes

$$[\mathbf{A}\nabla d]\cdot\mathbf{n} = 0 \qquad \text{on}\ \partial\mathcal{B}\ . \tag{5.20}$$

Comparing Equation 5.19 and Equation 5.14, it appears that proposed formulation A has an additional term $\nabla\cdot\left(\gamma\frac{\partial G_c}{\partial\nabla d}\right)$. When G_c is directionally independent, this term is zero, and in such cases the standard isotropic case is recovered.

5.4. Defining a Direction-Dependent Fracture Energy

The previous sections presented the general framework. The following sections, including this one, apply the model. In proposed formulation A, the fracture energy depends on both crack orientation, inferred from the crack normal, **m**, and mode-mixity. To isolate their individual effects, each dependency is proposed separately before establishing a formulation for the coupled function. As a result, this section focuses on formulating *a* direction-dependent fracture energy.

5.4.1. Possible Formulations

In the literature review, it was noted that in the classical formulation, the dependence of fracture energy on direction is implicitly defined through the structural tensor. The term involving the structural tensor is, by definition, a linear mapping that acts on the damage gradient. Li et al. [25] showed that the structural tensor formulation arises from a truncated Taylor series approximation of the fracture energy. However, in that regard, the consistent formulation is more flexible as it can accommodate *any* dependency on the crack orientation. Motivated by this, it is therefore reasonable to question whether the consistent approach is an extension of the classical approach.

Without loss of generality, two possible formulations for the direction-dependent fracture energy are considered, namely:

1. one designed to match the energetics of the structural tensor with one preferential orientation,
2. and another one that stems from Rezae et al. [24], wherein the fracture energy is defined as the sum of different energetic contributions.

It should be noted that this list is not exhaustive, and in fact, based on the nature of the material, any function deemed fit and thermodynamically consistent can be used to express the dependence of the fracture energy on crack orientation. Due to applications to composite materials, the focus of this thesis is on the first formulation. Furthermore, this aligns with the second research goal of the thesis. This is because a meaningful comparison requires a case in which both approaches exhibit equivalent energetics, ensuring that any differences arise solely from how anisotropy is introduced rather than from differences in the underlying energetic structure.

N.B. It is possible to consider similar analyses for other structural tensor formulations, but because this thesis is motivated by applications to unidirectional composites, weakly anisotropic structural tensors, i.e., structural tensors with one preferred orientation, are considered.

The second formulation is only included to show the versatility of the model. For completeness, its energetics are investigated, but no further analysis is performed using this formulation. For that, the interested reader is referred to the original paper by the authors [24].

5.4.2. Matching the Energetics of the Structural Tensor

As previously discussed, it is reasonable to wonder whether it is possible to fully match the energetic results and nature of the structural tensor using an explicitly defined direction-dependent fracture energy. The formulation of this function, such that the energetics are equivalent, is derived here. However, the formal comparison of the energetics and the corresponding natural boundary conditions that arise are discussed in Section 5.5 and Section 5.6, respectively.

To derive the fracture energy function of the consistent formulation such that the energetics are equivalent to the structural tensor, it is sufficient to require equivalence in the accumulated dissipation due to fracture. This is because, when the length scale is small compared to the crack length and the dimensions of the specimen, the accumulated dissipation due to fracture, denoted by D, is analogous to Griffith's critical energy release rate [22]. Hence, to match the energetics of the classical model, the following should hold:

$$D_{\text{classical}} = D_{\text{consistent}} \, . \tag{5.21}$$

For the classical model, it can be shown that in the localization zone, the accumulated dissipation per unit crack length is given as follows [22]:

$$D_{\text{classical}} = \int_{-\eta_0}^{+\eta_0} w_{\text{frac}}(d(\eta), d'(\eta)) \, \mathrm{d}\eta, \tag{5.22}$$

where $+\eta_0$ and $-\eta_0$ define the localization zone, and w_{frac} is the fracture contributions to the energy density. The latter is given by

$$w_{\text{frac}}(d, d') = G_c \left[\frac{1}{2l} d^2 + \frac{1}{2} l^* d'^2 \right], \tag{5.23}$$

where l^* denotes the anisotropic length scale.

Substituting Equation 5.23 into Equation 5.22 and performing the required integration allows one to obtain the dissipation over the determined localization zones. This is given as follows [22]:

$$D(l^*) = G_{c,0} \sqrt{\frac{l^*}{l}}, \qquad G_c(\mathbf{m}) = D(l^*). \tag{5.24}$$

From this derivation, it is evident that the use of such a structural tensor introduces the notion of the effective length scale. This is in accordance with what has been observed in the literature, where the crack is more diffuse in orthogonal directions. Teichtmeister et al. [22] define the crack surface density with the orientation-dependent length scale in the following manner:

$$\gamma = \frac{1}{2l} d^2 + \frac{1}{2} l^* d'^2 \, . \tag{5.25}$$

Equating Equation 5.25 to the standard expression of the anisotropic γ function, given by

$$\gamma = \frac{1}{2l} d^2 + \frac{1}{2} l (\nabla d \cdot \mathbf{A} \nabla d), \tag{5.26}$$

shows that the effective length scale should be defined in the following manner:

$$l^* |\nabla d|^2 = l \left(\nabla d \cdot \mathbf{A} \nabla d \right), \qquad \Rightarrow l^* = l \frac{\nabla d \cdot \mathbf{A} \nabla d}{|\nabla d|^2} = l \mathbf{m} \cdot \mathbf{A} \mathbf{m} \, . \tag{5.27}$$

Recall that the form of the structural tensor (for a transversely isotropic or 2D orthotropic material) is given by

$$\mathbf{A} = \mathbf{I} + \alpha (\mathbf{a} \otimes \mathbf{a}) \, . \tag{5.28}$$

The product in Equation 5.27 can be rewritten as follows using standard tensor product identities:

$$\begin{aligned} \nabla d \cdot \mathbf{A} \nabla d &= \nabla d \cdot (\mathbf{I} + \alpha \mathbf{a} \otimes \mathbf{a}) \nabla d \\ &= \nabla d \cdot \nabla d + \alpha \nabla d \cdot (\mathbf{a} \otimes \mathbf{a}) \nabla d \\ &= \nabla d \cdot \nabla d + \alpha \nabla d \cdot (\mathbf{a} \cdot \nabla d) \mathbf{a} \\ &= |\nabla d|^2 + \alpha (\mathbf{a} \cdot \nabla d)^2 \, . \end{aligned} \tag{5.29}$$

Substituting Equation 5.29 into Equation 5.24, the fracture energy function is given by

$$\begin{aligned} G_c(\mathbf{m}) &= G_{c,0}\sqrt{\frac{\nabla d \cdot \mathbf{A}\nabla d}{|\nabla d|^2}} = G_{c,0}\sqrt{\frac{|\nabla d|^2 + \alpha(\mathbf{a}\cdot\nabla d)^2}{|\nabla d|^2}} = G_{c,0}\sqrt{1+\alpha(\mathbf{a}\cdot\mathbf{m})^2} \\ &= G_{c,0}\sqrt{\mathbf{m}\cdot\mathbf{A}\mathbf{m}}\,. \end{aligned} \tag{5.30}$$

Intuitively, this expression makes sense as the lowest resistance to crack propagation is expected when the orientation of the crack is aligned with the preferred direction.

5.4.3. A Nonlinear Approach

To showcase the flexibility of the approach, a nonlinear $G_c(\theta)$ function as proposed by Rezaei et al. [24] is considered. In their proposed nonlinear formulation, the fracture energy function is the sum of several energy functions, namely

$$G_c(\theta) = \sum_m \beta_m \left[1 + \alpha_m \sin^2(m(\theta + \theta'_m))\right]\,. \tag{5.31}$$

This formulation is not extensively discussed here but rather mentioned for completeness. Regardless, the energetics of this formulation will be introduced.

5.5. Comparison of Energetics

The previous section derived *an* expression for $G_c(\mathbf{m})$; however, it is rather difficult to gain an intuitive understanding of what this function entails from its mathematical structure. In such a case, it is more convenient to understand and compare these formulations based on energetics, namely, by considering crack resistance and its reciprocal. For all subsequent discussion, the 2D case is analyzed. As a result, the crack orientation is now fully characterized by the angle θ and the preferential direction is characterized by the angle $\tilde{\theta}$. Furthermore, $G_c(\mathbf{m})$ can be written as $G_c(\theta)$.

As elaborated on in Chapter 2, under Griffith's criterion, the process of fracture occurs where the energy release rate reaches a critical value. Due to the material properties, loading, and boundary conditions, different material points will reach this value at different times (if ever) in the fracture process. This ultimately defines the observed crack path. In other words, the crack path, characterized by θ^*, is governed by the generalized maximum energy release rate criterion

$$\theta^* = \max_{\theta\in[0,2\pi]} \frac{G_c(\theta)}{G_c(\theta;\tilde{\theta})}. \tag{5.32}$$

In the anisotropic case, each direction is characterized by a different G_c value, and thus two specimens with identical loading and boundary conditions may exhibit different crack paths purely due to the different $G_c(\theta)$ functions used. Furthermore, it is trivial to recognize that the isotropic case is a special condition of the anisotropic case that occurs when the crack resistance is equal in all directions.

Another way of understanding the observed fracture path is by considering the polar plot of the reciprocal of the crack resistance as a function of the crack orientation, also termed the Frank plot [23]. The advantages of analyzing this plot are twofold: firstly, it relates to the well-posedness of the phase field equation of the problem, and secondly, it gives insight into the expected crack propagation angles. Regarding the first point, it has been noted that when the Frank plot does not possess angle-convexity, the corresponding phase field equations become ill-posed [23, 25]. Hence, it can be shown that the well-posedness of the problem is ensured through the second-order condition that [23]

$$\frac{\partial^2 G_c(\theta;\tilde{\theta})}{\partial\theta^2} + G_c(\theta;\tilde{\theta}) \geq 0\,. \tag{5.33}$$

Remark 5.3

Equation 5.33 also relates to the nature of fracture anisotropy in the material. In Chapter 4 is was identified that materials can either exhibit strong anisotropy or weak anisotropy, with the distinction that strongly anisotropic materials have *forbidden* directions as opposed to the *preferential* directions observed in weakly anisotropic materials. The difference between *forbidden* and *preferential* lies in the convexity of the Frank plot. A weakly anisotropic material has a convex polar plot and hence satisfies Equation 5.33, whereas a strongly anisotropic material is non-convex, that is, some segments may have negative curvature. Composites typically exhibit weak anisotropy, whereas crystalline structures exhibit strong anisotropy [107].

Secondly, analyzing the Frank plot also provides insight into the expected crack propagation angles. Based on the method proposed by Takei et al. [152], this direction can be graphically determined [22]. In this method, the crack angle is the point at which a vertical line moving from left to right tangentially coincides with the Frank plot. Denoting $r(\theta)$ to present the Frank plot parametrized using θ, this point occurs when the following condition holds:

$$\frac{dx}{d\theta} = 0, \quad \text{where} \quad x(\theta) = r(\theta)\cos\theta \,. \tag{5.34}$$

For the remainder of the analysis, both aspects are investigated for the two formulations in Section 5.5.1 and Section 5.5.2, respectively. Lastly, the main conclusions are summarized in Section 5.5.3.

5.5.1. Structural Tensor Inspired Approach

A comparison of the energetics is performed to assess whether the energetics of Equation 5.30 are identical to the behavior of the structural tensor. To verify this, the polar plots of $G_c(\theta)$ and $G_c^{-1}(\theta)$ are considered. Figure 5.2 presents these plots for both the classical and consistent formulations, evaluated over a range of anisotropic fracture energy parameters and for a preferential direction oriented at $45°$ with respect to the horizontal. In the figure, the classical formulation (CF) is shown using dashed lines, while the proposed formulation (PF) is represented by solid lines.

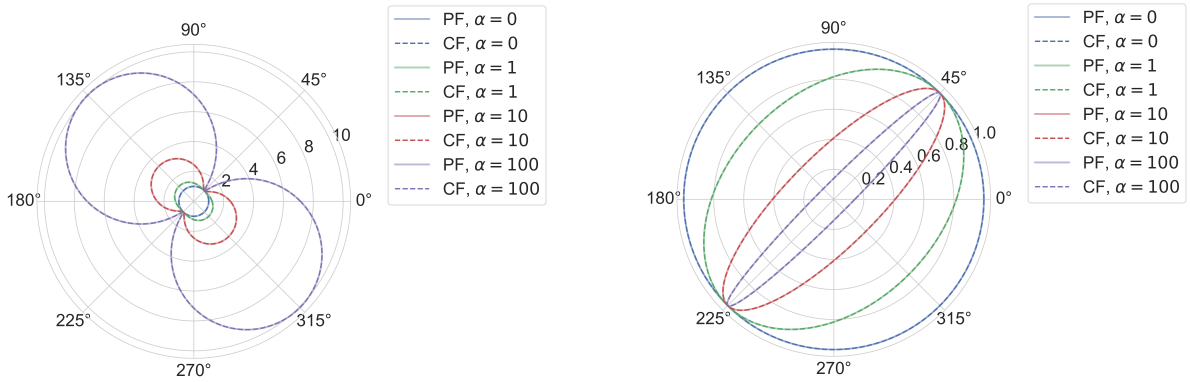

(a) $G_c(\theta)$ **(b)** $G_c^{-1}(\theta)$ (Frank plot)

Figure 5.2: Polar plots of G_c and G_c^{-1} for the classical formulation and the consistent formulation that match the energetics of the classical formulation.

From this figure, a few points are to be noted:

1. For equivalent anisotropic fracture energy parameters, both formulations result in the same energetics. This is expected as the $G_c(\theta)$ function of the consistent formulation was derived such that the accumulated dissipation is the same as for the classical formulation.
2. In all cases, the Frank plots possess angle-convexity and hence represent weakly anisotropic materials. This is expected because to represent strong anisotropy, using the classical formulation, fourth-order structural tensors are required [24].
3. As the magnitude of the anisotropic fracture energy parameter increases, the ellipsoids become sharper, that is, the aspect ratio increases. This increases the contrast between the fracture energy in the preferred direction and that in other orientations, making crack propagation increasingly favorable along the

preferred direction. To understand this further, the expected crack propagation angles are analyzed for the different cases.

From the $G_c^{-1}(\theta)$, the expected crack propagation angles for various anisotropic fracture energy parameters, namely $\alpha = 0, 1, 10, 100$, are graphically shown in Figure 5.3. Note that these four cases are split over two figures for ease of reading.

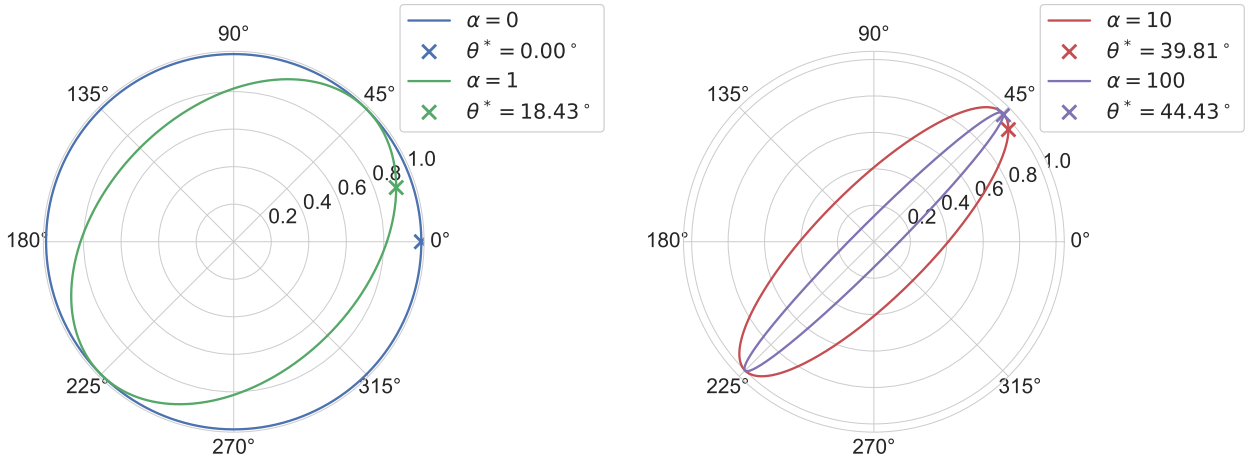

(a) $\alpha = 0,\ 1$ **(b)** $\alpha = 10,\ 100$

Figure 5.3: Expected crack propagation angles for various anisotropic fracture energy, α, parameters for a preferential orientation of $\pi/4$.

From these results, it is evident that as the anisotropic fracture energy parameter increases, the expected crack propagation angle approaches the preferential direction. However, this asymptotic relation is not in a linear manner. Figure 5.4 shows how the expected crack propagation angle changes for various anisotropic fracture energy parameters.

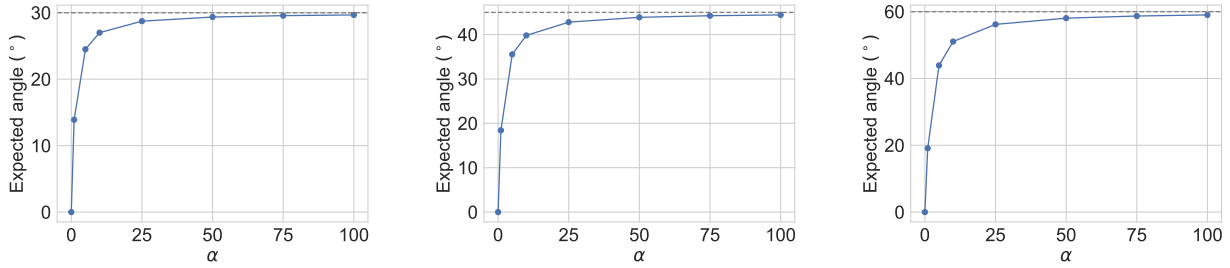

(a) $\tilde{\theta} = 30°$ **(b)** $\tilde{\theta} = 45°$ **(c)** $\tilde{\theta} = 60°$

Figure 5.4: Expected crack propagation angles for different preferential orientations as a function of the anisotropic fracture energy, α parameter.

5.5.2. Fully Nonlinear

The flexibility of the consistent approach is its ability to accommodate any function for the fracture energy. To showcase this, based on the works of Rezaei et al. [24], a nonlinear function of the form shown in Equation 5.35 and Equation 5.36 is considered, that is,

$$E_m(\theta) = \beta_m \left[1 + \alpha_m \sin^2(m(\theta + \theta'_m))\right], \tag{5.35}$$

$$G_c(\theta) = \sum_m E_m(\theta) = \sum_m \beta_m \left[1 + \alpha_m \sin^2(m(\theta + \theta'_m))\right], \qquad m \in \mathbb{Z}^+ . \tag{5.36}$$

For two different α parameters, the plots of $E_m(\theta)$ are given in Figure 5.5 for various m values.

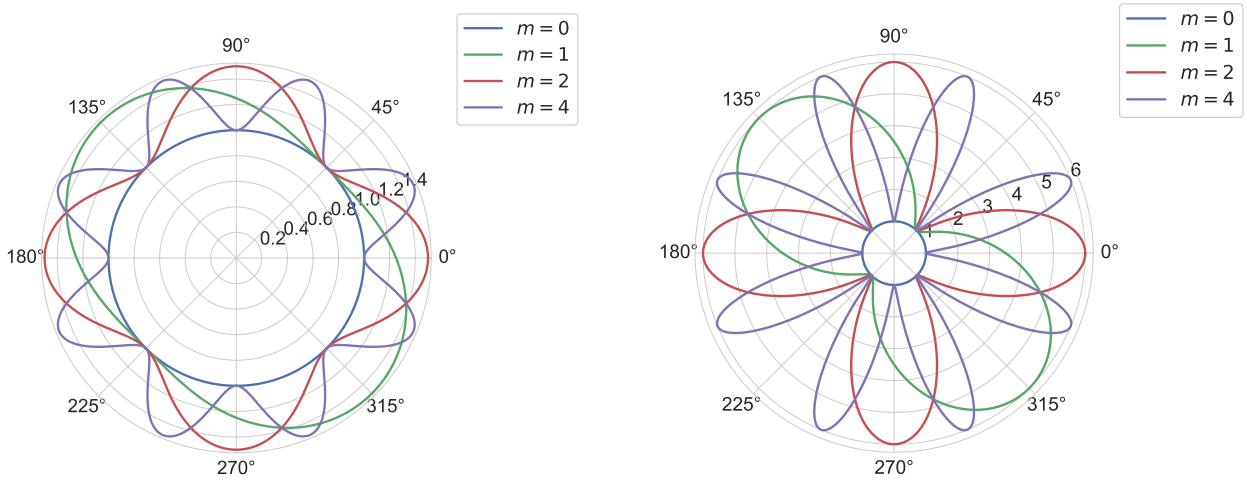

(a) $\alpha = 0.5$ **(b)** $\alpha = 5$

Figure 5.5: Polar plots of $E_m(\theta)$ for various m values and different α parameters.

The corresponding $G_c(\theta)$ functions are visualized in Figure 5.6.

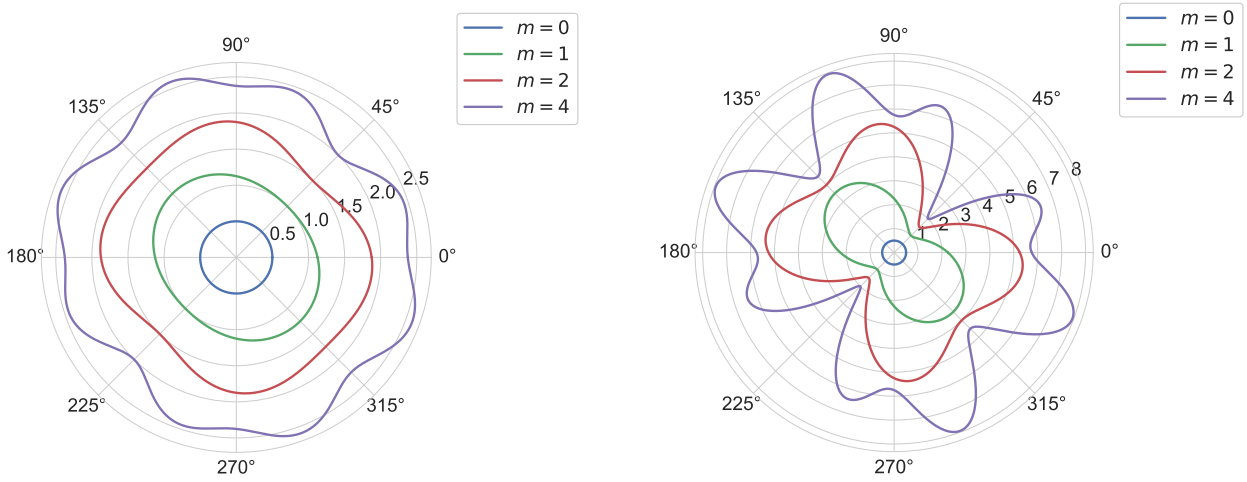

(a) $\alpha = 0.5$ **(b)** $\alpha = 5$

Figure 5.6: Polar plots of $G_c(\theta)$ for various m values and different α parameters.

The most critical distinction between Figure 5.3 and Figure 5.6 is that for certain choices of m namely if $m > 1$, then the $G_c^{-1}(\theta)$ contours are no longer ellipsoids. In such cases, the Frank plots do not possess angle convexity and thereby can be used to represent strongly anisotropic materials. Within a classical formulation, this is not possible as to represent strongly anisotropic materials, higher-order structural tensors are required. This is because the tensor should act on the higher-order gradient terms. Yet, within the consistent formulation, this is not necessary.

5.5.3. Section Conclusions

As this section introduced several new concepts, some notable insights are summarized below. These will prove to be useful in understanding subsequent sections as well.

- To understand the energetics of a formulation, it is important to consider both $G_c(\theta)$ and $G_c^{-1}(\theta)$.
- The nature of the Frank plot indicates the type of material anisotropy that can be modeled and the expected propagation angles. If the plot possesses angle-convexity, only weak anisotropy can be represented.
- By adequate choice of $G_c(\theta)$, the energetics of the consistent formulation can be made equivalent to the energetics of the classical formulation. In such cases, these formulations can *only* be used to model weak anisotropy. Furthermore, by increasing the magnitude of the anisotropic fracture energy parameter, the expected propagation angles align more closely with the preferential direction.
- By adequate choice of $G_c(\theta)$, the consistent formulation can be used to model strong anisotropy without requiring additional higher-order structural tensors and gradient terms.

5.6. Comparison of the Natural Boundary Conditions

The previous section established the energetic equivalence between the different formulations. However, such equivalence alone is not sufficient to guarantee full consistency between models; accordingly, the nature of the associated natural boundary conditions is examined. The fact that the consistent formulation was shown to match the energetics of the classical formulation does not imply that the resulting boundary conditions are identical. As a result, careful analysis of any discrepancies between them is discussed in the subsections below.

5.6.1. Deriving the Boundary Conditions

In this subsection, the natural boundary conditions arising from the classical formulation are compared with those of the consistent formulation. In the classical anisotropic formulation, the phase field boundary condition was derived in Section 4.2.1. For convenience, it is reiterated below

$$(\mathbf{A}\nabla d)\cdot\mathbf{n}=0 \quad \text{on } \partial\mathcal{B}, \tag{5.37}$$

where $\mathbf{n}$ is the outward normal vector on the boundary.

For a structural tensor of the form, $\mathbf{I}+\alpha(\mathbf{a}\otimes\mathbf{a})$, the term in parenthesis can be expanded as follows:

$$\mathbf{I}\nabla d+(\alpha\mathbf{a}\otimes\mathbf{a})\nabla d=\nabla d+\alpha(\nabla d\cdot\mathbf{a})\mathbf{a}\ . \tag{5.38}$$

As a result, Equation 5.37 can be rewritten to state

$$(\nabla d+\alpha(\nabla d\cdot\mathbf{a})\mathbf{a})\cdot\mathbf{n}=0 \quad \text{on } \partial\mathcal{B}\ . \tag{5.39}$$

For the consistent formulation, the general form of the natural boundary condition derived from Section 4.2.2 is reiterated below

$$\left(G_c\frac{\partial\gamma}{\partial\nabla d}+\gamma\frac{\partial G_c}{\partial\nabla d}\right)\cdot\mathbf{n}=0 \qquad \text{on } \partial\mathcal{B}\ . \tag{5.40}$$

The partial derivative of the crack surface density function with respect to the damage gradient is given by

$$\frac{\partial\gamma}{\partial\nabla d}=\frac{2l}{c_0}\nabla d\ . \tag{5.41}$$

Furthermore, for the fracture energy function proposed in Equation 5.30, its derivative with respect to the damage gradient can be computed using the chain rule, as follows:

$$G_c=G_{c,0}\sqrt{\lambda} \qquad \Rightarrow \frac{\partial G_c}{\partial\nabla d}=G_{c,0}\frac{1}{2}\frac{1}{\sqrt{\lambda}}\frac{\partial\lambda}{\partial\nabla d}, \tag{5.42}$$

where

$$\lambda=1+\alpha\frac{(\mathbf{a}\cdot\nabla d)^2}{|\nabla d|^2}\ . \tag{5.43}$$

Furthermore, the derivative $\frac{\partial\lambda}{\partial\nabla d}$ is given by

$$\frac{\partial\lambda}{\partial\nabla d}=2\alpha\frac{(\nabla d\cdot\mathbf{a})}{|\nabla d|^2}\mathbf{a}-2\alpha\frac{(\nabla d\cdot\mathbf{a})^2}{|\nabla d|^4}\nabla d\ . \tag{5.44}$$

Substituting Equation 5.42 and Equation 5.44 into the part in brackets in Equation 5.40, yields the following:

$$\begin{aligned} G_c\frac{\partial\gamma}{\partial\nabla d}+\gamma\frac{\partial G_c}{\partial\nabla d} &= G_{c,0}\sqrt{\lambda}\frac{2l}{c_0}\nabla d+\gamma G_{c,0}\frac{1}{2}\frac{1}{\sqrt{\lambda}}\left(2\alpha\frac{(\nabla d\cdot\mathbf{a})}{|\nabla d|^2}\mathbf{a}-2\alpha\frac{(\nabla d\cdot\mathbf{a})^2}{|\nabla d|^4}\nabla d\right)\\ &= G_{c,0}\sqrt{\lambda}\frac{2l}{c_0}\nabla d+G_{c,0}\alpha\frac{\gamma}{\sqrt{\lambda}}\frac{(\nabla d\cdot\mathbf{a})}{|\nabla d|^2}\left(\mathbf{a}-\frac{(\nabla d\cdot\mathbf{a})}{|\nabla d|^2}\nabla d\right)\ . \end{aligned} \tag{5.45}$$

By factoring the quantity $\frac{G_{c,0}}{\sqrt{\lambda}}$ Equation 5.45 reads

$$\left(G_c\frac{\partial\gamma}{\partial\nabla d}+\gamma\frac{\partial G_c}{\partial\nabla d}\right)=\frac{G_{c,0}}{\sqrt{\lambda}}\left(\lambda\frac{2l}{c_0}\nabla d+\gamma\alpha\frac{(\nabla d\cdot\mathbf{a})}{|\nabla d|^2}\left(\mathbf{a}-\frac{(\nabla d\cdot\mathbf{a})}{|\nabla d|^2}\nabla d\right)\right)\ . \tag{5.46}$$

While it may seem unnecessary now, factoring this term will prove useful for comparing the boundary conditions arising from the classical and consistent approaches.

Substituting the expression of λ, as given in Equation 5.43, into the term in brackets on the right-hand side of Equation 5.46 yields

$$\left(1+\alpha\frac{(\mathbf{a}\cdot\nabla d)^2}{|\nabla d|^2}\right)\frac{2l}{c_0}\nabla d+\gamma\alpha\frac{(\nabla d\cdot\mathbf{a})}{|\nabla d|^2}\left(\mathbf{a}-\frac{(\nabla d\cdot\mathbf{a})}{|\nabla d|^2}\nabla d\right)\,. \tag{5.47}$$

The last term of Equation 5.47 can be expanded by recalling the general form of the crack surface density function, and hence

$$\begin{aligned}\gamma\alpha\frac{(\nabla d\cdot\mathbf{a})}{|\nabla d|^2}\left(\mathbf{a}-\frac{(\nabla d\cdot\mathbf{a})}{|\nabla d|^2}\nabla d\right)&=\alpha\frac{1}{c_0}\left[\frac{1}{l}\vartheta(d)+l|\nabla d|^2\right]\frac{(\nabla d\cdot\mathbf{a})}{|\nabla d|^2}\left(\mathbf{a}-\frac{(\nabla d\cdot\mathbf{a})}{|\nabla d|^2}\nabla d\right)\\ \Rightarrow\alpha\frac{1}{c_0 l}\vartheta(d)\frac{(\nabla d\cdot\mathbf{a})}{|\nabla d|^2}\left(\mathbf{a}-\frac{(\nabla d\cdot\mathbf{a})}{|\nabla d|^2}\nabla d\right)&+\alpha\frac{l}{c_0}(\nabla d\cdot\mathbf{a})\left(\mathbf{a}-\frac{(\nabla d\cdot\mathbf{a})}{|\nabla d|^2}\nabla d\right)\,.\end{aligned} \tag{5.48}$$

Using Equation 5.48 in Equation 5.47 and rearranging yields

$$\begin{aligned}\frac{l}{c_0}\Bigg(2\nabla d+2\alpha\frac{(\mathbf{a}\cdot\nabla d)^2}{|\nabla d|^2}\nabla d+(\nabla d\cdot\mathbf{a})\alpha\mathbf{a}-\alpha\frac{(\nabla d\cdot\mathbf{a})^2}{|\nabla d|^2}\nabla d\Bigg)\\ +\alpha\frac{1}{c_0 l}\vartheta(d)\frac{(\nabla d\cdot\mathbf{a})}{|\nabla d|^2}\left(\mathbf{a}-\frac{(\nabla d\cdot\mathbf{a})}{|\nabla d|^2}\nabla d\right)\,.\end{aligned} \tag{5.49}$$

Equation 5.49 can be further simplified to read

$$\frac{l}{c_0}\left[2\nabla d+\alpha(\nabla d\cdot\mathbf{a})\mathbf{a}+\alpha\frac{(\mathbf{a}\cdot\nabla d)^2}{|\nabla d|^2}\nabla d\right]+\alpha\vartheta(d)\frac{1}{c_0 l}\frac{(\nabla d\cdot\mathbf{a})}{|\nabla d|^2}\left(\mathbf{a}-\frac{(\nabla d\cdot\mathbf{a})}{|\nabla d|^2}\nabla d\right)\,. \tag{5.50}$$

Now factoring out $\frac{l}{c_0}$, Equation 5.50 becomes

$$\left(\left(2+\alpha\frac{(\mathbf{a}\cdot\nabla d)^2}{|\nabla d|^2}-\alpha\frac{\vartheta(d)}{l^2}\frac{(\nabla d\cdot\mathbf{a})^2}{|\nabla d|^4}\right)\nabla d+\left(\alpha(\nabla d\cdot\mathbf{a})+\alpha\frac{\vartheta(d)}{l^2}\frac{(\nabla d\cdot\mathbf{a})}{|\nabla d|^2}\right)\mathbf{a}\right)\cdot\mathbf{n}=0\quad\text{on}\,\partial\mathcal{B}\,. \tag{5.51}$$

With a slightly different grouping of terms, Equation 5.51 can also be written as follows:

$$\left(\nabla d+\alpha(\nabla d\cdot\mathbf{a})\mathbf{a}+\left(1+\alpha\frac{(\mathbf{a}\cdot\nabla d)^2}{|\nabla d|^2}\right)\nabla d+\alpha\frac{\vartheta(d)}{l^2}\frac{(\nabla d\cdot\mathbf{a})}{|\nabla d|^2}\left(\mathbf{a}-\frac{(\nabla d\cdot\mathbf{a})}{|\nabla d|^2}\nabla d\right)\right)\cdot\mathbf{n}=0\quad\text{on}\,\partial\mathcal{B}\,. \tag{5.52}$$

Comment on terminology

To aid future analysis, the part in parentheses in this equation is hereafter referred to as the *boundary vector*, and the entire equation represents the *boundary condition*.

Equation 5.52 is rather insightful; it is evident that the first two terms are similar to the terms obtained when using the structural tensor. Yet, the terms relating to the $\vartheta(d)$ are completely new. The addition of these terms is expected because in the classical formulation, anisotropy is only introduced to the gradient term, and the geometric crack function is "untouched". However, in the consistent approach, the geometric crack function gets "exposed" to the effect of anisotropy.

Prior to comparing both boundary conditions, first some points regarding Equation 5.52 are noted, particularly with regard to the terms involving $\vartheta(d)$:

1. The fourth and fifth terms of Equation 5.52 involve $\vartheta(d)$. These terms are zero when either of the following conditions is true:
   - $\vartheta(d)=0$: this condition is trivial, as it refers to the case when there is no damage.
   - Alternatively, it is also zero if the following condition holds:

     $$\mathbf{a}-\frac{(\nabla d\cdot\mathbf{a})}{|\nabla d|^2}\nabla d=\mathbf{0}\,.$$

     This is the case when the damage gradient is aligned with the preferential direction.
2. In all other situations, these terms depend on the ratio $\frac{\vartheta(d)}{l^2}$, hereafter referred to as the *local crack geometry term*.

Mathematically, it is apparent that the two formulations are different. To understand how different these formulations are, it is helpful to visualize the boundary vectors and boundary conditions. This is considered below.

5.6.2. Boundary Vector Analysis

Firstly, a comparative study of the boundary vectors between the two formulations is performed for different anisotropic fracture energy parameters *and* different magnitudes for the local crack geometry term. The former indicates how the formulations respond to varying strengths of anisotropy. Whereas the latter indicates how the formulations respond to different damage states. The boundary vector plots are generated in the following manner:

Algorithm 1 Computation of Boundary Vector Fields

Input: Anisotropy parameter α, preferred direction angle $\tilde{\theta}$
Generate grid $\{(\nabla d_x, \nabla d_y)\}$ using mesh over $[-1,1]\times[-1,1]$ (where x and y refer to the standard Cartesian components).
for each grid point $(\nabla d_x, \nabla d_y)$ **do**
    $\nabla d \leftarrow [\nabla d_x, \nabla d_y]$
    if $\|\nabla d\| = 0$ **then**
        continue
    end if
    Compute the boundary vector for the classical formulation, $\mathbf{b}_s$ using Equation 5.37
    Compute the boundary vector for the consistent formulation, $\mathbf{b}_g$ using Equation 5.52
    Store $\mathbf{b}_s$ and $\mathbf{b}_g$
end for
Output: plot vector fields of $\mathbf{b}_s$ and $\mathbf{b}_g$

To begin, the case where the local crack geometry term is zero is considered for different anisotropic fracture energy parameters, namely 0, 1, 10, and 100. The case of 0 corresponds to the isotropic case, and is done as a sanity check. The different boundary vectors are visualized in Figure 5.7.

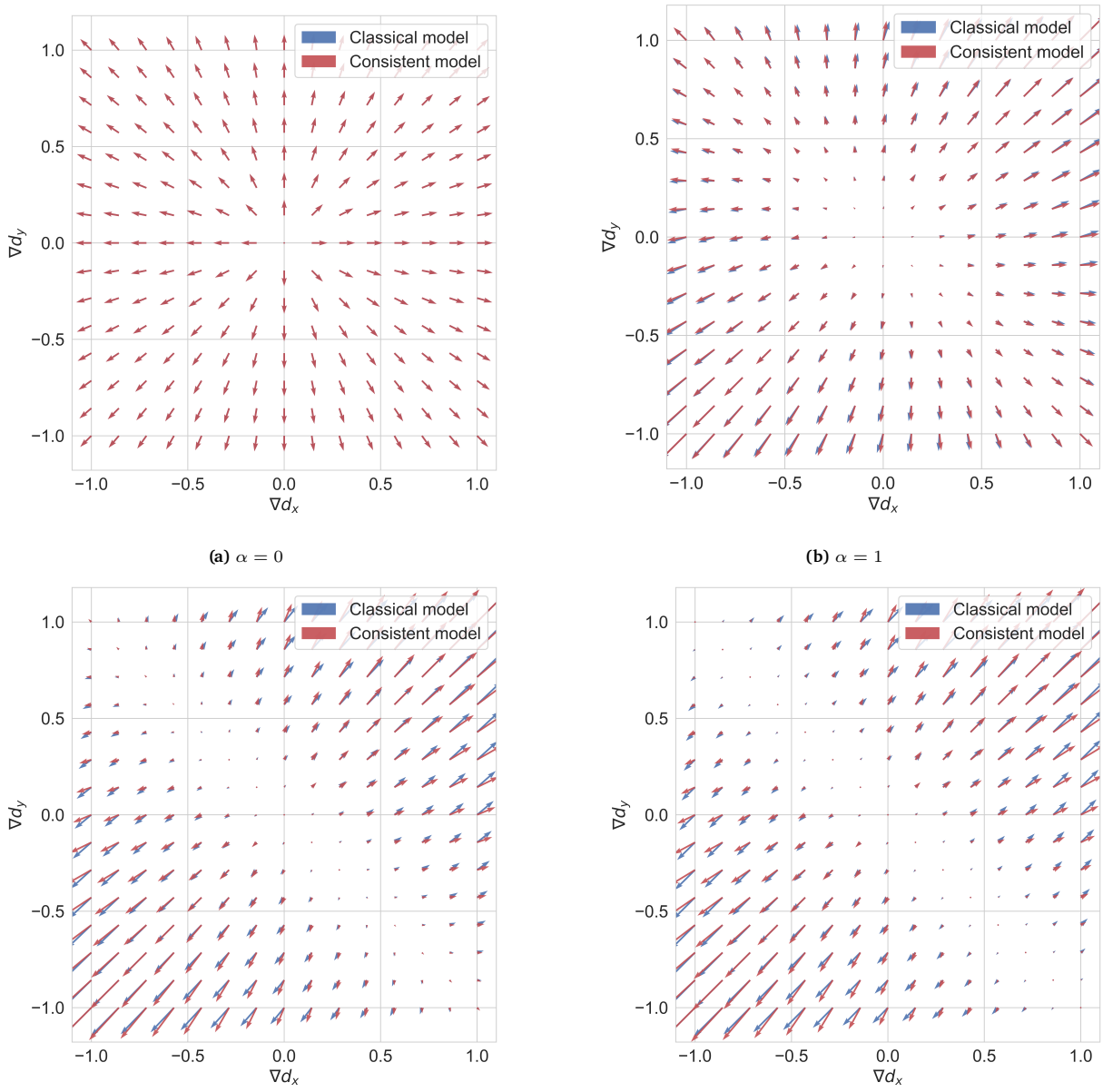

(a) $\alpha = 0$

(b) $\alpha = 1$

(c) $\alpha = 10$

(d) $\alpha = 100$

Figure 5.7: Comparison of the boundary vectors of the classical and consistent formulation for different anisotropic fracture energy parameters when the local crack geometry term is 0.

From these figures, some points are of interest:

- In the isotropic case, the classical and consistent formulation result in the same boundary vectors. The magnitude of these vectors is the same in all directions, and these vectors are orientated in the same direction as the original damage gradient vector. This is expected because in the isotropic case, there is no preferential direction.
- For the anisotropic case, the magnitude and direction of the boundary vectors of both formulations are different (for the same damage gradient vector).
- In the classical formulation, increasing the anisotropic fracture energy parameter causes the boundary vectors to progressively align with the preferred direction, regardless of the initial orientation of the damage gradient. At the same time, their magnitude becomes strongly direction-dependent: it is maximized along the preferential direction and minimized in directions orthogonal to it. As α increases, this contrast becomes more pronounced, as a band of low-magnitude vectors aligned perpendicular to the preferred orientation starts to form.
- In the consistent formulation, increasing the anisotropic fracture energy parameter does not cause the boundary vectors to progressively align with the preferential direction. Rather, the boundary vectors are tilted slightly away from the preferred direction. However, similar to the classical formulation,

the magnitude of the boundary vectors is strongly direction-dependent. A similar band-like artifact of low-magnitude vectors aligned orthogonal to the preferential orientation is observed.

- Comparing the boundary vectors of the classical and consistent formulations, it appears that the differences become more pronounced as the anisotropic fracture energy parameter increases.

The second case to consider is when the local crack geometry term is a very large number. In this case, a value of 10000 is considered. Similar to the previous case, the boundary vectors are plotted for different anisotropic fracture energy parameters. Note that the isotropic situation is not plotted as it is the same as Figure 5.7a. The results are visualized in Figure 5.8.

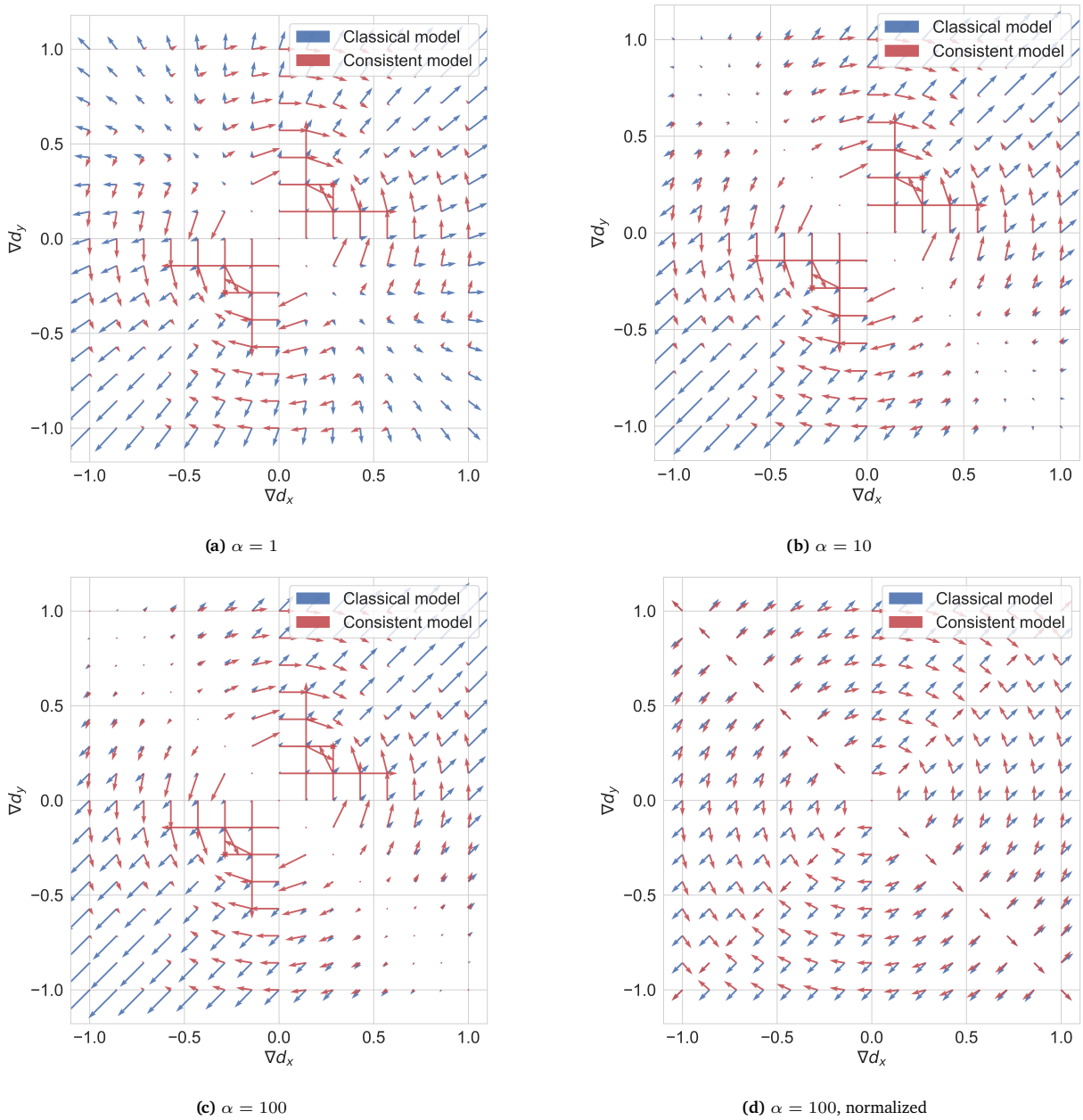

(a) $\alpha = 1$

(b) $\alpha = 10$

(c) $\alpha = 100$

(d) $\alpha = 100$, normalized

Figure 5.8: Comparison of the boundary vectors of the classical and consistent formulation for different anisotropic fracture energy parameters when the local crack geometry term is 10000.

From these figures, some points are of interest:

- As the classical formulation is independent of the local crack geometry term, the results obtained are identical to those in Figure 5.7. As a result, the observations have already been commented on.
- When comparing the results of the consistent formulation in Figure 5.7 to Figure 5.8, it is apparent that the results change drastically based on the value of the local crack geometry term.

- Similar to Figure 5.7c and Figure 5.7d, a band-like artifact of low-magnitude vectors aligned orthogonal to the preferred orientation is apparent in Figure 5.8b and Figure 5.8c.
- It appears that when the local crack geometry term is significantly large, the anisotropic fracture energy parameter does not change the boundary vectors significantly. This is expected because the fourth and fifth terms of Equation 5.52 dominate, and hence, the anisotropic fracture energy parameter acts as merely a scaling parameter.
- In the non-normalized plots, the boundary vectors corresponding to the consistent formulation attain large magnitudes in regions where the damage gradient is small. This behavior is expected, as several terms in Equation 5.52 involve division by the norm of the damage gradient.
- From the normalized plot of the boundary vectors, it appears that the classical and consistent formulation are in the same direction only when the initial damage gradient vector is aligned or orthogonal to the preferential direction. In all other cases, the two formulations result in vectors that are rather distinct from each other.

From these figures, it is evident that despite equivalence in energetics, the consistent and classical formulations are different.

5.6.3. Boundary Condition Analysis

The previous analysis established that there are differences between the classical and consistent formulations. To understand this further, a boundary condition analysis is performed for the two formulations. The comparative analysis is done for various anisotropic fracture energy parameters, local crack geometry term values, preferential orientations, and normal vectors. All the cases considered are presented in Table 5.1 and are defined with respect to the global Cartesian coordinate system.

Table 5.1: The preferential orientation, anisotropic fracture energy parameter, normal vector, and corresponding figure of the various cases considered for the boundary condition analysis.

Analysis Case	Preferential Orientation [°]	Anisotropic fracture energy parameter	Normal Vector	Relevant Figure
AC-00-10-00	0	10	$[1,0]^{\mathrm{T}}$	Figure 5.9
AC-00-100-00	0	100	$[1,0]^{\mathrm{T}}$	Figure 5.10
AC-30-10-00	30	10	$[1,0]^{\mathrm{T}}$	Figure 5.11
AC-30-100-00	30	100	$[1,0]^{\mathrm{T}}$	Figure 5.12
AC-30-10-45	30	10	$[\sqrt{2}/2, \sqrt{2}/2]^{\mathrm{T}}$	Figure 5.13
AC-90-10-00	90	10	$[1,0]^{\mathrm{T}}$	Figure 5.14
AC-90-100-00	90	100	$[1,0]^{\mathrm{T}}$	Figure 5.15

Remark 5.4

This set of cases is not exhaustive with respect to all possible parameter combinations. However, it is sufficiently comprehensive to highlight the differences between the formulations, while maintaining conciseness and avoiding unnecessary repetition.

For all cases, the boundary condition plots are constructed in the following manner:

Algorithm 2 Computation of Boundary Condition Fields

Input: Anisotropy parameter α, preferred direction angle $\tilde{\theta}$, normal vector, $\mathbf{n}$
Generate grid $\{(\nabla d_x, \nabla d_y)\}$ using mesh over $[-1, 1] \times [-1, 1]$
for each grid point $(\nabla d_x, \nabla d_y)$ **do**
    $\nabla d \leftarrow [\nabla d_x, \nabla d_y]$
    if $\|\nabla d\| = 0$ **then**
        continue
    end if
    Compute the boundary vector for the classical formulation, $\mathbf{b}_s$ using Equation 5.37
    Compute the boundary condition for the classical formulation, $\mathbf{b}_{s,bc}$
    Compute the boundary vector for the consistent formulation, $\mathbf{b}_g$ using Equation 5.52
    Compute the boundary condition for the consistent formulation, $\mathbf{b}_{g,bc}$
    Store the normalized $\mathbf{b}_{s,bc}$ and $\mathbf{b}_{g,bc}$
end for
Output: plot the contour fields of normalized $\mathbf{b}_{s,bc}$ and $\mathbf{b}_{g,bc}$ against $\nabla d_x, \nabla d_y$

Remark 5.5

It may seem as though it is unnecessary to consider such a wide range of values for the local crack geometry term. This is because it could be claimed that the length scale will be sufficiently small, and hence the local crack geometry term will be large. However, it should be recalled that phase field modeling has a diffuse representation of a crack, and hence, in the vicinity of a damaged region, there will be areas wherein the local crack geometry term is not that large.

Remark 5.6

The contour fields are normalized and displayed using 15 discrete levels. Since the value of the local crack geometry term can significantly alter the magnitude of the boundary condition, the resulting fields may differ in scale. To enable a meaningful comparison, the values are therefore normalized. This is an acceptable post-processing step as the primary feature of interest is the zero-level contour of the boundary condition. Additionally, a discrete contour representation is used to improve readability and to clearly distinguish the zero contour from neighboring levels.

Comparison between AC-00-10-00 and AC-00-100-00

The first case considered is for a preferential direction aligned with 0°, a normal vector oriented along $[1, 0]^{\mathrm{T}}$, and an anisotropic fracture energy parameter of 10. Figure 5.9 shows the results for the classical formulation and the consistent formulation for various values of the local crack geometry term.

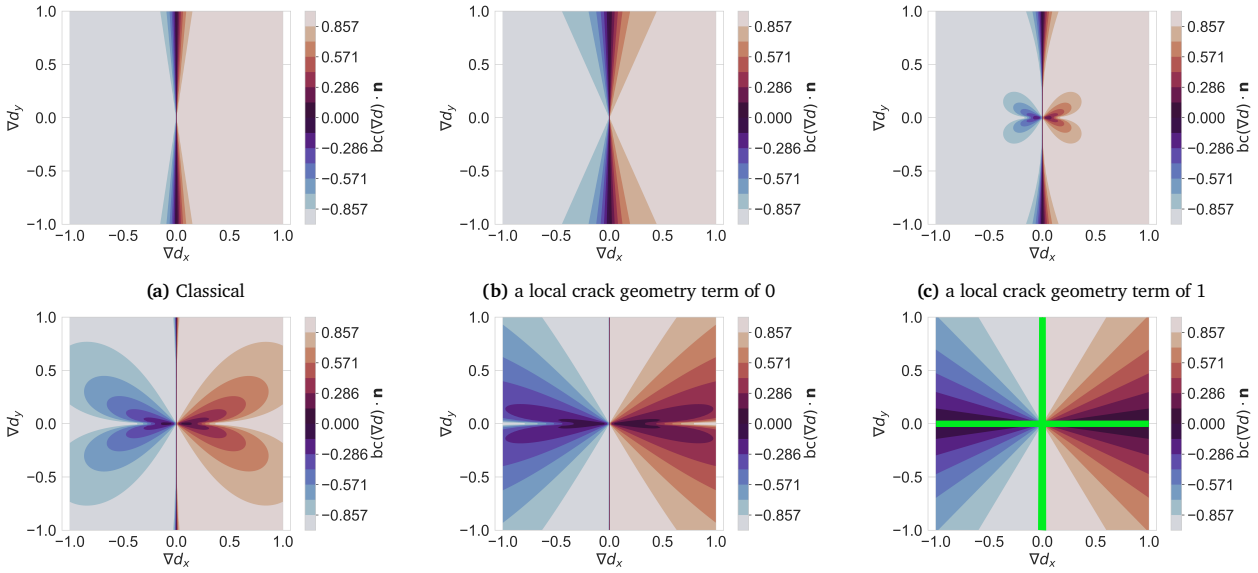

(a) Classical **(b)** a local crack geometry term of 0 **(c)** a local crack geometry term of 1

(d) a local crack geometry term of 10 **(e)** a local crack geometry term of 100 **(f)** a local crack geometry term of 10000

Figure 5.9: Contour plots of the boundary condition for the classical and consistent formulations for a preferential direction of $0°$, anisotropic fracture energy parameter $\alpha = 10$, and different local crack geometry term values. The zero-magnitude contour lines in the main damage region are emphasized in green for ease of reading.

Prior to analyzing Figure 5.9, the same analysis is repeated for an anisotropic fracture energy parameter of 100, and these results are visualized in Figure 5.10.

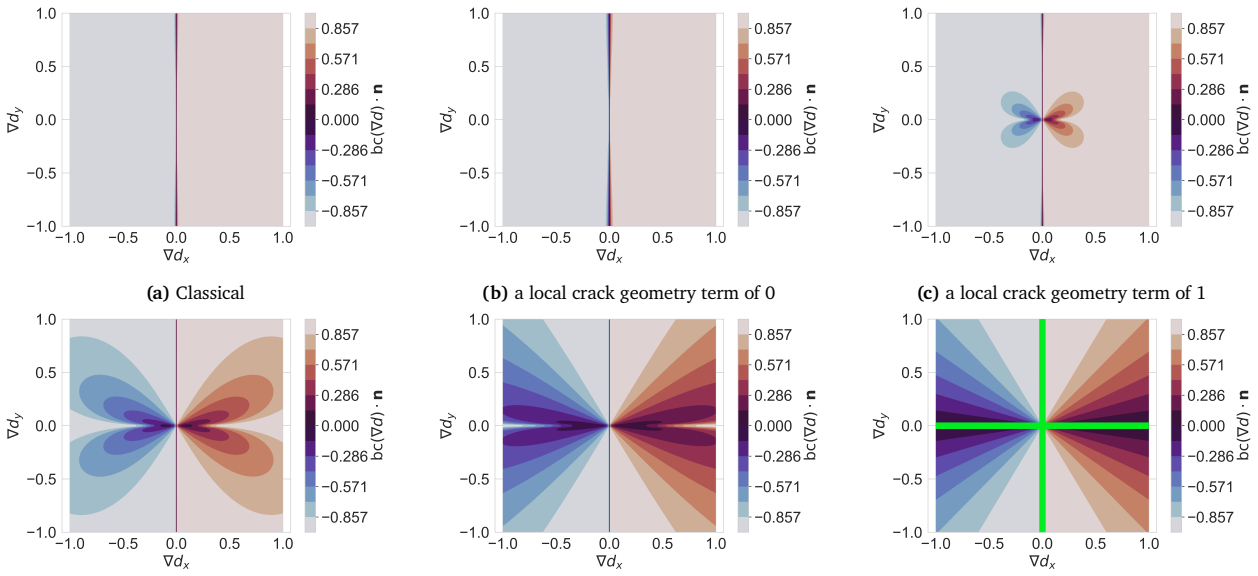

(a) Classical **(b)** a local crack geometry term of 0 **(c)** a local crack geometry term of 1

(d) a local crack geometry term of 10 **(e)** a local crack geometry term of 100 **(f)** a local crack geometry term of 10000

Figure 5.10: Contour plots of the boundary condition for the classical and consistent formulations for a preferential direction of $0°$, anisotropic fracture energy parameter $\alpha = 100$, and different local crack geometry term values. The zero-magnitude contour lines in the main damage region are emphasized in green for ease of reading.

From these figures, the following observations are relevant:

- The boundary conditions for the different formulations are most similar when the local crack geometry term is 0. This is expected, as from Figure 5.7 it was noted that it is under this condition that the boundary vectors are most similar.
- For the classical formulation, there is only one contour line on which the boundary condition is zero. This line is straight and oriented in the direction of a $[0, 1]^{\mathrm{T}}$ vector (defined in the global Cartesian coordinate system). This makes sense, as the crack propagating into the boundary will continue to align with the expected crack propagation angle within the domain. This is because the crack orientation is perpendicular to the damage gradient vector.

- For the consistent formulation, the zero contour lines depend greatly on the value of the local crack geometry term. However, unlike the classical case, provided the local crack geometry term is not zero or one, there is no single zero-magnitude contour line. Rather, the zero-magnitude contour exhibits a nonlinear shape that progressively resolves into two straight lines (see the green lines in Figure 5.9f and Figure 5.10f).
- In the case where the local crack geometry term is zero or one, there is one straight zero contour line aligned with the $[0, 1]^{\mathrm{T}}$ direction (similar to the classical formulation).
- When the local crack geometry term is 10, the "original" straight zero contour line is still present, but this is accompanied by two looped contours localized near the origin and symmetric around the $[1, 0]^{\mathrm{T}}$ direction.
- As the local crack geometry term increases to 100, the looped contour lines expand outwards along the $[1, 0]^{\mathrm{T}}$ direction.
- Lastly, for a local crack geometry term of 10000, this grows again to become a triangular region symmetric around the $[1, 0]^{\mathrm{T}}$.
- The looped contours that exist for the consistent formulation stem from the presence of the norm in the boundary vector expression. On the contrary, the classical formulation only has a direct dependence on the damage gradient and the preferential direction vector and thus always retains straight-lined contours.
- For large values of the local crack geometry term, the differences between the plots for $\alpha = 10$ and $\alpha = 100$ are marginal. This is expected because when the local crack geometry term is sufficiently high, the term involving the local crack geometry term dominates the boundary vector and hence the relative influence of α decreases (see Equation 5.52).
- On the contrary, when the value of the local crack geometry term is small, the effect of α is more prominent, where a higher α value results in a sharper (more narrow) zero-magnitude contour line (evident when comparing Figure 5.9b and Figure 5.9c to Figure 5.10b and Figure 5.10c, respectively).

Comparison between AC-30-10-00, AC-30-100-00, and AC-30-10-45

The same analysis is repeated for a preferential direction aligned with $30°$, a normal vector oriented along $[1, 0]^{\mathrm{T}}$, and an anisotropic fracture energy parameter of 10. Figure 5.11 shows the results for the classical formulation and the consistent formulation for various values of the local crack geometry term.

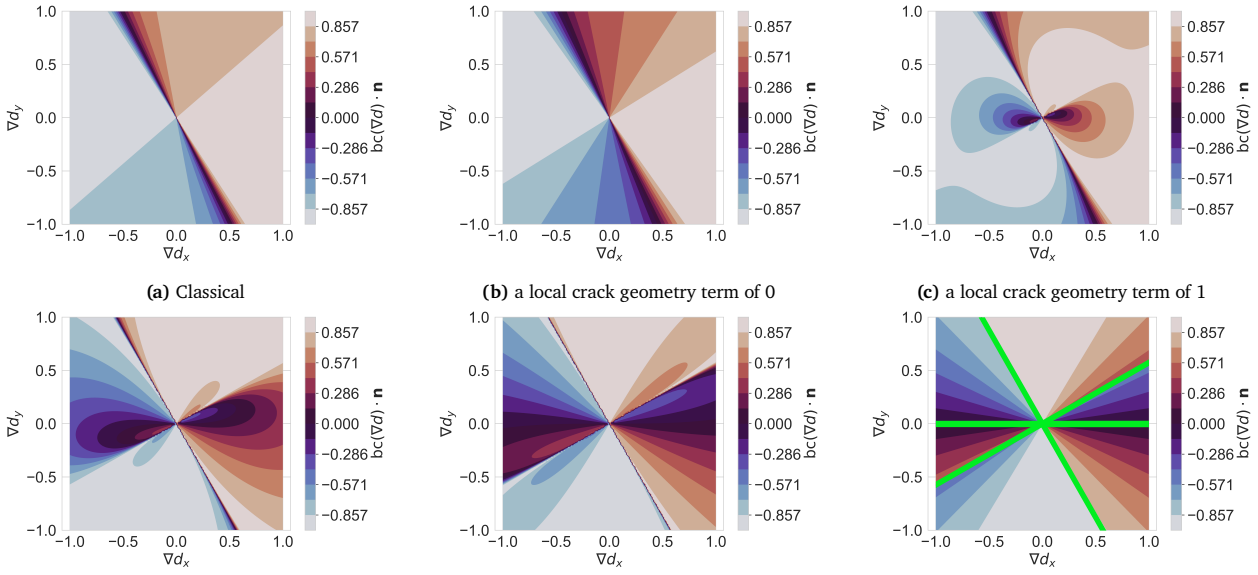

(a) Classical **(b)** a local crack geometry term of 0 **(c)** a local crack geometry term of 1

(d) a local crack geometry term of 10 **(e)** a local crack geometry term of 100 **(f)** a local crack geometry term of 10000

Figure 5.11: Contour plots of the boundary condition for the classical and consistent formulations for a preferential direction of $30°$, anisotropic fracture energy parameter $\alpha = 10$, and different local crack geometry term values. The zero-magnitude contour lines in the main damage region are emphasized in green for ease of reading.

The same analysis is repeated for an anisotropic fracture energy parameter of 100, and these results are visualized in Figure 5.12.

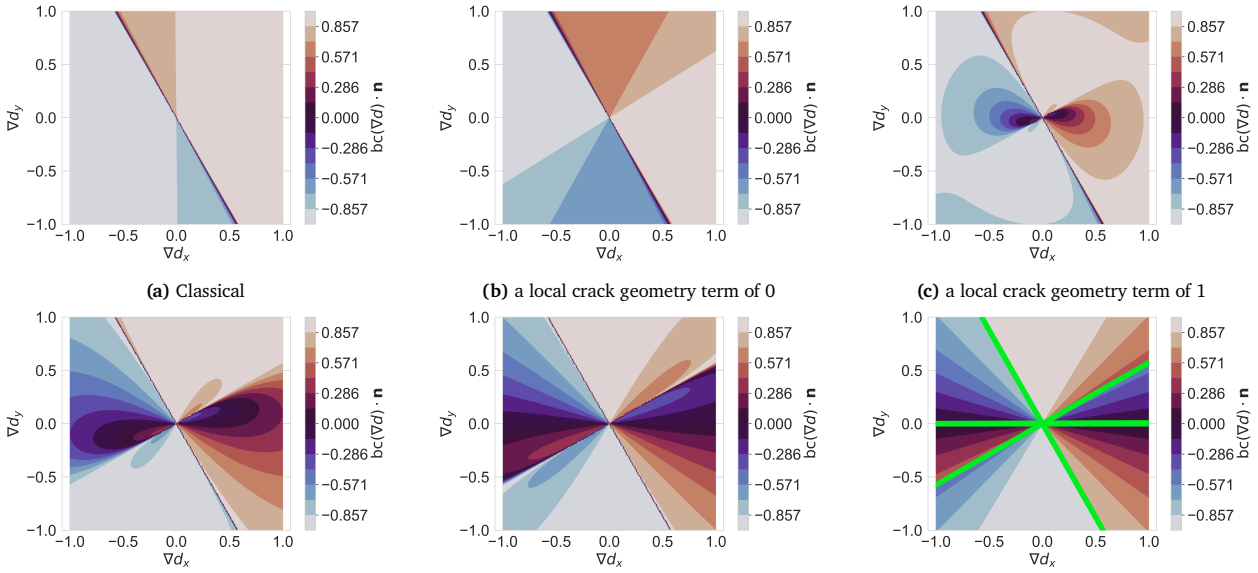

(a) Classical **(b)** a local crack geometry term of 0 **(c)** a local crack geometry term of 1

(d) a local crack geometry term of 10 **(e)** a local crack geometry term of 100 **(f)** the local crack geometry term of 10000

Figure 5.12: Contour plots of the boundary condition for the classical and consistent formulations for a preferential direction of $30°$, anisotropic fracture energy parameter $\alpha = 100$, and different local crack geometry term values. The zero-magnitude contour lines in the main damage region are emphasized in green for ease of reading.

From these figures, the following observations are relevant:

- Similar to the previous case, as expected, the boundary conditions for the different formulations are most similar when the local crack geometry term is 0.
- For the classical formulation, there is a unique contour line on which the boundary condition is satisfied. The orientation of this zero-magnitude contour line is dependent on the value of α. In fact, this orientation is exactly orthogonal to the expected crack propagation angle. This is expected as it results in the crack propagation path on the boundary being aligned with the crack propagation inside the domain. Hence, as α increases, the zero-magnitude contour line orientation approaches $120°$ with respect to the horizontal.
- For the consistent formulation, the zero contour lines depend greatly on the value of the local crack geometry term. Similar to Figure 5.9 and Figure 5.10, provided the local crack geometry term is not zero, the contour lines that satisfy the boundary condition are not unique. Rather, the zero-magnitude contour exhibits a nonlinear shape that progressively resolves into three straight lines (see the green lines in Figure 5.11f and Figure 5.12f).
- In the case where the local crack geometry term is 1, there is one straight zero contour line aligned orthogonal to the expected crack propagation direction (similar to the classical formulation), and a looped contour that is symmetric around an axis tilted in a direction that lies between the expected crack propagation angle and the normal vector (this is also discussed below).
- When the local crack geometry term is 10, both of these contours exist, but the looped contours start to expand.
- As the local crack geometry term increases to 100, the looped contour line separates into two curved contour lines, one oriented in a direction aligned with the expected crack propagation angle, and one oriented in the direction of the normal vector (in this case, aligned with the $[1, 0]^{\mathrm{T}}$ direction).
- When the local crack geometry term is 10000, the contour lines are along the same direction but have now resolved into straight lines.
- Furthermore, similar to the previous case, for large values of the local crack geometry term, the difference between the plots for $\alpha = 10$ and $\alpha = 100$ is marginal. In addition, when the value of the local crack geometry term is small, the effect of α is more prominent, where a higher α value results in a sharper zero-magnitude contour (evident when comparing Figure 5.11b and Figure 5.11c with Figure 5.12b and Figure 5.12c).

To show that the zero-magnitude contour line aligned with the $[1, 0]^{\mathrm{T}}$ direction stems from the normal vector, the same analysis is performed for a normal vector oriented along $[\sqrt{2}/2, \sqrt{2}/2]^{\mathrm{T}}$. In such a case, Figure 5.13 is obtained:

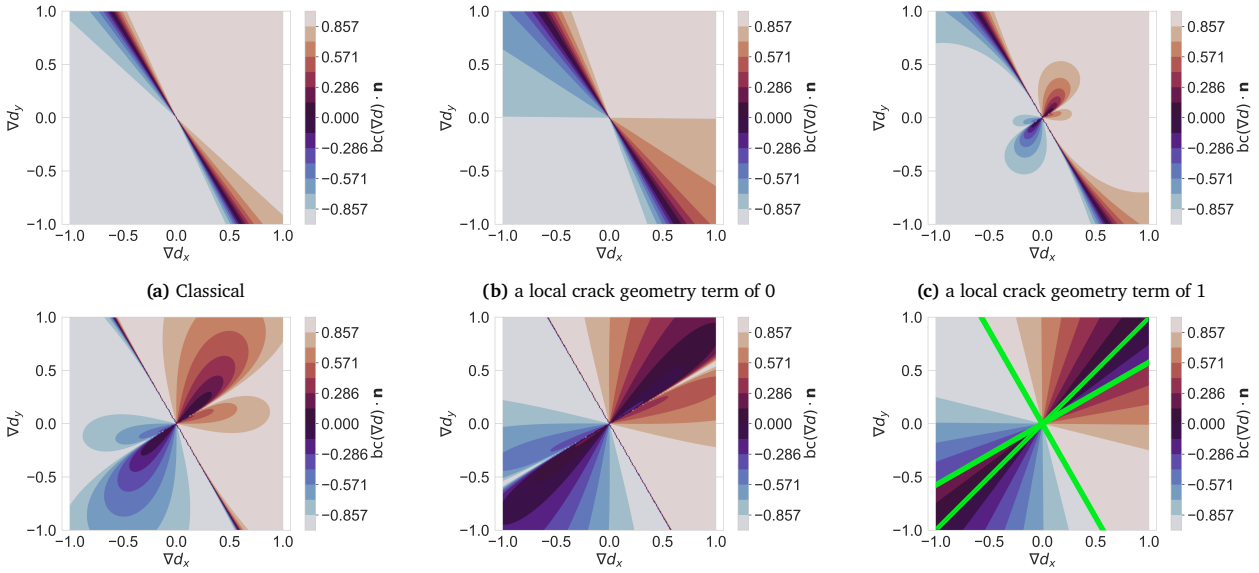

(a) Classical **(b)** a local crack geometry term of 0 **(c)** a local crack geometry term of 1

(d) a local crack geometry term of 10 **(e)** a local crack geometry term of 100 **(f)** a local crack geometry term of 10000

Figure 5.13: Contour plots of the boundary condition for the classical and consistent formulations for a preferential direction of $30°$, anisotropic fracture energy parameter $\alpha = 100$, normal vector is orientated at $45°$, and different local crack geometry term values. The zero-magnitude contour lines in the main damage region are emphasized in green for ease of reading.

From this figure, it is evident that as the value of the local crack geometry term increases, the third zero-magnitude contour line is aligned with the normal direction. In fact, the existence of these three zero-magnitude contour lines can be proved from Equation 5.52. As the local crack geometry term approaches a very high value, its effect dominates the expression, and hence, the zero-magnitude contour lines correspond to when the damage gradient satisfies the following condition:

$$\left(\alpha \frac{\vartheta(d)}{l^2} \frac{(\nabla d \cdot \mathbf{a})}{|\nabla d|^2} \left(\mathbf{a} - \frac{(\nabla d \cdot \mathbf{a})}{|\nabla d|^2} \nabla d\right)\right) \cdot \mathbf{n} = 0 \,. \tag{5.53}$$

This occurs in three situations:

1. ∇d is orthogonal to $\mathbf{a}$: in this case, $\nabla d \cdot \mathbf{a}$ is equal to zero, and hence the expression is zero.
2. ∇d is aligned with $\mathbf{a}$ (hence given by $c\mathbf{a}$ where c is a nonzero constant): in this case, the following holds:

$$\mathbf{a} \cdot \mathbf{n} - \frac{(\nabla d \cdot \mathbf{a})}{|\nabla d|^2} \nabla d \cdot \mathbf{n} = \mathbf{a} \cdot \mathbf{n} - \frac{c|\mathbf{a}|^2}{c^2|\mathbf{a}|^2} c\mathbf{a} \cdot \mathbf{n} = 0 \,. \tag{5.54}$$

3. ∇d is aligned with $\mathbf{n}$: in this case, the following holds:

$$\mathbf{a} \cdot \mathbf{n} - \frac{(\nabla d \cdot \mathbf{a})}{|\nabla d|^2} \nabla d \cdot \mathbf{n} = \mathbf{a} \cdot \mathbf{n} - \frac{c\mathbf{n} \cdot \mathbf{a}}{c^2|\mathbf{n}|^2} c\mathbf{n} \cdot \mathbf{n} = 0 \,. \tag{5.55}$$

Comparison between AC-90-10-00 and AC-90-100-00

The last case considered is for a preferential direction aligned with $90°$, a normal vector oriented along $[1, 0]^{\mathrm{T}}$, and an anisotropic fracture energy parameter of 10. Figure 5.14 shows the results for the classical formulation and the consistent formulation for various values of the local crack geometry term.

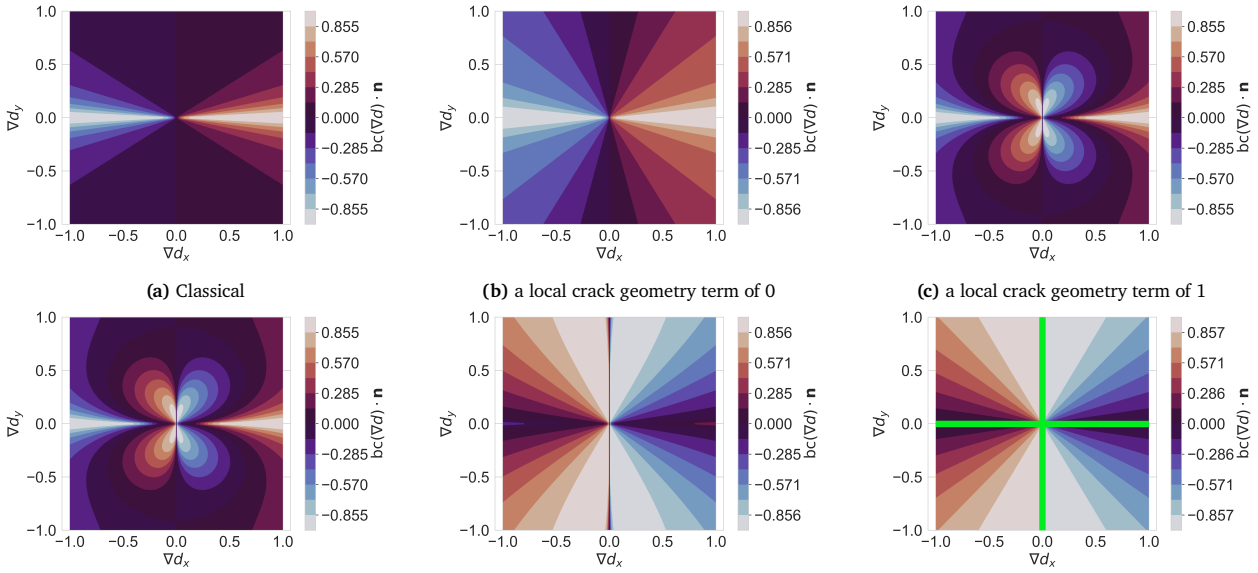

(a) Classical **(b)** a local crack geometry term of 0 **(c)** a local crack geometry term of 1

(d) a local crack geometry term of 10 **(e)** a local crack geometry term of 100 **(f)** a local crack geometry term of 10000

Figure 5.14: Contour plots of the boundary condition for the classical and consistent formulations for a preferential direction of $90°$, anisotropic fracture energy parameter $\alpha = 10$, and different local crack geometry term values. The zero-magnitude contour lines in the main damage region are emphasized in green for ease of reading.

Similar to before, the same analysis is repeated for an anisotropic fracture energy parameter of 100, and these results are visualized in Figure 5.15.

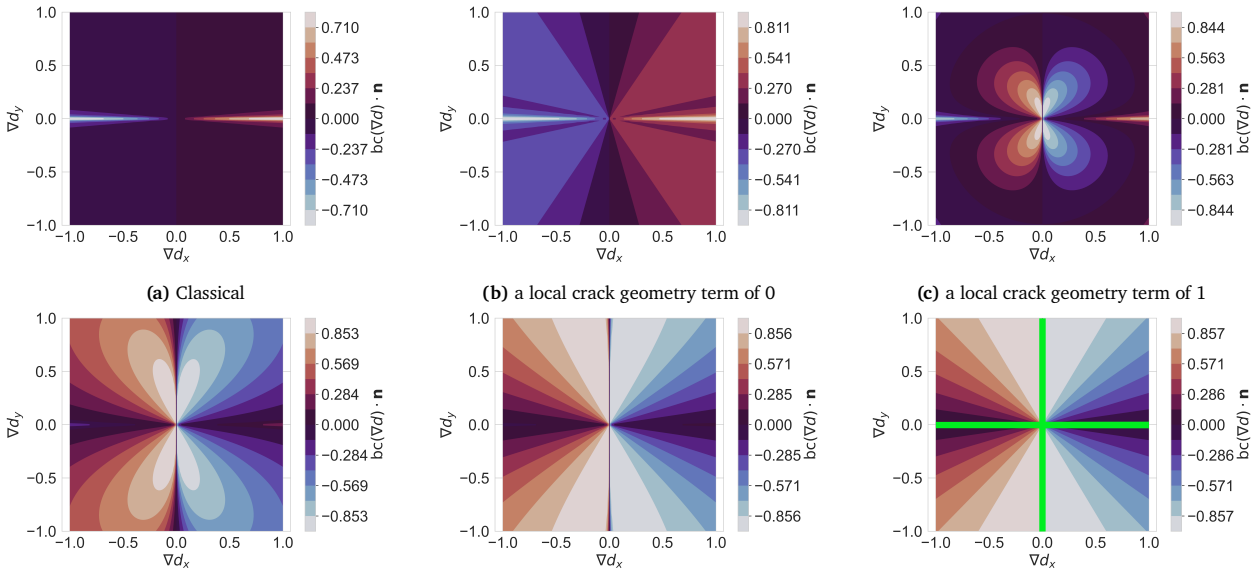

(a) Classical **(b)** a local crack geometry term of 0 **(c)** a local crack geometry term of 1

(d) a local crack geometry term of 10 **(e)** a local crack geometry term of 100 **(f)** a local crack geometry term of 10000

Figure 5.15: Contour plots of the boundary condition for the classical and consistent formulations for a preferential direction of $90°$, anisotropic fracture energy parameter $\alpha = 100$, and different local crack geometry term values. The zero-magnitude contour lines in the main damage region are emphasized in green for ease of reading.

From these figures, the following observations are relevant:

- Similar to the previous cases, the boundary conditions for the different formulations are most similar when the local crack geometry term is 0. However, even then, the contour fields appear rather different.
- For the classical formulation, there is only one contour line on which the boundary condition is zero. This line is straight and oriented in the direction of a $[0, 1]^{\mathrm{T}}$ vector. However, this is opposed to the trends seen so far; if the permissible damage gradient exists along the $[0, 1]^{\mathrm{T}}$ direction, then the crack orientation would be oriented along $[1, 0]^{\mathrm{T}}$. This suggests that as the crack approaches the boundary, the crack path ends horizontally.
- As visualized in the previous cases, for the consistent formulation, the zero contour lines depend greatly on the value of the local crack geometry term. Again, provided the local crack geometry term is not

zero, there is no single zero-magnitude contour line. Rather, the zero-magnitude contour exhibits a nonlinear shape that progressively resolves into two straight lines (see the green lines in Figure 5.14f and Figure 5.15f).

- In the case where the local crack geometry term is 1, there is one straight zero contour line aligned with the $[0, 1]^{\mathrm{T}}$ (similar to the classical formulation), and four looped contours. As the value of the local crack geometry term increases, the looped contours increase in size.
- When the local crack geometry term increases to 100, the looped contour line splits into two contour lines oriented along the $[1, 0]^{\mathrm{T}}$ direction and the $[0, 1]^{\mathrm{T}}$ direction. The contour line aligned with the x-axis is straight for small magnitudes of the damage gradient, but diverges into an upper and lower section for higher magnitudes.
- Lastly, when the local crack geometry term is 10000, the contour lines have fully resolved into straight lines for all magnitudes.

5.7. Defining a Mode-Dependent Fracture Energy

The discussions thus far have focused on introducing, defining, and analyzing a direction-dependent fracture energy. Another component of the proposed formulations is the treatment of mode-mixity. It is evident that as the opening mode changes, the associated fracture energy also changes [20]. As a result, two distinct aspects are of importance, namely:

1. Assuming the extent of mode-mixity is known, determine a relation between the extent of mode-mixity and the fracture energy.
2. Propose a method that can be used to determine the extent of mode-mixity.

Both aspects are addressed sequentially in the subsections below.

5.7.1. A Possible Formulation

In the context of this thesis, inspired by Zhao et al. [3], a mode-dependent fracture energy formulation is considered. In other words, the fracture energy is bounded by $G_c \in [G_{c,I}, G_{c,II}]$, and is prescribed by the following elliptic function:

$$G_c(\chi) = \sqrt{G_{cI}^2 \cos^2(\chi) + G_{cII}^2 \sin^2(\chi)}\,. \tag{5.56}$$

As evident from this equation, for the cases where χ is 0° and 90°, the fracture energy corresponds to the mode I and mode II fracture energies, respectively. To visualize this dependency, the mixed-mode and mode-independent fracture energies are plotted in Figure 5.16.

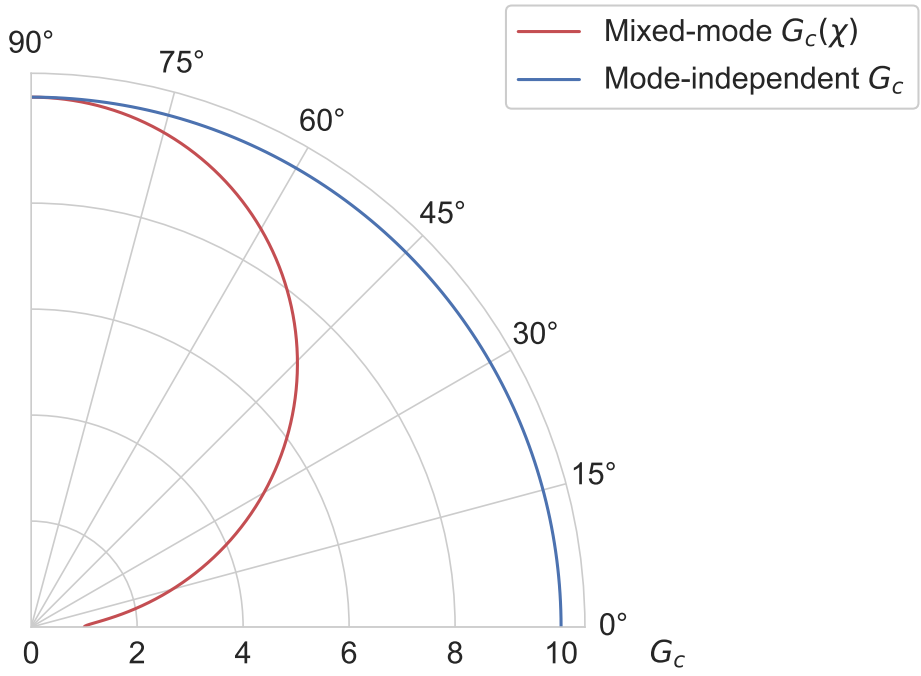

Figure 5.16: Dependency of fracture energy on mode-mixity.

From this figure, it becomes clear that under mode-independent conditions, the fracture energy is isotropic in a mode-mixity sense. Whereas, in a mode-dependent condition, the value of the fracture energy is strongly dependent on the extent of mode-mixity. Similar to the case of the direction-dependent fracture energy, this constitutes one specific formulation, while alternative formulations may be considered in other contexts.

5.7.2. Determining Mode-Mixity

The second aspect is to establish a method to quantify the extent of mode-mixity. The proposed method must remain sufficiently general so that it can be extended to anisotropic fracture contexts. This is not a trivial requirement to satisfy. To illustrate the challenge, the approach proposed by Zhao et al. [3] is first considered. Their work focuses on mixed-mode isotropic fracture, where the extent of mode-mixity is determined as follows:

- Mode-mixity is described as the angle between the crack propagation direction and the direction of the applied displacement.
- The crack evolution direction is obtained from the first eigenvector of the stress tensor (as this eigenvector can be seen as a proxy for the extent of mode-I opening).
- The displacement direction is obtained from the displacement vector.
- All individual components are taken to be history parameters and hence not explicitly solved for in a given damage and loading state.

Although the method above is acceptable for isotropic fracture conditions, it cannot be used in the context of anisotropic fracture. This is because, in an anisotropic setting, the eigenvectors of the stress tensor need not correlate to the mode-I opening. As a result, a different method is proposed in this thesis, namely:

- Mode-mixity is described based on the following ratio of the normal and tangential tractions

$$\frac{\langle \sigma \rangle}{\sqrt{\sigma^2 + \tau^2}}, \tag{5.57}$$

  where σ is the normal traction, τ is the tangential traction, and $\langle \cdot \rangle$ denotes the Macaulay bracket which returns σ if $\sigma > 0$ and 0 otherwise.
- The normal and tangential tractions are determined from the stress tensor and the crack normal vector.
- The crack normal is determined from the damage gradient.

5.8. Establishing a Direction- and Mode-Dependent Fracture Energy

Having established the independent dependencies of the fracture energy on crack orientation and mode-mixity, it remains to be defined how these effects combine in the case of mixed-mode anisotropic fracture. This is considered separately for the proposed formulations in the subsections below.

5.8.1. Proposed Formulation A

Within the proposed framework, any dependency between mode-mixity and fracture anisotropy could be conceptualized. To avoid having overly specific formulations that are difficult to parameterize, a simplified approach is adopted in this thesis. The mixed-mode anisotropic behavior is constructed by interpolating between mode-independent anisotropic and mixed-mode isotropic fracture conditions. This leads to the following expression for the fracture energy:

$$G_c(\chi, \mathbf{m}) = \sqrt{G_{cI}^2(\mathbf{m}) \cos^2 \chi + G_{cII}^2(\mathbf{m}) \sin^2 \chi}\,. \tag{5.58}$$

This formulation highlights the possibility of distinguishing between mode I and mode II energetics. While the fiber-dominated fracture energy is assumed to be relatively insensitive to the fracture mode, the matrix contribution exhibits a clear dependence on the opening mode. Consequently, the anisotropic fracture energy parameter, α, is allowed to vary with the mode-mixity. Under this assumption, the direction-dependent fracture energy can be interpreted as an interpolation between the two pure opening modes. This results in the following type of G_c and G_c^{-1} plots.

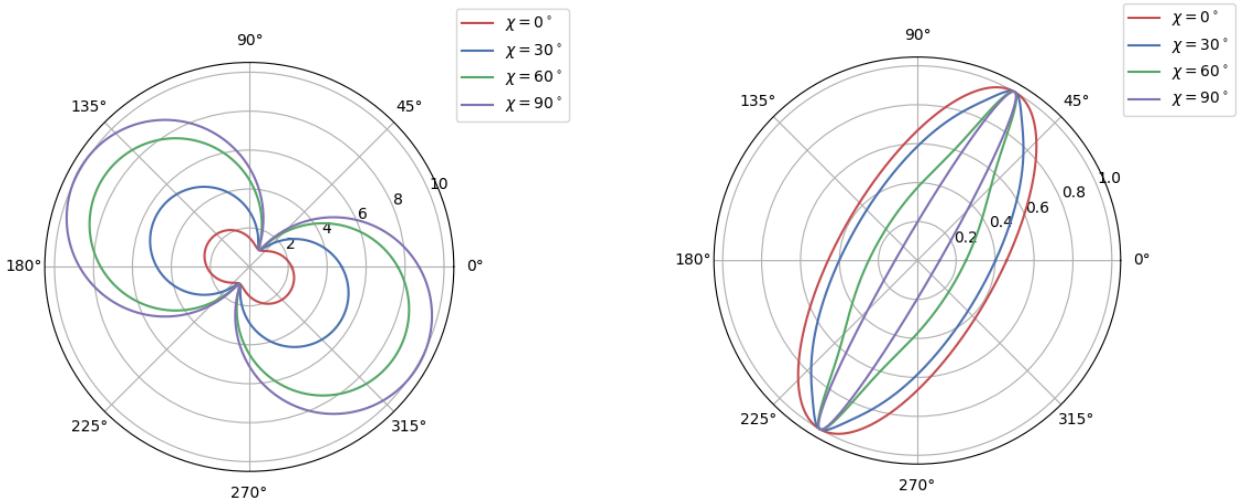

(a) $G_c(\theta)$ **(b)** $G_c^{-1}(\theta)$

Figure 5.17: Polar plots of G_c and G_c^{-1} for the proposed model.

5.8.2. Proposed Formulation B

For proposed formulation B, there is no direct coupling between the two; they are combined in a separable manner. As a result, the shape of the directional-dependent fracture energy remains the same, and mode-mixity only affects the magnitude of G_c. This can be seen as a special case of Equation 5.58, namely, when both Mode I and Mode II have the same directional dependence. To see why, consider the following:

$$G_{cI}(\mathbf{m}) = G_{cI}\sqrt{\mathbf{m}\cdot\mathbf{Am}}, \qquad G_{cII}(\theta) = G_{cII}\sqrt{\mathbf{m}\cdot\mathbf{Am}}\,. \tag{5.59}$$

Substituting Equation 5.59 into Equation 5.58 yields

$$\begin{aligned} G(\chi,\mathbf{m}) &= \sqrt{[G_{cI}\sqrt{\mathbf{m}\cdot\mathbf{Am}}]^2\cos^2\chi + [G_{cII}\sqrt{\mathbf{m}\cdot\mathbf{Am}}]^2\sin^2\chi} \\ &= \sqrt{\mathbf{m}\cdot\mathbf{Am}}\sqrt{G_{cI}^2\cos^2\chi + G_{cII}^2\sin^2\chi} \\ &= \sqrt{\mathbf{m}\cdot\mathbf{Am}}G_c(\chi)\,. \end{aligned} \tag{5.60}$$

5.9. Thermodynamic Considerations

To formalize the formulation, the thermodynamic consistency of the model is considered. It is known that the fracturing of solids is a dissipative process, and hence the dissipation rate should be non-negative. Assuming the fracture process occurs isothermally, the following should hold for every point in the domain:

$$\boldsymbol{\sigma} : \dot{\boldsymbol{\varepsilon}} - \dot{\mathcal{H}} \geq 0\,. \tag{5.61}$$

As presented during the literature review, in the case of a coupled displacement-damage system, the Helmholtz energy is given as the sum of the elastic and fracture energy density [62], i.e.,

$$\mathcal{H} = \psi_e(\varepsilon, d) + \psi_d(d, \nabla d)\,. \tag{5.62}$$

Based on this, the time rate of change of the Helmholtz energy is nominally given by

$$\dot{\mathcal{H}} = \frac{\partial \mathcal{H}}{\partial \boldsymbol{\varepsilon}} : \dot{\boldsymbol{\varepsilon}} + \frac{\partial \mathcal{H}}{\partial d}\dot{d} + \frac{\partial \mathcal{H}}{\partial \nabla d}\cdot\dot{\nabla} d\,. \tag{5.63}$$

In such a case, from Equation 5.63, it is evident that relevant partial derivatives are given by

$$\frac{\partial \mathcal{H}}{\partial \varepsilon} = \frac{\partial \psi_e}{\partial \varepsilon}, \qquad \frac{\partial \mathcal{H}}{\partial d} = \frac{\partial \psi_e}{\partial d} + \frac{\partial \psi_d}{\partial d}, \qquad \frac{\partial \mathcal{H}}{\partial \nabla d} = \frac{\partial \psi_d}{\partial \nabla d}\,. \tag{5.64}$$

However, in the case of the proposed model, the rate of Helmholtz energy is also affected by the rate of the fracture energy due to mode-mixity. In other words, Equation 5.63 can be written as

$$\left(\boldsymbol{\sigma} - \frac{\partial \psi_e}{\partial \boldsymbol{\varepsilon}}\right) : \dot{\varepsilon} - \left(\frac{\partial \psi_e}{\partial d} + \frac{\partial \psi_d}{\partial d}\right)\dot{d} - \frac{\partial \psi_d}{\partial \nabla d}\cdot\dot{\nabla} d - \frac{\partial \psi_d}{\partial G_c}\dot{G}_c \geq 0\,. \tag{5.65}$$

The first three terms in Equation 5.65 correspond to the standard contributions in the phase field formulation and are identical to the classical case, and hence their non-positivity is ensured. The last term is new, and thus it remains to be shown that the rate of the fracture energy is non-positive, namely

$$-\frac{\partial \psi_d}{\partial G_c}\dot{G}_c \geq 0 \qquad \Rightarrow \dot{G}_c \leq 0\,. \tag{5.66}$$

To enforce this condition under evolving mode-mixity, a history-dependent definition of the fracture energy is introduced. However, rather than interpreting this as a history-dependent variable, it is more natural to term this as a residual fracture energy that depends on the history of the loading (as a result, it implicitly becomes history dependent). Hence, the fracture energy is redefined to be the minimum between Equation 5.58 and the history value at t, i.e.,

$$G_c = \min_{\tau_t \leq t} G_c(\theta, \chi(\tau_t)) = \min_{\tau_t \leq t} \sqrt{G_{cI}^2(\theta)\cos^2\chi(\tau_t) + G_{cII}^2(\theta)\sin^2\chi(\tau_t)}\,. \tag{5.67}$$

where τ_t refers to any time step already or currently observed and t is the time step currently observed.

Remark 5.7

The concept of a history-dependent or "residual" fracture energy can be encountered in cohesive zone models. In these formulations, the traction–separation law evolves irreversibly with loading history. As a result, unloading and reloading do not follow the initial elastic–cohesive path, but instead proceed along a degraded response governed by the current damage state. Consequently, the remaining area under the traction–separation curve, representing the additional energy that can still be dissipated, is reduced compared to the pristine material response (compare the red area under the curve to the blue area under the curve in Figure 5.18).

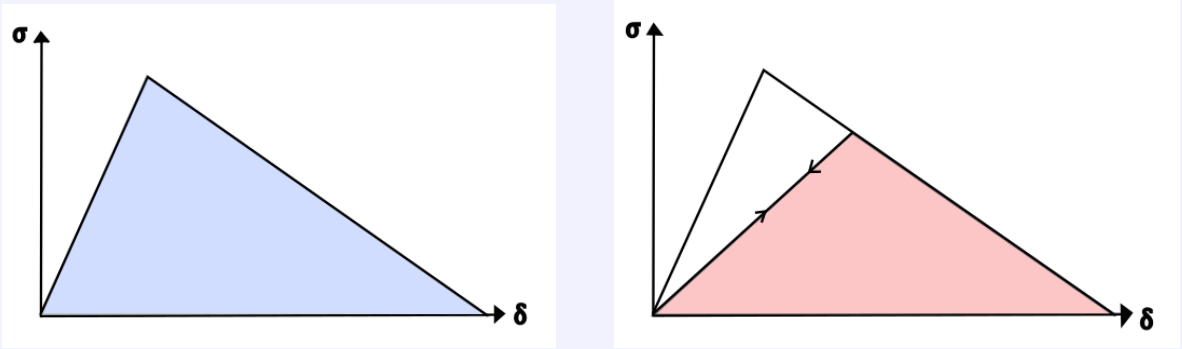

Figure 5.18: Comparison of pristine (left) and "effective" (right) fracture energy in cohesive zone modeling.

6: Numerical Implementation

In this chapter, the numerical implementation of the two formulations detailed in Chapter 5 is discussed. Firstly, the scope of the problem is identified in Section 6.1. This is followed by a discussion of the finite element framework in Section 6.2. The logic and nature of the coding solution are presented in Section 6.3. Lastly, some relevant modeling choices are detailed in Section 6.4.

6.1. Scope of Problem

The previous chapter established the mathematical formulation of the proposed models. However, in their current form, these equations remain in a continuous setting and cannot be directly used for computational analysis. To evaluate the behavior and practical applicability of the models, it is necessary to transition from this continuous description to a numerically implementable framework. Thus, the scope of this chapter aims to address the following objectives:

- Establish the numerical framework used to model the proposed formulations.
- Present and evaluate the logic of the solver.
- Discuss some supporting modeling choices.

The following sections discuss these aspects in more detail.

6.2. Finite Element Framework

As identified during the literature review in Chapter 3, it is a popular choice to solve the phase field problem within a finite element framework. When doing so, the method inherits many of the classical aspects, but the additional field equation adds some nuances. Particularly, in such a setting, the following points become relevant:

- The classical aspects of finite element methods.
- Details pertaining to the solver method choice.
- The treatment of damage irreversibility.
- Some remarks related to (possible) numerical issues.

The next few subsections detail these aspects in the same order.

6.2.1. Classical Aspects

As is traditional for finite element methods, the weak forms of the governing equations for the displacement and phase field are considered. The standard Bubnov-Galerkin finite element method is used, where the nodal values of the displacements and phase field are the unknowns.

For proposed formulation A, the governing equations are as follows:

$$\int_{\mathcal{B}} \boldsymbol{\sigma} : \delta\boldsymbol{\varepsilon} \, \mathrm{d}V - \int_{\mathcal{B}} \mathbf{b} \cdot \delta\mathbf{u} \, \mathrm{d}V - \int_{\partial\mathcal{B}} \mathbf{f}_0 \cdot \delta\mathbf{u} \, \mathrm{d}S = 0, \tag{6.1}$$

$$\int_{\mathcal{B}} \left[\frac{\partial \psi_e}{\partial d} + G_c \frac{\partial \gamma}{\partial d} - \nabla \cdot \left(G_c \frac{\partial \gamma}{\partial \nabla d} + \gamma \frac{\partial G_c}{\partial \nabla d} \right) \right] \delta d \, \mathrm{d}V + \int_{\partial\mathcal{B}} \left(G_c \frac{\partial \gamma}{\partial \nabla d} \cdot \mathbf{n} \right) \delta d \, \mathrm{d}S + \int_{\partial\mathcal{B}} \left(\gamma \frac{\partial G_c}{\partial \nabla d} \cdot \mathbf{n} \right) \delta d \, \mathrm{d}S = 0 \, . \tag{6.2}$$

For this thesis, the hybrid approach proposed by Ambati et al. [1] wherein the tension-compression split is kept for elastic energy, but the classical linear momentum balance relation is used. Hence,

$$\boldsymbol{\sigma} = g(d)\mathbb{C}\boldsymbol{\varepsilon} \, . \tag{6.3}$$

Within a finite element framework, the displacement field, $\mathbf{u}$, can be approximated using the shape function matrix $\mathbf{N}^u$ and nodal displacement vector $\mathbf{u}^e$, i.e.,

$$\mathbf{u} = \sum_{i=1}^{n} \mathbf{N}_i^u \mathbf{u} = \mathbf{N}^u \mathbf{u}^e \, . \tag{6.4}$$

Similarly, the phase field, d, can be approximated using the phase field shape function matrix $\mathbf{N}^d$ and the phase field nodal vector $\mathbf{d}^e$ i.e.,

$$d = \sum_{i=i}^{n} N_i^d d_i = \mathbf{N}^d \mathbf{d}^e. \tag{6.5}$$

The displacement and phase field shape function matrices are given by

$$\mathbf{N}^u = \begin{bmatrix} N_1 & 0 & ... & N_n & 0 \\ 0 & N_1 & ... & 0 & N_n \end{bmatrix}, \quad \text{and} \quad \mathbf{N}^d = \begin{bmatrix} N_1 & ... & N_n \end{bmatrix}, \tag{6.6}$$

where N_i $(i = 1, 2, ..., n)$ corresponds to the shape function at the $i-$th node, and n denotes the number of nodes per elements.

Having defined the discretized form of the displacement and phase fields, their gradients can be defined as follows:

$$\boldsymbol{\varepsilon} = \sum_{i=1}^{n} \mathbf{B}^u \mathbf{u}^i = \mathbf{B}^u \mathbf{u}^e, \qquad \nabla d = \sum_{i=1}^{n} \mathbf{B}_i^d d_i = \mathbf{B}^d \mathbf{d}^e, \tag{6.7}$$

where now the geometric matrices, $\mathbf{B}^u$ and $\mathbf{B}^d$ for both the displacement and phase fields, respectively, are given by

$$\mathbf{B}^u = \begin{bmatrix} N_{1,x} & 0 & ... & N_{n,x} & 0 \\ 0 & N_{1,y} & ... & 0 & N_{n,y} \\ N_{1,y} & N_{1,x} & ... & N_{n,y} & N_{n,x} \end{bmatrix}, \quad \text{and} \quad \mathbf{B}^d = \begin{bmatrix} N_{1,x} & ... & N_{n,x} \\ N_{1,y} & ... & N_{n,y} \end{bmatrix}. \tag{6.8}$$

Similar to the AT2 mode, using $\vartheta(d) = d^2$ and $g(d) = (1-d)^2$, the discretized weak form of proposed formulation A is

$$\begin{aligned} \int_{\mathcal{B}} \delta \mathbf{u}_e^T \mathbf{B}_u^T \mathbb{C}(d) \mathbf{B}_u \mathbf{u}_e \mathrm{d}V - \int_{\mathcal{B}} \delta \mathbf{u}_e^T \mathbf{N}_u^T \mathbf{b} \mathrm{d}V - \int_{\partial \mathcal{B}} \delta \mathbf{u}_e^T \mathbf{N}_u^T \mathbf{f}_0 \mathrm{d}S = 0, \\ \int_{\mathcal{B}} \delta \mathbf{d}_e^T \left[\left(2\psi_0^+ + \frac{G_c}{l} \right) \mathbf{N}_d^T \mathbf{N}_d \mathbf{d}_e + G_c l \mathbf{B}_d^T \mathbf{B}_d \mathbf{d}_e + \gamma \mathbf{B}_d^T \mathbf{g}_d - 2\psi_0^+ \mathbf{N}_d^T \right] \mathrm{d}V = 0, \end{aligned} \tag{6.9}$$

where, ψ_e^+ is the tensile contribution of the undamaged elastic energy and $\mathbf{g}_d$ is introduced to denote $\frac{\partial G_c}{\partial \nabla d}$.

Analogously, the discretized weak forms for proposed formulation B are given by

$$\begin{aligned} \int_{\mathcal{B}} \delta \mathbf{u}_e^T \mathbf{B}_u^T \mathbb{C}(d) \mathbf{B}_u \mathbf{u}_e \mathrm{d}V - \int_{\mathcal{B}} \delta \mathbf{u}_e^T \mathbf{N}_u^T \mathbf{b} \mathrm{d}V - \int_{\partial \mathcal{B}} \delta \mathbf{u}_e^T \mathbf{N}_u^T \mathbf{f}_0 \mathrm{d}S = 0, \\ \int_{\mathcal{B}} \delta \mathbf{d}_e^T \left[\left(2\psi_0^+ + \frac{G_c}{l} \right) \mathbf{N}_d^T \mathbf{N}_d \mathbf{d}_e + G_c l \mathbf{B}_d^T \mathbf{A} \mathbf{B}_d \mathbf{d}_e - 2\psi_0^+ \mathbf{N}_d^T \right] \mathrm{d}V = 0 \,. \end{aligned} \tag{6.10}$$

For this thesis, the tensile contribution is determined using the spectral decomposition of strain as proposed by Miehe et al. [64, 65]. In other words, it is defined as

$$\psi_e^{\pm} = \frac{1}{2} \boldsymbol{\varepsilon}_{\pm} \cdot \mathbb{C} \boldsymbol{\varepsilon}_{\pm}, \tag{6.11}$$

where

$$\boldsymbol{\varepsilon}_{\pm} = \sum_{a=1}^{3} \langle \varepsilon_{ea} \rangle_{\pm} \mathbf{n}_a \otimes \mathbf{n}_a \,. \tag{6.12}$$

where e_{ea}, $\mathbf{n}_a$ $(a = 1, 2, 3)$ refer to the principal strains and principal strain directions respectively.

6.2.2. Solver Method

Having obtained the discretized weak form, the next aspect to consider is the solver method. During the literature review in Section 3.3.2, it was identified that this system could be solved in either a monolithic manner or using a staggered approach. In this context, the distinction between the two becomes easy to identify. Under the monolithic approach, both equations are solved in a coupled manner, and hence all stiffness terms are relevant. As a result, the discretization of the weak form of the governing equations results in the following system of equations:

$$\begin{bmatrix} \mathbf{K}^{uu} & \mathbf{K}^{ud} \\ \mathbf{K}^{du} & \mathbf{K}^{dd} \end{bmatrix} \begin{bmatrix} \Delta \mathbf{u} \\ \Delta d \end{bmatrix} = \begin{bmatrix} \mathbf{R}^u \\ \mathbf{R}^d \end{bmatrix}, \tag{6.13}$$

where $\mathbf{K}^{uu}$ is the mechanical stiffness, $\mathbf{K}^{ud}$, $\mathbf{K}^{du}$ are the phase field displacement coupling matrices, $\mathbf{K}^{dd}$ is the phase field tangent matrix, and $\mathbf{R}_u$ and $\mathbf{R}_d$ are the residual vectors associated with the displacement and phase field equations, respectively.

However, within a staggered approach, the non-convex coupled system of equations is decoupled into two convex equations by neglecting the off-diagonal terms. In such a case, the following system of equations is retrieved:

$$\begin{bmatrix} \mathbf{K}^{uu} & 0 \\ 0 & \mathbf{K}^{dd} \end{bmatrix} \begin{bmatrix} \Delta\mathbf{u} \\ \Delta d \end{bmatrix} = \begin{bmatrix} \mathbf{R}^{u} \\ \mathbf{R}^{d} \end{bmatrix} . \tag{6.14}$$

For ease of numerical implementation, a fully coupled staggered approach was opted for, as opposed to a weakly coupled staggered approach, which would be without iterations. The consequence is that convergence may require several iterations. Thus, the increments of the degrees of freedom at iteration number $k+1$ for a displacement increment $i+1$ can be solved for in the following manner:

$$\begin{bmatrix} \Delta\mathbf{u}^{i+1}_{e,k+1} \\ \Delta\mathbf{d}^{i+1}_{e,k+1} \end{bmatrix} = \begin{bmatrix} \Delta\mathbf{u}^{i+1}_{e,k+1} - \Delta\mathbf{u}^{i+1}_{e,k} \\ \Delta\mathbf{d}^{i+1}_{e,k+1} - \Delta\mathbf{d}^{i+1}_{e,k} \end{bmatrix} = - \begin{bmatrix} \mathbf{K}^{i+1}_{uu,k+1} & 0 \\ 0 & \mathbf{K}^{i+1}_{dd,k+1} \end{bmatrix}^{-1} \begin{bmatrix} \mathbf{R}^{i+1}_{u,k+1} \\ \mathbf{R}^{i+1}_{d,k+1} \end{bmatrix} . \tag{6.15}$$

To determine the exact nature of the residual and stiffness terms, it is important to distinguish between the different methods to treat damage irreversibility. This is considered in the following subsection.

6.2.3. Treatment of Damage Irreversibility

As identified in the literature review in Section 3.2.7, there are mainly two ways of enforcing damage irreversibility, either through a history parameter or by using an augmented Lagrangian approach. Whereas the former is the more popular choice, it does suffer from variational inconsistency [56]. Nonetheless, the residual and stiffness terms obtained during this approach are also mentioned for completeness. On the contrary, the augmented Lagrangian approach is variationally consistent [70] and is opted for in this thesis.

History Parameter Based

When using the history parameter, the residual terms follow directly from the discretized weak form (for proposed formulation A) and hence are given by

$$\begin{aligned} \mathbf{R}^{i+1}_{u} &= \int_{\mathcal{B}} \mathbf{B}_u^T \mathbb{C}(d^i) \mathbf{B}_u \mathbf{u}_e^{i+1} \, \mathrm{d}V - \int_{\mathcal{B}} \mathbf{N}_u^T \mathbf{b} \, \mathrm{d}V, \\ \mathbf{R}^{i+1}_{d} &= \int_{\mathcal{B}} \left[\left(2\mathcal{H}_v^i + \frac{G_c^i}{l} \right) \mathbf{N}_d^T \mathbf{N}_d \mathbf{d}_e^{i+1} + G_c^i l \mathbf{B}_d^T \mathbf{B}_d \mathbf{d}_e^{i+1} + \gamma^i \mathbf{B}_d^T \mathbf{g}_d^i - 2\mathcal{H}_v^i \mathbf{N}_d^T \right] \mathrm{d}V , \end{aligned} \tag{6.16}$$

where $\mathcal{H}_v^i$ is the history variable of the tensile undamaged elastic energy. Recall, this is defined as

$$\mathcal{H}_v = \max_{0 \le \tau_t \le t} (\psi_0^+) . \tag{6.17}$$

The element stiffness matrices are defined as the derivatives of the residuals with respect to either the displacement or phase field. As a staggered solution scheme is opted for, only $\mathbf{K}_{uu}$ and $\mathbf{K}_{dd}$ are of interest. These are given as follows, respectively:

$$\begin{aligned} \mathbf{K}^{i+1}_{uu} &= \frac{\partial \mathbf{R}^{i+1}_{u}}{\partial \mathbf{u}_e} = \int_{\mathcal{B}} \mathbf{B}_u^T \mathbb{C}(d^i) \mathbf{B}_u \, \mathrm{d}V, \\ \mathbf{K}^{i+1}_{dd} &= \frac{\partial \mathbf{R}^{i+1}_{d}}{\partial \mathbf{d}_e} = \int_{\mathcal{B}} \left[\left(2\mathcal{H}_v^i + \frac{G_c^i}{l} \right) \mathbf{N}_d^T \mathbf{N}_d + G_c^i l \mathbf{B}_d^T \mathbf{B}_d \right] \mathrm{d}V . \end{aligned} \tag{6.18}$$

For proposed formulation B, the residual and stiffness terms are given in Equation 6.19 and Equation 6.20, respectively.

$$\begin{aligned} \mathbf{R}^{i+1}_{u} &= \int_{\mathcal{B}} \mathbf{B}_u^T \mathbb{C}(d^i) \mathbf{B}_u \mathbf{u}_e^{i+1} \, \mathrm{d}V - \int_{\mathcal{B}} \mathbf{N}_u^T \mathbf{b} \, \mathrm{d}V, \\ \mathbf{R}^{i+1}_{d} &= \int_{\mathcal{B}} \left[\left(2\mathcal{H}_v^i + \frac{G_c}{l} \right) \mathbf{N}_d^T \mathbf{N}_d \mathbf{d}_e^{i+1} + G_c l \mathbf{B}_d^T \mathbf{A} \mathbf{B}_d \mathbf{d}_e^{i+1} - 2\mathcal{H}_v^i \mathbf{N}_d^T \right] \mathrm{d}V, \end{aligned} \tag{6.19}$$

$$\begin{aligned} \mathbf{K}^{i+1}_{uu} &= \frac{\partial \mathbf{R}^{i+1}_{u}}{\partial \mathbf{u}_e} = \int_{\mathcal{B}} \mathbf{B}_u^T \mathbb{C}(d^i) \mathbf{B}_u \, \mathrm{d}V, \\ \mathbf{K}^{i+1}_{dd} &= \frac{\partial \mathbf{R}^{i+1}_{d}}{\partial \mathbf{d}_e} = \int_{\mathcal{B}} \left[\left(2\mathcal{H}_v^i + \frac{G_c}{l} \right) \mathbf{N}_d^T \mathbf{N}_d + G_c l \mathbf{B}_d^T \mathbf{A} \mathbf{B}_d \right] \mathrm{d}V . \end{aligned} \tag{6.20}$$

Augmented Lagrangian Method

When using the augmented Lagrangian method, rather than introducing a history variable, damage irreversibility is enforced through the formulation of the constrained minimization problem. In such a case, one aims to find a solution to the following problem [70]:

$$\begin{aligned} &\min\ \psi(\mathbf{u}, d, \nabla d) \\ &\quad \text{such that } d \in \{d | 0 \leq d^{n-1} \leq d \leq 1\}, \end{aligned} \tag{6.21}$$

where the previous solution $(\mathbf{u}^{n-1}, d^{n-1})$ is known.

This problem can be approximated as

$$\min\ \psi(\mathbf{u}, d, \nabla d) + \frac{1}{2\rho}||\langle \lambda_l + \rho(d^{n-1} - d)\rangle_+||^2, \tag{6.22}$$

where λ_l is the Lagrange multiplier and ρ is a penalty coefficient. For the observant reader, this is equivalent to what was discussed in Chapter 3, but with the exception that the term $\frac{1}{2\rho}||\langle \lambda + \rho(1-d)\rangle_-||^2$ has been omitted. This is because the boundedness of the phase field variable is inherently ensured by the choice of geometric crack function.

> ***Remark 6.1***
>
> Often, constrained minimization problems use either Lagrange multipliers *or* penalty-based methods. Yet in this case, both are used. The idea is that due to the presence of the Lagrange multiplier term, the magnitude of the penalty can be much lower. This avoids potential ill-conditioning. Furthermore, it is noted that at each step, the accuracy of λ_l (an estimate of the Lagrange multiplier) increases [70].

Based on these equations, it follows that the residual equations are

$$\begin{aligned} \mathbf{R}_u^{i+1} &= \int_{\mathcal{B}} \mathbf{B}_u^T \mathbb{C}(d^i) \mathbf{B}_u \mathbf{u}_e^{i+1}\, \mathrm{d}V - \int_{\mathcal{B}} \mathbf{N}_u^T \mathbf{b}\, \mathrm{d}V, \\ \mathbf{R}_d^{i+1} &= \int_{\mathcal{B}} \left(2\psi_0^{+\,i} + \frac{G_c^i}{l}\right) \mathbf{N}_d^T \mathbf{N}_d \mathbf{d}_e^{i+1} + G_c^i l \mathbf{B}_d^T \mathbf{B}_d \mathbf{d}_e^{i+1} + \gamma^i \mathbf{B}_d^T \mathbf{g}_d^i \\ &\qquad -2\psi_0^{+\,i} \mathbf{N}_d^T - \mathbf{N}_d^T \mathbf{N}(\lambda_l + \rho(\mathbf{d}_e^i - \mathbf{d}_e^{i+1}))\, \mathrm{d}V\ . \end{aligned} \tag{6.23}$$

This is equivalent to Equation 6.16, but with two notable differences: the tensile elastic energy is used instead of the history variable, and the addition of a new fifth term.

In addition, in such a case, the element stiffness matrices are given as follows for the displacement and phase field, respectively:

$$\begin{aligned} \mathbf{K}_{uu}^{i+1} &= \frac{\partial \mathbf{R}_u^{i+1}}{\partial \mathbf{u}_e} = \int_{\mathcal{B}} \mathbf{B}_u^T \mathbb{C}(d^i) \mathbf{B}_u\, \mathrm{d}V, \\ \mathbf{K}_{dd}^{i+1} &= \frac{\partial \mathbf{R}_d^{i+1}}{\partial \mathbf{d}_e} = \int_{\mathcal{B}} \left[\left(2\psi_0^{+\,i} + \frac{G_c^i}{l}\right) \mathbf{N}_d^T \mathbf{N}_d + G_c^i l \mathbf{B}_d^T \mathbf{B}_d + \rho \mathbf{N}^T \mathbf{N}\right] \mathrm{d}V\ . \end{aligned} \tag{6.24}$$

Furthermore, for completeness, for proposed formulation B, the residual and stiffness terms are given in Equation 6.25 and Equation 6.26, respectively.

$$\begin{aligned} \mathbf{R}_u^{i+1} &= \int_{\mathcal{B}} \mathbf{B}_u^T \mathbb{C}(d^i) \mathbf{B}_u \mathbf{u}_e^{i+1}\, \mathrm{d}V - \int_{\mathcal{B}} \mathbf{N}_u^T \mathbf{b}\, \mathrm{d}V, \\ \mathbf{R}_d^{i+1} &= \int_{\mathcal{B}} \left(2\psi_0^{+\,i} + \frac{G_c}{l}\right) \mathbf{N}_d^T \mathbf{N}_d \mathbf{d}_e^{i+1} + G_c l \mathbf{B}_d^T \mathbf{A} \mathbf{B}_d \mathbf{d}_e^{i+1} \\ &\qquad -2\psi_0^{+\,i} \mathbf{N}_d^T - \mathbf{N}_d^T \mathbf{N}(\lambda_l + \rho(\mathbf{d}_e^i - \mathbf{d}_e^{i+1}))\, \mathrm{d}V\ . \end{aligned} \tag{6.25}$$

$$\begin{aligned} \mathbf{K}_{uu}^{i+1} &= \frac{\partial \mathbf{R}_u^{i+1}}{\partial \mathbf{u}_e} = \int_{\mathcal{B}} \mathbf{B}_u^T \mathbb{C}(d^i) \mathbf{B}_u\, \mathrm{d}V, \\ \mathbf{K}_{dd}^{i+1} &= \frac{\partial \mathbf{R}_d^{i+1}}{\partial \mathbf{d}_e} = \int_{\mathcal{B}} \left[\left(2\psi_0^{+\,i} + \frac{G_c}{l}\right) \mathbf{N}_d^T \mathbf{N}_d + G_c l \mathbf{B}_d^T \mathbf{A} \mathbf{B}_d + \rho \mathbf{N}^T \mathbf{N}\right] \mathrm{d}V\ . \end{aligned} \tag{6.26}$$

6.2.4. Some Regularization Remarks

The governing equations derived above are formally complete; however, their direct numerical implementation leads to instability in the case of proposed formulation A. This issue arises because, as the damage gradient tends to zero, the term $\mathbf{g}_d$ becomes unbounded, resulting in numerical ill-conditioning. This limitation was also identified by Rezaei et al. [24] who employed a consistent formulation and encountered similar difficulties. To address this, they introduced a regularization strategy to bound the problematic term and ensure numerical robustness. Within the context of this thesis, the same regularization method is opted for, i.e.,

$$\mathbf{g}_d^i = \begin{cases} \left(\dfrac{\|\nabla d\|}{\|\nabla d\|_c} \right)^n \tilde{\mathbf{g}}_d^i & \text{if } \|\nabla d\| \leq \|\nabla d\|_c, \\ \tilde{\mathbf{g}}_d^i & \text{otherwise,} \end{cases} \tag{6.27}$$

where n is the order of regularization, $\tilde{\mathbf{g}}_d^i$ is the true parameter, $||\nabla d||_c$ is threshold below which regularization is applied, and $\mathbf{g}_d^i$ is the regularized parameter.

Rezaei et al. [24] note that $||\nabla d||_c$ should be chosen sufficiently large to avoid numerical issues. In this thesis, a value of 0.1 was found sufficient. To visualize how the order of regularization affects the response of $\tilde{\mathbf{g}}_d$, a plot of Equation 6.27 is made. This is shown in Figure 6.1. From the figure, the non-bounded nature of $\mathbf{g}_d$ in the unregularized case is apparent. All non-zero orders of n show bounded behavior. In accordance with Rezaei et al., in this thesis, n is taken to be two.

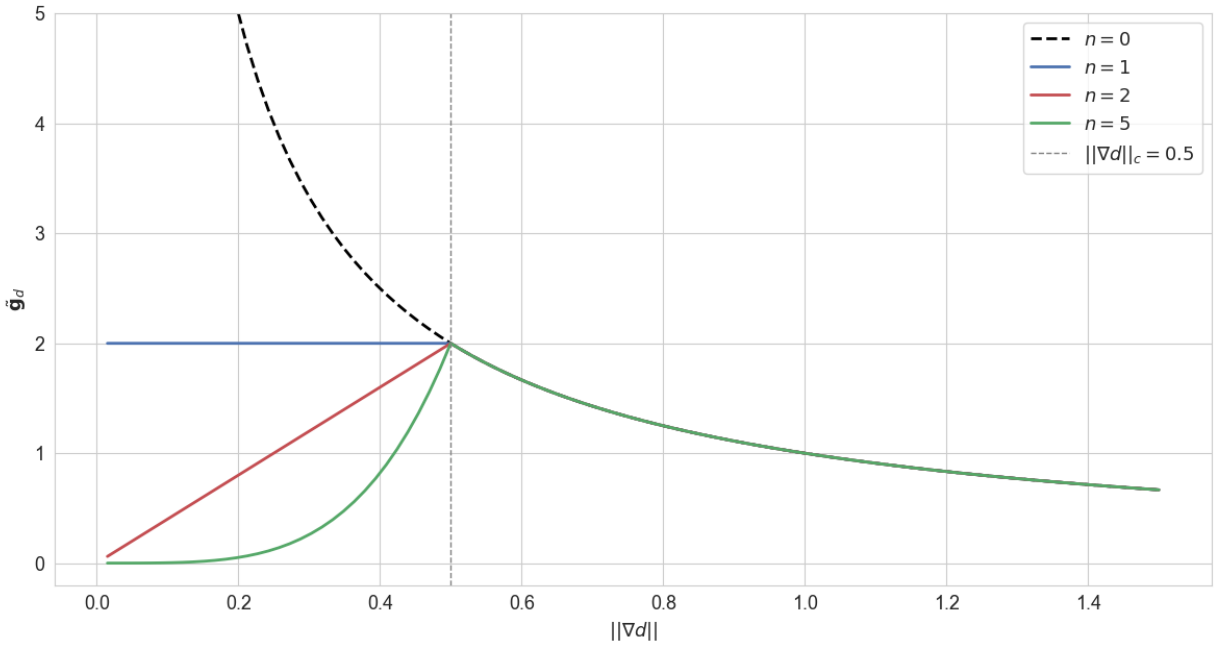

Figure 6.1: Plot of $\mathbf{g}_d^i$ for different values of orders of regularization as based on Equation 6.27.

6.2.5. Convergence Criteria

While opting for a staggered scheme does provide some implementation benefits, it does bring forth a question regarding convergence, namely, *when has an iteration converged?* Identifying an adequate stopping criterion is vital to the accuracy of the solution found. Ambati et al. [1] note that the natural quantity to determine convergence is by analyzing the energy of the system. Denoting the energy functional for a staggered iteration, k by E_k it is expected that for $k \to \infty$, the sequence E_k is decreasing, as with sufficiently many iterations the solution $\{(\mathbf{u}^k, d^k)\}$ will converge to a minimizer $(\mathbf{u}, d)$ of E. Under this premise, it is natural to define a staggered cycle to be converged when the change in energy between subsequent iterations is less than a specified tolerance, i.e.,

$$f(E_k) \leq tol \ . \tag{6.28}$$

where f is the function used to track the difference in energy between consecutive iterations. In the context of this thesis, in line with what is seen in the literature, the staggered iterations were continued until the difference between the phase field values of two consecutive iterations was less than the desired tolerance [88] [23].

6.3. Code Logic

The aspects so far detailed the specifics of the numerical implementation. Algorithm 3 describes the solution scheme to solve the problem.

Algorithm 3 Phase Field Model Solver Scheme

Initialize domain with pre-cracks (if any)
Set crack normal field $\mathbf{m} \leftarrow$ `None` where unknown
while simulation not finished **do**
    for each displacement increment **do**
        for staggered iteration $k = 1 \dots k_{\text{max}}$ **do**
            Solve displacement field $\mathbf{u}$
            if $\mathbf{m} \neq$ `None` **then**
                Compute mode-mixity
            end if
            Compute $\gamma(d, \nabla d)$, $G_c(\mathbf{m}, \chi)$ and $\dfrac{\partial G_c}{\partial(\nabla d)}$
            Solve phase field equation for d
            Determine relevant regions for crack normal update
            Compute crack normals $\mathbf{m}$ in those regions
        end for
    end for
end while

6.4. Additional Modeling Choices

The previous sections discussed the numerical implementation. However, some practical aspects are still to be mentioned. The following list summarizes some critical modeling choices and best practices that should be considered when performing simulations. Most of these aspects are related to the mesh.

- **Element type**: to avoid mesh-dependent anisotropic effects and favoring particular damage orientations artificially, it is recommended to use unstructured triangular linear elements [47], or near structured quadrilateral bilinear elements [59, 153]. It has been noted that other element types generally result in mis-evaluation of the fracture energy [57].
- **Element size and length scale**: to guarantee an accurate estimation of the fracture energy, it is necessary that the element size is much smaller than the length scale. Often, for brittle fracture, numerical simulations have shown that the element size should be at least half of the length scale. In the case of cohesive fracture, even smaller values are suggested, typically around $h \leq l/5$ [57].
- **Nature of mesh**: unless the direction of the crack is known as a priori, the mesh should be uniform, as non-uniformity can introduce artificial inhomogeneities and favor nucleation of cracks in refined zones [57].

Discussion of Results

7: Verification Plan & Isotropic Fracture Results

The proposed model, along with its mathematical formulation and numerical implementation, has been extensively discussed. Building on this foundation, the present chapter establishes the verification methodology. Section 7.1 provides the scope of the verification analysis. In this section, the relevant numerical tests and the rationale behind them are detailed. Thereafter, the results obtained for isotropic, mode-independent fracture are discussed. This is done in the following manner: firstly, the scope of the isotropic analysis is presented in Section 7.2, followed by a discussion of the results from the first numerical test in Section 7.3, and lastly, the numerical results of the second test in Section 7.4.

7.1. Verification Plan

Prior to using a numerical model, it is essential to perform model verification and validation. This is tackled in a sequential manner, where verification is conducted prior to validation. In fact, validation is only of relevance provided the model has been verified. To understand why, the following definitions are introduced for the two processes. Verification aims to ensure that the model is implemented correctly. Whereas, ensuring that the model accurately captures the complexities of the underlying physical phenomenon is assessed by validation. Thus, it is only natural to judge how well the numerical model aligns with reality once it is known that the numerical model is posed correctly.

In the present numerical framework, verification involves extensive testing to ensure the robustness, consistency, and reproducibility of the obtained results. To establish confidence in the implementation, a hierarchical verification strategy is adopted. This begins with unit testing, followed by module testing, and finally verification through analysis of the model response under representative physical conditions. Unit and module testing are carried out implicitly during development to ensure that individual components and their interactions function correctly, and are therefore not discussed in detail here. Instead, the focus is placed on the final stage of verification: assessing whether the model reproduces analytical and/or literature results under the appropriate conditions.

7.1.1. Choice of Experiments

Since the proposed framework incorporates both mixed-mode fracture and anisotropic fracture, it is crucial to verify that the model behaves correctly in the corresponding limit cases. A robust formulation should not only capture the fully coupled problem, but also recover established results when specific dependencies are removed. In other words, the model must reduce to well-known benchmark formulations in the appropriate edge cases.

To verify this, three fundamental conditions are considered:

1. When the dependencies of the fracture energy on both crack propagation direction and mode-mixity are suppressed, the formulation should reduce to mode-independent, isotropic fracture. Mathematically, this is described as
$$G_c(\chi, \nabla d) \rightarrow G_c \ . \tag{7.1}$$
2. When the dependency of the fracture energy on mode-mixity is removed while retaining directional dependence, the formulation should recover existing mode-independent, anisotropic fracture models. In this case the following holds:
$$G_c(\chi, \nabla d) \rightarrow G_c(\nabla d) \ . \tag{7.2}$$
3. When the dependency of the fracture energy on crack propagation direction is suppressed while retaining mode dependence, the formulation should reproduce isotropic mixed-mode fracture behavior. This is described by
$$G_c(\chi, \nabla d) \rightarrow G_c(\chi) \ . \tag{7.3}$$

To test these conditions, three sets of experiments are identified:

- **Mode-independent Isotropic Fracture**
    - Single-Edge Notched Tension (SENT) test.
    - Single-Edge Notched Shear (SENS) test.
- **Mode-independent Anisotropic Fracture**

- SENT test.
- Open Hole Tension (OHT) test.

- **Mixed-Mode Isotropic Fracture**
  - Uniaxial compression test for a specimen with one internal flaw.
  - Uniaxial compression test for a specimen with two internal flaws.

These experiments have known analytical and/or literature results allowing for direct comparison.

7.1.2. Verification Analyses

While the previous subsection identified the conditions that would allow for model verification, in this subsection, the analyses that are performed are elaborated on. To this end, three categories of analyses are noted, namely:

- *Convergence Analysis* - As the model is implemented in a discretized setting, it is expected that solutions approach a mesh- and increment-independent result as the spatial discretization and displacement increments are refined.
- *Sensitivity Analysis* - In some of the experiments considered (particularly concerning the anisotropic fracture cases), the framework depends on numerical parameters. Sensitivity analysis evaluates the influence of these parameters by systematically varying them and assessing the changes in model outputs.
- *Comparative Analysis* - Model predictions are compared against established results from verified models in the literature under equivalent conditions.

7.2. Scope of Mode-independent Isotropic Analysis

In this section, a more focused verification procedure for the model under isotropic, mode-independent conditions is explained. As identified in Section 7.1.1, this analysis considers two benchmark experiments: the SENT test and the SENS test. The analysis focuses on verifying the fundamental behavior of the formulation, including the implementation of tension-compression splitting. As there are no additional model parameters, a sensitivity analysis is not performed.

To verify the numerical results obtained for both experiments, the following analyses are performed:

1. **Comparison of crack paths:** Both experiments are well-established benchmark cases in the literature, making it possible to directly compare the predicted crack trajectories with reference solutions.
2. **Convergence analysis:** To ensure numerical convergence of the solution, the influence of mesh refinement and displacement increment size on the obtained results is investigated.
3. **Analysis of load-displacement results:** While the crack paths provide insight into the qualitative nature of crack propagation, the force-displacement response is also examined to provide quantitative insight.
4. **Effect of the length scale parameter:** Although the phase field length scale parameter is not strictly a numerical parameter, its influence on the solution is also investigated.

7.3. Single-Edge Notched Tension Specimen

The first benchmark problem considered is the SENT test. As previously mentioned, ever since it was introduced by Miehe et al. [65], it has become a popular example to test the numerical implementation. In the following subsections, the loading and boundary conditions, the mesh and numerical details, the observed crack paths, the relevant convergence analysis, and the load-displacement results of this experiment are discussed.

7.3.1. Loading and Boundary Conditions

As the name suggests, for the SENT test, a square specimen with a straight horizontal crack mid-span in length is located at mid-height and is loaded under tension. The geometry and boundary conditions are shown in Figure 7.1. For this numerical example, the geometry and material parameters are specified in Table 7.1.

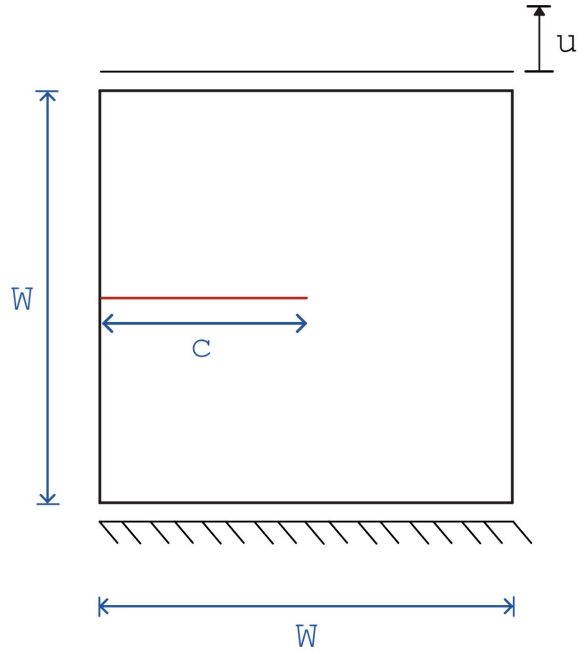

Figure 7.1: Specimen geometry, loading and boundary conditions used for the single-edge notched tension (SENT) test.

Table 7.1: Material and geometric parameters used for the single-edge notched tension (SENT) test.

Material Property	Value	Units
Young's modulus	210	GPa
Poisson's ratio	0.3	–
Fracture energy	$2.7 \cdot 10^{-3}$	kN/mm
Geometry Parameter	**Value**	**Units**
Specimen width, W	1.0	mm
Initial crack length, c	0.5	mm

7.3.2. Mesh and Numerical Details

The mesh was generated using Gmsh [154]. The geometry was discretized into 42450 quadrilateral elements that were meshed using the Frontal-Delaunay algorithm. It should be noted that this algorithm does not guarantee a structured mesh. During the convergence analysis, the number of elements in the mesh is varied, but in all cases, the same meshing algorithm is used. By using 42450 elements, the element size is approximately $1 \cdot 10^{-3}$ mm, allowing for a length scale of $4 \cdot 10^{-3}$ mm. Furthermore, similar to Ambati et al. [1], the displacement control is done with increments of $3.2 \cdot 10^{-6}$ mm.

Another point of relevance is the method by which the pre-crack is introduced. In general, there are two classes of methods for specifying the pre-crack in the specimen, namely:

- Through the mesh - leaving the nodes that form the pre-crack disconnected from the top and bottom:
  - **Option A**: an infinitely thin, geometrically sharp crack (see Figure 7.2a),
  - **Option B**: a one-element-wide crack depending on the discretization (see Figure 7.2b).
- Through the damage field - specifying the damage value on the nodes that form the pre-crack:
  - **Option C**: an infinitely thin crack by prescribing a damage value of unity at the crack nodes (see Figure 7.2c),
  - **Option D**: a one-element-wide crack by prescribing full damage and subsequently regularizing the sharp profile into a smeared crack (see Figure 7.2d).

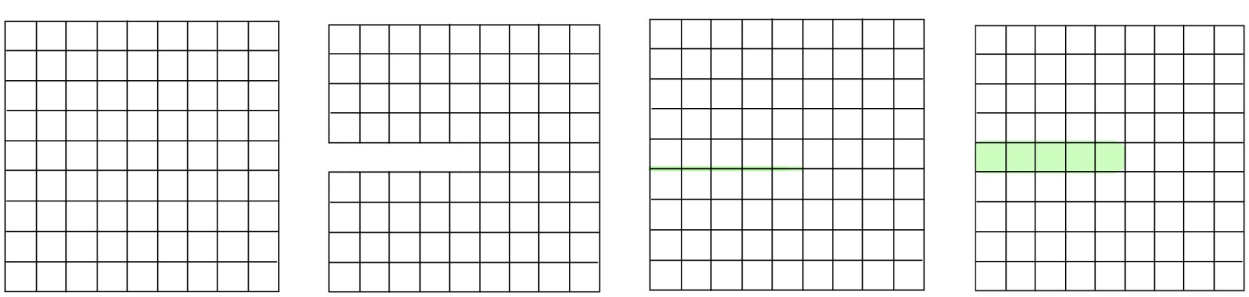

(a) Option A (sharp crack through the mesh)

(b) Option B (One-element wide crack through the mesh)

(c) Option C (sharp crack through the damage field)

(d) Option D (One-element wide crack through the damage field)

Figure 7.2: Different methods of introducing a pre-crack.

Both methods are valid approaches to instantiate the pre-crack. This is because, even if a non-zero damage field is instantiated, the staggered iterations will converge to find the displacement field that is consistent with the degraded stiffness in the cracked region. Similarly, if the pre-crack is instantiated through the mesh due to the discontinuity, the field equation will determine the damaged region. However, regardless of the method employed, Loiseau and Lazarus [155] note that it is important that the initial crack is one element wide. This is necessary to avoid introducing an artificial excess of energy to transition from the sharp crack representation to the smeared crack description. In other words, only the second and fourth options from Figure 7.2 are valid, and for this numerical test, the fourth option is used.

N.B. The same mesh is used for the SENS test, and hence the particularities of the mesh are not discussed in that section.

7.3.3. Model Results and Comparison

To compare the model results against the literature, both the crack paths and the global response are analyzed. In all cases, the reference solution is obtained from Ambati et al. [1].

Crack Paths

Firstly, a comparative analysis of the model results with reference results from the literature is done. For a consistent comparison, similar material properties, geometry, mesh, and solver details are used. The first part of the comparative analysis is to identify whether both models predict the same crack path. Thereafter, the load-displacement curves are compared. The crack paths of both the reference and model solution are shown in Figure 7.3.

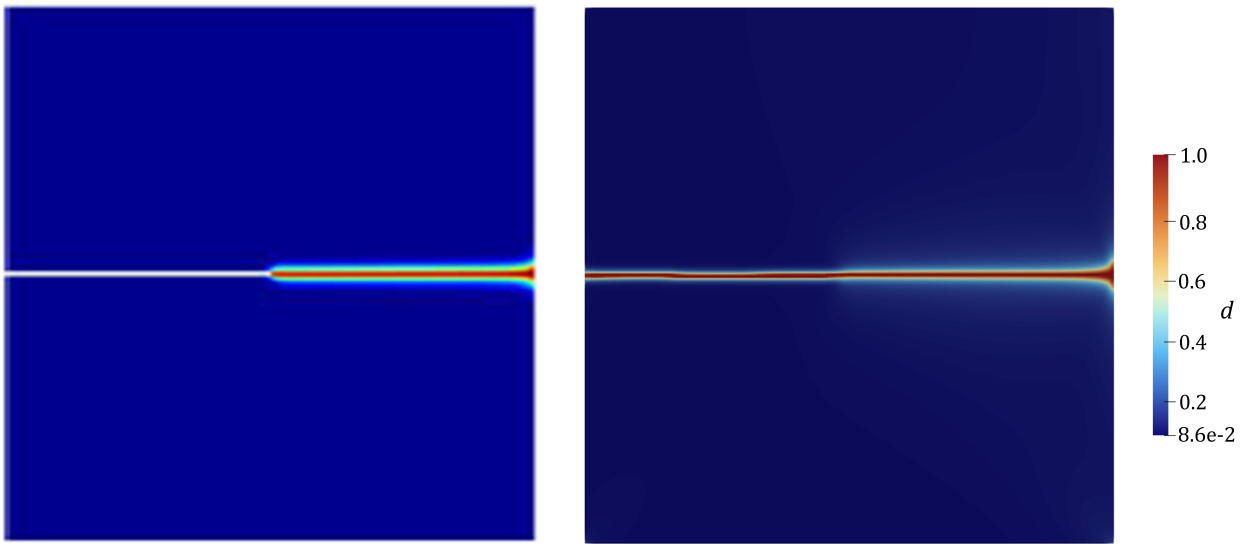

(a) Reference solution

(b) Proposed model solution

Figure 7.3: Comparison between the crack paths of the reference and proposed model solutions for the single-edge notched tension (SENT) test.

Comparing both figures, it is evident that the crack paths exhibited by the implemented model and the literature are identical up to the chosen mesh. This behavior is also in line with what is expected intuitively; when pulling on a specimen with a horizontal pre-crack, the specimen will crack into two along the direction of the pre-crack. What is worth noting is the behavior exhibited by both models as the crack approaches the right boundary. The right boundary does not have a prescribed traction, and hence, the natural boundary condition will materialize. This states

$$\nabla d \cdot \mathbf{n} = 0 \, . \tag{7.4}$$

In other words, the natural boundary condition prescribes that the damage gradient should be orthogonal to the normal. Thus, the crack should end aligned with the outward normal, because the crack propagation direction is perpendicular to the damage gradient. However, in the figures, it appears as though a small distance away from the boundary, the crack exhibits slight curvature. This is attributed to being a numerical artifact, as upon decreasing the mesh size and displacement increment, this effect decreases.

Convergence Analysis and Load-displacement Results

In this case, the crack paths are relatively intuitive. Since all simulations predict similar crack trajectories, a purely qualitative comparison is insufficient for assessing convergence behavior. In fact, doing so would only showcase the diffuse nature of the crack as the length scale increases. Therefore, the analysis is based on the corresponding load-displacement curves. To investigate the influence of discretization, two mesh sizes and three displacement increment sizes are considered. The resulting six simulation cases are summarized in Table 7.2.

Table 7.2: Test case identifiers and their respective element size and displacement increment used for the convergence analysis of the single-edge notched tension (SENT) test.

Test case	Element size [mm]	Displacement increment [mm]
TE1-D1	0.002	$3.2 \cdot 10^{-6}$
TE2-D1	0.001	$3.2 \cdot 10^{-6}$
TE1-D2	0.002	$4.6 \cdot 10^{-6}$
TE2-D2	0.001	$4.6 \cdot 10^{-6}$
TE1-D3	0.002	$6.4 \cdot 10^{-6}$
TE2-D3	0.001	$6.4 \cdot 10^{-6}$

The force-displacement curves obtained for each case, as well as from the reference solution, are plotted in Figure 7.4.

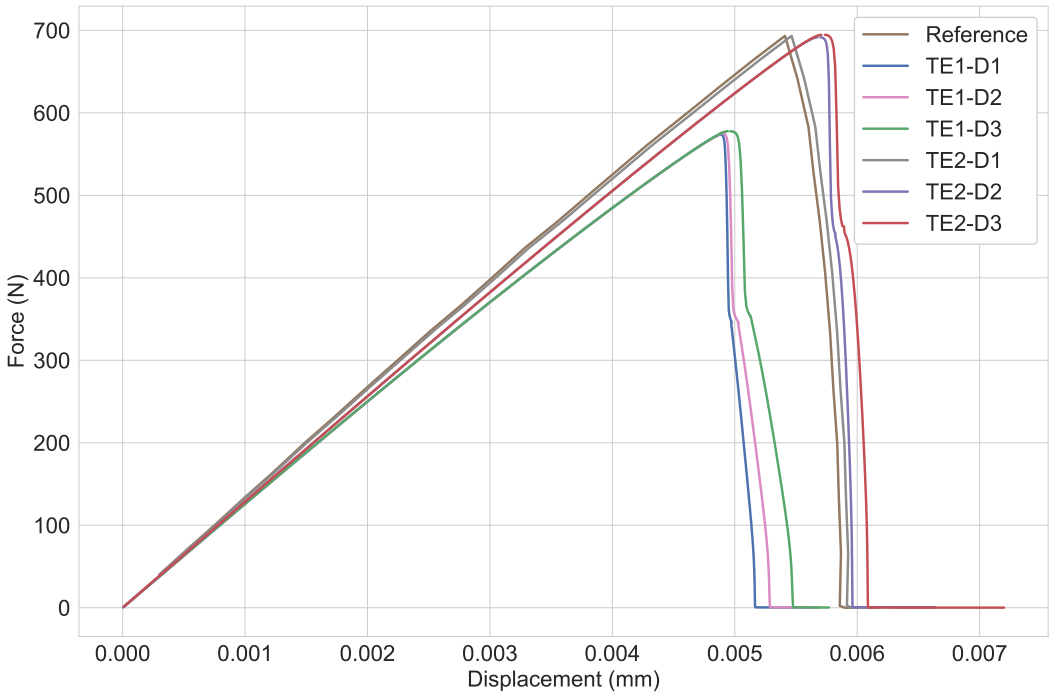

Figure 7.4: Comparison of the load-displacement results from the convergence analysis and reference solution for the single-edge notched tension (SENT) test.

From the force-displacement graphs, it is apparent that as the mesh becomes finer and the displacement increment decreases, the results converge to the reference solution. This is considering TE2-D1 (the finest mesh with the smallest displacement increment) is most similar to the reference solution. Furthermore, from the results, it is evident that the mesh size and displacement increment used affect the results obtained (although this is difficult to visualize from the crack paths alone). It appears that using a coarse mesh results in a lower peak load and failure displacement. This is expected, as for this study, the length scale was taken proportional to the element size. In Section 3.2.5, it was shown that the length scale is inversely proportional to the critical stress. Hence, increasing the length scale should result in lower peak loads.

From the figure, the effect of the displacement increment is also observed. For sufficiently small displacement increments, the post-peak behavior follows a smooth curve with a very steep slope. For larger displacement

increments, the initial behavior follows a steep slope; however, after a certain point, the response becomes more curved. This can be explained as follows: if the displacement increment is too high, the intermediate equilibrium states are missed, and so the model appears to retain some artificial stiffness.

Effect of Length Scale

Prior to concluding the verification analysis for this test, the effect of the length scale is considered. In Section 3.2.5, it was noted that the length scale is related to the failure stress of the material and hence is not purely a numerical parameter. Regardless, for purposes of verification and to illustrate the nature of this parameter, the crack paths under two different length scales are compared. This is shown in Figure 7.5.

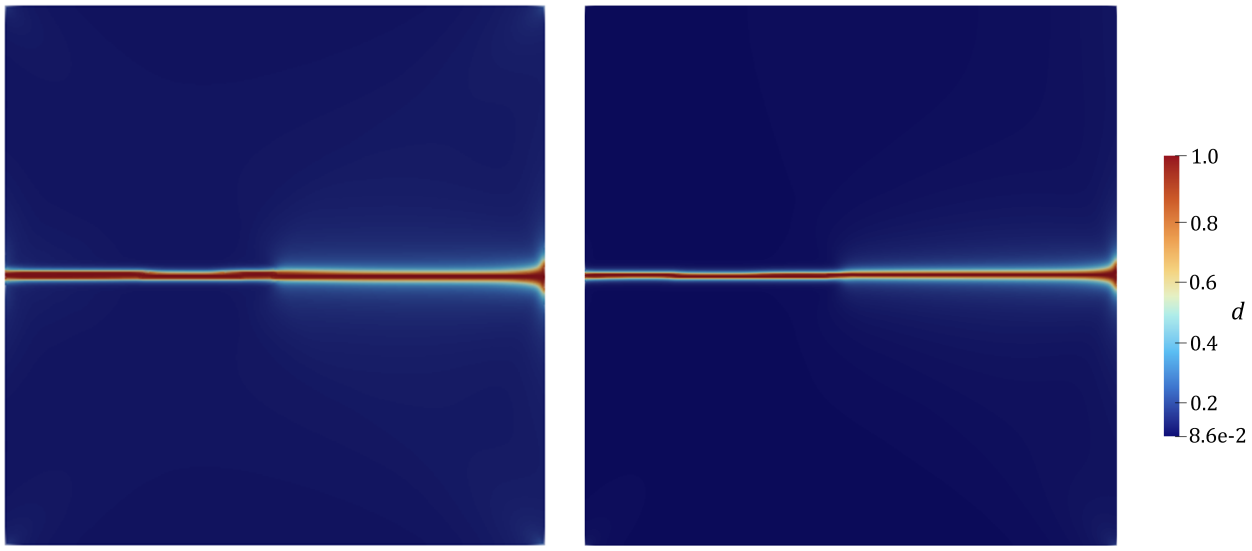

(a) $l = 6 \cdot 10^{-3}$ mm **(b)** $l = 4 \cdot 10^{-3}$ mm

Figure 7.5: Comparison of observed crack paths for single-edge notched tension (SENT) test under two length scales.

From this figure, it is observed that variations in the length scale in this experiment do not affect the crack path, as the same propagation behavior is observed for both cases. However, the length scale does influence the crack profile; larger length scales produce a more diffuse crack and a wider damage zone, whereas smaller length scales result in sharper localization. The numerical artifact at the right boundary is also more apparent at higher length scales.

7.4. Single-Edge Notched Shear Specimen

The second benchmark problem considered is the SENS test. This has also become a popular example to test the numerical implementation. In particular, this test provides insight into the nature of how the model handles tension-compression splitting. In the following subsections, the loading and boundary conditions, the mesh and numerical details, the observed crack paths, the relevant convergence analysis, and the load-displacement results of this experiment are discussed.

7.4.1. Loading and Boundary Conditions

As the name suggests, for the SENS test, a square specimen with a straight horizontal crack mid-span in length is located at mid-height and is loaded in shear. The geometry and boundary conditions are shown in Figure 7.6. For this numerical example, the geometry and material parameters are specified in Table 7.3.

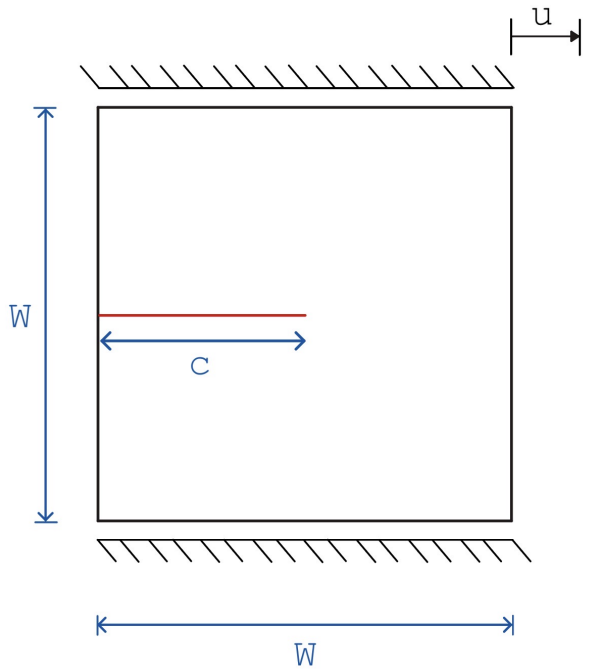

Figure 7.6: Specimen geometry, loading and boundary conditions used for the single-edge notched shear (SENS) test.

Table 7.3: Material and geometric parameters used for the single-edge notched shear (SENS) test.

Material Property	Value	Units
Young's modulus	210	GPa
Poisson's ratio	0.3	–
Fracture energy	$2.7 \cdot 10^{-3}$	kN/mm
Geometry Parameter	**Value**	**Units**
Specimen width, W	1.0	mm
Initial crack length, c	0.5	mm

7.4.2. Model Results and Comparison

Similar to before, to compare the model results against the literature, both the crack paths and the global response are analyzed. In all cases, the reference solution is taken from Ambati et al. [1].

Crack Path

The crack paths obtained are compared to reference results from the literature. These are visualized in Figure 7.7.

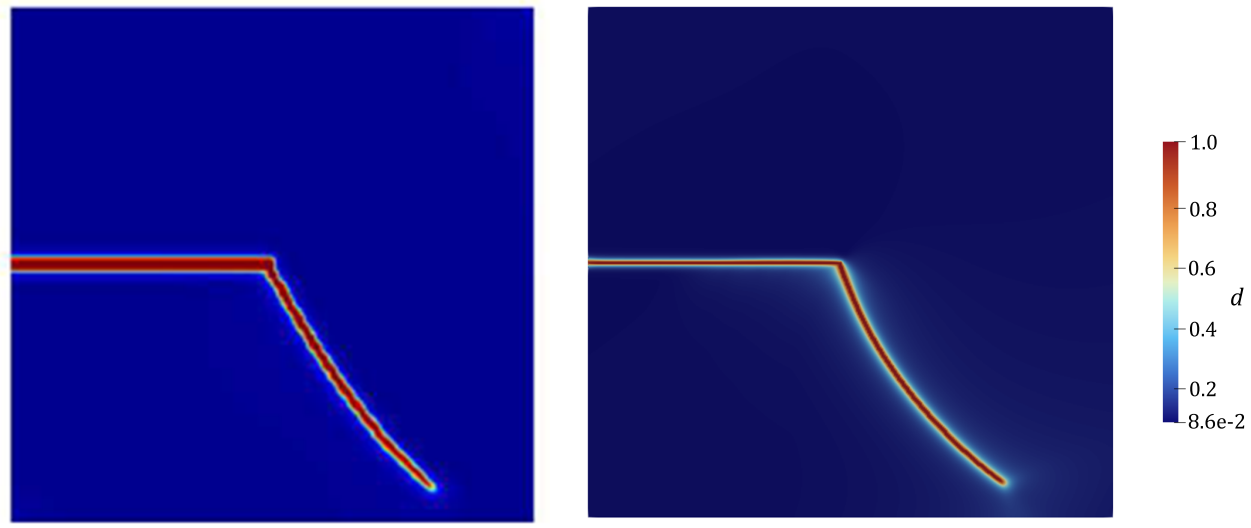

(a) Reference solution (Ambati et al. [1])

(b) Proposed model solution

Figure 7.7: Comparison between the crack paths of the reference and proposed model solutions for the single-edge notched shear (SENS) test.

To analyze the crack paths observed three points are of relevance. Firstly, it is noted that the reference and observed crack path solutions are largely identical. Both exhibit a curved crack path that moves towards the bottom-right boundary. To analyze these paths further, it is worth investigating the initial kink angle of the crack. From LEFM, it is known that under pure Mode II loading, the crack will not propagate in a straight path. Rather, the crack path that is followed satisfies the maximum tangential stress criterion. This criterion predicts

that "the crack will start to grow from its tip perpendicular to the direction along which the tangential stress is the maximum and the shear stress is zero." [156]. In such a case, it can be shown that the direction of crack propagation is as follows [156]:

$$\bar{\theta} = 2\tan^{-1}\left(\frac{1}{4}\left(\frac{K_I}{K_{II}} \pm \sqrt{\left(\frac{K_I}{K_{II}}\right)^2 + 8}\right)\right), \tag{7.5}$$

where $\bar{\theta}$ is the crack propagation angle, K_I is Mode I stress intensity factor and K_{II} is the Mode II stress intensity factor.

From this equation, it can be determined that under pure Mode II loading, the crack is expected to kink at 70.5°. From Figure 7.9 it is found that the initial kink angle of the observed crack path is 70.1°. Since the analytical solution in Equation 7.5 is derived for an infinite medium, while the numerical example is performed on a finite specimen, a deviation of less than 1% from the predicted angle is considered acceptable.

Lastly, as previously mentioned, this test serves as a verification point for the implementation of tension-compression splitting. In the case where tension-compression splitting is not considered, the crack will have two branches. The upper branch corresponds to crack propagation under compression, and the lower due to tension (see Figure 7.8). In other words, the upper branch is physically inadmissible. As a result, in a model in which tension-compression splitting is correctly taken into account, only the lower branch is observed.

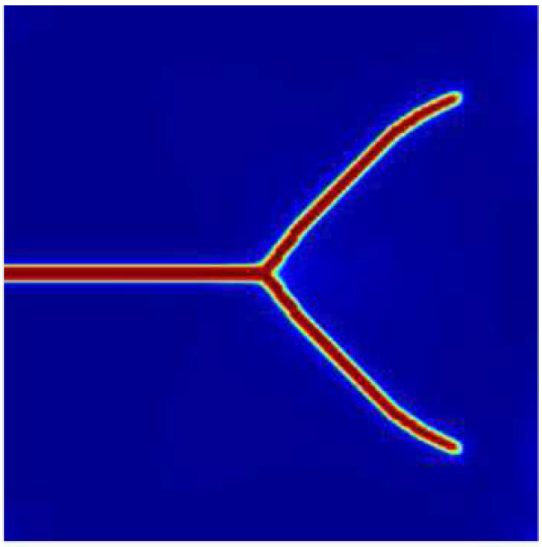

Figure 7.8: Crack path for the single-edge notched shear (SENS) test under no tension-compression splitting [1].

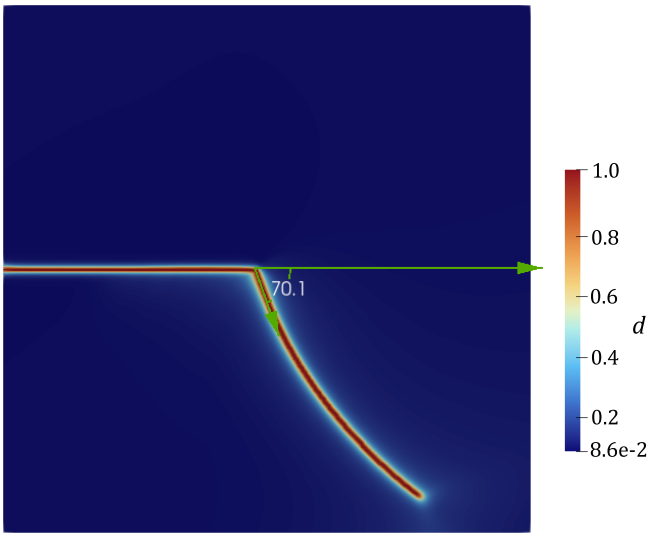

Figure 7.9: Kink angle observed in proposed model for the single-edge notched shear (SENS) test.

Convergence Analysis and Load-displacement Results

Similar to the SENT test, to perform the convergence analysis, two mesh sizes and three displacement increments are considered. These are the same as those used previously. As the crack paths remain the same for all cases, to aid the discussion, the load-displacement curves are used. For ease of reading, the cases are reiterated in Table 7.4.

Table 7.4: Test case identifiers and their respective element size and displacement increment used for the convergence analysis of the single-edge notched shear (SENS) test.

Test case	Element size [mm]	Displacement increment [mm]
TE1-D1	0.002	$3.2 \cdot 10^{-6}$
TE2-D1	0.001	$3.2 \cdot 10^{-6}$
TE1-D2	0.002	$4.6 \cdot 10^{-6}$
TE2-D2	0.001	$4.6 \cdot 10^{-6}$
TE1-D3	0.002	$6.4 \cdot 10^{-6}$
TE2-D3	0.001	$6.4 \cdot 10^{-6}$

The force-displacement curves obtained for each case, as well as from the reference solution, are plotted in Figure 7.10.

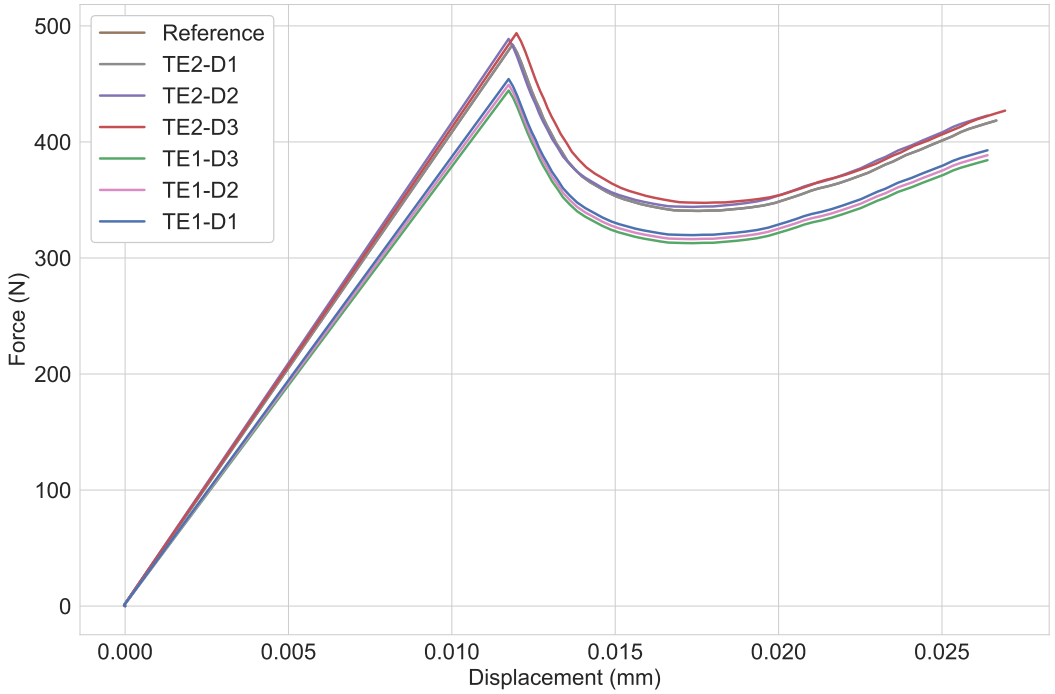

Figure 7.10: Comparison of the load-displacement results from the convergence analysis and reference solution for the single-edge notched shear (SENS) test.

Similar to the previous numerical example, as the mesh becomes finer and the displacement increment decreases, the results converge to the reference solution. This is evident as TE2-D1 (the finest mesh with the smallest displacement increment) is most similar to the reference solution. The results of this analysis also align with the notion that increasing the length scale decreases the peak load, as the TE1- tests consistently have a lower peak load compared to the TE2- tests. It is interesting to note how neither the reference nor the model results return to a zero load condition. This is a consequence of using the spectral decomposition of strain to account for tension-compression splitting. It appears that under this modeling choice, the crack propagates into the lower-right boundary and reaches a stage where no further propagation is possible; as a result, it does not completely fail.

Effect of Length Scale

Lastly, for completeness, the effect of the length scale on the SENS test is revisited.

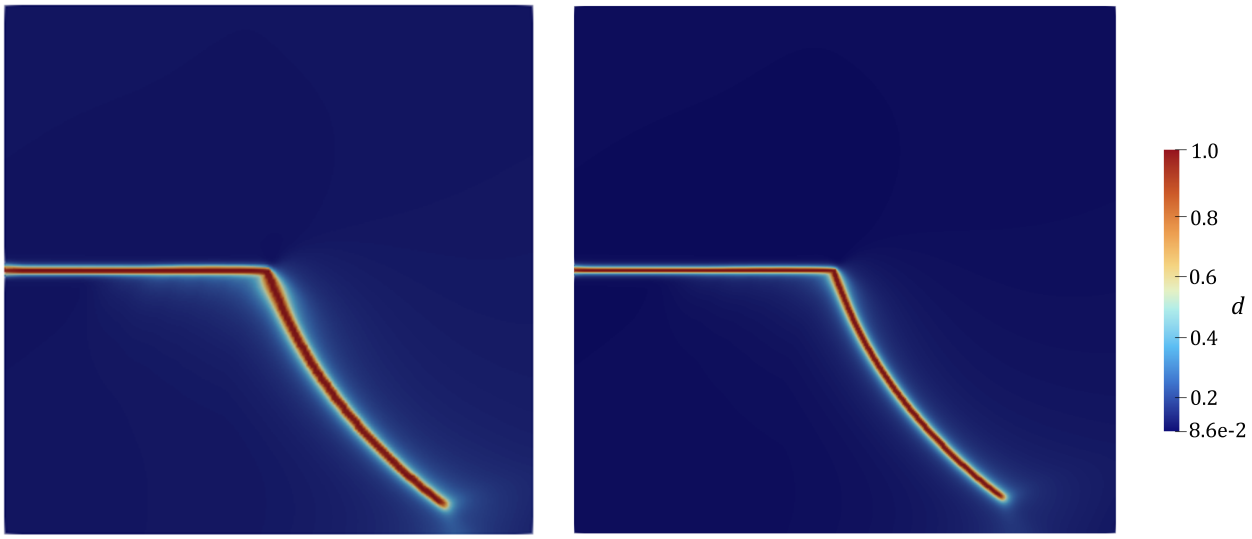

(a) $l = 6 \cdot 10^{-3}$ mm **(b)** $l = 4 \cdot 10^{-3}$ mm

Figure 7.11: Comparison of observed crack paths for single-edge notched shear (SENS) test under two length scales.

From this figure, it is observed that variations in the length scale do not affect the crack path, with the same propagation behavior across both cases. However, the length scale strongly influences the crack profile: larger length scales produce a more diffuse crack and a wider damage zone, whereas smaller length scales result in sharper localization. This is in accordance to what was observed in Figure 7.5.

8: Verification Under Anisotropic, Mode-Independent Conditions

In this chapter, the results of verification pertaining to mode-independent anisotropic fracture are discussed. Firstly, the scope of the analysis is identified in Section 8.1. This is followed by a discussion on the first numerical example, namely the SENT test, in Section 8.2. Thereafter, the second numerical example, namely the OHT test, is examined in Section 8.3.

8.1. Scope of Anisotropic Analysis

The verification of the implementation of anisotropy requires a more involved analysis compared to the isotropic case. This is partly due to the increased model complexity arising from the need for a direction-dependent fracture energy, but also due to the need for a comparative assessment between different model formulations. In particular, this chapter examines the differences between the classical and consistent formulations, where applicable. It also provides an opportunity to assess the model's capability to represent spatially non-homogeneous fiber orientations, as observed in VSCL. The following subsections outline the analyses performed, along with the numerical experiments used to support the findings.

8.1.1. Aspects to Consider

For the experiments discussed in this chapter, two types of verification analyses are considered. The first of which is a convergence analysis related to the discretization of the numerical approach. The second is a parametric and comparative analysis aiming to provide insight into the effect of modeling choices.

Convergence Analysis

As the implementation is still a discrete representation of a continuous problem, the effect of the mesh and the displacement increments on the solution is investigated. As a result, similar to before, two types of convergence analyses are performed, namely the effect of the mesh size and the effect of the displacement increment are assessed. In Chapter 7, the effect of the length scale was considered; however, in this chapter, it is taken to be a constant.

Parametric and Comparative Analysis

Unlike the isotropic case, three additional analyses are performed related to the implementation of anisotropic fracture:

- *Effect of the anisotropic fracture energy parameter,* α: in Chapter 5, it was identified that this parameter governs the degree of anisotropy in the fracture energy and as a result determines the expected crack propagation angle. Varying α will allow to understand whether the model results align with the expected, analytical angles.
- *Comparison between using a classical and consistent formulation*: in Chapter 5, a detailed analytical discussion between both formulations was presented. In a correctly implemented numerical model, it is expected that the same trends should be visible.
- *Allow for having spatially varying fiber orientations*: it is expected that the model will be capable of handling non-uniform material orientations. By prescribing spatially varying fiber directions, it can be verified whether the crack path adapts accordingly and remains aligned with the locally preferred fracture directions.

Comment on terminology

Throughout this chapter the terms *fiber direction* and *preferential direction* are used interchangeably.

8.1.2. Chosen Experiments and Rationale

To investigate the aspects mentioned above, two numerical experiments are considered. These are elaborated below:

1. *SENT*: this test is a well-controlled benchmark for studying anisotropic crack propagation. As the notch is predefined, the location of crack initiation is given, and thus, the focus is to investigate crack propagation behavior. The directional dependence of the fracture energy should be reflected in the crack path.

2. *OHT test*: this test has a more complex stress field due to the presence of the hole, which introduces stress concentrations. Unlike the previous test, there is no predefined crack, but rather it naturally emerges based on the interactions of the local stresses and the direction-dependent fracture energy. Due to the nontrivial nature of this test, it is also particularly suitable for verifying if the model can be applied to materials with spatially varying fiber directions.

8.2. Single-Edge Notched Tension Specimen

The first experiment considered to investigate anisotropic fracture propagation is the SENT test. While the test has been analyzed in an isotropic fracture scenario, it is revisited in the presence of a direction-dependent fracture energy. To investigate this numerical example, firstly, the loading and boundary conditions are considered. Thereafter, the expected propagation angles, the crack paths, and the convergence analysis are discussed. Lastly, a special case of when the fiber orientation is 90° is analyzed.

8.2.1. Loading and Boundary Conditions

Similar to the SENT test under isotropic conditions, in this test, a specimen with a pre-crack of mid-span length at mid-height is loaded under tension. However, in this case, a rectangular specimen is used rather than a square. This decision stems from a practical point, that if fiber orientations greater than 45° are imposed, then the full crack path would not be visible in a square specimen. Furthermore, the geometry and boundary conditions are shown in Figure 8.1. For this numerical example, the geometry and material parameters are specified in Table 8.1.

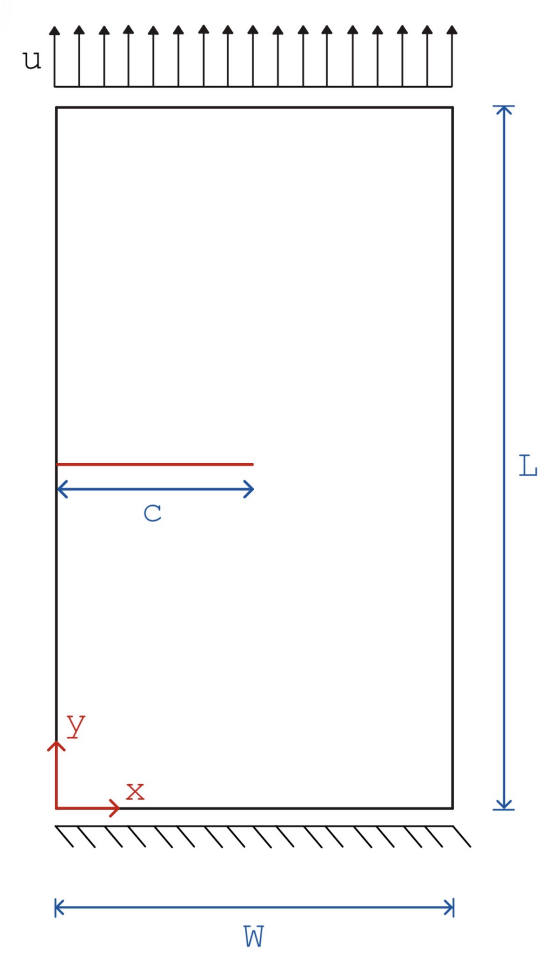

Figure 8.1: Specimen geometry, loading and boundary conditions used for the single-edge notched tension (SENT) test.

Table 8.1: Material and geometric parameters used for the single-edge notched tension (SENT) test.

Material Property	Value	Units
Young's modulus	210	GPa
ν	0.3	–
Reference fracture energy	0.27	N/mm
Geometry Parameter	**Value**	**Units**
Specimen width, W	1	mm
Specimen length, L	2	mm
Initial crack length, c	0.5	mm

Furthermore, for the direction-dependent fracture energy, three preferential directions, namely, 30°, 45°, and 60°, and two anisotropic fracture energy parameters ($\alpha = 10,$ and 100) are compared.

8.2.2. Expected Propagation Angles

Prior to presenting the model results, the expected propagation angles are given. In Chapter 5, it was discussed that the Frank plot can be used to determine the expected crack propagation angles. Although the method was discussed in that chapter, the main idea is reiterated for convenience. That is, the expected crack angle is defined as the point at which a vertical line moving from left to right tangentially coincides with the Frank plot [22, 152]. Based on this graphical method, the expected propagation angles for three fiber orientations (30°, 45°, and 60°) and two α parameters (10 and 100) are visualized in Figure 8.2.

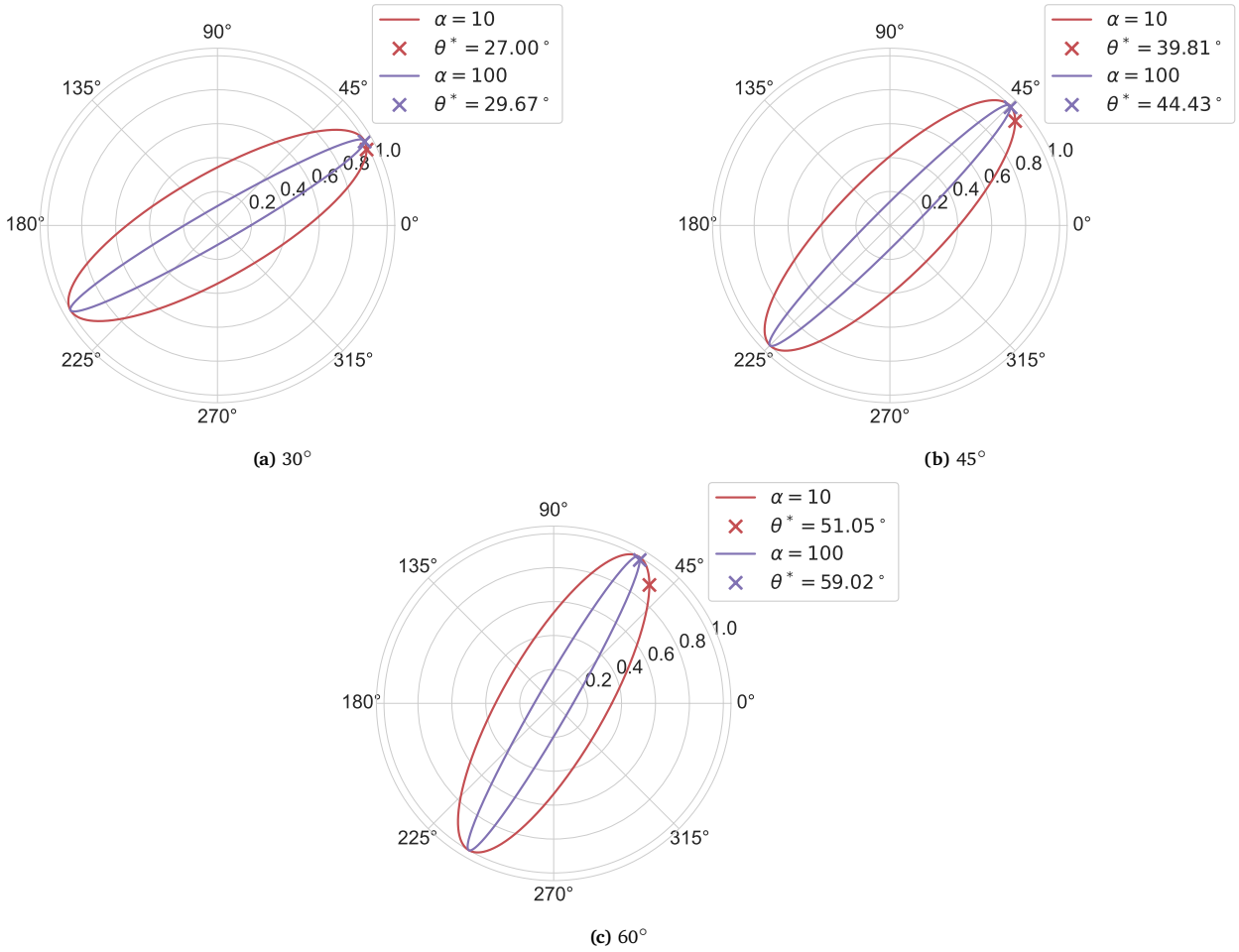

(a) 30° **(b)** 45° **(c)** 60°

Figure 8.2: Expected crack propagation angles for different fiber orientations and anisotropic fracture energy parameters.

These results are summarized in Table 8.2.

Table 8.2: Expected crack propagation angles for different fiber orientations and anisotropic fracture energy parameters.

α	Fiber orientation (°)		
	30	45	60
10	27.00	39.81	51.05
100	29.67	44.43	59.02

As expected, in all cases, as α increases, the expected crack propagation angle approaches the preferential orientation.

8.2.3. Mesh and Numerical Details

Similar to before, the mesh was generated using Gmsh [154]. The geometry was discretized into 65780 quadrilateral elements that were meshed using the Frontal-Delaunay algorithm. By using 65780 elements, the element size is approximately $3.5 \cdot 10^{-3}$ mm, allowing for a length scale of $7 \cdot 10^{-3}$ mm. In addition, equivalent to Chapter 7, the pre-crack is initialized in the form of a one-element wide damage region. Furthermore, the displacement control is done with increments of $3.2 \cdot 10^{-3}$ mm.

8.2.4. Crack Paths and Verification

The crack paths obtained for the three relevant fiber orientations using both the classical and consistent formulation are visualized in Figure 8.3, Figure 8.4, and Figure 8.5 for fiber orientations of 30°, 45°, and 60°, respectively. In all cases, the relevant discussion points are presented directly below the figure. The first case is when the fiber orientation is 30°.

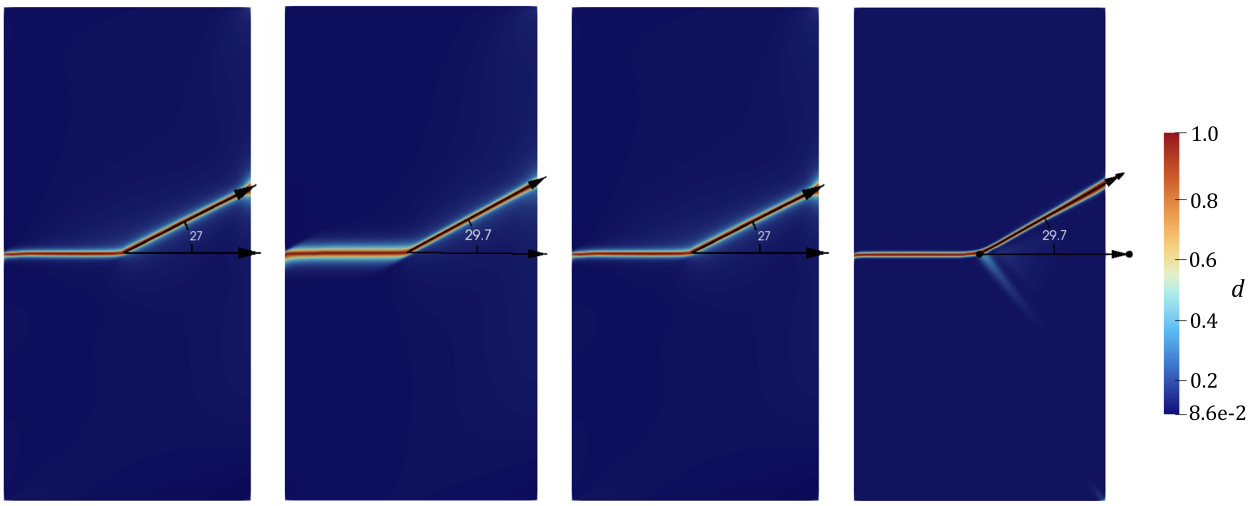

(a) Classical, $\alpha = 10$ **(b)** Classical, $\alpha = 100$ **(c)** Consistent, $\alpha = 10$ **(d)** Consistent, $\alpha = 100$

Figure 8.3: Crack paths observed using the classical and consistent formulation for fiber orientation of 30°.

From these figures, the following points are to be noticed:

- Both for the classical and the consistent formulation, the crack paths observed align with the expected crack propagation angles. This is expected because the energetics for both formulations dictate that the expected crack propagation angles should be the same.
- When comparing Figure 8.3a and Figure 8.3b, the effect of the direction-dependent length scale is apparent. Increasing the anisotropic fracture energy parameter causes the crack path to be more aligned with the preferential orientation. However, it also makes the crack more diffuse in directions not aligned with the preferential direction, see the horizontal crack segment for reference. This may appear to be a purely visual artifact, but that is not the case. In more complex conditions, introducing damage in regions where no physical damage should exist may lead to the nucleation of artificial cracks driven purely by numerical effects rather than by an underlying physical mechanism.
- Unlike the classical formulation, comparing Figure 8.3c and Figure 8.3d, the crack does not appear to become more diffuse due to increasing the anisotropic fracture energy parameter.
- In Chapter 5, it was identified that the boundary conditions for both formulations are not identical. For both formulations, one solution is that the crack path aligns with the expected crack propagation direction. However, for the consistent formulation, this solution is not unique. The crack can utilize a different boundary condition, either aligned with the preferential direction, perpendicular to the preferential orientation, or perpendicular to the normal vector of the boundary. Yet, it appears that for this numerical test, in all cases, the crack path ends aligned with the expected crack propagation orientation.

Next, the case of 45° is considered in the figures below.

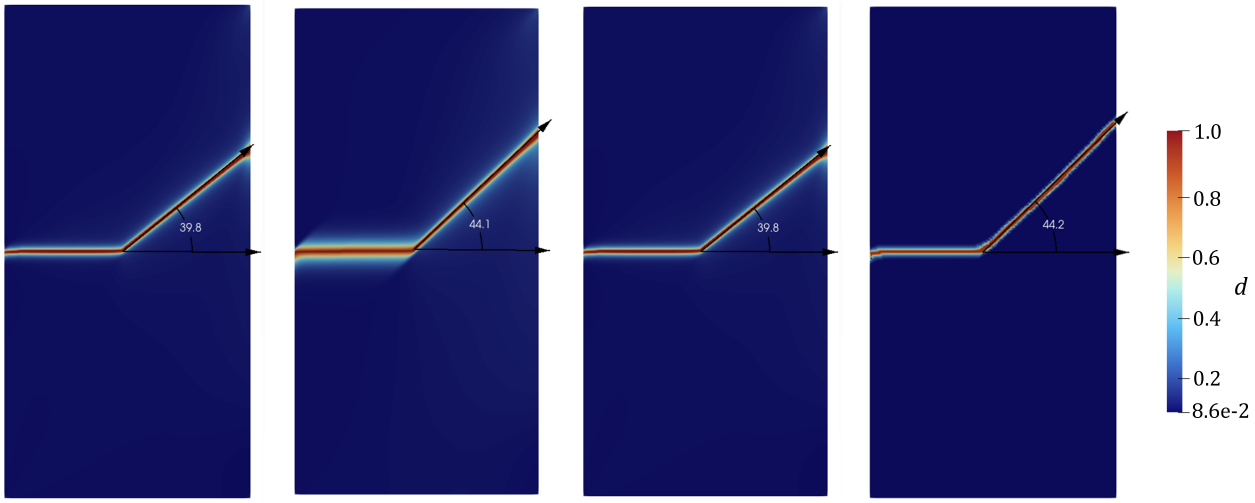

(a) Classical, $\alpha = 10$ **(b)** Classical, $\alpha = 100$ **(c)** Consistent, $\alpha = 10$ **(d)** Consistent, $\alpha = 100$

Figure 8.4: Crack paths observed using the classical and consistent formulation for fiber orientation of 45°.

From these figures, the following points are to be noticed:

- For both the classical and the consistent formulation, the crack paths observed align with the expected crack propagation angle when the anisotropic fracture energy parameter is 10.
- When the anisotropic fracture energy parameter is 100, the observed crack paths for neither formulation directly coincide with the expected crack propagation angle. The consistent formulation appears to have a slight improvement (0.1°); however, it can be argued that the difference is too small to be meaningful. In the present case, the angle measurement was performed using the angle tool in ParaView, where the angle is defined based on three manually selected points. As a result, the measured value is subject to a degree of human judgment. Furthermore, the deviation between the predicted and expected crack propagation angles is less than 1%, indicating that the differences are marginal.
- Similar to before, when comparing Figure 8.4a and Figure 8.4b, it appears the effect of the direction-dependent length scale is apparent. While increasing the anisotropic fracture energy parameter causes the crack path to be more aligned with the fiber orientation, it also makes the crack more diffuse.
- Unlike the classical formulation, comparing Figure 8.4c and Figure 8.4d, the crack does not appear to become more diffuse due to increasing the anisotropic fracture energy parameter.
- With regards to the boundary conditions, similar to when the fiber orientation was 30°, it appears that in all cases the crack path ends aligned with the expected crack propagation orientation.

Lastly, the case where the fiber orientation is $60°$ is analyzed.

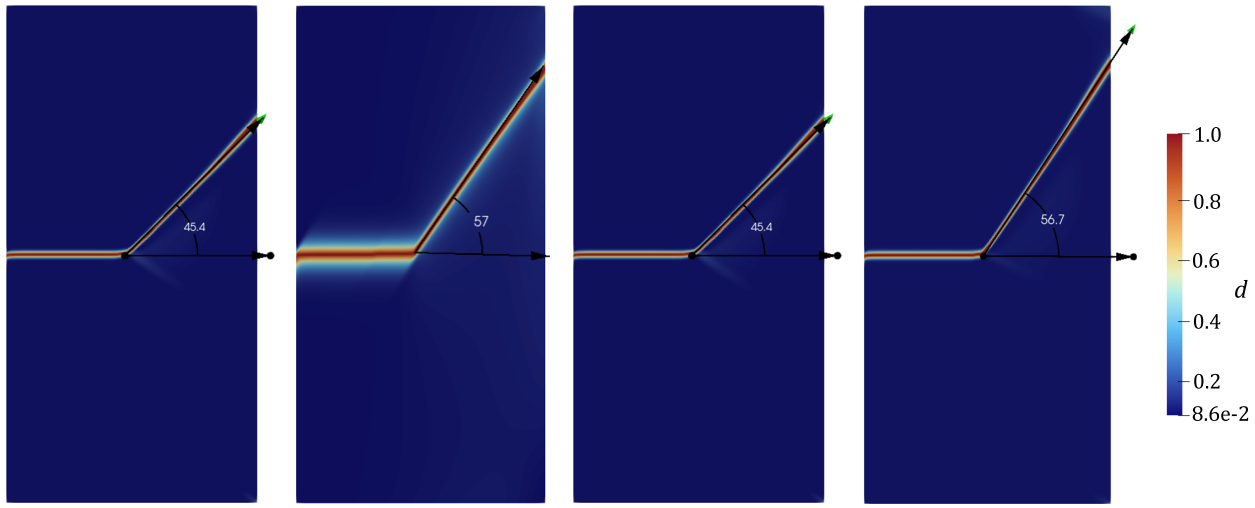

(a) Classical, $\alpha = 10$ **(b)** Classical, $\alpha = 100$ **(c)** Consistent, $\alpha = 10$ **(d)** Consistent, $\alpha = 100$

Figure 8.5: Crack paths observed using the classical and consistent formulation for fiber orientation of 60°.

From these figures, the following points are to be noticed:

- Unlike the previous cases, the crack paths from the classical and the consistent formulation do not exactly align with the expected crack propagation angle for both anisotropic fracture energy parameters.
- When the anisotropic fracture energy parameter is 10, although the observed crack paths do not coincide with the expected angles, both formulations observe the same crack path. In this case, the percentage error between the observed and expected is approximately 10%, significantly higher than the errors observed in Figure 8.3 and Figure 8.4.
- When the anisotropic fracture energy parameter is 100, the observed crack paths for both formulations neither directly coincide with the expected crack propagation angle nor themselves. In this case, the classical formulation shows marginal improvement (0.3°). However, given the previously discussed limitations, the significance of this difference is debatable. Furthermore, the percentage error between observed and expected results is approximately 3% (thus smaller than the error obtained for $\alpha = 10$).
- Similar to before, when comparing Figure 8.5a and Figure 8.5b, it appears the effect of the direction-dependent length scale is apparent. Furthermore, in comparison to the other two fiber orientation cases, the direction-dependent length scale effect is more evident.
- Unlike the classical formulation, comparing Figure 8.5c and Figure 8.5d, the crack does not appear to become more diffuse due to increasing the anisotropic fracture energy parameter.
- With regards to the boundary conditions, similar to previous cases, it appears that the crack path ends aligned with the expected crack propagation orientation.

8.2.5. Convergence and Parameter Analysis

To investigate the dependency of the numerical results on the mesh discretization and the displacement increment, a convergence analysis is performed. Similar to the isotropic case, three different displacement increments and two mesh refinements are considered. The coarse mesh has an element size of $5 \cdot 10^{-3}$ mm, whereas the fine mesh has an element size of $3.5 \cdot 10^{-3}$. Furthermore, to understand the influence of the displacement increment, three cases are considered, namely when the displacement increments are $3.2 \cdot 10^{-3}, 6.4 \cdot 10^{-3}$ and $12.8 \cdot 10^{-3}$ mm.

For three fiber orientations, two anisotropic fracture energy parameters, three displacement increments, two mesh refinements, and two model formulations, the number of crack paths to analyze becomes high. To avoid having several similar plots, two angles are introduced to characterize the crack paths, namely the initial and final crack propagation angles. Nominally, it is expected that the crack paths are straight as the imposed fiber orientation is homogeneous in the domain. However, it will be shown that under certain mesh and loading conditions, this may not hold. In such cases, it is noticed that the initial and final crack propagation angles are different. The initial crack propagation angle is defined as the kink angle of the crack with respect to the horizontal. Similarly, the final crack propagation angle is the angle made by the crack when it reaches the boundary with respect to the horizontal. The difference between the two provides an indication of the path curvature. To illustrate these definitions, the crack paths observed using a coarse mesh with $\alpha = 10$ are shown for fiber orientations at 30°, 45°, and 60° in Figure 8.6.

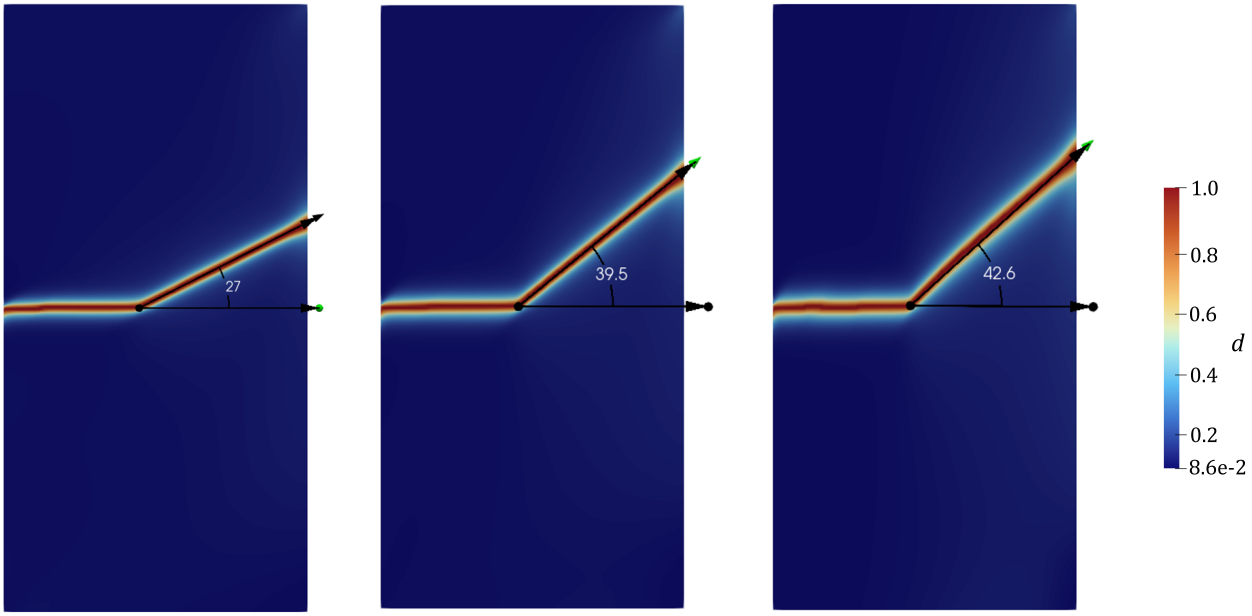

(a) 30° **(b)** 45° **(c)** 60°

Figure 8.6: Crack paths observed for preferential orientations of 30°, 45° and 60° under a coarse mesh and displacement increment.

From these figures, it appears that when the fiber orientation is 60° for a coarse mesh, the crack path exhibits a curved trajectory. This is because the initial and final crack propagation angles are different (see Figure 8.7). The initial angle is 47°, which has a percentage error of 7.5% compared to the expected propagation angle. Yet this becomes 42.6° (percentage error of 17.6%) for the final crack propagation angle.

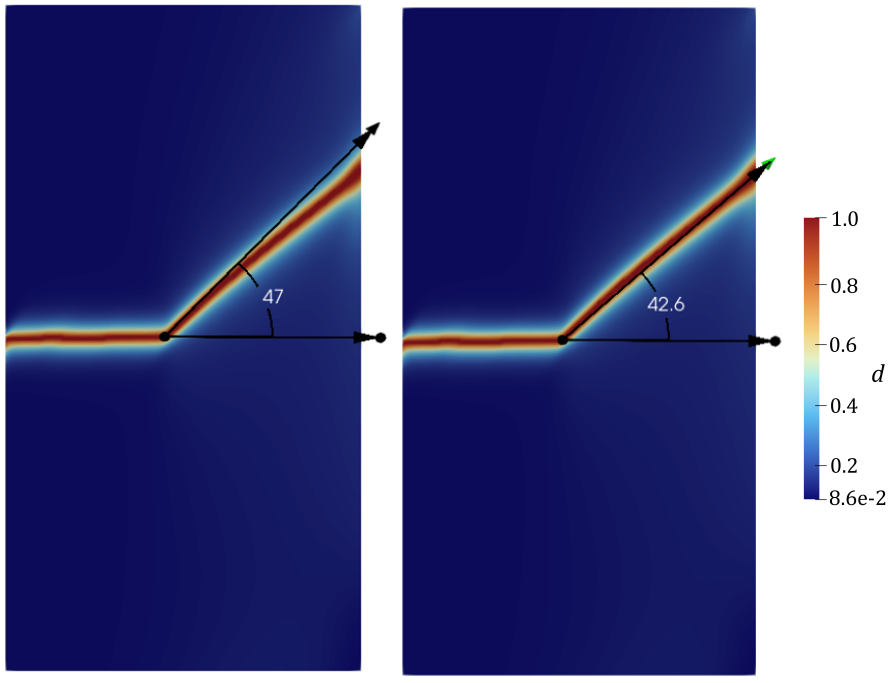

(a) ref. **(b)** sent

Figure 8.7: Comparison of the initial and final crack propagation angles in a specimen with a preferential orientation of 60° and anisotropic fracture energy parameter of 10 under tensile loading.

Having established the notation to characterize the crack paths, the results of the analysis are summarized in Table 8.3, Table 8.4, and Table 8.5. The comments related to the analysis are presented directly after each table for ease of reading.

Table 8.3: Expected and observed crack propagation angles for a preferential direction of 30° under different mesh and displacement increment sizes.

Mesh	α	Expected Angle [°]	Δu [mm]	Observed Angle [°] (classical)	Error [%] (classical)	Observed Angle [°] (consistent)	Error [%] (consistent)
Fine	10	27	$12.8 \cdot 10^{-3}$	27	-	27	-
			$6.4 \cdot 10^{-3}$	27	-	27	-
			$3.2 \cdot 10^{-3}$	27	-	27	-
	100	29.7	$12.8 \cdot 10^{-3}$	29.3	-	29.2	-
			$6.4 \cdot 10^{-3}$	29.6	-	29.5	-
			$3.2 \cdot 10^{-3}$	29.7	-	29.7	-
Coarse	10	27	$12.8 \cdot 10^{-3}$	27	-	27	-
			$6.4 \cdot 10^{-3}$	27	-	27	-
			$3.2 \cdot 10^{-3}$	27	-	27	-
	100	29.7	$12.8 \cdot 10^{-3}$	29	2.4	29.1	-
			$6.4 \cdot 10^{-3}$	29.3	-	29.3	-
			$3.2 \cdot 10^{-3}$	29.4	-	29.3	-

From these results, it is noted that:

- The error between the expected and observed crack angle is at most approximately 2.4%, this occurs for the coarse mesh under the highest displacement increment. In all other cases, the error is less than 2%, and hence it is deemed difficult to distinguish whether it is a numerical difference or a consequence of human judgment when using the angle tool in ParaView.
- For all cases, the initial crack propagation is aligned with the final crack propagation, and hence a distinction between the two is not made.
- Although the differences are small, as the mesh becomes finer and the displacement increment decreases, the results appear to converge to the expected behavior.
- The differences between the classical and consistent formulation are small.

For the case where the preferential direction is 45°, the following table is obtained:

Table 8.4: Expected and observed crack propagation angles for a preferential direction of 45° under different mesh and displacement increment sizes.

Mesh	α	Expected Angle [°]	Δu [mm]	Observed Angle [°] (classical)	Error [%] (classical)	Observed Angle [°] (consistent)	Error [%] (consistent)
Fine	10	39.8	$12.8 \cdot 10^{-3}$	39.2	-	39.2	-
			$6.4 \cdot 10^{-3}$	39.5	-	39.5	-
			$3.2 \cdot 10^{-3}$	39.8	-	39.8	-
	100	44.4	$12.8 \cdot 10^{-3}$	43.5	2	43.6	-
			$6.4 \cdot 10^{-3}$	43.9	-	43.9	-
			$3.2 \cdot 10^{-3}$	44.1	-	44.2	-
Coarse	10	39.8	$12.8 \cdot 10^{-3}$	39.0	2	39.0	2
			$6.4 \cdot 10^{-3}$	39.4	-	39.3	-
			$3.2 \cdot 10^{-3}$	39.5	-	39.7	-
	100	44.4	$12.8 \cdot 10^{-3}$	42.9	3.4	42.7	3.9
			$6.4 \cdot 10^{-3}$	43.7	-	43.6	-
			$3.2 \cdot 10^{-3}$	44.0	-	43.7	-

From this table, it follows that:

- For all cases, the initial crack propagation is aligned with the final crack propagation angle, and hence a distinction between the two is not made.

- The maximum error observed occurs for the coarse mesh under the highest displacement increment (as expected) and is 3.9 %. This is higher than the maximum error observed when the preferential direction is 30°.
- Except for the cases where the displacement increment is large, the error between the expected and observed crack propagation angles are marginal.
- Furthermore, the results show convergence as, upon refinement, the errors reduce and show progressively smaller changes.
- The differences between the classical and consistent formulation are small.

For the case where the preferential direction is 60°, the following table is obtained:

Table 8.5: Expected and observed crack propagation angles for a preferential direction of 60° under different mesh and displacement increment sizes.

Mesh	α	Expected Angle [°]	Δu [mm]	Observed Angle [°] (classical)	Error [%] (classical)	Observed Angle [°] (consistent)	Error [%] (consistent)
Fine	10	51.1	$12.8 \cdot 10^{-3}$	(46.1, 42.9)	(9.8, 16)	(46.1, 42.9)	(9.8, 16)
			$6.4 \cdot 10^{-3}$	(46.1, 43.2)	(9.8, 15.5)	(46.2, 43.1)	(9.6, 15.7)
			$3.2 \cdot 10^{-3}$	(46.1, 45.4)	(9.8, 11.2)	(46.3, 45.5)	(9.4, 10.9)
	100	59	$12.8 \cdot 10^{-3}$	(56.6, 55.8)	(4.1, 5.5)	(56.5, 55.7)	(4.2, 5.6)
			$6.4 \cdot 10^{-3}$	(57.1, 56.1)	(3.2, 5.0)	(57.2, 56.2)	(3.1, 4.7)
			$3.2 \cdot 10^{-3}$	(57.2, 57.0)	(3.0, 3.3)	(57.3, 56.7)	(2.9, 3.9)
Coarse	10	51.1	$12.8 \cdot 10^{-3}$	(45.5, 38.8)	(11.1, 24.1)	(45.4, 38.8)	(10.6, 24.1)
			$6.4 \cdot 10^{-3}$	(45.9, 41.5)	(10.1, 18.6)	(45.7, 41.7)	(10.1, 18.4)
			$3.2 \cdot 10^{-3}$	(47, 42.6)	(7.2, 17.6)	(47.4, 42.4)	(7.5, 17.0)
	100	59	$12.8 \cdot 10^{-3}$	(56.6, 52.1)	(4.1, 11.7)	(56.7, 52.3)	(3.9, 11.4)
			$6.4 \cdot 10^{-3}$	(56.6, 54.3)	(4.1, 8.0)	(56.8, 54.4)	(3.7, 7.8)
			$3.2 \cdot 10^{-3}$	(56.8, 54.9)	(3.7, 7.0)	(56.9, 54.9)	(3.6, 6.9)

From this table, it follows that:

- Unlike the previous cases, the initial and final crack propagation angles are notably different and hence both are reported in the table. The initial crack propagation angle is the first value in the brackets, and the final one corresponds to the second value.
- It appears that for all cases, the error of the initial crack propagation angle is smaller than the error made by the final crack propagation angle. For both mesh sizes, the initial error is lower when the anisotropic fracture energy parameter is higher. Regardless, in all cases, the magnitude of the error observed is higher than what has been seen in the previous tables.
- The difference between the initial and final error is not consistent. The results show that the difference between errors is higher when the mesh is coarser and when the displacement increment is higher.
- The differences between the classical and consistent formulation are small.

8.2.6. Special Case: Fiber Orientation at 90°

In the examples seen thus far, both formulations are rather similar (except for the direction-dependent length scale). However, to illustrate that the classical and consistent formulations are not identical, a special case is considered, namely when the fiber orientation is 90°. In Chapter 5, it was noted that the two formulations exhibit vastly different natural boundary conditions. Thus, it is reasonable to question whether the crack paths would also be different. For a consistent comparison, the anisotropic fracture energy parameter is set to 100 for both formulations.

For this example, the applied boundary conditions are revisited. This is because when displacement boundary conditions are imposed along the entire top edge, an artificial numerical resistance is introduced that hinders crack propagation into the loaded boundary region. Previously, this was not an issue, as it was known that the crack would propagate into the right edge. However, under a fiber orientation of 90°, this is no longer the case. To reduce the boundary condition effect, a second configuration is also considered. The two cases investigated are:

1. the same loading and boundary conditions as those discussed so far, that is, as described by Figure 8.8a,
2. the boundary condition on the bottom edge remains the same as Figure 8.1, however, the displacement loading is only applied to the left half of the top boundary, see Figure 8.8b.

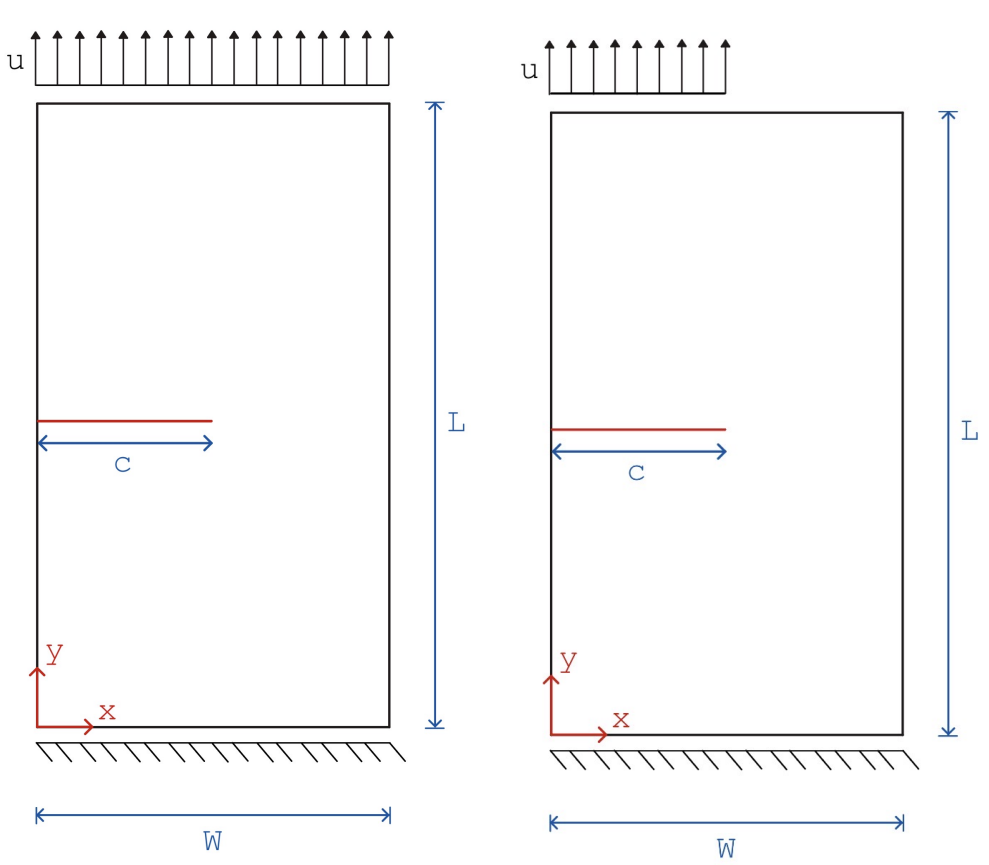

(a) Load applied to entire top edge.

(b) Load applied to half of the top edge.

Figure 8.8: Visualization of the two boundary condition cases considered for the single-edge notched tension test for fiber orientation at 90°.

The results of both of these cases are visualized in Figure 8.9.

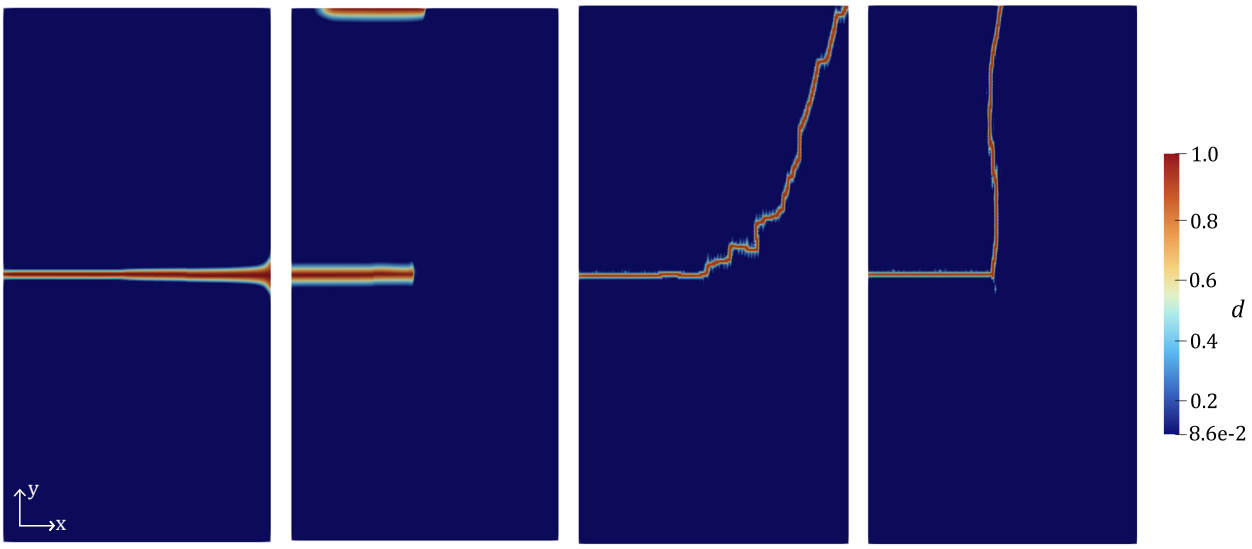

(a) Classical, full

(b) Classical, half

(c) Consistent, full

(d) Consistent, half

Figure 8.9: Crack paths observed using the classical and consistent formulation for fiber orientation of 90° when the loading is applied to the full top edge and half of the top edge.

From these figures, the following points are of interest:

- In the classical formulation, the crack path remains oriented along $[1, 0]^{\mathrm{T}}$ for both cases. This suggests that the fibers would be broken rather than observing matrix cracking. As it is much harder to break the fibers, it remains questionable whether this is a physically consistent result.
- The crack propagating along the top boundary in Figure 8.9b can be considered a numerical artifact. Due to the stress concentration at the load point, an artificial crack nucleates, and under further loading, it begins to propagate along the boundary. This is not a physically expected result; however, it shows that the classical model always predicts a horizontally propagating crack.
- In the case of Figure 8.9d, the following it noted. When the displacement boundary condition is applied to the entire top boundary, it becomes numerically difficult for the crack to propagate into the boundary. Yet, as the preferential direction is along $[0, 1]^{\mathrm{T}}$, the resulting crack path attempts to satisfy both conditions and, as a result, chooses a path that delays reaching the top boundary. However, when the displacement boundary condition is applied to a segment of the top edge, there is less numerical resistance for the crack to propagate into the top boundary. As a result, the crack follows the preferential direction. It appears that the non-uniqueness inherent to the consistent formulation permits a broader range of energetically admissible crack paths to emerge.
- Despite using the same boundary conditions, under the consistent approach, artificial crack nucleation is not observed. Rather, under such conditions, the crack propagates along the preferential direction. The crack path is not perfectly aligned with $[0, 1]^{\mathrm{T}}$; however, this can be attributed to the asymmetry of the mesh.

8.3. Open Hole Tension Test

The second experiment considered is the OHT test. Unlike the experiments discussed previously, the location of crack initiation is not prescribed in this case. Instead, crack nucleation and subsequent propagation arise naturally as a consequence of the applied loading and the specimen geometry. This experiment is also chosen to verify the implementation of spatially varying fiber orientations. Since the spatial variation in fiber orientation is expected to influence the crack propagation behavior, the parameterization used to describe the fiber orientation field is first introduced. This is followed by an overview of the applied loading and boundary conditions. Finally, the numerical results obtained from the model are compared with results available in the literature.

8.3.1. Characterizing Fiber Orientation Geometry

The first aspect considered is a method to characterize spatially non-homogeneous fiber orientation. In theory, any distribution is permissible; however, to aid the verification process, a case that has been investigated in the literature is considered. Thus, the distribution proposed by Yu et al. [88] is used. They propose introducing a spatial dependence given by the following family of curves:

$$\theta(x) = \theta_s + \frac{2(\theta_1 - \theta_0)}{W}\left|x - \frac{W}{2}\right| + \theta_0, \tag{8.1}$$

where θ_s, θ_0, and θ_1 are the constants that characterize the fiber path.

For the cases where θ_s is 0°, and θ_0 and θ_1 take on values of either 0° or 60°, the fiber paths are visualized in Figure 8.10.

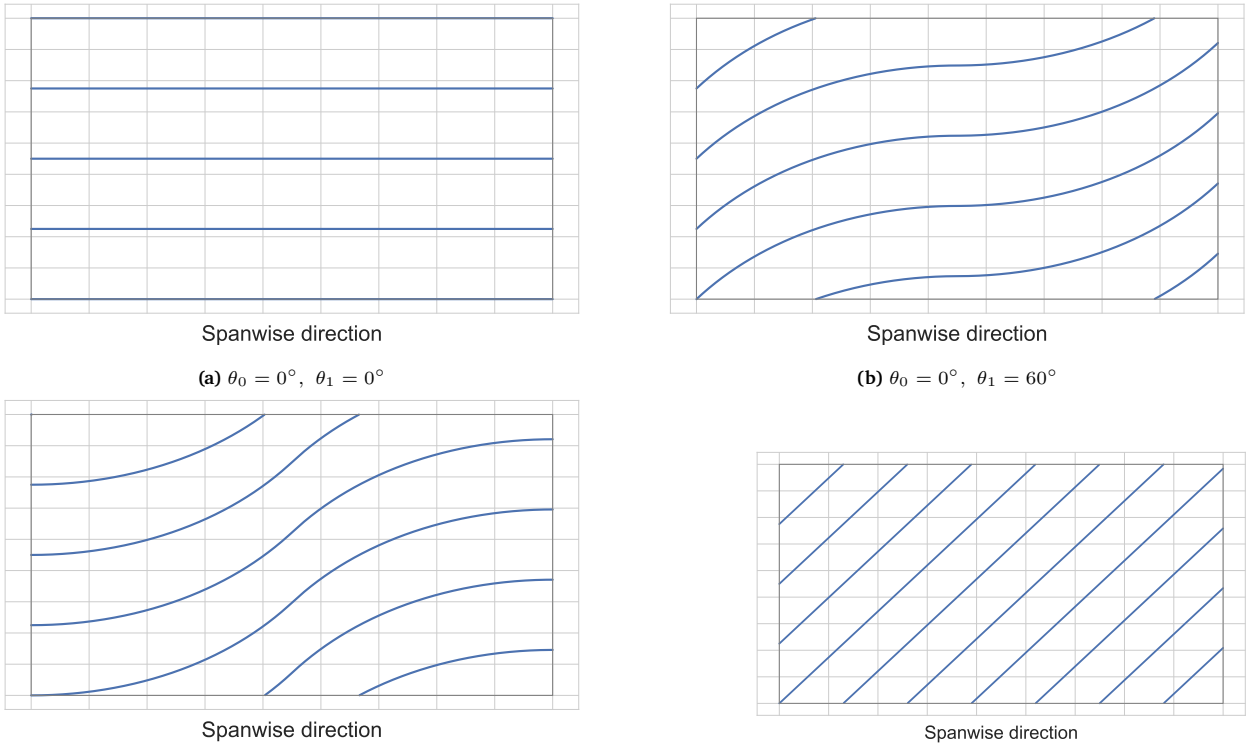

(a) $\theta_0 = 0^\circ,\ \theta_1 = 0^\circ$

(b) $\theta_0 = 0^\circ,\ \theta_1 = 60^\circ$

(c) $\theta_0 = 60^\circ,\ \theta_1 = 0^\circ$

(d) $\theta_0 = 60^\circ,\ \theta_1 = 60^\circ$

Figure 8.10: Expected fiber paths for different angles of θ_0 and θ_1 based on $\theta_s + \frac{2(\theta_1-\theta_0)}{W}\left|x - \frac{W}{2}\right| + \theta_0$ for $\theta_s = 0$.

From this figure, it becomes evident that when both θ_0 and θ_1 are the same value, the fiber paths are straight, implying that it resolves into the spatially homogeneous fiber orientation scenario. Hence, it is more interesting to consider the cases where θ_0 is not equal to θ_1. In the numerical examples, two situations are considered, namely when $\theta_0 = 0^\circ, 60^\circ$ and $\theta_1 = 60^\circ, 0^\circ$ respectively.

8.3.2. Loading and Boundary Conditions

In this numerical example, a rectangular specimen with a circular notch in the middle is loaded in tension. No pre-cracks are initialized, as the crack nucleation will be determined by the model. Furthermore, the geometry and boundary conditions are shown in Figure 8.11. For this numerical example, the geometry and material parameters are specified in Table 8.6.

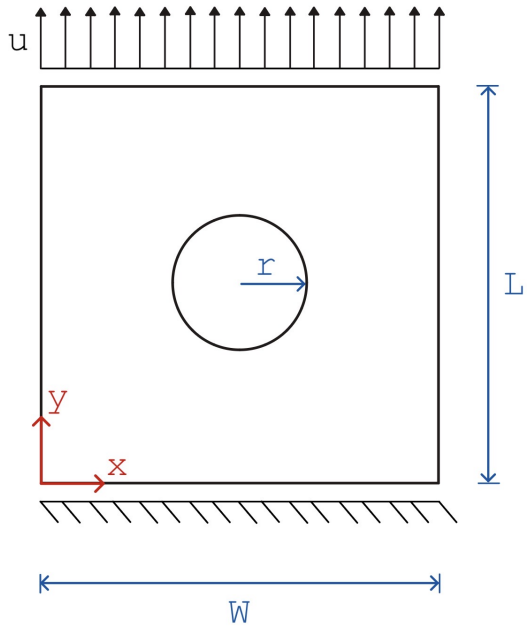

Figure 8.11: Specimen geometry, loading and boundary conditions used for the open hole tension (OHT) test.

Table 8.6: Material and geometric parameters used for the open hole tension (OHT) test.

Material Property	Value	Units
E_1	26.5	GPa
E_2	2.6	GPa
G_{12}	1.3	GPa
ν_{12}	0.35	–
Reference fracture energy	0.62	N/mm
Geometry Parameter	**Value**	**Units**
Specimen width, W	1	mm
Specimen length, L	1.5	mm
Radius of hole, r	0.15	mm

8.3.3. Mesh and Numerical Details

In this example, the geometry was discretized into 82882 quadrilateral elements that were meshed using the Frontal-Delaunay algorithm in Gmsh [154]. Unlike the previous cases, here a local refinement of the mesh was performed near the notch to allow for correctly identifying the crack nucleation points. By using 82882 elements, the maximum element size is approximately 0.005 mm, allowing for a length scale of 0.01 mm. These parameters were used to allow for direct comparison with the reference solution. As there is no pre-crack, the damage field was initialized to zero.

8.3.4. Model Results and Comparison: Case 1

The first numerical case considered has a fiber orientation characterized by $[\theta_s, \langle\theta_0, \theta_1\rangle] = [0°, \langle 60°, 0°\rangle]$. The crack paths observed for the classical and consistent formulation, along with the reference solutions, are plotted in Figure 8.12.

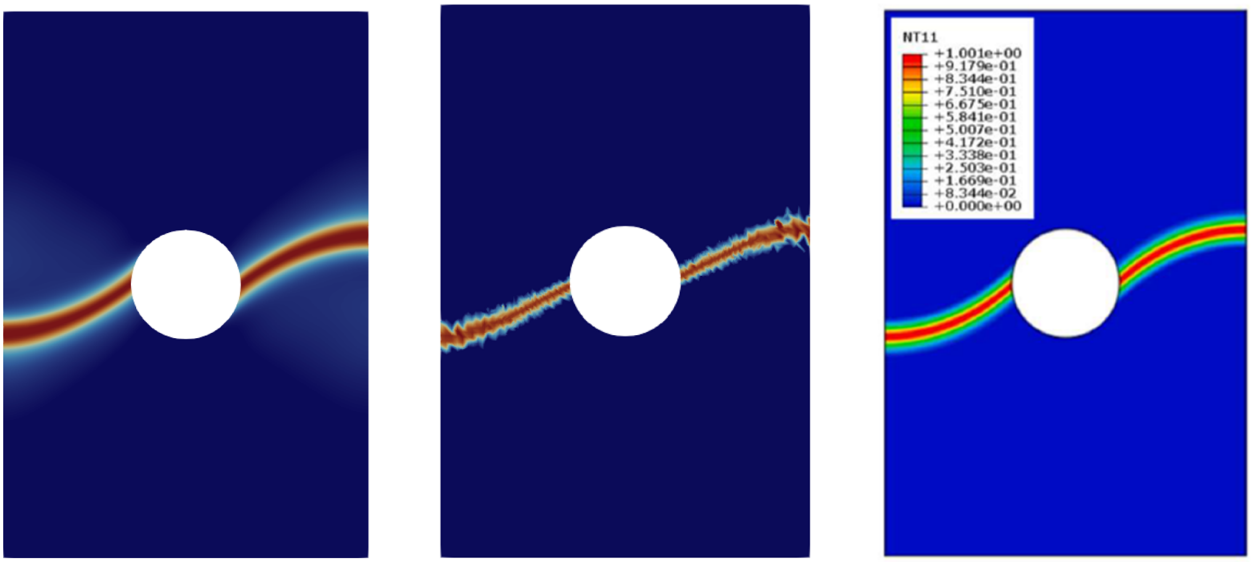

(a) Classical model **(b)** Consistent model **(c)** Reference solution (Yu et al. [88])

Figure 8.12: Comparison between different models for the open hole tension (OHT) test on a specimen with a spatially varying fiber orientation characterized by $[\theta_s, \langle\theta_0, \theta_1\rangle] = [0°, \langle 60°, 0°\rangle]$.

From these figures, the following points are to be noticed:

- In all cases, it appears that the crack nucleates at the left and right edges of the circular hole. This is expected as this is the point where the stress concentration is highest, and hence where damage will occur first.
- For both model formulations, the observed crack path aligns well with the imposed fiber orientation and the reference solution. This provides confidence that the model is able to correctly identify crack deflection due to changing fiber orientation.
- Although the consistent formulation follows the fiber orientation, the crack path is more jagged. A possible reason for this can be explained as follows. In the consistent formulation, the crack orientation is inferred from the damage gradient. Yet, the gradient is a numerically sensitive quantity as it is inferred from a diffuse damage field (regardless of how sharp the crack appears). Combining this with the spatially varying fiber orientations, small numerical perturbations may be amplified, leading to a less smooth crack trajectory. Introducing additional regularization of the orientation field or improved gradient evaluation could help in reducing numerical noise. However, these analyses are not considered within the scope of this thesis.
- The direction-dependent length scale effect is also present between both model formulations. While the width of the diffuse crack remains constant throughout the crack path in the consistent formulation, in the classical formulation, this is not the case. Even though the reference solution also uses the structural tensor, it appears that the direction-dependent length scale effect is not as apparent, which should be attributed to the resolution of the image.

To analyze this numerical example further, the load-displacement curves for the three model formulations are analyzed. This is plotted in Figure 8.13.

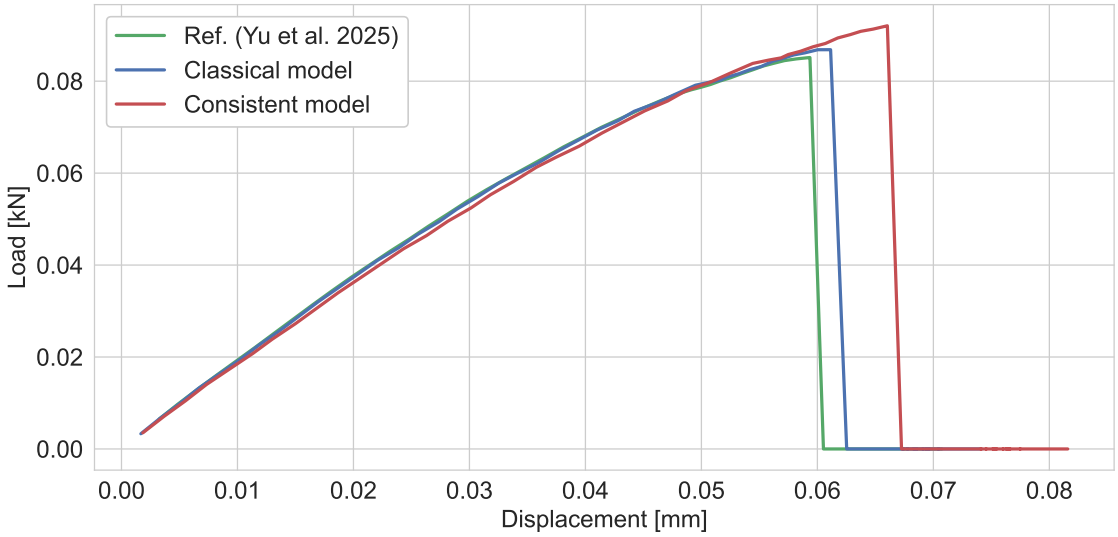

Figure 8.13: Comparison of load displacement curves between reference and model results for the open hole tension (OHT) test on a specimen with a spatially varying fiber orientation characterized by $[\theta_s, \langle \theta_0, \theta_1 \rangle] = [0°, \langle 60°, 0° \rangle]$.

Comparing the load-displacement curves, it appears that the initial elastic regime for all three cases is similar. This makes sense because, until the presence of damage, the behavior is governed by the elastic properties of the material. Furthermore, the results from the proposed models exhibit higher peak loads compared to the reference solution. One explanation for this could be the mesh. Yu et al. [88] made use of an adaptive remeshing algorithm allowing them to refine the mesh “on-the-fly” in regions of crack propagation. By doing so, the element size decreases in the vicinity of the crack, and hence a lower critical load is observed. This is in line with their conclusions, because they note that subsequent refinement of the mesh reduces the peak load observed [88]. The differences between the classical and consistent methods are also understandable, as despite having equivalence in energetics, it has been established that the models are not identical.

8.3.5. Model Results and Comparison: Case 2

The second numerical case considered has a fiber orientation characterized by $[\theta_s, \langle \theta_0, \theta_1 \rangle] = [0°, \langle 0°, 60° \rangle]$. The crack paths observed for the classical and consistent formulation, along with the reference solutions, are plotted in Figure 8.14.

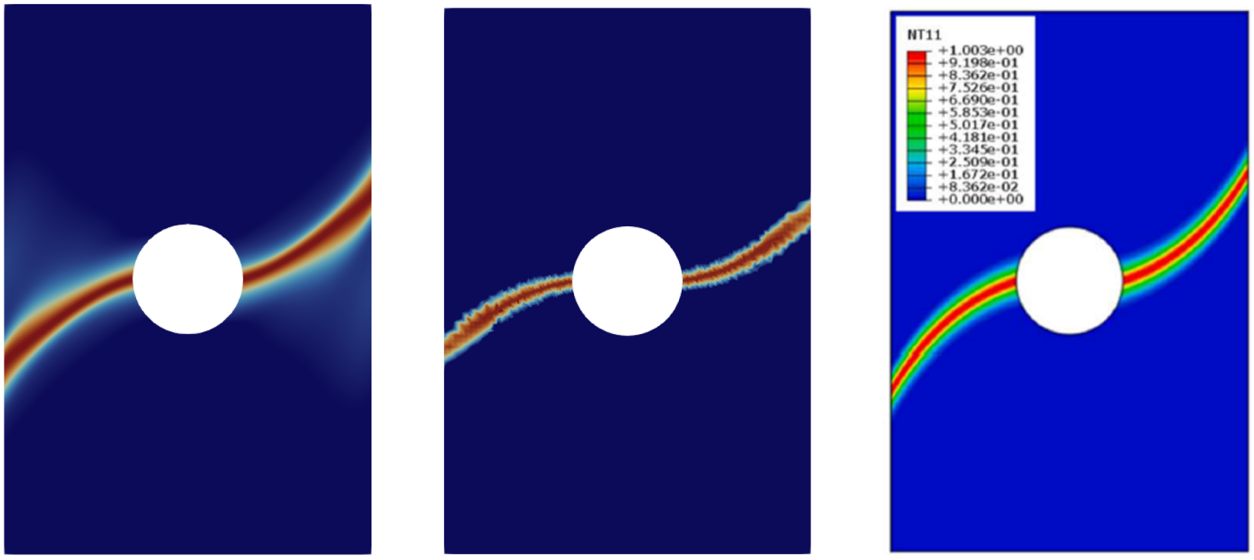

(a) Classical (proposed) model **(b)** Consistent (proposed) model **(c)** Reference solution (Yu et al. [88])

Figure 8.14: Comparison between different models for the open hole tension (OHT) test on a specimen with a spatially varying fiber orientation characterized by $[\theta_s, \langle\theta_0, \theta_1\rangle] = [0°, \langle 0°, 60°\rangle]$.

- In all cases, it appears that the crack nucleates at the left and right edges of the circular hole. This is expected as this is the point where the stress concentration is highest, and hence where damage will occur first.
- Again, similar to before, for both model formulations, the observed crack path aligns well with the imposed fiber orientation and the reference solution.
- Comparing Figure 8.14a and Figure 8.14b, it is evident that, likewise to the previous case, the consistent formulation exhibits a more jagged crack path (see the previous discussion on this point).
- Lastly, equivalent to before, in this numerical example, the direction-dependent length scale effect is present when comparing both model formulations.

To analyze this numerical example further, the load-displacement curves for the three model formulations are given. This is plotted in Figure 8.15. The trends in this figure align with what was observed in Figure 8.13, namely, the elastic behavior is the same for all three cases, the peak load is lower for the reference solution, and the classical and consistent formulations exhibit different behavior post-peak.

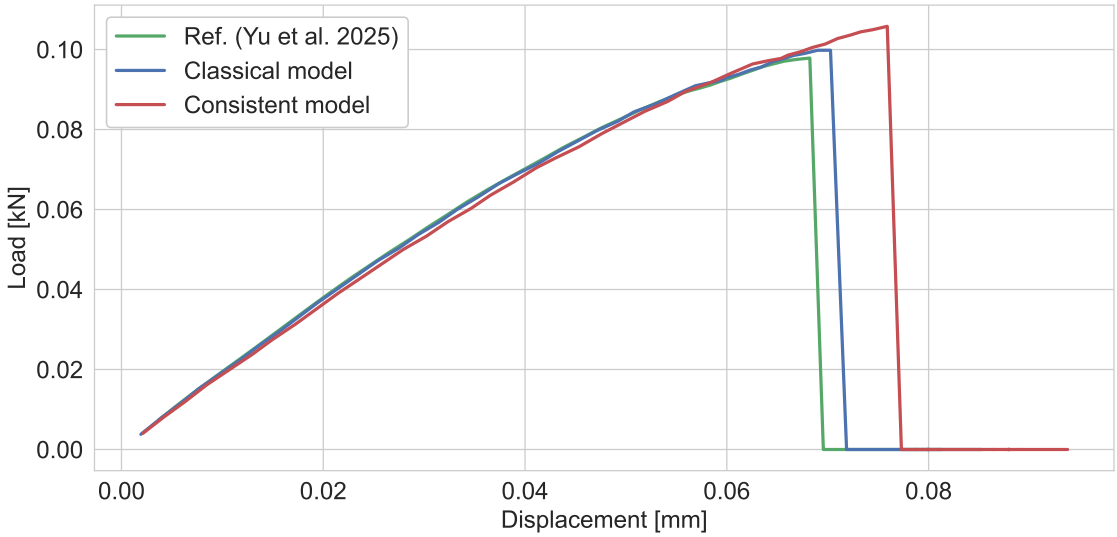

Figure 8.15: Comparison of load displacement curves between reference and model results for the open hole tension (OHT) test on a specimen with a spatially varying fiber orientation characterized by $[\theta_s, \langle\theta_0, \theta_1\rangle] = [0°, \langle 0°, 60°\rangle]$.

9: Comparison of Methods Under Isotropic Mixed-Mode Conditions

In this chapter, the proposed model is evaluated under isotropic mixed-mode conditions. As a result, the direction-dependence of the fracture energy is suppressed in the analyses presented. Since the proposed method for treating mode-mixity is new, a comparative study is conducted to assess the approach against existing methods. The scope of this comparative analysis is outlined in Section 9.1. Subsequently, the results of the first test are presented in Section 9.2, followed by a discussion of the second test in Section 9.3.

9.1. Scope of Comparative Analysis

In the present study, the comparative analysis is conducted under isotropic fracture conditions. The verification procedure adopted in this section differs slightly from the previous cases. In earlier investigations, direct comparisons with existing numerical results available in the literature were possible, as the underlying methodologies were the same. However, this is not the case here. Existing studies have focused on isotropic fracture behavior, whereas the proposed framework is intended to remain applicable in both isotropic and anisotropic fracture conditions. Consequently, a direct one-to-one comparison is not readily possible.

The objective is therefore to assess whether the proposed method is capable of reproducing the same trends in the literature for the isotropic case. Successful agreement in the isotropic regime provides confidence in the robustness of the framework prior to its extension toward anisotropic fracture applications. For this purpose, two benchmark experiments are considered:

1. Uniaxial compression of a specimen with one internal flaw.
2. Uniaxial compression of a specimen with two internal flaws.

9.2. Uniaxial Compression with One Internal Flaw

The first mixed-mode numerical example considered relates to a uniaxial compression test performed on a specimen with a flaw. Similar to all previous examples, firstly, the loading and boundary conditions are considered. The model results are then compared to the results in the literature.

9.2.1. Loading and Boundary Conditions

In this example, a rectangular specimen with a flaw tilted away from the vertical is subject to uniaxial compression in the vertical direction. The geometry and boundary conditions are shown in Figure 9.1. Furthermore, the geometry and material parameters are specified in Table 9.1.

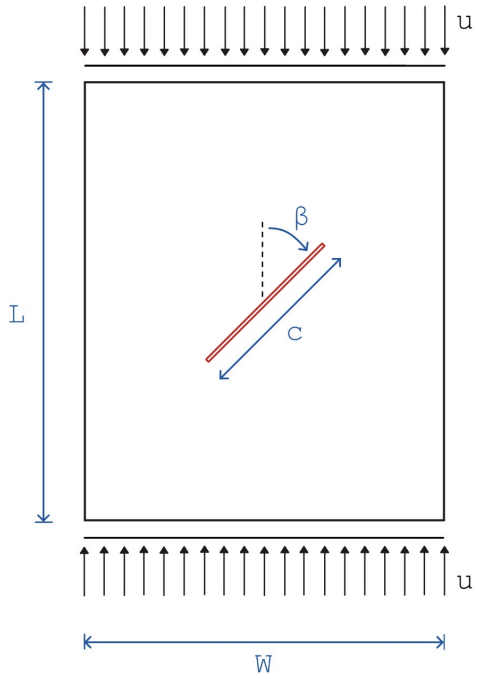

Figure 9.1: Specimen geometry, loading and boundary conditions used for the uniaxial compression test with one internal flaw.

Table 9.1: Material and geometric parameters used for the uniaxial compression test with one internal flaw.

Material Property	Value	Units
Young's modulus	6.2	GPa
Poisson's ratio	0.28	–
Fracture energy Mode I	$50 \cdot 10^{-6}$	kN/mm
Fracture energy Mode II	$50 \cdot 10^{-5}$	kN/mm
Geometry Parameter	**Value**	**Units**
Specimen width, W	50	mm
Specimen length, L	100	mm
Initial crack length, c	20	mm
Crack orientation, β	60	°

9.2.2. Mesh and Numerical Details

In this example, the geometry was discretized into 25870 quadrilateral elements that were meshed using the Frontal-Delaunay algorithm in Gmsh [154]. A local refinement of the mesh was performed near the flaw to allow for the correct identification of the crack nucleation points. By using 25780 elements, the maximum element size is approximately 0.5 mm, allowing for a length scale of 1 mm.

9.2.3. Model Results and Comparison

Prior to presenting the model results, some terminology is introduced to describe the fracture process observed experimentally. For specimens with internal flaw(s) under uniaxial compression, Wong and Einstein [2] note that several types of crack patterns can be observed. In the case of one internal flaw, the process is characterized mainly by the presence of tensile cracks that initiate near the two tips of the flaw. These cracks then propagate downwards towards the axial stress locations. Due to the curved trajectory of these cracks, they are also referred to as wing cracks. Although these are the most common, other types of crack patterns have also been observed [2]. Several possible trajectories are listed in Figure 9.2.

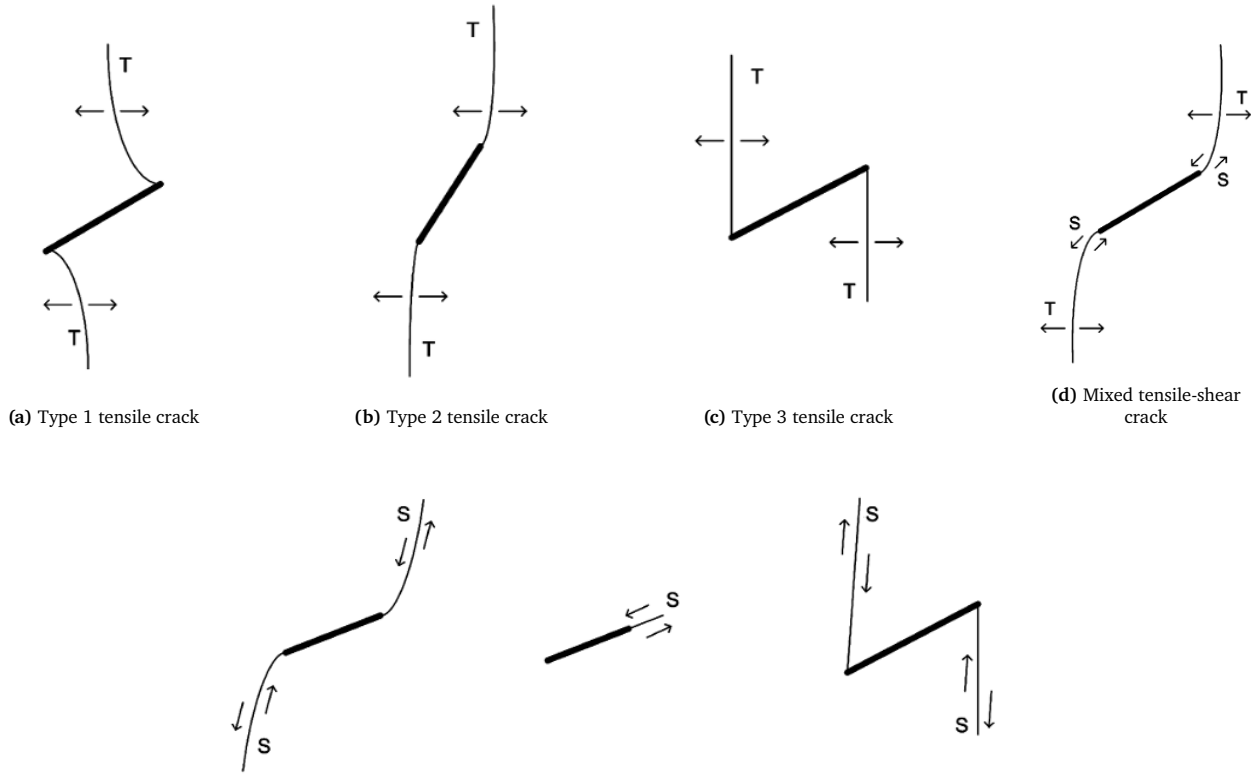

(a) Type 1 tensile crack **(b)** Type 2 tensile crack **(c)** Type 3 tensile crack **(d)** Mixed tensile-shear crack

(e) Type 1 shear crack **(f)** Type 2 shear crack **(g)** Type 3 shear crack

Figure 9.2: Possible crack types for a specimen with one internal flaw under uniaxial compression [2].

Thus, it is expected that the model results should show behavior described in Figure 9.2. To aid further comparison, a reference numerical solution from the literature is also considered, namely from the work of Xu et al. [157]. The crack path predicted by the model and the reference solution are visualized in Figure 9.3.

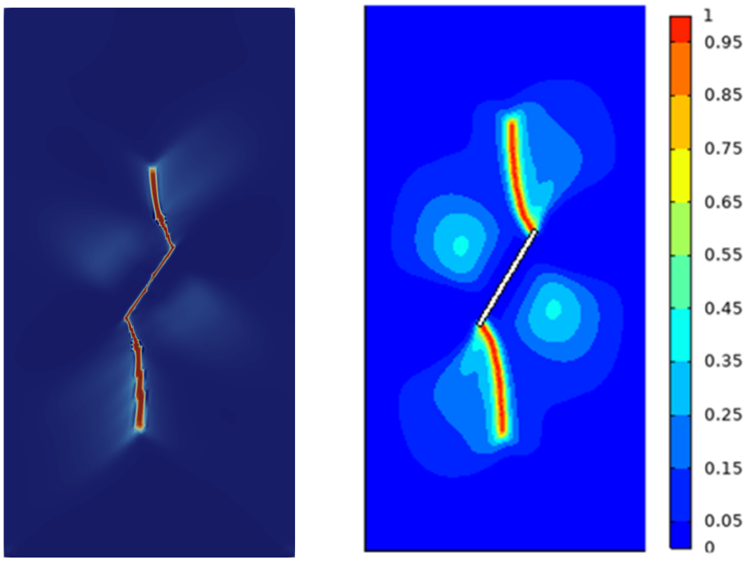

(a) Proposed model **(b)** Reference solution (Xu et al. [157])

Figure 9.3: Comparison of model results and reference solution for a specimen with one internal flaw under uniaxial compression.

A comparison of the figures reveals that type I tensile cracks are observed in both cases. Additionally, two distinct damage zones emerge away from the flaw. In the proposed model solution, the crack width appears to increase as the tensile cracks propagate outward. A likely explanation for this behavior lies in the mesh discretization; while the mesh is refined in the vicinity of the initial crack, it becomes progressively coarser farther away. Consequently, as the crack propagates into these coarser regions, the crack appears artificially

wider. Yet, except for this, the proposed method identifies the expected behavior correctly.

9.3. Uniaxial Compression with Two Internal Flaws

The second example is also a uniaxial compression test, however, in the presence of two flaws. These two flaws are aligned with each other and displaced by a certain distance. The loading and boundary conditions, along with the discussion of the results, are presented in the subsections below.

9.3.1. Loading and Boundary Conditions

The loading and boundary conditions are similar to the previous example, as it is also a uniaxial compression test; however, the geometry is different. The geometry and boundary conditions are shown in Figure 9.4. For this numerical example, the geometry and material parameters are specified in Table 9.2.

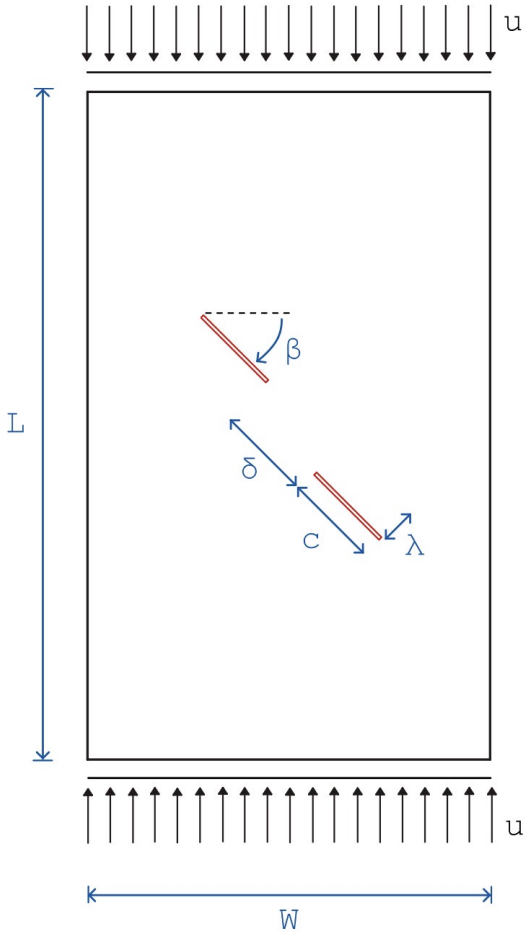

Figure 9.4: Specimen geometry, loading and boundary conditions used for the uniaxial compression test with two internal flaws.

Table 9.2: Material and geometric parameters used for the uniaxial compression test with two internal flaws.

Material Property	Value	Units
Young's modulus	6.2	GPa
Poisson's ratio	0.28	–
Fracture energy Mode I	$50 \cdot 10^{-6}$	kN/mm
Fracture energy Mode II	$50 \cdot 10^{-5}$	kN/mm
Geometry Parameter	**Value**	**Units**
Specimen width, W	76.2	mm
Specimen length, L	152.4	mm
Initial crack lengths, c	12.7	mm
Crack orientation, β	45	°
Crack offset, λ	0	mm
Crack distance, δ	12.7	mm

9.3.2. Mesh and Numerical Details

In this example, the geometry was discretized into 46980 quadrilateral elements that were meshed using the Frontal-Delaunay algorithm in Gmsh [154]. A local refinement of the mesh was performed near the flaw to allow for the correct identification of the crack nucleation points. By using 46980 elements, the maximum element size is approximately 0.5 mm, allowing for a length scale of 1 mm.

9.3.3. Model Results and Comparison

In the presence of two flaws, the crack process observed is relatively complex due to the interactions between the flaws and the newly developed cracks. In their work, Bobet and Einstein [4] describe the process as follows. In the beginning, tensile cracks (wing cracks) form at the internal and external tips of the flaws. These propagate outwards in a stable manner following a curvilinear path that aligns with the compressive load. As the process evolves, these primary cracks are accompanied by secondary cracks that initiate and propagate in a

plane coplanar or quasi-coplanar to the flaw from which they originate. Having understood the process, the model predictions are visualized in Figure 9.5.

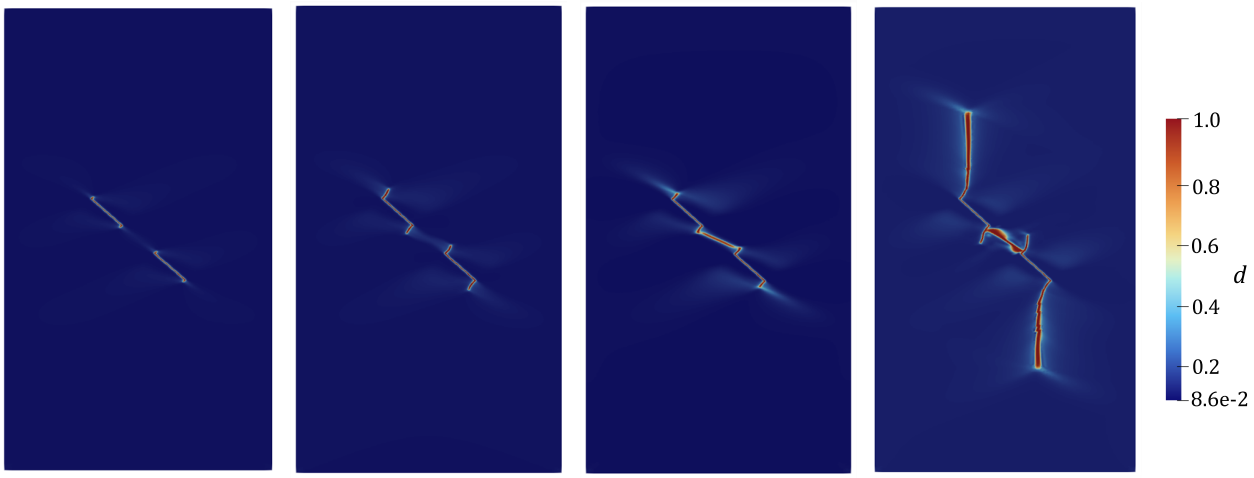

(a) Phase 1 **(b)** Phase 2 **(c)** Phase 3 **(d)** Phase 4

Figure 9.5: Proposed model results for fracture process observed for specimen with two internal flaws under uniaxial compression.

For comparison, the results obtained by Zhao et al. [3] are used. These are visualized in Figure 9.6.

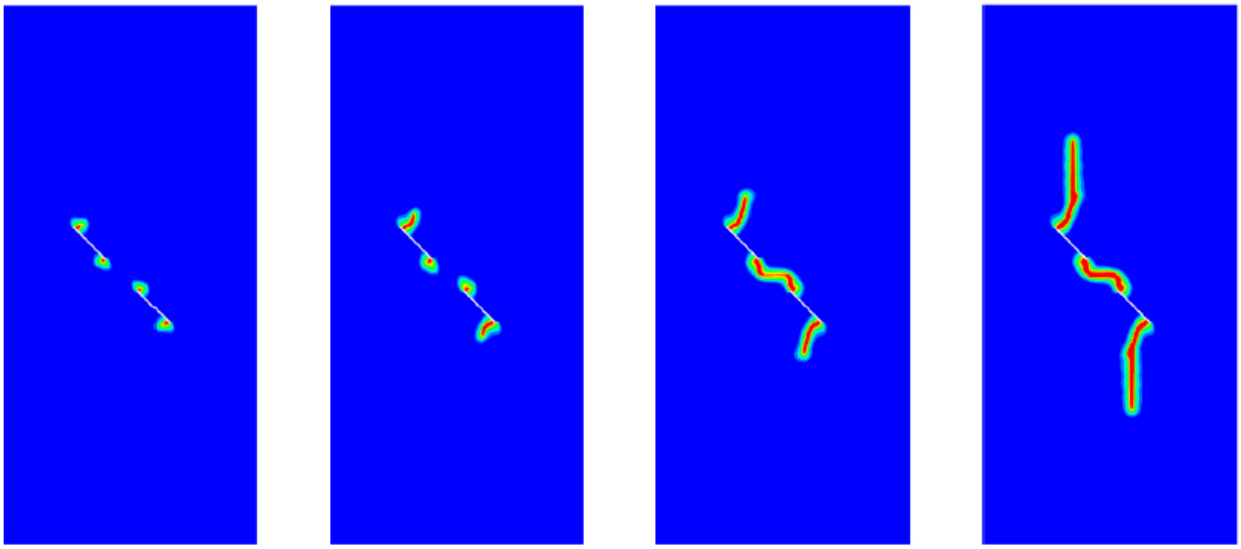

(a) phase 1 (b) phase 2 (c) phase 3 (d) phase 4

Figure 9.6: Reference solution for fracture process observed for specimen with two internal flaws under uniaxial compression [3].

Comparing Figure 9.5 to Figure 9.6, it appears that the proposed model can correctly predict the cracking process. Still, some points are of interest:

- The proposed model appears to correctly predict that the first cracks that nucleate occur near the tips of the flaws (as evident in phase 1). These cracks then propagate outwards as observed in Figure 9.5b.
- In the third phase, there is a slight difference between the two methods. In both cases, the tensile crack fronts at the internal tips of the flaws are bridged together. The reference solution predicts that this bridge is horizontal. Yet, in the proposed method, it appears nearly coplanar with the initial flaws. It will be shown that, on comparison with experimental evidence, see Figure 9.7, it is more likely that the bridging crack will be coplanar to the initial flaws.
- The fourth phase exhibits similar behavior in both models, with the wing cracks curving inward before propagating outward at comparable rates. This agreement is expected due to the symmetry of the problem. Specifically, rotating the configuration by 180° and reflecting the specimen yields an equivalent physical system, and therefore an identical fracture response is anticipated.

To better understand the origin of these discrepancies observed in the third phase, the differences between the two modeling approaches are explained. One evident distinction lies in the treatment of mode-mixity, particularly since the approach proposed in the present work has not previously been applied. However, additional differences also exist between the formulations. In the reference solution, the authors employ a multi-phase field framework in which two separate damage variables are introduced: one associated with the Mode I contribution and another associated with the Mode II contribution. Moreover, the degradation associated with the Mode I and Mode II components is treated independently. Given the similarity in the observed trends, the discrepancy likely arises from the multi-phase field formulation and the independent treatment of the degradation mechanisms, rather than from the treatment of mode-mixity itself. As the objective of this analysis is not to replicate their results, but rather to understand whether the proposed method is acceptable for treating mode-mixity, the results obtained are also compared to experimental evidence.

As hinted, this test has been performed, and hence it is worthwhile to compare the model results to experimental evidence. Although the load-displacement curves for these experiments are not given, they can be used to determine if the qualitative trends are correctly predicted. To do so, the works of Bobet and Einstein are considered [4, 158]. The crack paths are visualized in Figure 9.7.

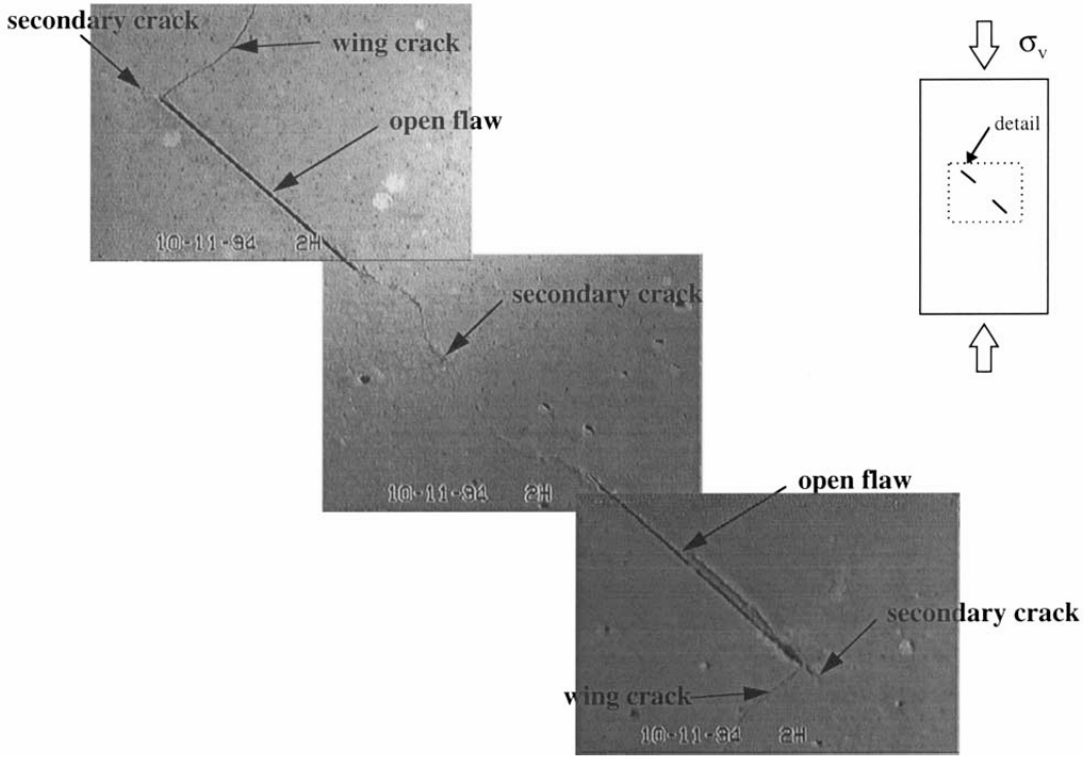

Figure 9.7: Experimental results of rock specimen with two flaws under uniaxial compression [4].

Comparing this figure to the numerical results, the qualitative trends are the same. There are two wing cracks located on the tips of the flaws that curve inwards and then propagate outwards in a straight manner. In addition, the inner tips of the flaws have secondary cracks that coalesce towards each other. Furthermore, similar to the behavior predicted by the proposed model, the experimental results indicate that the coalescence path remains approximately coplanar with the initial flaws.

As a sanity check, the same numerical example is revisited by suppressing the mode-mixity-based fracture energy. In other words, the experiment is re-run under isotropic, mode-independent conditions. The differences between these results and the previous results will indicate the effect, if any, of having a mode-mixity-based fracture energy. These results are visualized in Figure 9.8.

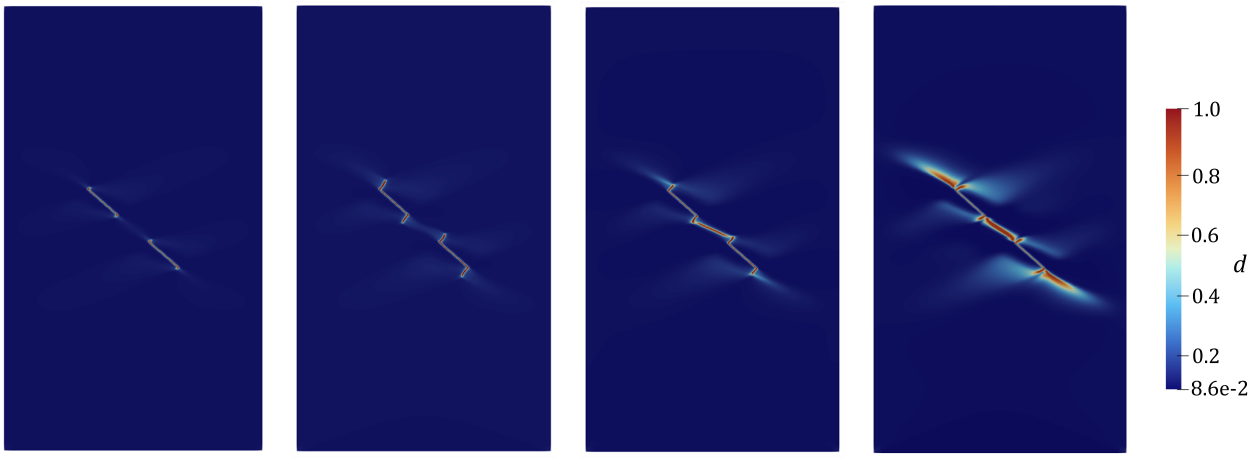

(a) Phase 1 **(b)** Phase 2 **(c)** Phase 3 **(d)** Phase 4

Figure 9.8: Model results for fracture process observed for specimen with two internal flaws under uniaxial compression with suppressed mode-mixity effects.

On comparison, the first three phases appear identical between Figure 9.8 and Figure 9.5. However, the fourth phase between the two figures is different. Under mode-independent conditions, the wing crack does not propagate downwards. Instead, it propagates towards the left and right boundaries in a coplanar manner. These wing cracks are also accompanied by secondary cracks that appear to propagate inwards. The significant difference in crack paths provides further confidence that the proposed method accurately captures mode-mixity effects and highlights the importance of incorporating mode-mixity.

10: Model Results for Complex Fracture Processes

This is the final chapter in the series discussing the model results. It focuses on showcasing the model's predictive performance in the context of some more complex fracture processes observed in composites involving both mode-mixity and anisotropy. Firstly, the scope of the analysis is presented in Section 10.1. This is followed by a discussion of the first numerical example, namely the crack migration test in Section 10.2. Thereafter, in Section 10.3, the second numerical example of transverse matrix cracking is discussed.

10.1. Scope of Analysis

Having verified the limit behavior of the model, the following analyses focus on tests that demonstrate the flexibility and predictive capabilities of the proposed formulation. As the present work is limited to 2D analyses, only cross-ply laminate examples are considered, in which both mode-mixity and anisotropic fracture behavior play an important role. To this end, two representative test cases are investigated, namely the crack migration test and the transverse matrix cracking test. Both problems involve complex crack propagation mechanisms influenced by the interaction between material anisotropy and mixed-mode fracture conditions, making them suitable benchmark cases for assessing the robustness of the model. Furthermore, both tests have been studied experimentally in the literature, thereby providing a reliable basis for qualitative validation. Consequently, these benchmark cases serve to evaluate whether the proposed formulation is capable of accurately capturing the underlying physical fracture mechanisms and reproducing the experimentally observed crack propagation behavior.

10.2. Crack Migration Test

The first example considered is a crack migration test for a cross-ply specimen. To discuss this example, firstly, the test description and the underlying physical mechanisms involved are presented. Thereafter, the model results and a comparison of these results to experimental evidence are provided.

10.2.1. Test Description

In this test, a specimen made from IM7/8552 carbon-epoxy with a cross-ply layup and a pre-crack located at the interface between a $0°$ ply and a stack of $90°$ plies is subject to an applied load. The geometry, loading, and boundary conditions are visualized in Figure 10.1. The geometry parameters and material properties are given in Table 10.1. The material properties are taken from [159], and the geometry is based on [5].

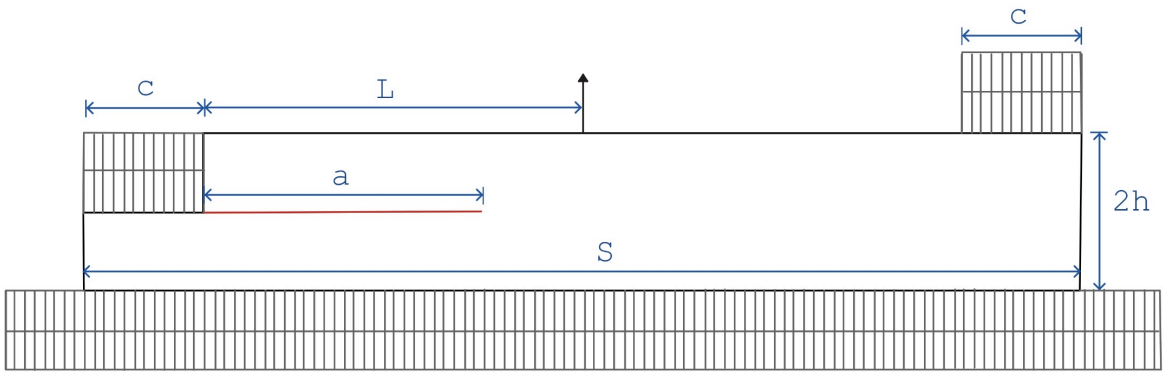

Figure 10.1: Setup of the crack migration test.

Table 10.1: Material and geometric parameters used for the crack migration test.

Material Properties [159]			**Geometry Parameters**		
Property	Value	Units	Parameter	Value	Units
E_1	161	GPa	Specimen height, $2h$	5.25	mm
E_2	11.38	GPa	Specimen length, S	95	mm
G_{12}	5.2	GPa	Clamp length, r	12.7	mm
ν_{12}	0.32	–	Initial crack length, a	57	mm
Fracture energy Mode I	0.212	N/mm			
Fracture energy Mode II	0.774	N/mm			
Intralaminar fracture energy	0.212	N/mm			

N.B. For the interface (where the delamination front exists), the mode I fracture energy refers to mode I with a crack normal vector that is perpendicular to the 0/90 interface, and analogously, the mode II fracture energy refers to mode II with a crack normal vector that is perpendicular to the 0/90 interface. Furthermore, the intralaminar fracture energy refers to the mode I energy for a matrix crack.

In Figure 10.1, the load is visualized as a point load. However, during the numerical implementation, it was noticed that specifying a displacement condition on a single point led to an artificial crack nucleation site. As a result, to avoid this singularity, the load was applied to a small width of elements in that location. In addition, the location of this point is not specified as it is taken to be a fractional multiple of a. Furthermore, the specimen layup is given by $[90_4/0_3/(90/0)_{2s}/0_3/90_4/T/90_4/0/0/(90/0)_{2s}/0/0/90_3/0/90]$ where left to right reads top to bottom, and the thickness of each ply is given as 0.12 mm.

10.2.2. Understanding the Physics

Prior to discussing the results, some theory is presented on the physical mechanisms at play. As the name suggests, in this test, it is expected that the crack will migrate. Migration here refers to the process in which the crack at an interface relocates to a different one. It is characterized by a kinking of the delamination that progresses into a matrix crack, which reaches a different interface and propagates along it. This phenomenon occurs in composite materials due to the nucleation of local microcracks ahead of the crack tip. Once it becomes energetically favorable, these local microcracks accumulate and start to propagate as a matrix crack, opposed to propagating on the interface as delamination [160].

One way of understanding this process is by considering the plies bounding the delamination to be distinct materials. In such a case, the onset of migration is related to the kinking of cracks on a bi-material interface. The necessary condition for this to occur is as follows [160, 161]:

$$\frac{G^{\beta}_{\text{max}}}{G^{\beta}_{c}} > \frac{G_T}{G^{\text{interface}}_{c}}, \tag{10.1}$$

where G^{β}_{max} is the energy release rate for crack growth into material β, G^{β}_{c} is the energy release rate of material β, G_T is the energy release rate for crack growth along the interface, and $G^{\text{interface}}_{c}$ is the energy release rate of the interface.

Thus, for a crack to kink from an interface between two materials, α and β, into one of those materials, in this case β, the ratio of the fracture energy associated with its growth into that material and the fracture energy of that material should be higher than the ratio of the fracture energy associated with continued growth along the interface and the fracture energy of the interface. For the cross-ply example at hand, material α would refer to the 0° ply stack and material β would refer to the 90° ply stack.

This process can be further understood by analyzing the loading conditions acting on the specimen. Ratcliffe et al. [162] describe this as follows. As the point load is applied, the opening deformation near the pre-crack is coupled with the shear stresses acting across it. This occurs due to the geometry of the specimen and the mismatch in bending stiffness between the 0° ply and the 90° ply stack. The nature of shear stresses acting across the delamination front determines whether delamination will continue across the interface or whether crack kinking will occur. To this end, two situations can be identified:

- If the delamination length is less than the load location, the shear stresses favor crack kinking towards the baseplate. Yet because the 0° ply below the interface prevents this from happening, delamination along the interface continues.
- If the delamination length is greater than the load location, the shear stresses promote crack kinking into the 90° ply stack. This process materializes once it becomes energetically favorable.

The following sections consider the details to determine whether the numerical model is capable of predicting this behavior.

10.2.3. Mesh and Numerical Details

The geometry was discretized using approximately 75820 quadrilateral elements and meshed using the Frontal-Delaunay algorithm in Gmsh [154]. By using 75820 elements, a length scale of 0.06 mm was possible. The mesh was locally refined near the midplane front of the pre-crack, as this is where the expected crack propagation and migration lie. Furthermore, it was ensured that the interface between plies would be represented by at least two rows of elements, and that each ply would have 10 elements in the height direction. Furthermore, the pre-crack was initialized through the mesh, rather than specifying a damage region.

10.2.4. Model Results

The crack paths obtained using the proposed model are visualized in Figure 10.2, Figure 10.3, and Figure 10.4. These figures correspond to the cases where the load point is located at $l/a = 1.0, 1.1, 1.2$, respectively. Due to the scale of the specimen, the zoomed-in crack paths are visualized. These figures are given for qualitative reference; the crack migration offsets are discussed in Section 10.2.5.

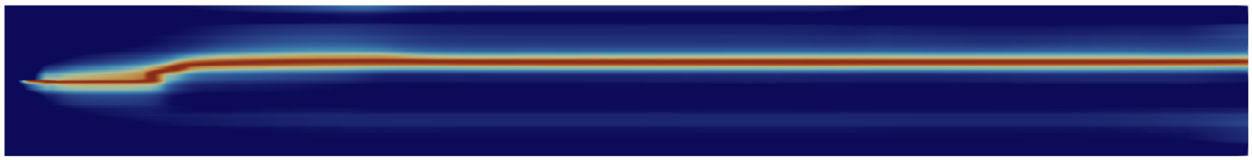

Figure 10.2: Zoomed-in crack path predicted by the model for an l/a ratio of 1.0.

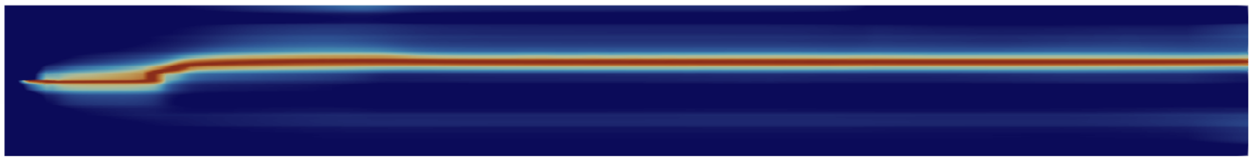

Figure 10.3: Zoomed-in crack path predicted by the model for an l/a ratio of 1.1.

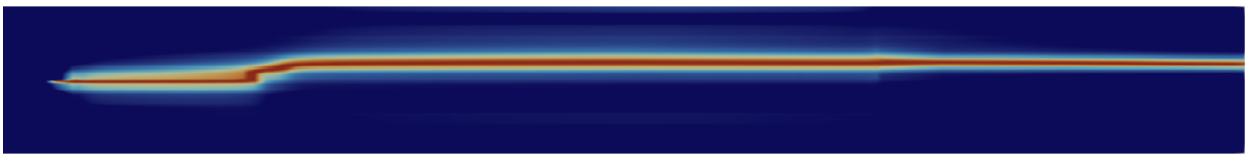

Figure 10.4: Zoomed-in crack path predicted by the model for an l/a ratio of 1.2.

From these figures, it appears that the model is able to predict crack migration. In all cases, the crack initially propagates through delamination, and once it becomes energetically favorable to migrate, it does so. The migration process is characterized by an initial steep segment followed by a curved transition towards the $0/90$ interface. Comparing the figures, it is evident that changing the location of the load changes the point at which delamination occurs, with the trend that as the load moves to the right, the crack migration offset moves to the right.

To understand the effect, if any, of incorporating mode-mixity, the same problem was re-investigated but under mode-independent conditions. In such a case, the zoomed-in crack migration shown in Figure 10.5 was obtained.

Figure 10.5: Zoomed-in crack path predicted by the model for an l/a ratio of 1.0 under mode-independent conditions.

Comparing Figure 10.5 to Figure 10.2, it appears that with suppressed mode-mixity the migration path is more abrupt. Rather than having a curved transition that spans multiple elements horizontally, the migration path is purely vertical.

10.2.5. Comparison of Results

To validate the model, the results obtained are compared to experimental evidence. The crack migration process observed is visualized in Figure 10.6.

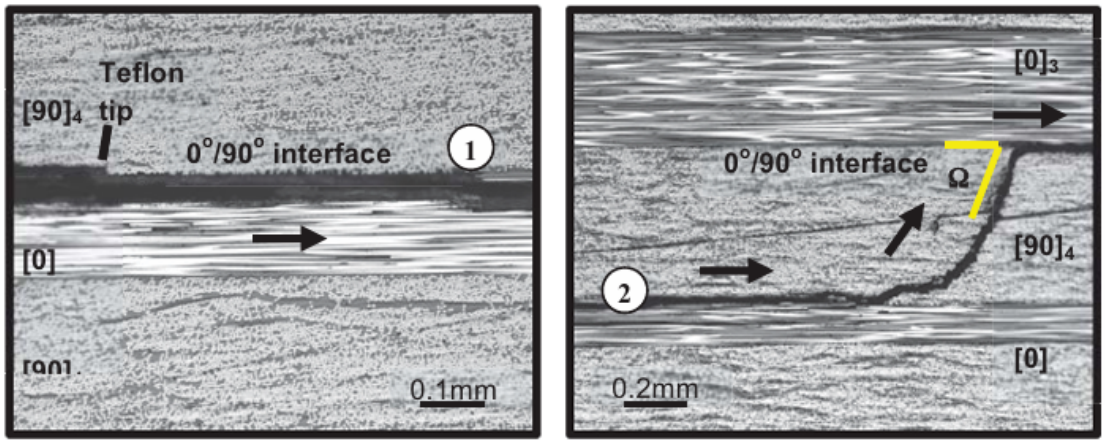

Figure 10.6: Experimentally observed crack migration process [5].

To further quantify these results, the crack migration offset (defined from the initial crack) predicted by the model is compared to the results obtained experimentally for different l/a ratios. These are summarized in Table 10.2.

Table 10.2: Comparison between the crack migration offsets observed using the proposed model and experimentally.

l/a	Crack migration offset, Δx (proposed model)	Crack migration offset, Δx Ratcliffe et al. [162]
1.0	7.0	9.3
1.1	8.3	14.8
1.2	12.3	16.8

Based on these results, the following points can be noted:

- The proposed model correctly identifies the presence of crack migration and the location to which the crack should migrate.
- The model successfully captures the experimentally observed trend that the migration offset distance (defined from the initial crack) increases as the load application point increases. Several explanations for this behavior have been proposed in the literature. One interpretation is that, under mixed-mode loading conditions, the location of the applied load influences the stress state at the delamination front prior to migration. Consequently, the effective fracture energy of the interface changes, altering the point at which crack kinking becomes energetically favorable. Another proposed explanation is that the fracture energy of the interface may depend on the rate of delamination. Hence, variations in crack propagation speed could influence the migration location and the resulting offset distance [5].
- The kink angle observed in the model results is less steep than the ones seen in experiments. However, to make a meaningful remark on this, it is necessary to revisit the effect of the length scale. Under a diffuse

representation of the crack migration process, it is difficult to determine the exact kinking angle. To analyze this further, a significantly finer mesh would be required.

10.3. Transverse Matrix Crack Test

The second example considered is a transverse matrix cracking test for a cross-ply specimen. Similar to before, to discuss this example, the test description is presented. Thereafter, the model results and a comparison of these results to experimental evidence are provided.

10.3.1. Test Description

In this test, a specimen made of a cross-ply layup given by $[0_2/90_4]_s$ with a small initial notch at the center is loaded in tension. The geometry, loading, and boundary conditions are visualized in Figure 10.7. It should be noted that in the figure, the notch is not drawn to scale. It appears larger than numerically implemented for ease of visualization. The geometry parameters and material properties are given in Table 10.3, where the values are equivalent to those used by [7].

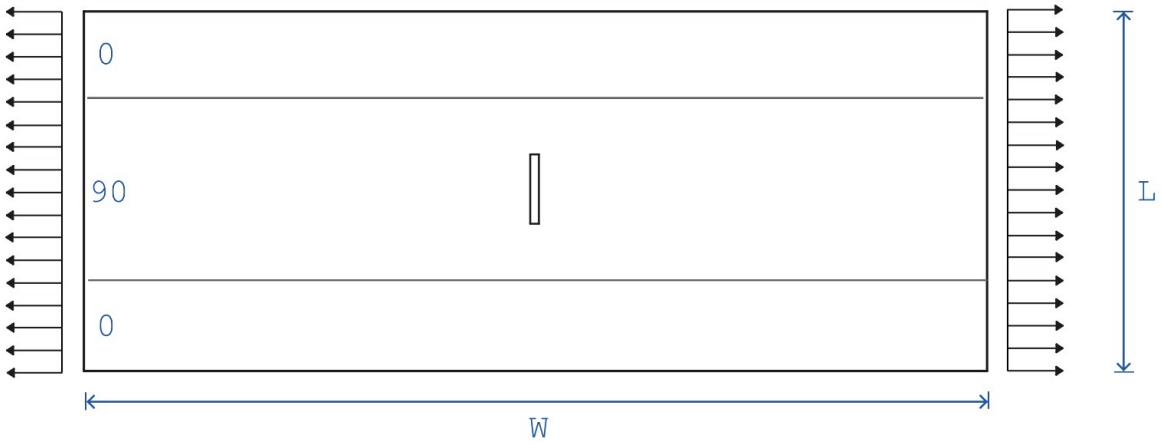

Figure 10.7: Setup of the transverse matrix cracking test.

Table 10.3: Material and geometric parameters used for the transverse matrix cracking test.

Material Properties [7]			**Geometry Parameters**		
Property	Value	Units	Parameter	Value	Units
E_1	171	GPa	Specimen width, W	4	mm
E_2	9.08	GPa	Specimen length, L	20	mm
G_{12}	5.29	GPa			
ν_{12}	0.32	–			
Fracture energy Mode I	0.277	N/mm			
Fracture energy Mode II	0.788	N/mm			
Fiber fracture energy	97.8	N/mm			

N.B. The fiber fracture energy refers to mode I with a crack normal that is in the direction of the fibers (so that the opening direction is perpendicular to the fibers). For the interface, the mode I fracture energy refers to mode I with a crack normal vector that is perpendicular to the interface, and analogously, the mode II fracture energy refers to mode II with a crack normal vector that is perpendicular to the interface.

10.3.2. Mesh and Numerical Details

The geometry was discretized using approximately 48500 quadrilateral elements and meshed using the Frontal-Delaunay algorithm in Gmsh [154]. By using 48500 elements, the maximum element size was restricted to 0.025 mm, and hence the length scale was set to be 0.05 mm. Furthermore, the loading was applied under displacement-controlled conditions using an increment of $\Delta u = 1 \cdot 10^{-3}$ mm.

10.3.3. Model Results

The crack paths obtained using the proposed model are visualized in Figure 10.8.

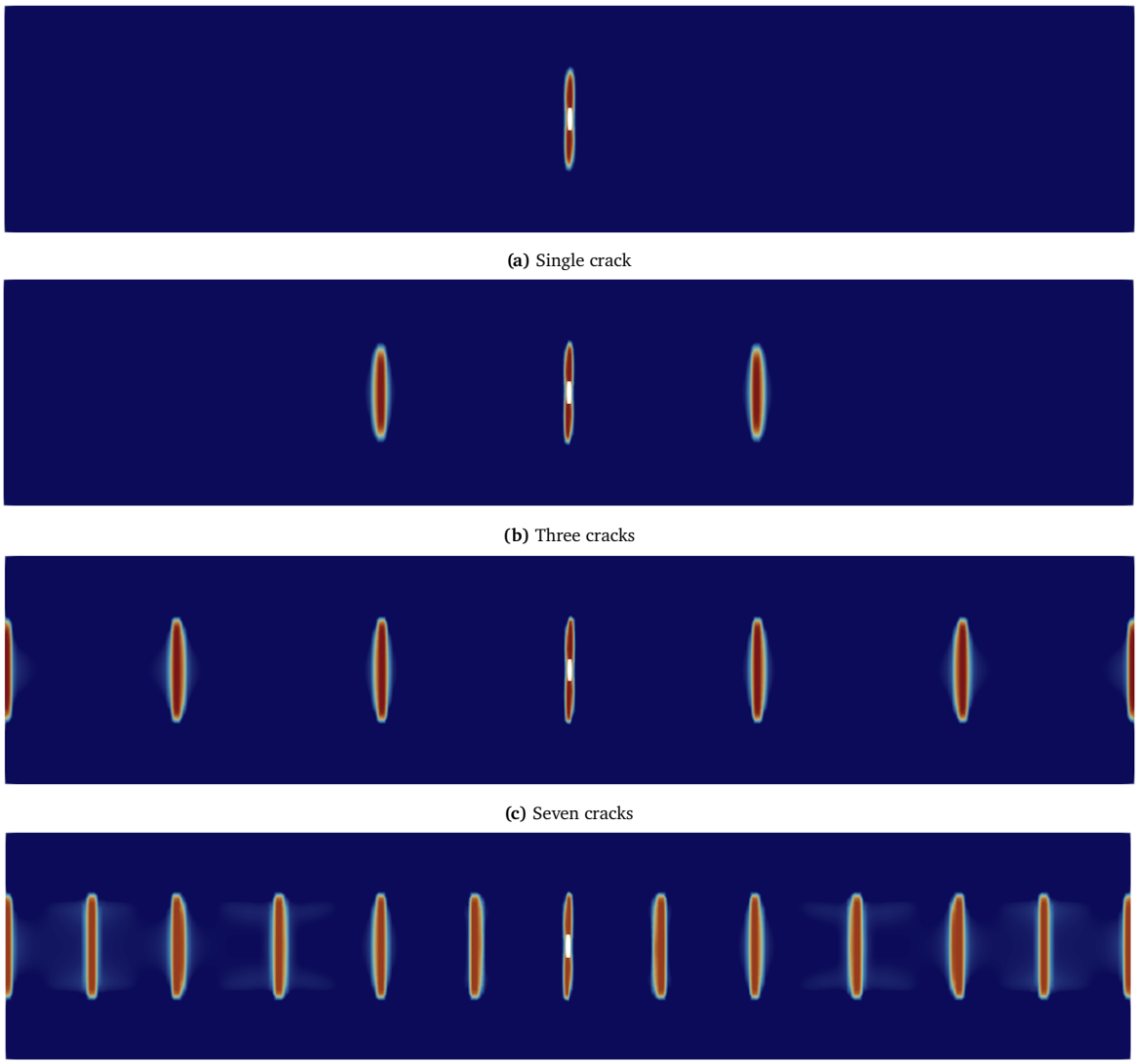

(a) Single crack

(b) Three cracks

(c) Seven cracks

(d) Thirteen cracks

Figure 10.8: Numerical predictions of the transverse matrix cracking test at various points during the fracture process.

From these figures, it appears that the first crack occurs at the location of the notch. This is expected as the notch forms a stress concentration. However, the crack does not propagate through the width of the specimen; the crack halts propagation upon encountering the 0° plies. This makes sense as the fracture energy required to break through those plies is much higher. As a result, upon increasing the load, additional transverse cracks start to form. In all cases, the cracks are parallel and distributed in a symmetric manner (which is expected due to the symmetry of the problem). These results are compared to the literature in the following subsection.

10.3.4. Comparison of Results

To compare the model results, two reference results are considered. The first stems from an experimental study performed and hence can be used for validation purposes. The second is a numerical phase field model. Both of these results are visualized below.

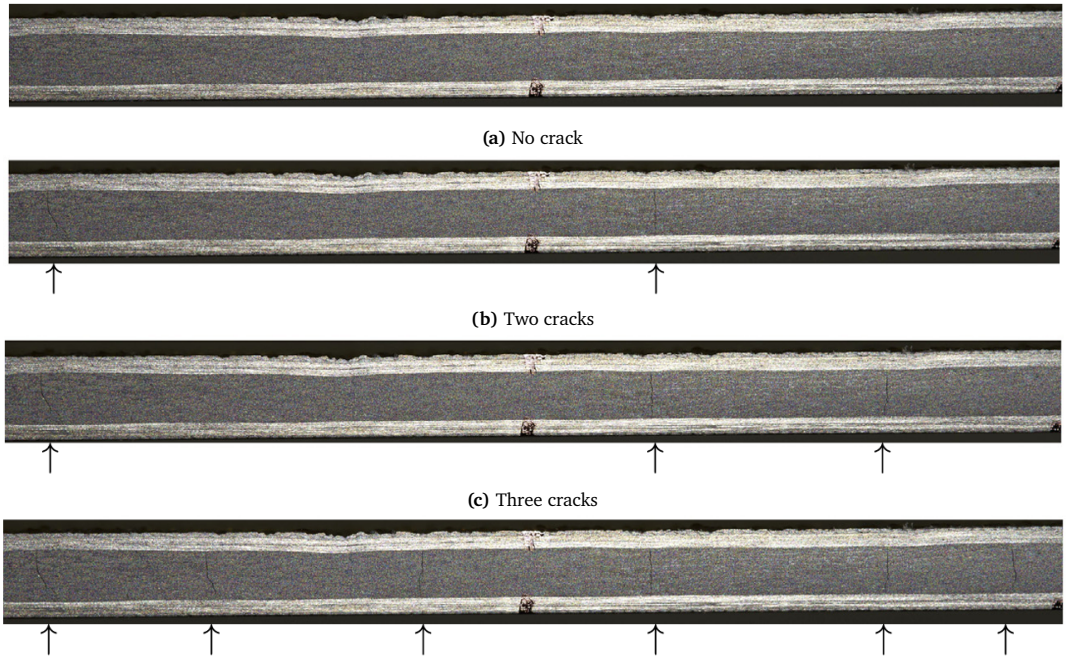

(a) No crack

(b) Two cracks

(c) Three cracks

(d) Six cracks

Figure 10.9: Experimental results of the transverse matrix cracking test at various points during the fracture process [6].

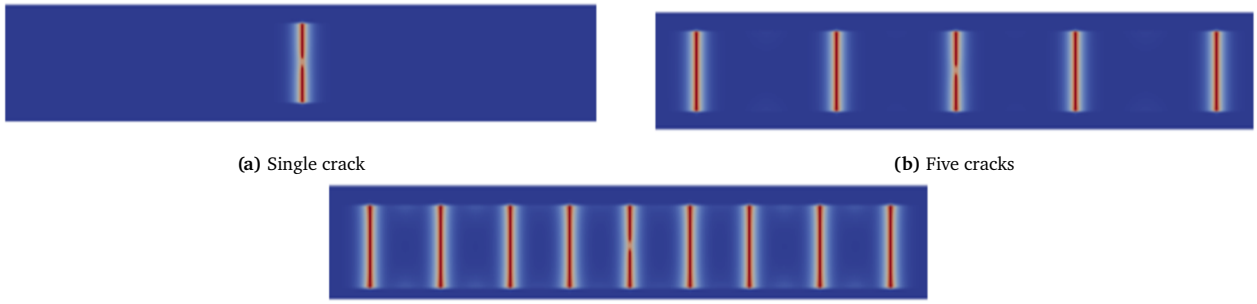

(a) Single crack

(b) Five cracks

(c) Nine cracks

Figure 10.10: Reference numerical results of the transverse matrix cracking test at various points during the fracture process [7].

- Both numerical methods and the experimental evidence show the presence of parallel transverse matrix cracks.
- To characterize the cracks, it is important to consider both their spacing and their angle. For both numerical models, the cracks appear symmetrically and are perfectly aligned with $[0, 1]^{\mathrm{T}}$. This makes sense as the orientation is imposed to 90° in the middle of the specimen and the problem is symmetric with respect to the midplane.
- From Figure 10.9, it appears as though the parallel cracks are not formed symmetrically. However, this claim is inconclusive because the load point and the location of these images with respect to the span of the specimen are not known. To exemplify, if the center of the specimen is between the two cracks in Figure 10.9b, it is possible that the remaining cracks are formed symmetrically, but the other side of the specimen is just not visualized in the figures.
- Furthermore, unlike the numerical examples, the cracks seen in the experiments are not fully straight, and in fact, some of them occur at an angle. In the literature, these are termed oblique cracks and occur after transverse cracks are present. It is noted that they occur due to the microstructure of the composite [163]. As the microstructure is not explicitly modeled, it exceeds the scope of this formulation to be able to capture such phenomena.

Closure

11: Conclusion

This thesis aimed to model anisotropic fracture in a consistent manner using phase field modeling. Motivated by the fracture behavior observed in composites, the work focused on developing a generalized modeling approach capable of capturing the effects of fracture anisotropy and mode-mixity on crack propagation. The main research question guiding the thesis was as follows:

How can advanced fracture processes be modeled in a unified thermodynamically consistent framework?

Alongside this, four research goals were identified, Section 11.1 examines and discusses the attempt made to address them. Thereafter, Section 11.2 returns to the research question and presents some final remarks.

11.1. Reflection on the Research Goals

The following paragraphs discuss the extent to which each goal was met based on the mathematical and numerical results presented in this thesis.

1. Develop a thermodynamically consistent, generalized framework that can account for both anisotropic fracture and varying mode-mixity.

A generalized framework was proposed in which the effects of anisotropy and mode-mixity are embedded directly within the fracture energy formulation. The crack orientation is inferred from the damage gradient, and mode-mixity is characterized by the stress state. Unlike available methods in the literature for computing mode-mixity, this approach has the benefit that it is robust enough to be used in anisotropic contexts. An important characteristic of the proposed approach is that it naturally recovers several well-established formulations as limiting cases. Specifically, when both anisotropy and mode-mixity are suppressed, the formulation reduces to the classical isotropic mode-independent case. Similarly, when either anisotropy or mode-mixity is independently suppressed, the approach recovers the isotropic mixed-mode and anisotropic mode-independent formulations, respectively.

To verify the proposed formulation, several benchmark problems corresponding to these limiting cases were investigated. For the isotropic mode-independent case, the single-edge notched tension and single-edge notched shear tests were considered. For the anisotropic mode-independent case, the single-edge notched tension problem was revisited under imposed preferential fracture directions, together with the open hole tension test. Finally, for the isotropic mixed-mode case, uniaxial compression tests on specimens containing one and two internal flaws were studied. In all cases, the numerical results showed good agreement with reference solutions available in the literature.

Following verification against established benchmark problems, the formulation was applied to more advanced fracture processes observed in composite materials, namely, crack migration and transverse matrix cracking. For the crack migration test, the model successfully reproduced the experimentally observed trend that the migration offset increases as the ratio between the load application point and the delamination front increases. Similarly, in the transverse matrix cracking simulations, the formation of parallel crack patterns was captured successfully, consistent with experimental observations. However, experimentally observed oblique cracking patterns were not reproduced. This limitation is attributed to the homogenized nature of the present formulation, as capturing such mechanisms would require modeling at a finer spatial scale.

2. Present a critical comparison of a structural tensor-based formulation with a direction-dependent fracture energy-based formulation for anisotropic fracture.

The structural tensor-based formulation (also referred to as the classical formulation) remains one of the most widely adopted approaches for incorporating anisotropic fracture behavior within phase field fracture models. However, it introduces two significant shortcomings: the emergence of an orientation-dependent length scale and restrictions to the possible energetic structure. In contrast, the proposed consistent formulation addresses anisotropy by explicitly embedding directional dependence within the fracture energy term itself. As

a consequence, the orientation-dependent length scale artifact is eliminated, while simultaneously allowing greater flexibility in prescribing material-specific fracture behavior. To compare how anisotropy is introduced in the two formulations, a direction-dependent fracture energy that matches the energetics of the classical formulation was derived.

It was demonstrated that the consistent formulation can be calibrated to match the energetics of the classical model. Nevertheless, an important distinction exists in the associated natural boundary conditions. In the classical formulation, a unique admissible damage gradient orientation satisfies the boundary condition, namely, the configuration in which the damage gradient is perpendicular to the crack propagation direction. In contrast, in the limit of the sharp crack, the consistent formulation admits multiple energetically permissible orientations. Specifically, damage gradients aligned with the crack propagation direction, orthogonal to it, and aligned with the normal vector to the boundary are all admissible solutions.

The two formulations were also compared numerically. The single-edge notched tension test performed under varying anisotropic fracture energy parameters showed that the orientation-dependent length scale artifact disappeared in the consistent formulation while maintaining energetic equivalence with the classical approach. For sufficiently refined meshes and small displacement increments, the predicted crack propagation angles agreed well with the expected orientations in both formulations. However, for coarse meshes and/or large displacement increments, curved crack paths emerged for certain preferential orientations. This behavior was attributed to the necessity of maintaining small displacement increments to reach intermediate equilibrium states. Furthermore, a particularly notable case corresponded to a preferential direction oriented at $90°$. Under these conditions, the classical formulation predicted horizontal crack propagation, implying fracture through the fibers. The consistent formulation, however, did not exhibit this behavior, highlighting a fundamental difference in how anisotropy is represented within both approaches.

3. Determine a method to account for varying mode-mixity in a thermodynamically permissible manner that is compatible with anisotropic fracture.

Most existing approaches for incorporating mode-mixity within phase field fracture formulations were originally developed for isotropic fracture conditions. More recently, Zhao et al.[3] proposed a stress-based strategy in which the first eigenvector of the stress tensor is interpreted as a proxy for the mode I contribution. Combined with the displacement field, this allows the angle between the loading and crack opening direction to be quantified, thereby characterizing the extent of mode-mixity. However, within anisotropic fracture settings, the principal stress direction does not necessarily coincide with the mode I contribution. Consequently, a different strategy was proposed in this work based on the crack normal vector. By exploiting the damage gradient, the crack normal can be determined. Once identified, the normal and tangential traction components acting on the crack plane can be determined. The ratio between these components is then used to quantify the degree of mode-mixity.

To assess the validity of the proposed strategy, the framework was evaluated under isotropic mixed-mode conditions, where comparisons with existing methods in the literature were possible. Although the proposed approach differs fundamentally from existing formulations, it was expected that comparable fracture behavior would be obtained. Two benchmark problems were therefore considered: uniaxial compression tests on specimens with one internal flaw and two internal flaws. The numerical results were compared against both reference simulations and experimental observations.

The obtained results showed good agreement with existing approaches reported in the literature, providing confidence in the proposed methodology. For the specimen containing two internal flaws, the predicted crack trajectories differed slightly from the reference numerical solution. This discrepancy was attributed to the fact that the reference model employed separate degradation functions for the mode I and mode II contributions through a multi-damage phase field framework. Nevertheless, the proposed formulation exhibited trends that aligned more closely with experimental observations. As an additional verification step, the same simulations were repeated while suppressing the mode-mixity contribution. In this case, substantially different crack paths were obtained, further highlighting the importance of incorporating mode-mixity.

4. Specialize the proposed framework to the case of VSCL.

Finally, the proposed framework was extended to VSCL characterized by spatially varying fiber orientations. To investigate this capability, the open hole tension test was considered using both the classical and consistent anisotropic fracture formulations. In both cases, the predicted crack trajectories aligned closely with the prescribed fiber paths, demonstrating that the framework successfully captured crack deflection induced by spatially varying fiber orientations. Furthermore, comparison with reference numerical solutions showed good agreement in the load-displacement response. Although the present simulations exhibited slightly higher peak loads, this difference was attributed primarily to mesh resolution effects.

In this test, a notable distinction between the classical and consistent formulations was observed in the nature of the crack paths. The consistent formulation produced comparatively rougher and more jagged crack trajectories. This behavior is likely associated with the manner in which crack orientation is determined in the consistent framework, namely through the damage gradient, which is inherently sensitive to numerical fluctuations. When combined with varying fiber orientations, sharp local variations in the gradient field resulted in less smooth crack trajectories.

11.2. Closing Remarks on the Research Question

Phase field modeling offers a powerful framework for describing fracture evolution in a thermodynamically consistent manner. This thesis has shown that embedding the directional dependence and constitutive characteristics of the material into the fracture energy term is a promising approach for consistently modeling fracture processes. The proposed methodology has direct applications to composite materials due to their inherent anisotropy in fracture properties and dependence on fracture modes. However, the general structure of the proposed method naturally allows extensions to broader constitutive settings, thereby providing a unified framework for several classes of methods that have previously been explored independently or under very specific loading settings in the literature.

12: Recommendations & Next Steps

This thesis introduced a generalized thermodynamically consistent framework for modeling anisotropic and mixed-mode fracture using phase field modeling. While the proposed framework demonstrated the capability to capture several complex fracture phenomena observed, the work primarily served as a proof-of-concept study. Consequently, several aspects of the framework remain open for further investigation and refinement. To provide structure to the recommendations presented in this chapter, future work is categorized into three broad themes:

1. To expand on the scale of the problem investigated.
2. To refine the numerical implementation of the proposed framework.
3. To extend the modeling framework.

Scale of the problem

1. The current framework was formulated and investigated in a 2D setting. A natural extension of this work is its implementation within a 3D context. While the governing continuum equations remain fundamentally unchanged, such an extension would require the development of a 3D finite element implementation. The advantages of this are twofold. Firstly, it allows for capturing the coupling and interactions between the different failure mechanisms exhibited by composites. Secondly, it would allow for the consideration of laminate layups beyond cross-ply configurations.
2. Another manner to expand on the scale concerns mesh refinement and spatial resolution. In the crack migration test investigated, it was noted that to accurately resolve the crack kinking angle, a significantly finer mesh would be required due to the diffuse nature of the crack representation. By considering finer discretizations, this modeling framework could be leveraged to better resolve microstructural fracture behavior and localized crack path transitions.
3. The proposed framework also provides a basis for broader parametric investigations. In particular, for the case where the preferential direction is at $90°$, clear differences were observed between the structural tensor-based approach and direction-dependent fracture energy-based formulations (when under the same energetics). Future studies could therefore investigate the influence of the anisotropic fracture energy parameter on crack propagation behavior in a systematic manner. Such analyses would provide further insight into how the relative fracture energies associated with fibers and matrix constituents influence crack deflection and preferred fracture paths.

Refining the numerical implementation

1. In the numerical example related to the open hole tension test performed with varying fiber orientations using the consistent approach, the crack path was observed to be jagged. This was attributed to the fact that the crack orientation was inferred from the damage gradient. This could potentially be improved by considering one (or both) of the methods below:

   - *Higher-order regularization*: in the current model, the crack surface density only uses the damage gradient and hence $d \in H^1(\Omega)$. However, it could also be considered to incorporate higher-order gradients. In such a case, the crack surface density would be modified to be of the form

   $$\gamma(d, \nabla d, \Delta d) = \frac{1}{c_0 l}\left(\vartheta(d) + l^2|\nabla d|^2 + l^4(\Delta d)^2\right) \ . \tag{12.1}$$

   It has been noted that such formulations lead to greater regularity of the exact solution [78]. By having a smoother damage field, the computed crack orientation obtained from the damage gradient may become less sensitive to local numerical oscillations and mesh-induced irregularities.
   - *Filtering*: rather than modifying the underlying damage field, one could consider inferring the gradient from a filtered field. Examples could be using a Gaussian or Helmholtz filter to smooth the damage field.

2. In the cases considered in this thesis, the mesh remained fixed throughout the simulation. However, as the spatial and geometric complexity of the problem increases, and when crack propagation paths are not known a priori, the mesh requirements can become increasingly demanding. To address this, adaptive meshing algorithms could be employed to locally refine the mesh in regions of high gradients or evolving damage. To reduce the computational overhead associated with repeated remeshing, and inspired by Yu et al. [88], a strategy based on performing remeshing only after the final solution is obtained is suggested.

Extensions to the modeling framework

1. A particularly interesting extension would be the introduction of direction-dependent failure strength in addition to direction-dependent fracture energy. This is because composites exhibit orientation-dependent failure strength. It is known that typically, the failure strength is associated with the length scale value. However, in cohesive-zone-inspired phase field formulations, it has been shown that the global structural response can be independent of the length scale. In such cases, the failure strength is prescribed in the degradation function. To exemplify, Wu [57] introduced a degradation function of the form

$$g(d) = \frac{(1-d)^2}{(1-d)^2 + a_1 d + a_1 a_2 d^2 + a_1 a_2 a_3 d^3}, \tag{12.2}$$

   where, a_1 is given by

$$a_1 = \frac{2E_0 G_c}{f_t^2} \frac{\xi}{c_0 l}, \tag{12.3}$$

   and a_2 and a_3 are related to the target softening law.

   In the case of direction-dependent strength, this could be modified as follows:

$$a_1 = \frac{2E_0 G_c(\nabla d)}{f_t^2(\nabla d)} \frac{\xi}{c_0 l}. \tag{12.4}$$

   In other words, the degradation function is modified to incorporate a failure strength that is orientation-dependent. Under this formulation, the variational problem would have to be revisited (as now the degradation function also had a dependency on the damage gradient).
2. The proposed formulation represents only one possible approach for the anisotropic fracture energy distribution, the mixed-mode dependency, and the coupling anisotropy and mixed-mode fracture within a phase field framework. Numerous alternative formulations remain unexplored. For instance, in the case of crystalline materials, the framework allows for considering strong anisotropy coupled with mode-mixity using a single gradient term. Future work should therefore investigate different approaches for incorporating mode-mixity and anisotropic fracture resistance.

Bibliography

[1] Ambati, M., Gerasimov, T., and Lorenzis, L. D., "A review on phase-field models of brittle fracture and a new fast hybrid formulation," *Computational Mechanics*, Vol. 55, 2015. doi:10.1007/s00466-014-1109-y, URL https://doi.org/10.1007/s00466-014-1109-y.

[2] Wong, L., and Einstein, H., "Systematic evaluation of cracking behavior in specimens containing single flaws under uniaxial compression," *International Journal of Rock Mechanics and Mining Sciences*, Vol. 46, No. 2, 2009, pp. 239–249. doi:https://doi.org/10.1016/j.ijrmms.2008.03.006, URL https://www.sciencedirect.com/science/article/pii/S136516090800066X.

[3] Zhao, D., Yin, B., Storm, J., and Kaliske, M., "A phase-field formulation incorporating mode-dependent fracture toughness for fracture modeling in rock-like materials," *Engineering Fracture Mechanics*, Vol. 289, 2023, p. 109345. doi:https://doi.org/10.1016/j.engfracmech.2023.109345, URL https://www.sciencedirect.com/science/article/pii/S001379442300303X.

[4] Bobet, A., and Einstein, H., "Fracture coalescence in rock-type materials under uniaxial and biaxial compression," *International Journal of Rock Mechanics and Mining Sciences*, Vol. 35, No. 7, 1998, pp. 863–888. doi:https://doi.org/10.1016/S0148-9062(98)00005-9, URL https://www.sciencedirect.com/science/article/pii/S0148906298000059.

[5] Ratcliffe, J. G., and De Varvalho, N. V., "Investigating Delamination Migration in Composite Tape Laminates," Tech. Rep. NASA/CR-2014-218289, NASA Langley Research Center, Hampton, Virginia, July 2014. URL https://ntrs.nasa.gov/api/citations/20140011508/downloads/20140011508.pdf, nIA Report No. 2014-218289.

[6] Sebaey, T., Costa, J., Maimí, P., Batista, Y., Blanco, N., and Mayugo, J., "Measurement of the in situ transverse tensile strength of composite plies by means of the real time monitoring of microcracking," *Composites Part B: Engineering*, Vol. 65, 2014, pp. 40–46. doi:https://doi.org/10.1016/j.compositesb.2014.02.001, URL https://www.sciencedirect.com/science/article/pii/S1359836814000687, damage Mechanics.

[7] Quintanas-Corominas, A., Reinoso, J., Casoni, E., Turon, A., and Mayugo, J., "A phase field approach to simulate intralaminar and translaminar fracture in long fiber composite materials," *Composite Structures*, Vol. 220, 2019, pp. 899–911. doi:https://doi.org/10.1016/j.compstruct.2019.02.007, URL https://www.sciencedirect.com/science/article/pii/S0263822318339928.

[8] Griffith, A. A., "VI. The phenomena of rupture and flow in solids," *Philosophical Transactions of the Royal Society of London, Series A: Containing Papers of a Mathematical or Physical Character*, Vol. 221, No. 582-593, 1921, pp. 163–198. doi:10.1098/rsta.1921.0006, URL https://doi.org/10.1098/rsta.1921.0006.

[9] Barenblatt, G., "The Mathematical Theory of Equilibrium Cracks in Brittle Fracture," Elsevier, 1962, pp. 55–129. doi:https://doi.org/10.1016/S0065-2156(08)70121-2, URL https://www.sciencedirect.com/science/article/pii/S0065215608701212.

[10] Murakami, S., and Liu, Y., "Application of Continuum Damage Mechanics to Fracture Analysis and Its Related Problems," *Computational Mechanics '95*, edited by S. N. Atluri, G. Yagawa, and T. Cruse, Springer Berlin Heidelberg, Berlin, Heidelberg, 1995, pp. 1164–1169.

[11] Silling, S., "Reformulation of elasticity theory for discontinuities and long-range forces," *Journal of the Mechanics and Physics of Solids*, Vol. 48, No. 1, 2000, pp. 175–209. doi:https://doi.org/10.1016/S0022-5096(99)00029-0, URL https://www.sciencedirect.com/science/article/pii/S0022509699000290.

[12] Francfort, G., and Marigo, J.-J., "Revisiting brittle fracture as an energy minimization problem," *Journal of the Mechanics and Physics of Solids*, Vol. 46, No. 8, 1998, pp. 1319–1342. doi:https://doi.org/10.1016/S0022-5096(98)00034-9, URL https://www.sciencedirect.com/science/article/pii/S0022509698000349.

[13] Miehe, C., Hofacker, M., Schänzel, L.-M., and Aldakheel, F., "Phase field modeling of fracture in multi-physics problems. Part II. Coupled brittle-to-ductile failure criteria and crack propagation in thermo-elastic–plastic solids," *Computer Methods in Applied Mechanics and Engineering*, Vol. 294, 2015, pp. 486–522. doi:https://doi.org/10.1016/j.cma.2014.11.017, URL https://www.sciencedirect.com/science/article/pii/S0045782514004435.

[14] Bourdin, B., Larsen, C. J., and Richardson, C. L., "A time-discrete model for dynamic fracture based on crack regularization," *International Journal of Fracture*, Vol. 168, 2011. doi:10.1007/s10704-010-9562-x, URL https://doi.org/10.1007/s10704-010-9562-x.

[15] Huang, C., and Gao, X., "Phase field modeling of hydrogen embrittlement," *International Journal of Hydrogen Energy*, Vol. 45, No. 38, 2020, pp. 20053–20068. doi:https://doi.org/10.1016/j.ijhydene.2020.05.015, URL https://www.sciencedirect.com/science/article/pii/S0360319920317432.

[16] Wu, J.-Y., Nguyen, V. P., Thanh Nguyen, C., Sutula, D., Bordas, S., and Sinaie, S., "Phase field modelling of fracture," *Advances in Applied Mechanics*, Vol. 53, 2019, pp. 1–183, https://www.sciencedirect.com/-science/article/pii/S0065215619300134.

[17] Dalpadulo, E., Russo, M., Gherardini, F., and Leali, F., "Towards the Design-Driven Carbon Footprint Reduction of Composite Aerospace and Automotive Components: An Overview," *CO2 Reduction for Transportation Systems Conference*, SAE International, 2024. doi:https://doi.org/10.4271/2024-37-0032, URL https://doi.org/10.4271/2024-37-0032.

[18] Rivas-Padilla, J. R., Boston, D. M., Boddapati, K., and Arrieta, A. F., "Aero-structural optimization and actuation analysis of a morphing wing section with embedded selectively stiff bistable elements," *Journal of Composite Materials*, Vol. 57, No. 4, 2023, pp. 737–757. doi:10.1177/00219983231155163, URL https://doi.org/10.1177/00219983231155163.

[19] Kwon, Y., and Liu, C., "Study of damage evolution in composites using damage mechanics and micromechanics," *Composite Structures*, Vol. 38, 1997, p. 133–139. doi:10.1016/S0263-8223(97)00049-4.

[20] Haldar, S., Lopes, C., and González, C., "Interlaminar and Intralaminar Fracture Behavior of Carbon Fiber Reinforced Polymer Composites," *Key Engineering Materials*, Vol. 713, 2016, pp. 325–328. doi:10.4028/www.scientific.net/KEM.713.325.

[21] Blackman, B., Sun, F., Teixeira de Freitas, S., de Barros, S., Moreira Arouche, M., and Ivankovic, A., "17 - Understanding fracture mode-mixity and its effects on bond performance," *Advances in Structural Adhesive Bonding (Second Edition)*, edited by D. A. Dillard, Woodhead Publishing in Materials, Woodhead Publishing, 2023, second edition ed., pp. 579–613. doi:https://doi.org/10.1016/B978-0-323-91214-3.00015-6, URL https://www.sciencedirect.com/science/article/pii/B9780323912143000156.

[22] Teichtmeister, S., Kienle, D., Aldakheel, F., and Keip, M.-A., "Phase field modeling of fracture in anisotropic brittle solids," *International Journal of Non-Linear Mechanics*, Vol. 97, 2017, pp. 1–21. doi:https://doi.org/10.1016/j.ijnonlinmec.2017.06.018, URL https://www.sciencedirect.com/science/article/pii/S0020746217301944.

[23] Prajapati, N., Schöller, L., Reder, M., Schneider, D., and Nestler, B., "A physically consistent and quantitative phase-field model for anisotropic fracture in brittle multiphase solids," *Computer Methods in Applied Mechanics and Engineering*, Vol. 450, 2026, p. 118602. doi:https://doi.org/10.1016/j.cma.2025.118602, URL https://www.sciencedirect.com/science/article/pii/S0045782525008746.

[24] Rezaei, S., Mianroodi, J. R., Brepols, T., and Reese, S., "Direction-dependent fracture in solids: Atomistically calibrated phase-field and cohesive zone model," *Journal of the Mechanics and Physics of Solids*, Vol. 147, 2021, p. 104253. doi:https://doi.org/10.1016/j.jmps.2020.104253, URL https://www.sciencedirect.com/science/article/pii/S0022509620304634.

[25] Li, B., Peco, C., Millán, D., Arias, I., and Arroyo, M., "Phase-field modeling and simulation of fracture in brittle materials with strongly anisotropic surface energy," *International Journal for Numerical Methods in Engineering*, Vol. 102, No. 3-4, 2015, pp. 711–727. doi:https://doi.org/10.1002/nme.4726, URL https://onlinelibrary.wiley.com/doi/abs/10.1002/nme.4726.

[26] Cotterell, B., "The past, present, and future of fracture mechanics," *Engineering Fracture Mechanics*, Vol. 69, No. 5, 2002, pp. 533–553. doi:https://doi.org/10.1016/S0013-7944(01)00101-1, URL https://www.sciencedirect.com/science/article/pii/S0013794401001011.

[27] da Vinci, L., "Codex Atlanticus," *Codex Atlanticus*, edited by Pinati, Biblioteca Ambrosiana, Milano, 1894. Manuscript dated ca. 1504.

[28] Galileo, G., *Dialogues Concerning Two New Sciences*, University of Illinois Press, 1936.

[29] Biggs, W. D., *The Brittle Fracture of Steel*, MacDonald and Evans, London, 1960.

[30] Inglis, C. E., "Stresses in a Plate Due to the Presence of Cracks and Sharp Corners," *Proceedings of the Institution of Naval Architects*, Vol. 55, 1913, pp. 219–230.

[31] Wieghardt, K., "Über das Spalten und Zerreißen elastischer Körper," *Zeitschrift für Mathematik und Physik*, Vol. 55, 1907, pp. 60–103.

[32] Irwin, G. R., "Analysis of Stresses and Strains Near the End of a Crack Traversing a Plate," *Journal of Applied Mechanics*, Vol. 24, No. 3, 2021, pp. 361–364. doi:10.1115/1.4011547, URL https://doi.org/10.1115/1.4011547.

[33] Meguid, S. A., *Linear Elastic Fracture Mechanics*, Springer Nature Switzerland, Cham, 2024, pp. 185–225. doi:10.1007/978-3-031-56085-9_8, URL https://doi.org/10.1007/978-3-031-56085-9_8.

[34] Wells, A. A., "Unstable Crack Propagation in Metals: Cleavage and Fast Fracture," *Proceedings of the Crack Propagation Symposium*, Vol. 1, 1961, p. Paper 84.

[35] Zheltov, Y. P., and Kristianovich, S. A., "Hydraulic Fracture of an Oil-Bearing Stratum," *Izvestiya Akademii Nauk SSSR, Otdelenie Tekhnicheskikh Nauk*, , No. 3, 1955, pp. 3–41.

[36] Dugdale, D., "Yielding of steel sheets containing slits," *Journal of the Mechanics and Physics of Solids*, Vol. 8, No. 2, 1960, pp. 100–104. doi:https://doi.org/10.1016/0022-5096(60)90013-2, URL https://www.sciencedirect.com/science/article/pii/0022509660900132.

[37] Rahulkumar, P., Jagota, A., Bennison, S., and Saigal, S., "Cohesive element modeling of viscoelastic fracture: application to peel testing of polymers," *International Journal of Solids and Structures*, Vol. 37, No. 13, 2000, pp. 1873–1897. doi:https://doi.org/10.1016/S0020-7683(98)00339-4, URL https://www.sciencedirect.com/science/article/pii/S0020768398003394.

[38] Suo, Z., Ortiz, M., and Needleman, A., "Stability of solids with interfaces," *Journal of the Mechanics and Physics of Solids*, Vol. 40, No. 3, 1992, pp. 613–640. doi:https://doi.org/10.1016/0022-5096(92)80006-C, URL https://www.sciencedirect.com/science/article/pii/002250969280006C.

[39] Hui, C. Y., Ruina, A., Long, R., and Jagota, A., "Cohesive Zone Models and Fracture," *The Journal of Adhesion*, Vol. 87, No. 1, 2011, pp. 1–52. doi:10.1080/00218464.2011.538315, URL https://doi.org/10.1080/00218464.2011.538315.

[40] Needleman, A., "A Continuum Model for Void Nucleation by Inclusion Debonding," *Journal of Applied Mechanics*, Vol. 54, No. 3, 1987, pp. 525–531. doi:10.1115/1.3173064, URL https://doi.org/10.1115/1.3173064.

[41] Park, K., Paulino, G. H., and Roesler, J. R., "A unified potential-based cohesive model of mixed-mode fracture," *Journal of the Mechanics and Physics of Solids*, Vol. 57, No. 6, 2009, pp. 891–908. doi:https://doi.org/10.1016/j.jmps.2008.10.003, URL https://www.sciencedirect.com/science/article/pii/S0022509608001713.

[42] Dimitri, R., Trullo, M., Zavarise, G., and De Lorenzis, L., "A consistency assessment of coupled cohesive zone models for mixed-mode debonding problems," *Frattura ed Integrità Strutturale*, Vol. 8, 2014, pp. 266–283. doi:10.3221/IGF-ESIS.29.23.

[43] Melenk, J., and Babuška, I., "The partition of unity finite element method: Basic theory and applications," *Computer Methods in Applied Mechanics and Engineering*, Vol. 139, No. 1, 1996, pp. 289–314. doi:https://doi.org/10.1016/S0045-7825(96)01087-0, URL https://www.sciencedirect.com/science/article/pii/S0045782596010870.

[44] Zhuang, X., Zhou, S., Huynh, G., Areias, P., and Rabczuk, T., "Phase field modeling and computer implementation: A review," *Engineering Fracture Mechanics*, Vol. 262, 2022, p. 108234. doi:https://doi.org/10.1016/j.engfracmech.2022.108234, URL https://www.sciencedirect.com/science/article/pii/S0013794422000029.

[45] Simo, J., and Ju, J., "Strain- and stress-based continuum damage models—I. Formulation," *International Journal of Solids and Structures*, Vol. 23, No. 7, 1987, pp. 821–840. doi:https://doi.org/10.1016/0020-7683(87)90083-7, URL https://www.sciencedirect.com/science/article/pii/0020768387900837.

[46] Bažant, Z., and Jirásek, M., "Nonlocal Integral Formulations of Plasticity and Damage: Survey of Progress," *Journal of Engineering Mechanics*, Vol. 128, 2002. doi:10.1061/(ASCE)0733-9399(2002)128:11(1119).

[47] Pham, K., Amor, H., Marigo, J.-J., and Maurini, C., "Gradient Damage Models and Their Use to Approximate Brittle Fracture," *International Journal of Damage Mechanics*, Vol. 20, 2010, pp. 618–652. doi:10.1177/1056789510386852.

[48] Isiet, M., Mišković, I., and Mišković, S., "Review of peridynamic modelling of material failure and damage due to impact," *International Journal of Impact Engineering*, Vol. 147, 2021, p. 103740. doi:https://doi.org/10.1016/j.ijimpeng.2020.103740, URL https://www.sciencedirect.com/science/article/pii/S0734743X20308101.

[49] Friedrich, L. F., Iturrioz, I., Colpo, A. B., and Vantadori, S., "Fracture failure of quasi-brittle materials by a novel peridynamic model," *Composite Structures*, Vol. 323, 2023, p. 117402. doi:https://doi.org/10.1016/j.compstruct.2023.117402, URL https://www.sciencedirect.com/science/article/pii/S0263822323007481.

[50] Xia, Q., Lai, S., Kim, J., and Li, Y., "Phase field modeling of melting and solidification dynamics in metallic powders during the bed fusion process," *Communications in Nonlinear Science and Numerical Simulation*, Vol. 146, 2025, p. 108762. doi:https://doi.org/10.1016/j.cnsns.2025.108762, URL https://www.sciencedirect.com/science/article/pii/S100757042500173X.

[51] Nguyen, S., Folch, R., Verma, V. K., Henry, H., and Plapp, M., "Phase-field simulations of viscous fingering in shear-thinning fluids," *Physics of Fluids*, Vol. 22, No. 10, 2010, p. 103102. doi:10.1063/1.3494550, URL https://doi.org/10.1063/1.3494550.

[52] Li, P., Li, W., Li, B., Yang, S., Shen, Y., Wang, Q., and Zhou, K., "A review on phase field models for fracture and fatigue," *Engineering Fracture Mechanics*, Vol. 289, 2023, p. 109419. doi:https://doi.org/10.1016/j.engfracmech.2023.109419, URL https://www.sciencedirect.com/science/article/pii/S0013794423003776.

[53] Bourdin, B., Francfort, G., and Marigo, J.-J., "Numerical experiments in revisited brittle fracture," *Journal of the Mechanics and Physics of Solids*, Vol. 48, No. 4, 2000, pp. 797–826. doi:https://doi.org/10.1016/S0022-5096(99)00028-9, URL https://www.sciencedirect.com/science/article/pii/S0022509699000289.

[54] Ambrosio, L., and Tortorelli, V. M., "Approximation of functional depending on jumps by elliptic functional via t-convergence," *Communications on Pure and Applied Mathematics*, Vol. 43, No. 8, 1990, pp. 999–1036. doi:https://doi.org/10.1002/cpa.3160430805, URL https://onlinelibrary.wiley.com/doi/abs/10.1002/cpa.3160430805.

[55] Braides, A., "INTRODUCTION," *Gamma-Convergence for Beginners*, Oxford University Press, 2002. doi:10.1093/acprof:oso/9780198507840.003.0001, URL https://doi.org/10.1093/acprof:oso/9780198507840.003.0001.

[56] Barki, A., Zghal, J., Gallimard, L., Bruant, I., Chevaugeon, N., and Davenne, L., "Enforcement of the irreversibility condition in the phase field damage model: Influence of the history variable approximation," *Engineering Fracture Mechanics*, Vol. 328, 2025, p. 111518. doi:https://doi.org/10.1016/j.engfracmech.2025.111518, URL https://www.sciencedirect.com/science/article/pii/S0013794425007192.

[57] Wu, J.-Y., "A unified phase-field theory for the mechanics of damage and quasi-brittle failure," *Journal of the Mechanics and Physics of Solids*, Vol. 103, 2017, pp. 72–99. doi:https://doi.org/10.1016/j.jmps.2017.03.015, URL https://www.sciencedirect.com/science/article/pii/S0022509616308341.

[58] Lorentz, E., Cuvilliez, S., and Kazymyrenko, K., "Modelling large crack propagation: From gradient damage to cohesive zone models," *International Journal of Fracture*, Vol. 178, 2012. doi:10.1007/s10704-012-9746-7.

[59] Lorentz, E., Cuvilliez, S., and Kazymyrenko, K., "Convergence of a gradient damage model toward a cohesive zone model," *Comptes Rendus Mécanique*, Vol. 339, No. 1, 2011, pp. 20–26. doi:https://doi.org/10.1016/j.crme.2010.10.010, URL https://www.sciencedirect.com/science/article/pii/S1631072110001671.

[60] Hai, L., and Feng, Y., "A phase-field cohesive fracture model free from the length scale constraints," *Computer Methods in Applied Mechanics and Engineering*, Vol. 447, 2025, p. 118374. doi:https://doi.org/10.1016/j.cma.2025.118374, URL https://www.sciencedirect.com/science/article/pii/S0045782525006462.

[61] Huber, W., and Asle Zaeem, M., "Length Scale Insensitive Phase-Field Fracture Methodology for Brittle and Ductile Materials," *Theoretical and Applied Fracture Mechanics*, Vol. 133, 2024, p. 104500. doi:https://doi.org/10.1016/j.tafmec.2024.104500, URL https://www.sciencedirect.com/science/article/pii/S0167844224002490.

[62] Zhang, P., Kai, M.-F., Hu, X.-F., and Dai, J.-G., "A phase field model for mixed-mode cohesive failure through fracture energy dissipation at crack surfaces," *Engineering Fracture Mechanics*, Vol. 316, 2025, p. 110869. doi:https://doi.org/10.1016/j.engfracmech.2025.110869, URL https://www.sciencedirect.com/science/article/pii/S0013794425000700.

[63] Amor, H., Marigo, J.-J., and Maurini, C., "Regularized formulation of the variational brittle fracture with unilateral contact: Numerical experiments," *Journal of the Mechanics and Physics of Solids*, Vol. 57, No. 8, 2009, pp. 1209–1229. doi:https://doi.org/10.1016/j.jmps.2009.04.011, URL https://www.sciencedirect.com/science/article/pii/S0022509609000659.

[64] Miehe, C., Welschinger, F., and Hofacker, M., "Thermodynamically consistent phase-field models of fracture: Variational principles and multi-field FE implementations," *International Journal for Numerical Methods in Engineering*, Vol. 83, No. 10, 2010, pp. 1273–1311. doi:https://doi.org/10.1002/nme.2861, URL https://onlinelibrary.wiley.com/doi/abs/10.1002/nme.2861.

[65] Miehe, C., Hofacker, M., and Welschinger, F., "A phase field model for rate-independent crack propagation: Robust algorithmic implementation based on operator splits," *Computer Methods in Applied Mechanics and Engineering*, Vol. 199, No. 45, 2010, pp. 2765–2778. doi:https://doi.org/10.1016/j.cma.2010.04.011, URL https://www.sciencedirect.com/science/article/pii/S0045782510001283.

[66] Zhang, S., Jiang, W., and Tonks, M. R., "A new phase field fracture model for brittle materials that accounts for elastic anisotropy," *Computer Methods in Applied Mechanics and Engineering*, Vol. 358, 2020, p. 112643. doi:https://doi.org/10.1016/j.cma.2019.112643, URL https://www.sciencedirect.com/science/article/pii/S0045782519305274.

[67] Ruan, H., and Peng, X.-L., "Phase-field modeling of anisotropic fracture of additively manufactured parts," *Engineering Fracture Mechanics*, Vol. 323, 2025, p. 111160. doi:https://doi.org/10.1016/j.engfracmech.2025.111160, URL https://www.sciencedirect.com/science/article/pii/S0013794425003613.

[68] Wu, J.-Y., and Nguyen, V. P., "A length scale insensitive phase-field damage model for brittle fracture," *Journal of the Mechanics and Physics of Solids*, Vol. 119, 2018, pp. 20–42. doi:https://doi.org/10.1016/j.jmps.2018.06.006, URL https://www.sciencedirect.com/science/article/pii/S0022509618302643.

[69] Wang, L., Su, H., and Zhou, K., "A phase-field model for mixed-mode cohesive fracture in fiber-reinforced composites," *Computer Methods in Applied Mechanics and Engineering*, Vol. 421, 2024, p. 116753. doi:https://doi.org/10.1016/j.cma.2024.116753, URL https://www.sciencedirect.com/science/article/pii/S0045782524000094.

[70] Wheeler, M., Wick, T., and Wollner, W., "An augmented-Lagrangian method for the phase-field approach for pressurized fractures," *Computer Methods in Applied Mechanics and Engineering*, Vol. 271, 2014, pp. 69–85. doi:https://doi.org/10.1016/j.cma.2013.12.005, URL https://www.sciencedirect.com/science/article/pii/S0045782513003459.

[71] Bharali, R., Larsson, F., and Jänicke, R., "A micromorphic phase-field model for brittle and quasi-brittle fracture," *Computational Mechanics*, Vol. 73, 2024. doi:10.1007/s00466-023-02380-1, URL https://doi.org/10.1007/s00466-023-02380-1.

[72] Geelen, R. J., Liu, Y., Hu, T., Tupek, M. R., and Dolbow, J. E., "A phase-field formulation for dynamic cohesive fracture," *Computer Methods in Applied Mechanics and Engineering*, Vol. 348, 2019, pp. 680–711. doi:https://doi.org/10.1016/j.cma.2019.01.026, URL https://www.sciencedirect.com/science/article/pii/S0045782519300519.

[73] Molnár, G., and Gravouil, A., "2D and 3D Abaqus implementation of a robust staggered phase-field solution for modeling brittle fracture," *Finite Elements in Analysis and Design*, Vol. 130, 2017, pp. 27–38. doi:https://doi.org/10.1016/j.finel.2017.03.002, URL https://www.sciencedirect.com/science/article/pii/S0168874X16304954.

[74] Bhowmick, S., and Liu, G. R., "A phase-field modeling for brittle fracture and crack propagation based on the cell-based smoothed finite element method," *Engineering Fracture Mechanics*, Vol. 204, 2018, pp. 369–387. doi:https://doi.org/10.1016/j.engfracmech.2018.10.026, URL https://www.sciencedirect.com/science/article/pii/S0013794418306209.

[75] Zhou, S., Rabczuk, T., and Zhuang, X., "Phase field modeling of quasi-static and dynamic crack propagation: COMSOL implementation and case studies," *Advances in Engineering Software*, Vol. 122, 2018, pp. 31–49. doi:https://doi.org/10.1016/j.advengsoft.2018.03.012, URL https://www.sciencedirect.com/science/article/pii/S0965997818300061.

[76] Hirshikesh, Natarajan, S., and Annabattula, R. K., "Modeling crack propagation in variable stiffness composite laminates using the phase field method," *Composite Structures*, Vol. 209, 2019, pp. 424–433. doi:https://doi.org/10.1016/j.compstruct.2018.10.083, URL https://www.sciencedirect.com/science/article/pii/S0263822318325935.

[77] Tian, T., Chen, C., He, L., and Wei, H., "Adaptive finite element method for phase field fracture models based on recovery error estimates," *Journal of Computational and Applied Mathematics*, Vol. 472, 2026, p. 116732. doi:https://doi.org/10.1016/j.cam.2025.116732, URL https://www.sciencedirect.com/science/article/pii/S0377042725002468.

[78] Borden, M. J., Hughes, T. J., Landis, C. M., and Verhoosel, C. V., "A higher-order phase-field model for brittle fracture: Formulation and analysis within the isogeometric analysis framework," *Computer Methods in Applied Mechanics and Engineering*, Vol. 273, 2014, pp. 100–118. doi:https://doi.org/10.1016/j.cma.2014.01.016, URL https://www.sciencedirect.com/science/article/pii/S0045782514000292.

[79] Amiri, F., Millán, D., Arroyo, M., Silani, M., and Rabczuk, T., "Fourth order phase-field model for local max-ent approximants applied to crack propagation," *Computer Methods in Applied Mechanics and Engineering*, Vol. 312, 2016, pp. 254–275. doi:https://doi.org/10.1016/j.cma.2016.02.011, URL https://www.sciencedirect.com/science/article/pii/S0045782516300330, phase Field Approaches to Fracture.

[80] Aldakheel, F., Hudobivnik, B., Hussein, A., and Wriggers, P., "Phase-field modeling of brittle fracture using an efficient virtual element scheme," *Computer Methods in Applied Mechanics and Engineering*, Vol. 341, 2018, pp. 443–466. doi:https://doi.org/10.1016/j.cma.2018.07.008, URL https://www.sciencedirect.com/science/article/pii/S0045782518303396.

[81] Chen, Y., Vasiukov, D., Gélébart, L., and Park, C. H., "A FFT solver for variational phase-field modeling of brittle fracture," *Computer Methods in Applied Mechanics and Engineering*, Vol. 349, 2019, pp. 167–190. doi:https://doi.org/10.1016/j.cma.2019.02.017, URL https://www.sciencedirect.com/science/article/pii/S004578251930088X.

[82] Ma, R., and Sun, W., "FFT-based solver for higher-order and multi-phase-field fracture models applied to strongly anisotropic brittle materials," *Computer Methods in Applied Mechanics and Engineering*, Vol. 362, 2020, p. 112781. doi:https://doi.org/10.1016/j.cma.2019.112781, URL https://www.sciencedirect.com/science/article/pii/S0045782519306735.

[83] Kristensen, P. K., and Martínez-Pañeda, E., "Phase field fracture modelling using quasi-Newton methods and a new adaptive step scheme," *Theoretical and Applied Fracture Mechanics*, Vol. 107, 2020, p. 102446. doi:https://doi.org/10.1016/j.tafmec.2019.102446, URL https://www.sciencedirect.com/science/article/pii/S0167844219305580.

[84] Heister, T., Wheeler, M. F., and Wick, T., "A primal-dual active set method and predictor-corrector mesh adaptivity for computing fracture propagation using a phase-field approach," *Computer Methods in Applied Mechanics and Engineering*, Vol. 290, 2015, pp. 466–495. doi:https://doi.org/10.1016/j.cma.2015.03.009, URL https://www.sciencedirect.com/science/article/pii/S0045782515001115.

[85] Wick, T., "Goal functional evaluations for phase-field fracture using PU-based DWR mesh adaptivity," *Computational Mechanics*, Vol. 57, No. 6, 2016, p. 1017–1035. doi:10.1007/s00466-016-1275-1, URL https://doi-org.tudelft.idm.oclc.org/10.1007/s00466-016-1275-1.

[86] Badnava, H., Msekh, M. A., Etemadi, E., and Rabczuk, T., "An h-adaptive thermo-mechanical phase field model for fracture," *Finite Elements in Analysis and Design*, Vol. 138, 2018, pp. 31–47. doi:https://doi.org/10.1016/j.finel.2017.09.003, URL https://www.sciencedirect.com/science/article/pii/S0168874X17303347.

[87] Zhou, S., and Zhuang, X., "Adaptive phase field simulation of quasi-static crack propagation in rocks," *Underground Space*, Vol. 3, No. 3, 2018, pp. 190–205. doi:https://doi.org/10.1016/j.undsp.2018.04.006, URL https://www.sciencedirect.com/science/article/pii/S2467967418300151, computational Modeling of Fracture in Geotechnical Engineering Part I.

[88] Yu, Y., and Hou, C., "Adaptive phase field model for constant/variable stiffness composite laminates based on remeshing technique," *Composite Structures*, Vol. 372, 2025, p. 119620. doi:https://doi.org/10.1016/j.compstruct.2025.119620, URL https://www.sciencedirect.com/science/article/pii/S0263822325007858.

[89] Nguyen-Thanh, N., Li, W., Huang, J., and Zhou, K., "Multi phase-field modeling of anisotropic crack propagation in 3D fiber-reinforced composites based on an adaptive isogeometric meshfree collocation method," *Computer Methods in Applied Mechanics and Engineering*, Vol. 393, 2022, p. 114794. doi:https://doi.org/10.1016/j.cma.2022.114794, URL https://www.sciencedirect.com/science/article/pii/S0045782522001281.

[90] Borden, M. J., Hughes, T. J., Landis, C. M., Anvari, A., and Lee, I. J., "A phase-field formulation for fracture in ductile materials: Finite deformation balance law derivation, plastic degradation, and stress triaxiality effects," *Computer Methods in Applied Mechanics and Engineering*, Vol. 312, 2016, pp. 130–166. doi:https://doi.org/10.1016/j.cma.2016.09.005, URL https://www.sciencedirect.com/science/article/pii/S0045782516311069, phase Field Approaches to Fracture.

[91] Kuhn, C., Noll, T., and Müller, R., "On phase field modeling of ductile fracture," *GAMM-Mitteilungen*, Vol. 39, No. 1, 2016, pp. 35–54. doi:https://doi.org/10.1002/gamm.201610003, URL https://onlinelibrary.wiley.com/doi/abs/10.1002/gamm.201610003.

[92] Hofacker, M., and Miehe, C., "Continuum phase field modeling of dynamic fracture: Variational principles and staggered FE implementation," *International Journal of Fracture*, Vol. 178, 2012. doi:10.1007/s10704-012-9753-8.

[93] Alessi, R., Vidoli, S., and De Lorenzis, L., "A phenomenological approach to fatigue with a variational phase-field model: The one-dimensional case," *Engineering Fracture Mechanics*, Vol. 190, 2018, pp. 53–73. doi:https://doi.org/10.1016/j.engfracmech.2017.11.036, URL https://www.sciencedirect.com/science/article/pii/S0013794417308469.

[94] Carrara, P., Ambati, M., Alessi, R., and De Lorenzis, L., "A framework to model the fatigue behavior of brittle materials based on a variational phase-field approach," *Computer Methods in Applied Mechanics and Engineering*, Vol. 361, 2020, p. 112731. doi:https://doi.org/10.1016/j.cma.2019.112731, URL https://www.sciencedirect.com/science/article/pii/S0045782519306218.

[95] Schreiber, C., Kuhn, C., and Müller, R., "On phase field modeling in the context of cyclic mechanical fatigue," *PAMM*, Vol. 19, No. 1, 2019, p. e201900104. doi:https://doi.org/10.1002/pamm.201900104, URL https://onlinelibrary.wiley.com/doi/abs/10.1002/pamm.201900104.

[96] Schreiber, C., Kuhn, C., Müller, R., and Zohdi, T., "A phase field modeling approach of cyclic fatigue crack growth," *International Journal of Fracture*, Vol. 225, 2020. doi:10.1007/s10704-020-00468-w, URL https://doi.org/10.1007/s10704-020-00468-w.

[97] Schreiber, C., Müller, R., and Kuhn, C., "Phase field simulation of fatigue crack propagation under complex load situations," *Archive of Applied Mechanics*, Vol. 91, 2021. doi:10.1007/s00419-020-01821-0.

[98] Zhang, X., Sloan, S. W., Vignes, C., and Sheng, D., "A modification of the phase-field model for mixed mode crack propagation in rock-like materials," *Computer Methods in Applied Mechanics and Engineering*, Vol. 322, 2017, pp. 123–136. doi:https://doi.org/10.1016/j.cma.2017.04.028, URL https://www.sciencedirect.com/science/article/pii/S0045782516304297.

[99] Fei, F., and Choo, J., "Double-phase-field formulation for mixed-mode fracture in rocks," *Computer Methods in Applied Mechanics and Engineering*, Vol. 376, 2021, p. 113655. doi:https://doi.org/10.1016/j.cma.2020.113655, URL https://www.sciencedirect.com/science/article/pii/S0045782520308409.

[100] Bryant, E. C., and Sun, W., "A mixed-mode phase field fracture model in anisotropic rocks with consistent kinematics," *Computer Methods in Applied Mechanics and Engineering*, Vol. 342, 2018, pp. 561–584. doi:https://doi.org/10.1016/j.cma.2018.08.008, URL https://www.sciencedirect.com/science/article/pii/S0045782518303943.

[101] Hirshikesh, Natarajan, S., Annabattula, R. K., and Martínez-Pañeda, E., "Phase field modelling of crack propagation in functionally graded materials," *Composites Part B: Engineering*, Vol. 169, 2019, pp. 239–248. doi:https://doi.org/10.1016/j.compositesb.2019.04.003, URL https://www.sciencedirect.com/science/article/pii/S135983681930229X.

[102] Asur Vijaya Kumar, P., Dean, A., Reinoso, J., Lenarda, P., and Paggi, M., "Phase field modeling of fracture in Functionally Graded Materials: Γ-convergence and mechanical insight on the effect of grading," *Thin-Walled Structures*, Vol. 159, 2021, p. 107234. doi:https://doi.org/10.1016/j.tws.2020.107234, URL https://www.sciencedirect.com/science/article/pii/S0263823120311046.

[103] Bhong, M., Khan, T. K., Devade, K., Vijay Krishna, B., Sura, S., Eftikhaar, H., Pal Thethi, H., and Gupta, N., "Review of composite materials and applications," *Materials Today: Proceedings*, 2023. doi:https://doi.org/10.1016/j.matpr.2023.10.026, URL https://www.sciencedirect.com/science/article/pii/S2214785323049313.

[104] Zhang, P., Hu, X., Bui, T. Q., and Yao, W., "Phase field modeling of fracture in fiber reinforced composite laminate," *International Journal of Mechanical Sciences*, Vol. 161-162, 2019, p. 105008. doi:https://doi.org/10.1016/j.ijmecsci.2019.07.007, URL https://www.sciencedirect.com/science/article/pii/S0020740318341729.

[105] Clayton, J., and Knap, J., "Phase field modeling of directional fracture in anisotropic polycrystals," *Computational Materials Science*, Vol. 98, 2015, pp. 158–169. doi:https://doi.org/10.1016/j.commatsci.2014.11.009, URL https://www.sciencedirect.com/science/article/pii/S0927025614007769.

[106] Nguyen, T. T., Réthoré, J., and Baietto, M.-C., "Phase field modelling of anisotropic crack propagation," *European Journal of Mechanics - A/Solids*, Vol. 65, 2017, pp. 279–288. doi:https://doi.org/10.1016/j.euromechsol.2017.05.002, URL https://www.sciencedirect.com/science/article/pii/S0997753816303321.

[107] Pranavi, D., Rajagopal, A., and Reddy, J. N., "Phase field modeling of anisotropic fracture," *Continuum Mechanics and Thermodynamics*, Vol. 36, 2024. doi:10.1007/s00161-023-01260-6, URL https://doi.org/10.1007/s00161-023-01260-6.

[108] Li, B., and Maurini, C., "Crack kinking in a variational phase-field model of brittle fracture with strongly anisotropic surface energy," *Journal of the Mechanics and Physics of Solids*, Vol. 125, 2019, pp. 502–522. doi:https://doi.org/10.1016/j.jmps.2019.01.010, URL https://www.sciencedirect.com/science/article/pii/S0022509618308664.

[109] Noii, N., Fan, M., Wick, T., and Jin, Y., "A quasi-monolithic phase-field description for orthotropic anisotropic fracture with adaptive mesh refinement and primal–dual active set method," *Engineering Fracture Mechanics*, Vol. 258, 2021, p. 108060. doi:https://doi.org/10.1016/j.engfracmech.2021.108060, URL https://www.sciencedirect.com/science/article/pii/S0013794421004744.

[110] Su, H., Wang, L., and Chen, B., "A phase-field framework for modeling multiple cohesive fracture behaviors in laminated composite materials," *Composite Structures*, Vol. 347, 2024, p. 118458. doi:https://doi.org/10.1016/j.compstruct.2024.118458, URL https://www.sciencedirect.com/science/article/pii/S0263822324005865.

[111] Bleyer, J., and Alessi, R., "Phase-field modeling of anisotropic brittle fracture including several damage mechanisms," *Computer Methods in Applied Mechanics and Engineering*, Vol. 336, 2018, pp. 213–236. doi:https://doi.org/10.1016/j.cma.2018.03.012, URL https://www.sciencedirect.com/science/article/pii/S0045782518301373.

[112] Bijaya, A., Sagar, S., and Roy Chowdhury, S., "A consistent multi-phase-field formulation for anisotropic brittle fracture," *Engineering Fracture Mechanics*, Vol. 295, 2024, p. 109825. doi:https://doi.org/10.1016/j.engfracmech.2023.109825, URL https://www.sciencedirect.com/science/article/pii/S001379442300783X.

[113] Esteves, C., Boldrini, J., and Bittencourt, M., "Brittle fracture prediction using a degradation tensor-based phase field model," *Engineering Fracture Mechanics*, Vol. 327, 2025, p. 111423. doi:https://doi.org/10.1016/j.engfracmech.2025.111423, URL https://www.sciencedirect.com/science/article/pii/S0013794425006241.

[114] Petrini, A., Esteves, C., Boldrini, J., and Bittencourt, M., "A fourth-order degradation tensor for an anisotropic damage phase-field model," *Forces in Mechanics*, Vol. 12, 2023, p. 100224. doi:https://doi.org/10.1016/j.finmec.2023.100224, URL https://www.sciencedirect.com/science/article/pii/S2666359723000598.

[115] Bui, T. Q., and Hu, X., "A review of phase-field models, fundamentals and their applications to composite laminates," *Engineering Fracture Mechanics*, Vol. 248, 2021, p. 107705. doi:https://doi.org/10.1016/j.engfracmech.2021.107705, URL https://www.sciencedirect.com/science/article/pii/S0013794421001582.

[116] Song, L., Xue, Z., Xia, Z., Wang, K., Xu, C., and Qi, H., "Collaborative multiscale phase-field model for trans-scale fracture propagation of fiber-reinforced composites," *Journal of the Mechanics and Physics of Solids*, Vol. 189, 2024, p. 105686. doi:https://doi.org/10.1016/j.jmps.2024.105686, URL https://www.sciencedirect.com/science/article/pii/S0022509624001522.

[117] Mitrou, A., Arteiro, A., Reinoso, J., and Camanho, P. P., "Modeling fracture of multidirectional thin-ply laminates using an anisotropic phase field formulation at the macro-scale," *International Journal of Solids and Structures*, Vol. 273, 2023, p. 112221. doi:https://doi.org/10.1016/j.ijsolstr.2023.112221, URL https://www.sciencedirect.com/science/article/pii/S002076832300118X.

[118] Yue, J., and Yuan, Z., "A triple-damage model for fibrous composite material with intra- and inter-laminar decomposition, reduced-order-homogenization and phase field method," *International Journal of Solids and Structures*, Vol. 321, 2025, p. 113490. doi:https://doi.org/10.1016/j.ijsolstr.2025.113490, URL https://www.sciencedirect.com/science/article/pii/S0020768325002768.

[119] Verhoosel, C. V., and de Borst, R., "A phase-field model for cohesive fracture," *International Journal for Numerical Methods in Engineering*, Vol. 96, No. 1, 2013, pp. 43–62. doi:https://doi.org/10.1002/nme.4553, URL https://onlinelibrary.wiley.com/doi/abs/10.1002/nme.4553.

[120] May, S., Vignollet, J., and de Borst, R., "A numerical assessment of phase-field models for brittle and cohesive fracture: Γ-Convergence and stress oscillations," *European Journal of Mechanics - A/Solids*, Vol. 52, 2015, pp. 72–84. doi:https://doi.org/10.1016/j.euromechsol.2015.02.002, URL https://www.sciencedirect.com/science/article/pii/S0997753815000157.

[121] Freddi, F., and Iurlano, F., "Numerical insight of a variational smeared approach to cohesive fracture," *Journal of the Mechanics and Physics of Solids*, Vol. 98, 2017, pp. 156–171. doi:https://doi.org/10.1016/j.jmps.2016.09.003, URL https://www.sciencedirect.com/science/article/pii/S0022509616304860.

[122] Feng, Y., Fan, J., and Li, J., "Endowing explicit cohesive laws to the phase-field fracture theory," *Journal of the Mechanics and Physics of Solids*, Vol. 152, 2021, p. 104464. doi:https://doi.org/10.1016/j.jmps.2021.104464, URL https://www.sciencedirect.com/science/article/pii/S002250962100137X.

[123] Feng, Y., and Li, J., "Phase-field cohesive fracture theory: A unified framework for dissipative systems based on variational inequality of virtual works," *Journal of the Mechanics and Physics of Solids*, Vol. 159, 2022, p. 104737. doi:https://doi.org/10.1016/j.jmps.2021.104737, URL https://www.sciencedirect.com/science/article/pii/S0022509621003446.

[124] Quintanas-Corominas, A., Maimí, P., Casoni, E., Turon, A., Mayugo, J. A., Guillamet, G., and Vázquez, M., "A 3D transversally isotropic constitutive model for advanced composites implemented in a high performance computing code," *European Journal of Mechanics - A/Solids*, Vol. 71, 2018, pp. 278–291. doi:https://doi.org/10.1016/j.euromechsol.2018.03.021, URL https://www.sciencedirect.com/science/article/pii/S0997753817303935.

[125] Yuan, J., Mao, Y., and Chen, C., "Multiple-phase-field modeling for fracture of composite materials," *Mechanics of Advanced Materials and Structures*, Vol. 29, No. 28, 2022, pp. 7476–7490. doi:10.1080/15376494.2021.2000081, URL https://doi.org/10.1080/15376494.2021.2000081.

[126] Asur Vijaya Kumar, P. K., Fleischhacker, R., Dean, A., Rolfes, R., and Pettermann, H. E., "Revisiting multi-phase field model for FRCs using Puck theory," *Composite Structures*, Vol. 372, 2025, p. 119549. doi:https://doi.org/10.1016/j.compstruct.2025.119549, URL https://www.sciencedirect.com/science/article/pii/S0263822325007147.

[127] Wang, H.-J., and Chen, J.-F., "Anisotropic phase-field model for fracture analysis of thin fiber-reinforced composites," *Theoretical and Applied Fracture Mechanics*, Vol. 136, 2025, p. 104855. doi:https://doi.org/10.1016/j.tafmec.2025.104855, URL https://www.sciencedirect.com/science/article/pii/S0167844225000138.

[128] Kumar, A., and Sain, T., "A 3D multi-phase-field model for orientation-dependent complex crack interaction in fiber-reinforced composite laminates," *Engineering Fracture Mechanics*, Vol. 303, 2024, p. 110097. doi:https://doi.org/10.1016/j.engfracmech.2024.110097, URL https://www.sciencedirect.com/science/article/pii/S0013794424002601.

[129] Zhang, Y., Guo, J., Shu, Z., Guan, Y., and Ademiloye, A., "Fracture simulation of fiber reinforced composite panels with holes," *Composite Structures*, Vol. 351, 2025, p. 118627. doi:https://doi.org/10.1016/j.compstruct.2024.118627, URL https://www.sciencedirect.com/science/article/pii/S0263822324007554.

[130] Wang, T., Hu, X., Jin, Q., and Yao, W., "Phase field modelling of interlaminar failure in composites using Reddy's higher-order shear deformation theory," *Engineering Fracture Mechanics*, Vol. 324, 2025, p. 111258. doi:https://doi.org/10.1016/j.engfracmech.2025.111258, URL https://www.sciencedirect.com/science/article/pii/S001379442500459X.

[131] Sagar, S., Tiwari, A. K., and Roy Chowdhury, S., "Thermodynamically consistent elastoplastic phase-field fracture model for micromechanical analysis of fibre-reinforced polymer composites," *Composite Structures*, Vol. 357, 2025, p. 118908. doi:https://doi.org/10.1016/j.compstruct.2025.118908, URL https://www.sciencedirect.com/science/article/pii/S026382232500073X.

[132] Jain, I., Muixí, A., Annavarapu, C., Mulay, S. S., and Rodríguez-Ferran, A., "Adaptive phase-field modeling of fracture in orthotropic composites," *Engineering Fracture Mechanics*, Vol. 292, 2023, p. 109673. doi:https://doi.org/10.1016/j.engfracmech.2023.109673, URL https://www.sciencedirect.com/science/article/pii/S0013794423006318.

[133] Mrunmayee, S., Rajagopal, A., Rakesh, K., Basant, K., and Reddy, J., "Phase field approach to predict mixed-mode delamination and delamination migration in composites," *Composite Structures*, Vol. 337, 2024, p. 118074. doi:https://doi.org/10.1016/j.compstruct.2024.118074, URL https://www.sciencedirect.com/science/article/pii/S0263822324002022.

[134] Zhang, N., Yan, X., Guo, X., and Liew, K., "A phase field approach for fiber-reinforced composites incorporating the LaRC03 failure criterion," *Composites Part A: Applied Science and Manufacturing*, Vol. 202, 2026, p. 109451. doi:https://doi.org/10.1016/j.compositesa.2025.109451, URL https://www.sciencedirect.com/science/article/pii/S1359835X25007468.

[135] Guo, W., Ma, Y. E., Chen, P., and Natarajan, S., "An adaptive micropolar phase field model for anisotropic fracture of fiber-reinforced composites," *Composite Structures*, Vol. 378, 2026, p. 119938. doi:https://doi.org/10.1016/j.compstruct.2025.119938, URL https://www.sciencedirect.com/science/article/pii/S0263822325011031.

[136] Konica, S., and Sain, T., "Phase-field fracture modeling for unidirectional fiber-reinforced polymer composites," *European Journal of Mechanics - A/Solids*, Vol. 100, 2023, p. 105035. doi:https://doi.org/10.1016/j.euromechsol.2023.105035, URL https://www.sciencedirect.com/science/article/pii/S0997753823001274.

[137] Yu, Y., Hou, C., and Zhao, M., "A unified anisotropic phase field model for progressive failure of fiber-reinforced composite materials," *Journal of the Mechanics and Physics of Solids*, Vol. 197, 2025, p. 106063. doi:https://doi.org/10.1016/j.jmps.2025.106063, URL https://www.sciencedirect.com/science/article/pii/S0022509625000390.

[138] Arian Nik, M., Fayazbakhsh, K., Pasini, D., and Lessard, L., "Optimization of variable stiffness composites with embedded defects induced by Automated Fiber Placement," *Composite Structures*, Vol. 107, 2014, pp. 160–166. doi:https://doi.org/10.1016/j.compstruct.2013.07.059, URL https://www.sciencedirect.com/science/article/pii/S0263822313003978.

[139] Hossain, M., Hsueh, C.-J., Bourdin, B., and Bhattacharya, K., "Effective toughness of heterogeneous media," *Journal of the Mechanics and Physics of Solids*, Vol. 71, 2014, pp. 15–32. doi:https://doi.org/10.1016/j.jmps.2014.06.002, URL https://www.sciencedirect.com/science/article/pii/S0022509614001215.

[140] Brach, S., Hossain, M., Bourdin, B., and Bhattacharya, K., "Anisotropy of the effective toughness of layered media," *Journal of the Mechanics and Physics of Solids*, Vol. 131, 2019, pp. 96–111. doi:https://doi.org/10.1016/j.jmps.2019.06.021, URL https://www.sciencedirect.com/science/article/pii/S0022509619303333.

[141] Liu, S., Hao, S., and Shen, Y., "Asymptotic homogenization for phase field fracture of heterogeneous materials and application to toughening," *Composite Structures*, Vol. 339, 2024, p. 118134. doi:https://doi.org/10.1016/j.compstruct.2024.118134, URL https://www.sciencedirect.com/science/article/pii/S0263822324002629.

[142] Ma, P.-S., Liu, X.-C., Luo, X.-L., Li, S., and Zhang, L.-W., "Asymptotic homogenization of phase-field fracture model: An efficient multiscale finite element framework for anisotropic fracture," *International Journal for Numerical Methods in Engineering*, Vol. 125, No. 13, 2024, p. e7489. doi:https://doi.org/10.1002/nme.7489, URL https://onlinelibrary.wiley.com/doi/abs/10.1002/nme.7489.

[143] Li, G., Yin, B., Zhang, L., and Liew, K., "Modeling microfracture evolution in heterogeneous composites: A coupled cohesive phase-field model," *Journal of the Mechanics and Physics of Solids*, Vol. 142, 2020, p. 103968. doi:https://doi.org/10.1016/j.jmps.2020.103968, URL https://www.sciencedirect.com/science/article/pii/S0022509620302039.

[144] Jeulin, D., "Towards crack paths simulations in media with a random fracture energy," *International Journal of Solids and Structures*, Vol. 184, 2020, pp. 279–286. doi:https://doi.org/10.1016/j.ijsolstr.2019.06.017, URL https://www.sciencedirect.com/science/article/pii/S002076831930294X, physics and Mechanics of Random Structures: From Morphology to Material Properties.

[145] Liu, N., and Yuan, Z., "Phase field method based on reduced-order-homogenization for fibrous composite material," *International Journal of Solids and Structures*, Vol. 285, 2023, p. 112530. doi:https://doi.org/10.1016/j.ijsolstr.2023.112530, URL https://www.sciencedirect.com/science/article/pii/S0020768323004274.

[146] You, H., Xiang, M., Jing, Y., Guo, L., and Yang, Z., "A strain gradient phase field model for heterogeneous materials based on two-scale asymptotic homogenization," *Journal of the Mechanics and Physics of Solids*, Vol. 200, 2025, p. 106104. doi:https://doi.org/10.1016/j.jmps.2025.106104, URL https://www.sciencedirect.com/science/article/pii/S0022509625000808.

[147] Hirshikesh, Martínez-Pañeda, E., and Natarajan, S., "Adaptive phase field modelling of crack propagation in orthotropic functionally graded materials," *Defence Technology*, Vol. 17, No. 1, 2021, pp. 185–195. doi:https://doi.org/10.1016/j.dt.2020.03.004, URL https://www.sciencedirect.com/science/article/pii/S221491471931342X.

[148] Sidharth, P. C., and Rao, B. N., "An investigation on optimized exponential finite element shape functions in phase-field modeling of fracture," *International Journal for Computational Methods in Engineering Science and Mechanics*, Vol. 0, No. 0, 2025, pp. 1–17. doi:10.1080/15502287.2025.2586281, URL https://doi.org/10.1080/15502287.2025.2586281.

[149] Pc, S., and Rao, B., "Mixed-Mode Fracture in Orthotropic FGMs: A Phase-Field Approach with Exponential Finite Elements," *Acta Mechanica Solida Sinica*, 2025. doi:10.1007/s10338-025-00641-5.

[150] Sidharth, P., and Rao, B., "Phase-field modeling of brittle fracture in functionally graded materials using exponential finite elements," *Engineering Fracture Mechanics*, Vol. 291, 2023, p. 109576. doi:https://doi.org/10.1016/j.engfracmech.2023.109576, URL https://www.sciencedirect.com/science/article/pii/S0013794423005349.

[151] Pan, Z., Zhang, L., and Liew, K., "A phase-field framework for failure modeling of variable stiffness composite laminae," *Computer Methods in Applied Mechanics and Engineering*, Vol. 388, 2022, p. 114192. doi:https://doi.org/10.1016/j.cma.2021.114192, URL https://www.sciencedirect.com/science/article/pii/S0045782521005235.

[152] Takei, A., Roman, B., Bico, J., Hamm, E., and Melo, F., "Forbidden Directions for the Fracture of Thin Anisotropic Sheets: An Analogy with the Wulff Plot," *Phys. Rev. Lett.*, Vol. 110, 2013, p. 144301. doi:10.1103/PhysRevLett.110.144301, URL https://link.aps.org/doi/10.1103/PhysRevLett.110.144301.

[153] Li, T., Marigo, J.-J., Guilbaud, D., and Potapov, S., "Gradient damage modeling of brittle fracture in an explicit dynamics context," *International Journal for Numerical Methods in Engineering*, Vol. 108, 2016. doi:10.1002/nme.5262.

[154] Geuzaine, C., and Remacle, J.-F., "Gmsh: A 3-D Finite Element Mesh Generator with Built-in Pre- and Post-Processing Facilities," *International Journal for Numerical Methods in Engineering*, Vol. 79, 2009, pp. 1309 – 1331. doi:10.1002/nme.2579.

[155] Loiseau, F., and Lazarus, V., "How to introduce an initial crack in phase field simulations to accurately predict the linear elastic fracture propagation threshold?" , 02 2025. doi:10.48550/arXiv.2502.03900.

[156] Eftekhari, M., and Xu, C., "Evaluating MTS criterion in predicting mixed-mode crack extension under different loading conditions," *Fatigue & Fracture of Engineering Materials & Structures*, Vol. 46, No. 1, 2023, pp. 96–110. doi:https://doi-org.tudelft.idm.oclc.org/10.1111/ffe.13850, URL https://onlinelibrary-wiley-com.tudelft.idm.oclc.org/doi/abs/10.1111/ffe.13850.

[157] Xu, B., Xu, T., Xue, Y., Heap, M., Ranjith, P., Wasantha, P., and Li, Z., "Phase-field modeling of crack growth and interaction in rock," *Geomechanics and Geophysics for Geo-Energy and Geo-Resources*, Vol. 8, No. 6, 2022. doi:10.1007/s40948-022-00497-w, URL https://doi.org/10.1007/s40948-022-00497-w.

[158] Bobet, A., "The Initiation of Secondary Cracks in Compression," *Engineering Fracture Mechanics - ENG FRACTURE MECH*, Vol. 66, 2000, pp. 187–219. doi:10.1016/S0013-7944(00)00009-6.

[159] Krueger, R., "Development and Application of Benchmark Examples for Mixed-Mode I/II Quasi-Static Delamination Propagation Predictions," Tech. Rep. NASA/CR-2012-217562, NASA Langley Research Center, Hampton, Virginia, April 2012. URL https://ntrs.nasa.gov/api/citations/20120007197/downloads/20120007197.pdf, nIA Report No. 2012-217562.

[160] De Carvalho, N., Chen, B., Pinho, S., Ratcliffe, J., Baiz, P., and Tay, T., "Modeling delamination migration in cross-ply tape laminates," *Composites Part A: Applied Science and Manufacturing*, Vol. 71, 2015, pp. 192–203. doi:https://doi.org/10.1016/j.compositesa.2015.01.021, URL https://www.sciencedirect.com/science/article/pii/S1359835X15000329.

[161] He, M.-Y., and Hutchinson, J. W., "Kinking of a Crack Out of an Interface," *Journal of Applied Mechanics*, Vol. 56, No. 2, 1989, pp. 270–278. doi:10.1115/1.3176078, URL https://doi.org/10.1115/1.3176078.

[162] Ratcliffe, J. G., Czabaj, M. W., and O'Brien, T. K., "Characterizing Delamination Migration in Carbon/Epoxy Tape Laminates," Tech. Rep. NASA/CR-2012-0016321, NASA Langley Research Center, Hampton, Virginia, October 2012. URL https://ntrs.nasa.gov/api/citations/20120016321/downloads/20120016321.pdf, nIA Report No. 2012-0016321.

[163] Jalalvand, M., Wisnom, M. R., Hosseini-Toudeshky, H., and Mohammadi, B., "Experimental and numerical study of oblique transverse cracking in cross-ply laminates under tension," *Composites Part A: Applied Science and Manufacturing*, Vol. 67, 2014, pp. 140–148. doi:https://doi.org/10.1016/j.compositesa.2014.08.004, URL https://www.sciencedirect.com/science/article/pii/S1359835X14002371.

A: Supporting Derivations for Global Response

In Section 3.2.5, the length scale dependency of the global response of commonly used phase field models was presented. In this appendix, the supporting derivations to obtain those results are provided.

AT2
To derive the relation between the length scale and critical stress of the AT2 model, a 1D case without the influence of the gradient term is considered. To this end, the simplified strong form of the phase field equation is considered, namely

$$\frac{G_c}{l} d - 2(1-d)\psi = 0 \, . \tag{A.1}$$

For the 1D linear elastic case, the Young's modulus is denoted by E_0, and the strain energy is given by

$$\psi = \frac{1}{2} E_0 \varepsilon^2 \, . \tag{A.2}$$

Substituting Equation A.2 into Equation A.1 yields the following expression:

$$d \left(\frac{G_c}{l} + E_0 \varepsilon^2 \right) = E_0 \varepsilon^2 \, . \tag{A.3}$$

In fact, this expression shows the inherent boundedness of the AT2 model, namely that the value of d always remains between 0 and 1.

An expression for the stress can be obtained using Equation A.3, namely

$$\sigma = (1-d)^2 E_0 \varepsilon = E_0 \varepsilon \left(\frac{G_c}{G_c + E_0 l \varepsilon^2} \right)^2 \, . \tag{A.4}$$

The critical strain, that is, the strain at which the maximum stress is observed before the softening regime, can be found by differentiating Equation A.4 with respect to strain. Thus, for the AT2 model, the critical stress is given by

$$\sigma_{cr} = \frac{3}{16} \sqrt{\frac{3 E_0 G_c}{l}} \quad \Rightarrow l = \frac{27 E_0 G_c}{256 \sigma_{cr}^2} \, . \tag{A.5}$$

The second relation follows naturally; as E_0, G_c, and σ_{cr} are material properties, to satisfy Equation A.5 for critical stress, the length scale must be chosen appropriately.

AT1
For the AT1 model, the governing equation in strong form, when neglecting the gradient terms, is

$$\frac{3 G_c}{8 l} d - 2(1-d)\psi = 0 \, . \tag{A.6}$$

When substituting the expression for the ungraded strain energy and then solving for d, the following expression is obtained:

$$d = 1 - \frac{3 G_c}{8 l E_0 \varepsilon^2} \, . \tag{A.7}$$

From this expression, it is apparent that while the upper bound is inherently enforced, the lower bound tends to go to ∞ as $\varepsilon \to 0$. As this bound must be enforced explicitly, it leads to the following condition:

$$d = \begin{cases} 0 & \text{if } \varepsilon \leq \sqrt{\frac{3 G_c}{8 l E_0}} \\ 1 - \frac{3 G_c}{8 l E_0 \varepsilon^2} & \text{else} \end{cases} \tag{A.8}$$

Using a similar procedure to before, yields the following expression for the critical stress, and thereby for the length scale parameter

$$\sigma_{cr} = \sqrt{\frac{3 E_0 G_c}{8 l}} \quad \Rightarrow l = \frac{3 E_0 G_c}{8 \sigma_{cr}^2} \, . \tag{A.9}$$